University of Warsaw

Faculty of Physics

Phd Thesis

Multi-Component Dark Matter and Extensions of the Standard Model Scalar Sector

Aleksandra Drozd

Supervisor:

Prof. Bohdan Grzadkowski

October 2014

Acknowledgements

First and foremost, I am indebted to my advisor, Bohdan Grzadkowski. He has afforded me the opportunity to work on fascinating research topics on the brink of cosmology and particle physics. He has always been extremely supportive, encouraging and understanding and his thoughtful advice has proved invaluable in matters of physics, academia and otherwise. He helped me in many ways to be a better scientist (and a much better speaker).

I would like to thank my collaborators and mentors. Jack F. Gunion, for his invaluable collaboration, insights and his helpful advice. Jose Wudka, for all the discussions about physics and also about the other aspects of life. I have learned so much from our work together, for which I am very grateful; I am also immensely appreciative of the support both Jose and Jack provided during the postdoctoral application process.

I would also like to thank my friends I have made during the past few years. Yun, for his devotion to physics and hard work, which will always be a great source of inspiration for me. Subha, who shows me that it is indeed possible to be a scientist in academia, while also having a wonderful and happy family. I also owe special thanks to Aqeel, who was so kind to proofread parts of this thesis and gave me valuable advice. I would like to thank my friends from our room at Hoza Street for numerous discussions about physics and not only physics, especially Wojtek, Mateusz and Adaś.

I would like to thank Beranger Dumont, Sabine Kraml, Jack Gunion and Yun Jiang for their thorough, complete analysis of the Two Higgs Doublet Model and sharing their results for our 2HDMS project.

And last, but not least I would like to thank my family. My parents for their support all along the way. And Nadbor, without whom I would not find the strength in me to finish this work.

Contents

Preface

Work presented in this thesis is based on the following papers, here listed in chronological order:

- Aleksandra Drozd, Bohdan Grzadkowski and Jose Wudka
  Multi-Scalar-Singlet Extension of the Standard Model - the Case for Dark Matter and an Invisible Higgs Boson
  JHEP, 1204:006, 2012, arXiv:1112.2582

- Aleksandra Drozd, Bohdan Grzadkowski, Jose Wudka
  Cosmology of Multi-Singlet-Scalar Extensions of the Standard Model
  Acta Phys. Polon. B42 (2011) 11, 2255, arXiV:1310.2985
  Conference: C11-09-12.4 Proceedings

- Aleksandra Drozd, Bohdan Grzadkowski, John F. Gunion, and Yun Jiang
  Two-Higgs-Doublet Models and Enhanced Rates for a 125 GeV Higgs.
  JHEP, 1305:072, 2013, arXiv:1211.3580

- Aleksandra Drozd, Bohdan Grzadkowski, John F. Gunion, Yun Jiang
  2HDM and Enhanced Rates in $\gamma\gamma$ Channel
  Acta Phys.Polon. B44 (2013) 7, 1417-1428
  Conference: C13-01-07.5 Proceedings

- Subhadittya Bhattacharya, A. Drozd, Bohdan Grzadkowski and Jose Wudka
  Two-Component Dark Matter
  JHEP, 1310:158, 2013, arXiv:1309.2986,

- Subhadittya Bhattacharya, A. Drozd, Bohdan Grzadkowski and Jose Wudka
  Constraints on Two-Component Dark Matter
  Acta Phys.Polon. B44 (2013) 11, 2373-2379, arXiv:1310.7901
  Conference: C13-09-01.2 Proceedings

- Aleksandra Drozd, Bohdan Grzadkowski, John F. Gunion and Yun Jiang
  Extending two-Higgs-doublet models by a singlet scalar field - the Case for Dark Matter
  arXiv:1408.2106, submitted to JHEP

I. INTRODUCTION

The Standard Model of Elementary Interactions (SM) is arguably the most successful theory in physics. It is unrivaled in the accuracy of its predictions and range of explained phenomena. Nevertheless, there is mounting evidence from experimental, observational and theoretical sources that it is not a complete description of elementary particles and interactions.

Dark Matter

One of the biggest drawbacks of the SM is its inability to explain the existence of non-luminous dark matter (DM), which accounts for almost 85% of matter present in the Universe [1].

DM's existence is well established, based on numerous astrophysical and cosmological observations. Many beyond the SM models has been proposed to explain its peculiar properties. The most popular theories assume that DM consists of weakly-interacting massive particles (WIMPs) of a single kind (*eg.* the lightest supersymmetric particle, LSP). Such models can predict the present density of DM in the Universe, however they often face difficulties when confronted with other experimental results from DM searches, like conflicting DM direct detection results (that will be discussed later in this thesis).

Another DM-related mystery is the core-cusp problem [2] concerning discrepancies between predicted DM density in the center of galaxies and the observations. The core-cusp problem is still investigated, a promising solution is e.g. introduction of DM with special properties like multi-component structure or significant self-interaction. To account for discrepancies between direct detection experiments models with *i.e.* isospin-violating DM were proposed. Examples of such models will be discussed in this thesis.

Matter-Antimatter Imbalance

The SM also fails to resolve the problem of matter-antimatter imbalance. Every macroscopic object that has ever been observed seems to be made entirely out of ordinary matter with antimatter contributing a negligible amount to the composition of the Universe. This asymmetry again cannot be explained within the SM alone and new physics is required.

Many physicists introduce hypothetical processes of baryogenesis (leptogenesis), that might produce a baryon–antibaryon (lepton–antilepton) asymmetry. Any theory that can explain baryogenesis (leptogenesis) must neccessarily allow for more severe CP violation than present in the SM [3].

LHC results

The Standard Model contains a single scalar particle, a Higgs boson, that was first observed in 2012 in the Large Hadron Collider (LHC) experiments ATLAS [4] and CMS [5]. Both collaborations measure signal strenghts of the Higgs boson decay modes and, as of today, observe some enhancement in the $\gamma\gamma$ channel, relative to the SM prediction. If the enhancement remains after the 14 TeV run of the LHC, it might be an indication of physics beyond the Standard Model. Such enhancement is possible if an extended scalar sector is introduced, for example within a Two-Higgs Doublet Model [6–12] or other models (*eg.* [13]).

Theoretical Issues

Further problems the SM is facing are theoretical inconsistencies within the model itself. One of them is *the little hierarchy problem* [14], that concerns the quantum corrections to the Higgs boson (h) mass (m_h). A 1-loop calculation of m_h within the SM shows very large corrections, that need to cancel with unnatural precision to account for Higgs mass in GeV range ($m_h \simeq 125$ GeV). For the applicability of the perturbative calculation, NLO loop contributions should be at most of the same order as the measured Higgs mass.

The the discovery of the SM Higgs boson and first measurement of its mass followed a very precise calculation of the effective potential (for the NNLO results see [15]). These calculations indicate the SM vacuum is not stable but rather in a metastable state (there exists another minimum, but the tunnelling time to that minimum was estimated to be much longer than the present age of the Universe). This result holds for values of the SM parameters that are within 2σ deviation from current measurements. It is rather disturbing, and calls for an explanation - which would necessarily involve physics beyond the SM.

Over the years a myriad of models extending SM were developed to account for some

or all of those issues[1]. So far none has been completely successful. In this thesis some models that address the aforementioned issues will be discussed. The extensions of the SM that will be considered are: the O(N) Singlet Scalar Model, the Two-Higgs Doublet Model (2HDM), Two-Higgs Doublet Model with a Scalar Singlet (2HDMS) and Two-Component Dark Matter Model (2CDMM).

A. Structure of the Thesis

In Chapter II we remind the reader basic facts of cosmology, that are necessary for understanding the physics of dark matter (DM). In Chapter III we discuss theoretical foundations of DM, its detection methods and current status of experiments related to DM searches. In Chapter IV we introduce the O(N) Singlet Scalar Model - a minimalistic model of N-component DM. We discuss its properties and constraints on its parameter space. In Chapter V we introduce the Two-Higgs Doublet Model (2HDM) and discuss its implications on the Higgs boson phenomenology and LHC searches. In Chapter VI we discuss the Two-Higgs Doublet Model with a Scalar Singlet (2HDMS) and concentrate on its implications for DM phenomenology. In Chapter VII we discuss phenomenology of a minimal 2-component DM model (2CDMM), with one singlet scalar and one singlet fermion DM components.

All Feynman rules for beyond SM interactions are given in Appendix A. Details concerning calculations of the thermally averaged cross section, in particular temperature expansion and cross sections within particular models are given in Appendix B. In Appendix C we discuss the technical details behind elastic scattering of DM off a nuclei and direct detection cross section calculations.

The references are given in the same order, as they appear in the text.

[1] There are also other problems of the SM, that are not mentioned here, as they are not relevant in the discussions in this thesis. One of them would be the presence of neutrino oscillations, that cannot be described within the SM. This problem can be managed if heavy right-handed neutrinos are introduced, which does not influence our analysis.

B. Constants and Conventions

In the text we use the following acronyms (defined also when used for the first time):

DM = Dark Matter

SM = Standard Model (of Elementary Interactions)

WIMP = Weakly-Interacting Massive Particle

CDM = Cold Dark Matter

FIDM = Feebly Interacting Dark Matter

IVDM = Isospin-Violating Dark Matter

2HDM = Two-Higgs Doublet Model

2HDMS = Two-Higgs Doublet Model with a Scalar Singlet

2CDMM = Two-Component Dark Matter Model

BEQ = Boltzmann Equation

GGF = Gluon Gluon Fusion

VBF = Vector Boson Fusion

SSB = Spontaneous Symmetry Breaking

LO = leading order

NLO = next-to-leading order

NNLO = next-to-next-to-leading order

We use units, in which the light speed c, the reduced Planck constant $\hbar$ and the Boltzmann constant k_B are equal to 1, $c = \hbar = k_B = 1$. The Planck mass

$$m_{Pl} = \sqrt{\hbar c/G} = 1.2209 \times 10^{19}\ \text{GeV}, \tag{1}$$

where G is the gravitational constant, in this units

$$G = 6.7087 \times 10^{-39}\ \text{GeV}^{-2}. \tag{2}$$

We also use $(+,-,-,-)$ metric signature.

II. COSMOLOGY

In this chapter we will briefly introduce the reader to the theoretical foundations of cosmology. In Section II A we will discuss mathematical formalism necessary for describing the physics of homogenous and isotropic Universe, whereas in Section II B we will discuss the basics thermodynamical issues related to cosmology.

A. Homogenous and Isotropic Universe

The fundamental assumption of the standard model of cosmology is known as the cosmological principle and is an extension of the Copernican principle. It states that the large scale structure of the Universe must be such that it looks the same for all observers. In terms of spacetime geometry it means that the geometry is:

- homogenous i.e. same everywhere (invariant under translations)
- isotropic i.e. same in every direction (invariant under rotations)

Both assumptions are demonstrably true at least for the part of the Universe that we can observe. The most general metric describing a Universe with properties of homogeneity and isotropy is the Friedmann–Lemaître–Robertson–Walker (FLRW) metric [16],

$$\begin{gathered} ds^2 = g_{\mu\nu}dx^\mu dx^\nu = -dt^2 + a^2(t)\left(\frac{dr^2}{1-kr^2} + r^2 d\Omega^2\right), \\ d\Omega^2 = d\theta^2 + \sin^2\theta d\phi^2, \end{gathered} \tag{3}$$

where k equal to $-1, 0, 1$, corresponds to negative, zero or positive spacial curvature, respectively. The dynamics of the FLRW Universe is captured in the evolution of the scale factor $a(t)$ which is determined by the Einstein's equations:

$$R_{\mu\nu} - \frac{1}{2}g_{\mu\nu}R + g_{\mu\nu}\Lambda = 8\pi G T_{\mu\nu} \tag{4}$$

where $R_{\mu\nu}$ is the Ricci curvature tensor (see [16]), $R = R^\mu_\mu$ is the scalar curvature, Λ is the cosmological constant, G is Newton's gravitational constant and $T_{\mu\nu}$ is the stress–energy tensor. $T_{\mu\nu}$ is a diagonal, perfect fluid tensor, with mass density ρ and pressure p:

$$T_{\mu\nu} = \mathrm{diag}(\rho, p, p, p)_{\mu\nu} \tag{5}$$

From (4) one can derive a set of Friedman equations, describing the expansion of space in FLRW Universe:

$$\frac{\dot{a}^2 + k}{a^2} = \frac{8\pi G\rho + \Lambda}{3} \tag{6}$$

$$\frac{\ddot{a}}{a} = -\frac{4\pi G}{3}(\rho + 3p) + \frac{\Lambda}{3}. \tag{7}$$

We will define the Hubble constant, measuring the rate of expansion,

$$H \equiv \frac{\dot{a}}{a}, \tag{8}$$

and density related to the cosmological constant Λ,

$$\rho_\Lambda \equiv \frac{\Lambda}{8\pi G}. \tag{9}$$

Then, for the density ρ being a combination of matter and radiation densities, $\rho = \rho_m + \rho_r$, the equation (6) reads:

$$H^2 = \frac{8\pi G\rho}{3}(\rho_m + \rho_r + \rho_\Lambda) - \frac{k}{a^2} \tag{10}$$

We define critical density ρ_{crit} as the density for which the Universe is flat ($k = 0$). This happens for

$$\rho_m + \rho_r + \rho_\Lambda = \rho_{crit} \equiv \frac{3H^2}{8\pi G}. \tag{11}$$

We also define Ω, as the ratio of density, to the critical density,

$$\Omega \equiv \frac{\rho}{\rho_{crit}}, \tag{12}$$

which is usually evaluated for present times for baryonic matter Ω_b, dark matter, Ω_{DM}, and dark energy, Ω_Λ.

The Friedman equations can be integrated to get the present age of the Universe, as a function of cosmological parameters. It is an easy calculation for the special case of radiation dominated Universe (RD), when the energy scales like $\rho/\rho_0 = (a/a_0)^{-4}$ and matter dominated Universe (MD) with $\rho/\rho_0 = (a/a_0)^{-3}$. For a general perfect fuid with $p = \omega\rho$, we have:

$$\begin{aligned} \rho &\propto a^{-3(1+\omega)} \\ a &\propto t^{2/3(1+\omega)} \end{aligned} \tag{13}$$

where $\omega = 1/3$ for RD, $\omega = 0$ for MD. In a Universe dominated by cosmological constant we have $\omega = -1$ and $a \propto \exp(Ht)$.

B. Thermodynamics of the Universe

The number density n, energy density ρ and pressure p of an interacting gas of particles ϕ with g_ϕ internal degrees of freedom, reads

$$\begin{aligned} n_\phi(t) &= \frac{g_\phi}{(2\pi)^3}\int \tilde{f}_\phi(\mathbf{p},x,t)d^3\mathbf{p}, \\ \rho_\phi(t) &= \frac{g_\phi}{(2\pi)^3}\int E\tilde{f}_\phi(\mathbf{p},x,t)d^3\mathbf{p}, \\ p_\phi(t) &= \frac{g_\phi}{(2\pi)^3}\int \frac{|\vec{\mathbf{p}}|^3}{3E}\tilde{f}_\phi(\mathbf{p},x,t)d^3\mathbf{p}. \end{aligned} \tag{14}$$

Where $\tilde{f}(\mathbf{p},x,t)$ is the phase space distribution. In homogenous and isotropic Universe, we have $\tilde{f}(\mathbf{p},x,t)=\tilde{f}(E,t)$. For Fermi-Dirac or Bose-Einstein particles in equilibrium we can define the corresponding equilibrium number density n^{EQ}, energy density ρ^{EQ}, and pressure p^{EQ} using the equilibrium distribution

$$\begin{aligned} n_\phi^{EQ}(T) &= \frac{g_\phi}{(2\pi)^3}\int \tilde{f}_\phi^{EQ}(E,T)d^3\mathbf{p}, \\ \rho_\phi^{EQ}(T) &= \frac{g_\phi}{(2\pi)^3}\int E\tilde{f}_\phi^{EQ}(E,T)d^3\mathbf{p}, \quad \tilde{f}_\phi^{EQ}(E,T)=(e^{(E-\mu)/T}\pm 1)^{-1}, \\ p_\phi^{EQ}(T) &= \frac{g_\phi}{(2\pi)^3}\int \frac{|\vec{\mathbf{p}}|^3}{3E}\tilde{f}_\phi^{EQ}(E,T)d^3\mathbf{p}, \end{aligned} \tag{15}$$

where $+$ corresponds to fermions, $-$ to bosons. T is the temperature of ϕ and μ is the chemical potential. In the relativistic limit ($T \gg m_\phi$, $T \gg \mu$) for both bosons and fermions we have [16]:

$$\begin{aligned} n_\phi^{EQ} &= \begin{cases} \frac{\zeta(3)}{\pi^2}g_\phi T^3 & \text{(bosons)} \\ \frac{3}{4}\frac{\zeta(3)}{\pi^2}g_\phi T^3 & \text{(fermions)} \end{cases} \\ \rho_\phi^{EQ} &= \begin{cases} \frac{\pi^2}{30}g_\phi T^4 & \text{(bosons)} \\ \frac{7}{8}\frac{\pi^2}{30}g_\phi T^4 & \text{(fermions)} \end{cases} \\ p_\phi^{EQ} &= \frac{1}{3}\rho_\phi^{EQ} \end{aligned} \tag{16}$$

In the non-relativistic limit ($T \ll m_\phi$) we have the same number density, energy and pressure for both bosons and fermions:

$$\begin{aligned} n_\phi^{EQ} &= g_\phi\left(\frac{m_\phi T}{2\pi}\right)^{3/2}\exp(-(m_\phi-\mu)/T) \\ \rho_\phi^{EQ} &= m_\phi n_\phi^{EQ} \\ p_\phi^{EQ} &= n_\phi^{EQ}T \end{aligned} \tag{17}$$

We can evaluate total energy density ρ_R and pressure p_R for all species present in the Universe. Since the energy density and pressure of non-relativistic particles is exponentially smaller than relativistic particles, we only include relativistic degrees of freedom in ρ_R and p_R, namely:

$$\begin{aligned} \rho_R &= \frac{\pi^2}{30} g_* T^4 \\ p_R &= \frac{\pi^2}{90} g_* T^4 \\ g_* &= \sum_{bosons} g_i \left(\frac{T_i}{T}\right) + \frac{7}{8} \sum_{fermions} g_i \left(\frac{T_i}{T}\right) \end{aligned} \tag{18}$$

where we normalize temperatures of each particle species to the photon temperature T (as in general each particle species i might have a thermal distribution of different temperature T_i). During the radiation dominated epoch when $\rho \simeq \rho_R$, $g_* \simeq const$, $p_R \simeq \rho_r/3$ and $a(t) \propto t^{1/2}$, we have

$$t = \frac{1}{2H} = \frac{1}{2KT^2}, \qquad K = \sqrt{\frac{4\pi^2 g_*(T)}{45 m_{Pl}^2}} \tag{19}$$

where $m_{Pl} = (8\pi G)^{-1/2}$ is the Planck mass. Note that the factor K is actually a function of temperature, hidden in $g_*(T)$, the number of relativistic degrees of freedom.

The Hubble constant is usually written as $H = hH_0$, where $H_0 = 100\,\mathrm{km/s/Mpc}$ and all the uncertainty relative to the value of H is relegated on h.

III. DARK MATTER

In this chapter we would like to remind the reader of theoretical foundations behind DM cosmology and its detection methods. In Section III A we introduce the evidence towards DM presence in our Universe. We discuss the basic properties of DM in Section III B and then follow with a detailed discussion of relic density in Section III C. The theory behind DM direct detection experiments and its current status are contained in Section III D.

A. Evidence for Dark Matter

The first person to postulate the existence of DM was a Dutch astronomer Jan Oort [17]. In 1932 he studied velocities of stars in the Milky Way and their distribution relative to the center of the galaxy. He noticed that the visible mass could not account for the velocities of the stars and postulated that some mass remains undetected. In 1933 Fritz Zwicky came to a similar conclusion in his studies of the Coma galaxy cluster [18] - he also noticed the necessary existence of some kind of unseen matter.

Since the time of Oort and Zwicky the evidence for the existence of DM has been growing steadily and we will review some of them.

Rotation Curves

The expected orbital velocities of stars in various observed galactic disks do not match the velocities expected from calculations based on the visible mass of those galaxies [19], see Fig. 1. The difference between the expected and observed rotation can be attributed to the presence of DM and its gravitational interaction. However, there are also theories alternative to DM, like modified gravity (MOND), that can explain the rotation curves without presence of the additional mass.

Gravitational Lenses

Gravitational lensing is the distortion of light of a distant astronomical object by the gravitational influence of another heavy object. All lensing phenomena are categorized into three groups:

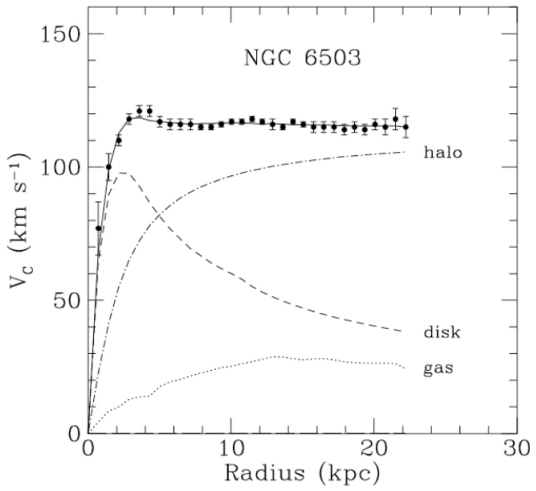

Figure 1: Data points and fit to the rotation curve of NGC 6503, together with rotation curves established from analysis of visible components (disk), gas and the missing dark component (halo). Source: [19]

- strong lensing - easily visible distortions such as the formation of Einstein rings, arcs, and multiple images
- weak lensing - smaller distortions only to be detected by detailed analysis
- microlensing - no distinguishable distortions but brightness changing over time

When it comes to DM searches, weak lensing is of particular interest [20]. After statistical analysis of shapes and orientations of galaxies in a chosen area, we can reconstruct the mass distribution that is distorting the image, see Fig. 2. This corresponds to reconstructing the DM structure present in the foreground, between the galaxies and the observer on Earth.

Considering all the evidence from the sources described above as well and other sources not mentioned, one can say that the idea of DM presence in our Universe is well established (for a review see for example [21]). However, despite many experimental efforts, the nature of DM remains unknown. The SM particles have been excluded as significant contributors to DM [22] which forces us to look for solutions beyond the SM. For more than 20 years theoretical physicists were trying to explain the mystery of DM considering a variety of theories/models. The most popular ideas can be put into 2 categories:

- various extensions of the SM providing new particles, for example weakly-interacting

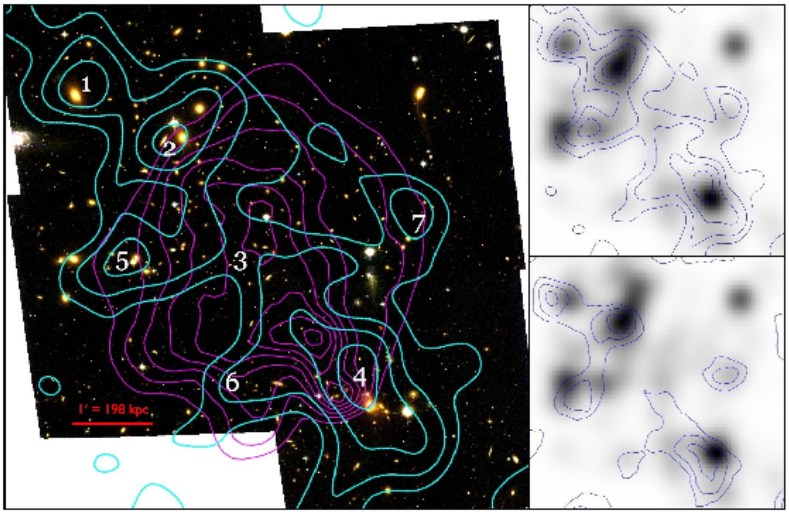

Figure 2: Mosaic images with the weak lensing surface density reconstruction overlayed in cyan contours and the Chandra X-ray derived gas surface density in magenta contours. The weak lensing contours show steps in surface density of 2×10^8 $M_\odot/\mathrm{kpc}^2$, and the gas mass contours show steps of 7.4×10^6 $M_\odot/\mathrm{kpc}^2$. The numerical labels corresponds to specific regions of structures in M07 and J12, for details see the source [20].

massive particles (WIMPs) or axions;

- models of modified gravity (MOND).

However, MOND have difficulties explaining phenomena related to colliding galaxy clusters, like the Bullet cluster.

The Bullet Cluster

The Bullet Cluster (1E0657-558) is yet another source of compelling astronomical evidence for DM [23, 24]. It is a peculiar object, a galaxy cluster in a system of two colliding clusters. In Fig. 3 one can see spacial separation of the fluid-like dust (gas) and the 2 centers of mass inferred from weak gravitational lensing. As mentioned before, this behaviour is difficult to explain by employing modifications of gravity and therefore supports claims of the particle nature of DM.

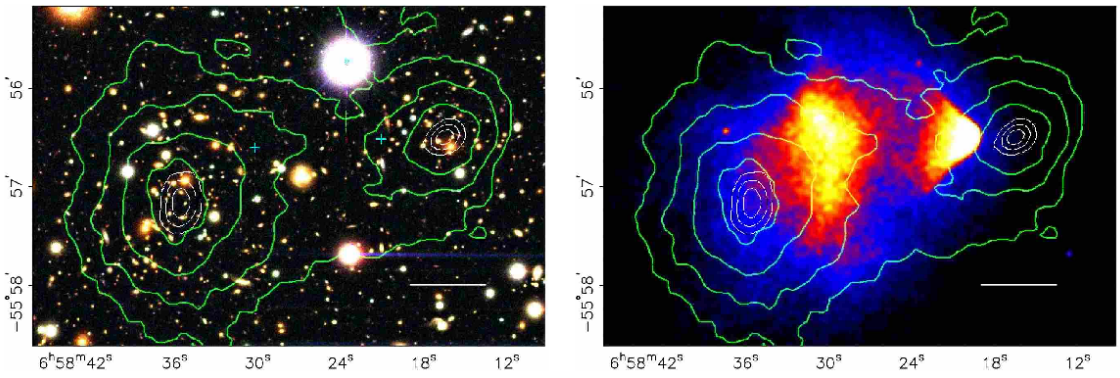

Figure 3: Images of the Bullet cluster (1E0657-558) [24]. Green contours correspond the weak lensing mass reconstruction. The blue crosses on the left panel show the location of the centers of masses of the plasma clouds, as depicted on the right panel.

In this thesis we follow the assumption of particle nature of DM. We discuss models with candidates for a single-component DM, namely the 2HDMS model and the $N = 1$ case of a O(N) model. However, we also discuss models with more complex, multi-component structure of DM (the O(N) model and 2CDMM). There are studies of multi-component DM in the literature, see for example, [25–33]. Multi-component DM models are especially interesting in context of ameliorating discrepancies between direct detection experiments (see Section III D 3) and the *core-cusp problem* .

The *core-cusp problem* (or *cuspy halo problem*) is related to the comparison of observed DM density distribution in the galaxies with results from cosmological simulations (for a review see [2]). It seems that numerical simulations of cold dark matter (CDM) halo profiles indicate that CDM forms cusps in the galactic centers — that is, a sharply increased high concentration in the most dense areas of the universe. However, from the observations it seems unlikely that the centers of galaxies form such structures, density near the center seems rather constant. This issue has been adressed within numerical simulations including baryonic physics [34], self-interacting DM [35, 36] or multi-component DM [37, 38] and the issue of flattening the cusps is still not resolved. However, we believe that studies of models of self-interacting DM and also multi-component have a viable motivation. Also, we should keep in mind that there is much more DM than visible matter in the Universe. If one realises the complexity of visible matter, than indeed a question arises of why should DM be just a single particle?

B. Dark Matter Properties, Related Observables and Detection

DM presence was discovered due to its gravitational interactions with other elementary particles. Massless particles were excluded as DM candidates due to the large scale structure studies. However, DM's proposed mass varies substantially, depending on the DM model; starting from approximately 10^{-6} to 1 eV for axions [39], to cold WIMPS in the 1 GeV - 10 TeV mass range. What kind of observables are there, that can help us narrow down the list of candidates for DM? The main observable is definitely the density of DM in the Universe. Based on current measurements of the anisotropy of the CMB, one can estimate baryonic matter and non-baryonic DM densities to be [1]

$$\begin{aligned} \Omega_b^{(exp)} h^2 &= 0.02214 \pm 0.00024 \\ \Omega_{DM}^{(exp)} h^2 &= 0.1187 \pm 0.0017 \end{aligned} \tag{20}$$

as calculated from combined Planck+WP+highL+BAO data with 68% CL limit. The dimensionless constant h in (20) conveys the error in the measurement of Hubble's constant H, $H = 100\ h$ km s^{-1} Mpc^{-1}.

Even though we are sure that DM interacts gravitationally with ordinary matter, other ways of such interaction seem possible. For example, DM could interact weakly with the SM in such a way that a decay into SM particles or an annihilation into SM particles, or scattering off ordinary matter would be possible.

In models of DM that we will discuss in this thesis, DM is always stable. However, it does not necessarily have to be true. In the simplest generalization one allows for a DM decay, however the decay time should be larger than present age of the Universe. Also another scenarios are possible, within multi-component DM structure, see [40].

Various channels of DM interaction are shown in the diagram in Fig 4. In principle all of them could be constrained by observations. The processes of DM annihilation would imply DM thermal production in the early Universe, therefore would influence the relic density of DM. Also, the signals of DM annihilation in the Galactic centre can be registered on Earth (see *indirect detection* discussed in Section **??**). DM production in colliders, although not yet observed, might account for some missing energy signatures (see for example [41]). There are

also many experiments prepared for observation of the DM scattering off a nucleus. These *direct detection* attempts will be discussed in details in Section III D.

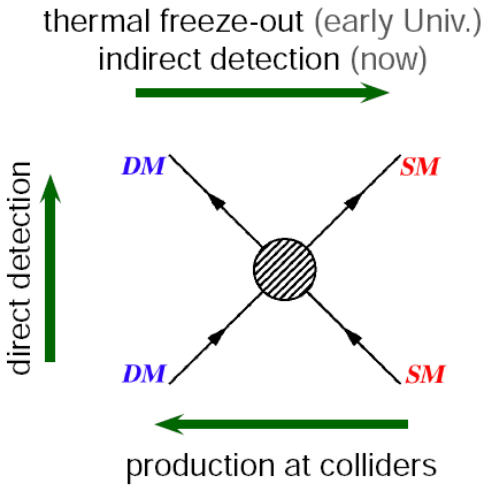

Figure 4: Various channels of WIMP dark matter interaction with Standard Model particles. The same amplitude is relevant for thermal production in the early Universe, indirect detection, direct detection, and production in collider experiments. Source: www.mpi-hd.mpg.de

C. Relic Density

Dark matter relic density in the Universe is known with great precision, thanks to the detailed study of Cosmic Microwave Background radiation (CMB) [1]. For a WIMP DM candidate, the usual scenario of DM density evolution in the Universe assumes thermal equilibrium with 'regular' matter in the very early Universe. This is indeed true, if the interaction rate of DM with SM particles is strong in comparison to the expansion rate of the Universe (H). As the Universe expands, and the temperature gets smaller, the interaction rate also decreases. Then, at some point DM can decouple from equilibrium and freeze-out, with almost constant density over T^3, see Fig. 5. This is the standard scenario of the thermal production of DM in the universe. This behaviour is a solution to the Boltzmann equation (BEQ), describing a one-component system interacting with SM particles in equilibrium [16]. In this thesis we will discuss in detail not only one-component scenarios, but also multi-component DM, where the BEQs might provide solutions with different dynamics of

density evolution. We also will also discuss a case of feebly interacting DM (FIDM). In such a case the interaction rate of DM with SM is not strong enough for DM to equilibrate in the very early times, and therefore we again observe different density dynamics.

1. The Boltzmann Equation

To discuss the dynamics of matter density one needs to include both the expansion rate of the Universe and the changes in number density related to quantum processes like decay, annihilation, etc. The corresponding differential equation, the Boltzmann equation, can be written simply as [16, 42]

$$\hat{L}[\tilde{f}] = \hat{C}[\tilde{f}] \tag{21}$$

where $\hat{L}$ is the Liouvile operator and $\hat{C}$ is the collision operator, acting on the space distribution function $\tilde{f} = \tilde{f}(p, x, t)$. If the right hand side is zero, this equation is know as Liouville equation. We assume that our Universe is homogenous and isotropic, therefore we use an appropriate form of the Liouville operator, in FLRW metric:

$$\hat{L}[\tilde{f}] = E\frac{\partial \tilde{f}}{\partial t} - \frac{\dot{a}}{a}|\vec{p}|^2\frac{\partial \tilde{f}}{\partial E} \tag{22}$$

where $\tilde{f}(p, x, t) = \tilde{f}(E, t)$ and a is the scale factor (see Section II). Then we can write (21) as:

$$\frac{dn}{dt} + 3\frac{\dot{a}}{a}n = \frac{g}{(2\pi)^3}\int \frac{d^3p}{E}\hat{C}[\tilde{f}(E, t)]. \tag{23}$$

where the number density n is defined in (14). The dominant contributions to the collision terms usually come from the DM annihilation processes $DM\ DM' \rightarrow X_1\ X_2$[2] and coannihilations $DM\ Y_1 \rightarrow X_1\ X_2$. For the models discussed in this thesis, only annihilation processes are present. The collision term for $DM + DM' \rightarrow X_1 + X_2$ reads:

$$\begin{aligned}\frac{g}{(2\pi)^3}\int \frac{d^3p}{E}\hat{C}[\tilde{f}(E, t)] = -\int d\Pi^{DM} d\Pi'^{DM} d\Pi^{X_1} d\Pi^{X_2}(2\pi)^4\delta^4(P)\times \\ (|M_A|^2\tilde{f}_{DM}\tilde{f}'_{DM}(1 \pm \tilde{f}_{X_1})(1 \pm \tilde{f}_{X_2}) - |M_X|^2(1 \pm \tilde{f}_{DM})(1 \pm \tilde{f}'_{DM})\tilde{f}_{X_1}\tilde{f}_{X_2})\end{aligned} \tag{24}$$

where $P =$ (outoing momenta $-$ incoming momenta), $+$ is for bosons and $-$ is for fermions, $\tilde{f}_X = \tilde{f}_X(E, t)$ is the phase space density of species X. The unpolarized invariant amplitudes

[2] DM' is either DM or anti-DM particle

$|M_A|^2$ and $|M_X|^2$ are obtained using the usual Feynman rules (with all appropriate symmetry factors, averaged over initial and final spins, see [43]). We sum over all final states of $DM\, DM' \to X_1 + X_2$. No additional factor of $\frac{1}{2}$ is required for 2 identical particles in the initial state. After integration over the final states in (24) we get:

$$\int d\Pi^{X_1} d\Pi^{X_2} (2\pi)^4 \delta^4(P) |M_A|^2 = F \sigma_{DM+DM' \to X_1 X_2} \tag{25}$$

where $F = 4\sqrt{(p_{DM} p'_{DM})^2 - m^2_{DM} m'^2_{DM}}$. Using the relation of time t to the photon temperature T from (19), we can change variables $t \to T$. The photon temperature T is also the temperature of all other particle species, as long as they remain in thermal equilibrium. For a further simplification of (24), we also assume that soon after annihilation takes place, X_1 and X_2 quickly thermalize and their distribution is an equilibrium distribution. We also assume zero chemical potential and approximate

$$\tilde{f}_X(E,T) = e^{-E/T}. \tag{26}$$

From the energy conservation we have

$$\tilde{f}_{X_1} \tilde{f}_{X_2} = e^{-E_{X_1}/T} e^{-E_{X_2}/T} = e^{-E_{DM}/T} e^{-E'_{DM}/T} = \tilde{f}^{EQ}_{DM} \tilde{f}'^{EQ}_{DM}, \tag{27}$$

therefore after approximating $(1 \pm f_X) \sim 1$ we have

$$\frac{g}{(2\pi)^3} \int \frac{d^3p}{E} \hat{C}[\tilde{f}(E,t)] = -\int d\Pi^{DM} d\Pi'^{DM} F \sigma (\tilde{f}_{DM} \tilde{f}'_{DM} - \tilde{f}^{EQ}_{DM} \tilde{f}'^{EQ}_{DM}), \tag{28}$$

where above $\sigma = \sigma_{DM+DM' \to X_1 X_2}$.

One can define the thermally averaged cross section,

$$\langle \sigma_{DM+DM' \to X_1 X_2} |v| \rangle \equiv \frac{1}{{n^{EQ}_{DM}}^2} \int d\Pi^{DM} d\Pi'^{DM} F \sigma_{DM+DM' \to X_1 X_2} \tilde{f}^{EQ}_{DM} \tilde{f}'^{EQ}_{DM}, \tag{29}$$

which is discussed in details in Appendix B. We have introduced the Moller velocity, $|v| = F/(E_1 E_2)$. Using (29) one can simplify substantially the BEQ, assuming also that $\tilde{f}_{DM} \propto \tilde{f}^{EQ}_{DM}$ (see [44]), and therefore:

$$\frac{dn_{DM}}{dt} + 3Hn_{DM} = -\langle \sigma_{DM} |v| \rangle \left(n^2_{DM} - \left(n^{EQ}_{DM} \right)^2 \right) \tag{30}$$

where $\langle \sigma_{DM} |v| \rangle$ is the thermally averaged cross section for DM annihilation summed over all final states with $2 \to 2$ processes. Equation (30) describes a single component DM

system, interacting with SM particles. If DM is a multi-component system, we should modify our analysis and include other species. If again the dominant contribution to the DM-SM interaction comes from $2 \to 2$ annihilations, we can write the following set of N BEQ equations for N-component DM system:

$$\frac{dn_i}{dt} + 3Hn_i = -\langle\sigma_{i-SM}|v|\rangle \left(n_i^2 - \left(n_i^{EQ}\right)^2\right) - \sum_{j\neq i} \left(\langle\sigma_{i-j}|v|\rangle n_i^2 - \langle\sigma_{j-i}|v|\rangle n_j^2\right) \tag{31}$$

where by $i - SM$ we mean $DM_i + DM_i' \to SM + SM'$ interaction and $i - j$ stands for $DM_i + DM_i' \to DM_j + DM_j'$, $i, j = 1, \ldots, N$. Please, note that $\langle\sigma_{i-j}|v|\rangle$ is not the same as $\langle\sigma_{j-i}|v|\rangle$, however those cross sections are related,

$$\left(n_i^{EQ}\right)^2 \langle\sigma_{i-j}|v|\rangle = \left(n_j^{EQ}\right)^2 \langle\sigma_{j-i}|v|\rangle. \tag{32}$$

2. CASE 1: WIMP Single-Component DM and Thermal Relics

In the case of single-component WIMP, that decouples from equilibrium at non-relativistic temperatures (which corresponds to cold dark matter), one can make some simple approximations to the BEQ to get an analytical solution for the relic density at low temperatures. It is common in the literature to use number density normalised to the total entropy density of the Universe, $Y = n/s$ (see for example [16]). However, in this thesis for the simplicity of notation we will define and use the number density normalized by T^3, f_X:

$$f_X \equiv \frac{n_X}{T^3}. \tag{33}$$

Now we can rewrite (30) in this notation:

$$\frac{df_{DM}}{dT} = f'_{DM} = \frac{\langle\sigma_{DM}|v|\rangle}{K} \left(f_{DM}^2 - \left(f_{DM}^{EQ}\right)^2\right). \tag{34}$$

In general we have $s \propto T^3$, therefore the difference between the two choices of variables is just a matter of constants. If we introduce a deviation from equilibrium $\Delta_X = f_X - f_X^{EQ}$ to equation (34), we get

$$\Delta'_{DM} = \frac{\langle\sigma_{DM}|v|\rangle}{K} \Delta_{DM} \left(\Delta_{DM} + 2f_{DM}^{EQ}\right) - {f'_{DM}}^{EQ} \tag{35}$$

As described in the beginning of this section, for equilibrium intial condition, at some temperature T_f DM decouples from the equilibrium and freezes-out with almost constant $f(T)$,

see Fig. 5. If T_f is non-relativistic, $x_f = m_{DM}/T_f \gtrsim 3$, we consider this a cold dark matter (CDM) case. Understanding the behaviour of the solutions will help us find approximations that leads to analytical expressions for the relic density.

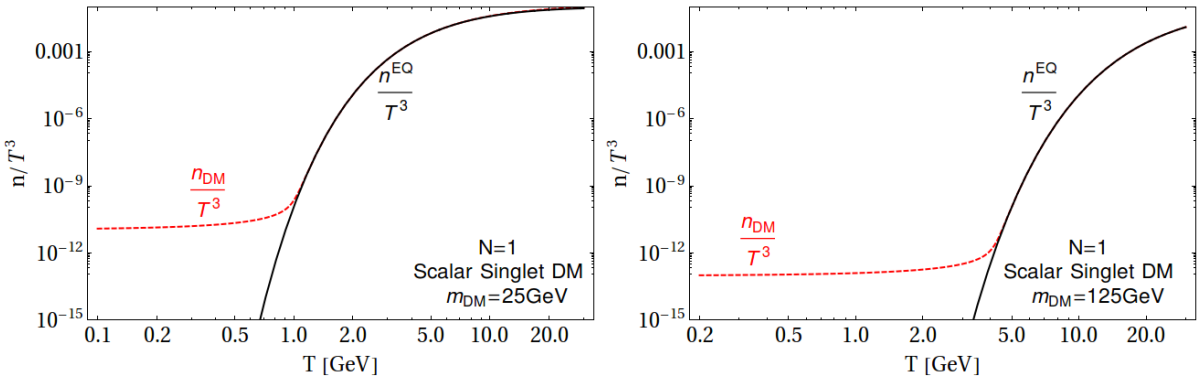

Figure 5: Solution to BEQ in a case of single-component cold WIMP.

For early times ($1 < x = m_{DM}/T \ll x_f$) we have $f_{DM} \sim f_{DM}^{EQ}$ and $|\Delta_{DM}|$ and $|\Delta'_{DM}|$ are small. Therefore we can set $\Delta'_{DM} = 0$ and

$$\Delta_{DM} \sim \frac{{f'_{DM}}^{EQ}}{\frac{\langle\sigma_{DM}|v|\rangle}{K}\left(\Delta_{DM} + 2f_{DM}^{EQ}\right)} \sim \frac{{f'_{DM}}^{EQ}}{2\frac{\langle\sigma_{DM}|v|\rangle}{K} f_{DM}^{EQ}} \sim \frac{1}{2\frac{\langle\sigma_{DM}|v|\rangle}{K}} \frac{m_{DM}}{T^2}. \tag{36}$$

For non-relativistic temperatures (see [16]) the equilibrium distribution is equal to:

$$\begin{aligned} f_{DM}^{EQ} &= \frac{g}{(2\pi)^{3/2}} \left(\frac{m_{DM}}{T}\right)^{3/2} e^{-m_{DM}/T}, \\ \frac{{f'_{DM}}^{EQ}}{f_{DM}^{EQ}} &= \frac{m_{DM}}{T^2} - \frac{3}{2T} \sim \frac{m_{DM}}{T^2}. \end{aligned} \tag{37}$$

For small temperatures ($x \gg x_f$) we have $f_{DM} \gg f_{DM}^{EQ}$ and therefore

$$\Delta'_{DM} \sim \frac{\langle\sigma_{DM}|v|\rangle}{K} \Delta_{DM}^2. \tag{38}$$

Integrating (38) from T_f to T in general requires a temperature expansion of the thermally averaged cross section, which is presented in details in Appendix B. The general formula reads

$$\langle\sigma_{DM}|v|\rangle(T) = \langle\sigma_{DM}|v|\rangle_0 + \frac{T}{m_{DM}}\langle\sigma_{DM}|v|\rangle_1 + \dots \tag{39}$$

For the constant approximation of the cross section, $\langle\sigma_{DM}|v|\rangle \simeq \langle\sigma_{DM}|v|\rangle_0$, we have:

$$\Delta_{DM}(T) = \frac{1}{\frac{\langle\sigma_{DM}|v|\rangle}{K}(T_f - T) + \Delta_{DM}(T_f)}. \tag{40}$$

Note that, after the decoupling of DM, the photon temperature T present in our equations is no longer DM temperature. We are especially interested in DM abundance today, therefore we can take $T = T_\gamma$ (present photon temperature) and neglect contribution from $\Delta_{DM}(T_f)$, which gives us a simplified formula for the normalized number density:

$$f_{DM}(T = T_\gamma) \simeq \frac{K}{\langle \sigma_{DM}|v| \rangle T_f} \tag{41}$$

From (36) we can calculate $\Delta_{DM}(T_f)$, assuming that $\Delta_{DM}(T_f) = c_{DM} f^{EQ}_{DM}$, which gives us an equation for T_f, that can be solved numerically:

$$c_{DM} f^{EQ}_{DM}(T_f) \sim \frac{1}{(2 + c_{DM}) \frac{\langle \sigma_{DM}|v| \rangle}{K}} \frac{m_{DM}}{T_f^2}. \tag{42}$$

From numerical analysis (see [16]) we learn that the best choice for the parameter c_{DM} is $c_{DM}(c_{DM} + 2) \cong 2$.

3. CASE 2: Feebly-Interacting Dark Matter

As already mentioned, for DM to thermalize with SM species its interaction rate $\Gamma = n_{DM} \langle \sigma_{DM}|v| \rangle$ should be larger than the expansion rate of the Universe, H. If DM-SM interaction rate is very small (with couplings $\lesssim 10^{-9}$), such DM candidate would not equilibrate until very late times.

The first discussion of FIDM we are aware of is by McDonald in [45], who analised the scalar singlet extension of the SM. There have also been other studies of the scalar singlet DM model within FIDM framework, see [26, 46, 47], and FIDM realisation of other models [48, 49].

In this subsection we will assume that DM interacts with SM so feebly, that it never thermalizes and it is never in equilibrium with the Standard Model. We can call this process, a thermal generation of DM, after [45], or a freeze-in mechanism [46].

We will neglect the number density of DM at the very early times (just after the reheating), and then solve the BEQ (34). This can be done numerically, however note that $f_{DM} \ll f^{EQ}_{DM}$ until very late times. Therefore one can simplify the BEQ in the following way:

$$f'_{DM} = -\frac{\langle \sigma_{DM}|v| \rangle}{K} f^{EQ\,2}_{DM} \tag{43}$$

This equation can be integrated from a high initial temperature $T \gg$ EW scale to the freeze-in temperature. For evaluation of the relic density in a specific model, see Section IV E.

4. CASE 3: Multi-Component Dark Matter

If one accepts a multi-component DM scenario, many new possibilities appear. Dark Matter does not have to necessarily consist of only stable or long-lived particles (for further reading see the dynamical DM framework in [40]). In a general case of N-components, the evolution of DM density can be described by the following set of BEQs (expressed in terms of the number density normalized by temperature cubed $f_i, i = 1, \ldots, N$):

$$f_i' = \frac{\langle \sigma_{i-SM}|v| \rangle}{K} \left(f_i^2 - \left(f_i^{EQ} \right)^2 \right) + \sum_{i \neq j} \left(\frac{\langle \sigma_{i-j}|v| \rangle}{K} f_i^2 - \frac{\langle \sigma_{j-i}|v| \rangle}{K} f_j^2 \right). \tag{44}$$

We would like to further discuss only a particular scenario of 2-component DM, for a full description of the model see Section VII. In this scenario only one DM component (a singlet scalar φ) interacts with the SM particles at the tree level, second component (a neutral fermion ν) has no tree-level interactions with the SM. The appropriate set of the BEQs is:

$$\begin{aligned} f_\varphi' &= \frac{\langle \sigma_{\varphi-SM}|v| \rangle}{K} \left(f_\varphi^2 - \left(f_\varphi^{EQ} \right)^2 \right) + \frac{\langle \sigma_{\varphi-\nu}|v| \rangle}{K} f_\varphi^2 - \frac{\langle \sigma_{\nu-\varphi}|v| \rangle}{K} f_\nu^2 \\ f_\nu' &= \frac{\langle \sigma_{\nu-\varphi}|v| \rangle}{K} f_\nu^2 - \frac{\langle \sigma_{\varphi-\nu}|v| \rangle}{K} f_\varphi^2 \end{aligned} \tag{45}$$

One can study approximations of this set of differential equations in search for analytical solutions. In this particular scenario, the behaviour of the solutions changes substantially with mass hierarchy ($m_\varphi > m_\nu$, $m_\nu > m_\varphi$). Such analysis and approximations were thoroughly described in [32], using the same framework as in the single-component DM case.

5. Dark Matter Relic Abundance

The DM density parameter Ω_{DM} is defined as follows:

$$\Omega_{DM} = \frac{\rho_{DM}}{\rho_{crit}} \tag{46}$$

where ρ_{DM} is the actual density of Dark Matter in a unit volume and ρ_{crit} is the critical density. The density ρ_{DM} can be calculated from the normalized density f_{DM}, assuming DM is non-relativistic in present times we have

$$\rho_{DM} = m_{DM} f_{DM}(T_\gamma) T_\gamma^3, \tag{47}$$

where T_γ is current photon temperature, $T_\gamma = 2.725$ K $= 0.2348$ meV. The current most precise experimental results of DM relic density, that result from the analysis of CMB done by the Planck collaboration [1], were given in Section III B.

Note, that from (46) and (41) one can easily conclude that $\Omega_{DM} \propto \frac{1}{\langle\sigma|v|\rangle}$. For a proper DM abundance the effective coupling of DM to the SM cannot be too small, as it implies overabundance of DM (unless we are in the FIDM regime). Also too strong coupling is excluded, unless there are more sources of DM present.

D. Direct Detection

Can we observe a DM particle interaction with a nucleus on Earth?

Many of the most popular new physics models, like supersymmetric extensions of the SM, provide DM candidates that can interact with nuclei with quite strong cross sections. In many models, the estimated DM-nuclei interaction rates seemed to be strong enough for the collision to be observable in a detector on Earth. Theoretical analysis of such detection was discussed since the 80's, see for example [50, 51], for a review see *eg.*[21, 52, 53].

There are many factors that influence the event rate of DM-nucleus collisions:

- local DM density in Earth's vicinity
- DM speed distribution
- Earth's motion
- cross section for DM-nucleus interaction

We will discuss those effects on direct detection in the following 2 subsections.

1. DM's Astrophysics

The DM direct detection rate depends on its local density, $\rho_0 = \rho(R_0)$ where $R_0 = (8.0 \pm 0.5)$ kpc is the Sun's distance from the center of the Milky Way [54]. The DM density profile of the Milky Way, $\rho(R)$, can be evaluated based on measurements of the Milky Way's rotation curve then applied to a certain theoretical model of the Galaxy. Therefore, an estimation of ρ_0 strongly depends on the specific theoretical model. For example in [55] the

authors estimate the local DM density to vary from 0.2 to 0.4 GeV/cm^3, including various cuspy and cored DM halo profiles. For a simple approximation of $\rho \propto r^{-2}$ one finds that $\rho_0 = (0.3 \pm 0.05)$ GeV/cm^{-3}.

The velocity distribution of DM, $f(v)$ is conventionally a Gaussian distribution for velocities below the escape velocity, $v < v_{esc}$, estimated to be 498 km/s $< v_{esc} <$ 608 km/s for our Galaxy (median value $v_{esc}^{med} = 544$ km/s), see [56]). For $v > v_{esc}$, particles are not gravitationally bounded and $f(v) = 0$. The average velocity of the Solar System estimated within r^{-2} profile is $v_S = 220$km/s [57]. It is a reasonable first approximation, however unlikely to be accurate.

The motion of the Earth also should be taken into account. The interesting fact is that given an Earth's orbit around the Sun, the velocity distribution of DM changes through the year. Therefore we should observe annual modulation in DM detection signals [58, 59]. Such modulations in the events of DM detection are claimed to be observed by DAMA collaboration (see for example [60]).

2. DM-nucleus interaction

The crucial property of DM relevant to the study of DM direct detection is the cross section for the scattering of DM off a nucleus Z_A (with Z protons and $A - Z$ neutrons). As we have previously discussed in Section III C 5, a small, but not too small coupling of DM to ordinary matter is expected by the CDM model of the evolution of matter in the Early Universe, such that DM is not overabundant in present times. Therefore we also expect a nonzero coupling of DM to a nucleus Z_A (see Fig. 4 for an illustration). Following [51], we define the cross section at zero momentum transfer of DM-nucleus (DM-Z_A) scattering:

$$\sigma_{\mathrm{DM}-Z_A} = \int_0^{4\mu_{Z_A}^2 v^2} \frac{d\sigma(q=0)}{d|\mathbf{q}|^2} d|\mathbf{q}|^2, \quad \mu_{Z_A} = \frac{m_{Z_A} m_{DM}}{m_{Z_A} + m_{DM}} \tag{48}$$

where $\mathbf{q}$ is the momentum transfer, v is the relative velocity, m_{Z_A} is the mass of the nucleus. It is reasonable to simplify our calculation using a non-relativistic limit while evaluating this cross section, see Appendix C for details.

To calculate the DM-Z_A interaction rate we need to understand both the distribution of nucleons in the nuclei and the distribution of quarks in the nucleons. In addition we have to know the amplitudes of DM-quark and DM-gluon interactions.

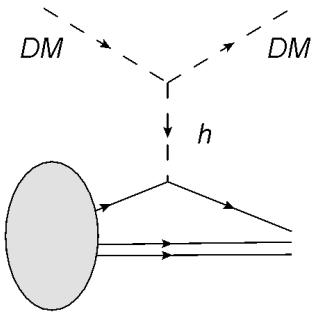

Figure 6: The scattering of DM off a nucleus, through a Higgs boson exchange.

In the models we will be discussing in this thesis, a DM candidate interacts with quarks through the Higgs boson exchange (see Fig. 6). Therefore there is no spin interaction and we will discussed only the case of spin-independent cross section [50]. The effective interaction terms for DM-SM interaction for a real scalar DM candidate φ or a fermion DM candidate ψ are:

$$\mathcal{L}_{\varphi q} = \zeta_q \bar{q} q \varphi^2, \quad \mathcal{L}_{\psi q} = \xi_q \bar{q} q \bar{\psi} \psi, \tag{49}$$

where ζ_q, ξ_q can be expressed through the fundamental couplings of a theory and they depend on a particular model[3]. The non-relativistic matrix elements of the light quark operators in a nucleon state in the first order calculation are defined as follows:

$$\langle N | m_q \bar{q} q | N \rangle_{\mathcal{NR}} = f_{Tq}^N m_N, \quad q = u, d, s \tag{50}$$

where m_N is the nucleon's mass, $N = n, p$, the form factors f_{Tq}^N are obtained from the measurements of pion-nucleon scattering, see [61, 62]. We present the most recent values of the form factors in Table I.

q	u	d	s
f_{Tq}^p	0.0153	0.0191	0.0447
f_{Tq}^n	0.0110	0.0273	0.0447

TABLE I: Form factors extracted from micrOMEGAs 3.0 [63].

[3] Use of effective theory is here justified by $q \to 0$.

Heavy quarks also contribute to the nucleon mass through the 1-loop Higgs-gluon anomaly, see Fig. 7, [52, 53, 61, 62]. In heavy quark expansion ($Q = c, t, b$) the following substitution can be made for each Q in a nucleon matrix element,

$$m_Q \bar{Q} Q \to -\frac{2\alpha_s}{24\pi} G_{\mu\nu} G^{\mu\nu}. \tag{51}$$

The trace of the QCD energy-momentum tensor is then

$$\theta^\mu_\mu = \sum_q m_q \bar{q} q + \sum_Q m_Q \bar{Q} Q - \frac{7\alpha_s}{8\pi} G_{\mu\nu} G^{\mu\nu} \to \sum_q m_q \bar{q} q - \frac{9\alpha_s}{8\pi} G_{\mu\nu} G^{\mu\nu} \tag{52}$$

The matrix element for this tensor in a nuclear state is equal to nucleon mass, therefore

$$m_N = \sum_q \langle N | m_q \bar{q} q | N \rangle - \langle N | \frac{9\alpha_s}{8\pi} G_{\mu\nu} G^{\mu\nu} | N \rangle. \tag{53}$$

Using (51) we get

$$\langle N | m_Q \bar{Q} Q | N \rangle_{\mathcal{NR}} = \frac{2}{27} \left(1 - \sum_{q=u,d,s} f^N_{Tq} \right) m_N = \frac{2}{27} f^N_{TGQ} m_N, \quad Q = c, b, t \tag{54}$$

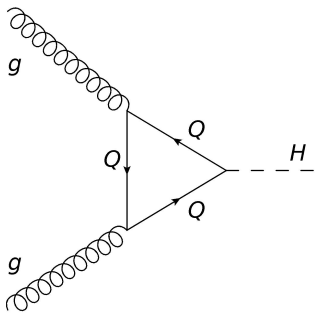

Figure 7: 1-loop contributions to the Higgs-gluon interaction from heavy quarks Q.

The amplitudes for the elastic scattering of DM-nucleon (DM-N) for DM=φ, ψ are given by:

$$\begin{aligned} \mathcal{M}_{\varphi q} &= 2 \left(\langle N\varphi | \zeta_q \varphi^2 \bar{q} q | \varphi N \rangle_{\mathcal{NR}} + \langle N\varphi | \zeta_Q \varphi^2 \bar{Q} Q | \varphi N \rangle_{\mathcal{NR}} \right) \bar{u}_N u_N \\ \mathcal{M}_{\psi q} &= \left(\langle N\psi | \xi_q \bar{\psi} \psi \bar{q} q | \psi N \rangle_{\mathcal{NR}} + \langle N\psi | \xi_Q \bar{\psi} \psi \bar{Q} Q | \psi N \rangle_{\mathcal{NR}} \right) \bar{u}_N u_N \bar{u}_\psi u_\psi \end{aligned} \tag{55}$$

where the factor of 2 in the first line is a symmetry factor from the Feynman rule of $\varphi^2 \bar{q} q$ vertex. A corresponding factor of 2 should appear in the fermionic case, for a Majorana DM

candidate. Then we have

$$\begin{aligned}\sigma_{\varphi-N} &= \frac{\mu_{Z_A}^2}{16\pi m_\varphi^2 m_N^2}\overline{|\mathcal{M}_{\varphi q}|^2} = \frac{4\mu_{Z_A}^2}{\pi} f_{\varphi-N}^2 \\ \sigma_{\psi-N} &= \frac{\mu_{Z_A}^2}{16\pi m_\psi^2 m_N^2}\overline{|\mathcal{M}_{\psi q}|^2} = \frac{4\mu_{Z_A}^2}{\pi} f_{\psi-N}^2\end{aligned} \tag{56}$$

where the corresponding $DM-N$ couplings $f_{\varphi-N}$ and $f_{\psi-N}$ are:

$$\begin{aligned}f_{\varphi-N} &= \frac{m_N}{2m_\varphi}\left(\sum_q \zeta_q \frac{f_{Tq}^N}{m_q} + \sum_Q \zeta_Q \frac{2}{27}\frac{f_{TGQ}^N}{m_Q}\right) \\ f_{\psi-N} &= m_N\left(\sum_q \frac{\xi_q}{2}\frac{f_{Tq}^N}{m_q} + \sum_Q \frac{\xi_Q}{2}\frac{2}{27}\frac{f_{TGQ}^N}{2m_Q}\right)\end{aligned} \tag{57}$$

where we summed over the quark indices $q = u, d, s$ and $Q = c, b, t$. For a consistency check with the micrOMEGAs manual [52], note that they assume DM to be a Majorana fermion, therefore an additional factor of $1/2$ in $f_{\psi-N}$ disappears due to the symmetry factor.

The next step is to evaluate the interaction rate with the nucleus. We will use the results of (56) and evaluate matrix elements of the nucleon operators in a nuclear state. At non-relativistic limit those operators are just nucleon counters and the amplitude is proportional to the number of nucleons [51]. The differential cross section for the DM-Z_A spin independent interaction is [51]:

$$\frac{d\sigma_{\mathrm{DM}-Z_A}}{d|\mathbf{q}|^2} = \frac{1}{\pi v^2}\left(Z f_{\mathrm{DM-p}} F_{Z_A}^p(|\mathbf{q}|) + (A-Z) f_{\mathrm{DM-n}} F_{Z_A}^n(|\mathbf{q}|)\right)^2 \tag{58}$$

where $f_{\mathrm{DM-N}}$ is the DM-N coupling ($N = p, n$), as given in (57), and $F_{Z_A}^N(|\mathbf{q}|)$ is the nuclear form factor related to the nucleon number operator, normalized to 1 at zero energy transfer. The total cross section for DM-Z_A scattering at zero momentum transfer, as defined in (48), is equal to:

$$\sigma_{DM-Z_A} = \frac{4\mu_{Z_A}^2}{\pi}\left(Z f_{\mathrm{DM-p}} + (A-Z) f_{\mathrm{DM-n}}\right)^2 \tag{59}$$

Now we can translate the cross sections to the actual event rate of DM-nuclei collisions in a detector on Earth. We will include the density of DM in the vicinity of the Earth and the velocity distribution of DM, $f(v)$, as previously discussed. Also one needs to remember that detectors do have energy thresholds E_T (are unsensitive to nuclear recoils below E_T). In general one can express the event rate as follows:

$$R = N_T n_{DM}\int d|\mathbf{q}|^2 \int_{v_{min}}^{v_{max}} d^3v f(v) v \frac{d\sigma}{d|\mathbf{q}|^2} \tag{60}$$

where N_T is the number of target nuclei, n_{DM} is the number density of DM. We can assume that the nuclear form factors $F^p_{Z_A}(|\mathbf{q}|) \sim F^n_{Z_A}(|\mathbf{q}|)$, as the effects of their difference are much smaller than any other interesting features of this calculation (for example the differences between the nucleon form factors for quark distributions f^n_{Tq} and f^p_{Tq}). Therefore the event rate can be written in this simple form:

$$R = \sigma_{DM-Z_A} I_A, \quad I_A = N_T n_{DM} \int d|\mathbf{q}|^2 \int_{v_{min}}^{v_{max}} d^3v f(v) \frac{1}{4\mu^2_{Z_A} v} \tag{61}$$

All dependence on astrophysics, nuclear physics and detector's properties is hidden in the function I_A. However, the detectors are usually made out of elements containing various isotopes. We should modify the event rate to include that:

$$R_X = \sum_I \eta_I \sigma_{DM-A_I} I_{A_I} = \sigma_{DM-p} \sum_I \eta_I \frac{\mu^2_{A_I}}{\mu^2_p} I_{A_I} \left(Z + (A_I - Z) \frac{f_n}{f_p} \right)^2 \tag{62}$$

where X indexes the detector type, I runs over all isotopes, η_I are percentages of each isotope in the compound and $\mu_p(\mu_{A_I})$ is the reduced mass for DM and the proton p (the nucleus Z_{A_I}). We have also omitted the DM index in the DM-N coupling using f_N instead of f_{DM-N} and we omit this index from now on. The cross section σ_{DM-p} is the cross section for DM-proton scattering,

$$\sigma_{DM-p} = \frac{4\mu^2_p}{\pi} f^2_p. \tag{63}$$

For some cases it is convenient to use an approximation of $f_n \simeq f_p$. If so, we have

$$\sigma_{DM-Z_A} \simeq \frac{4\mu^2_p}{\pi} A^2 f^2_p \tag{64}$$

and the event rate $R \propto A^2$. This is a common assumption when translating the observations in an event detector into limits on scattering cross section vs WIMP mass plane. For details, see the following subsection.

3. Current Status of Direct Detection Experiments

Currently, there are various experimental results available from direct detection studies, while many experiments are still running or are planned. The strongest of currently available exclusion limits, obtained from a non-observation of a DM-nuclei scattering for large WIMP

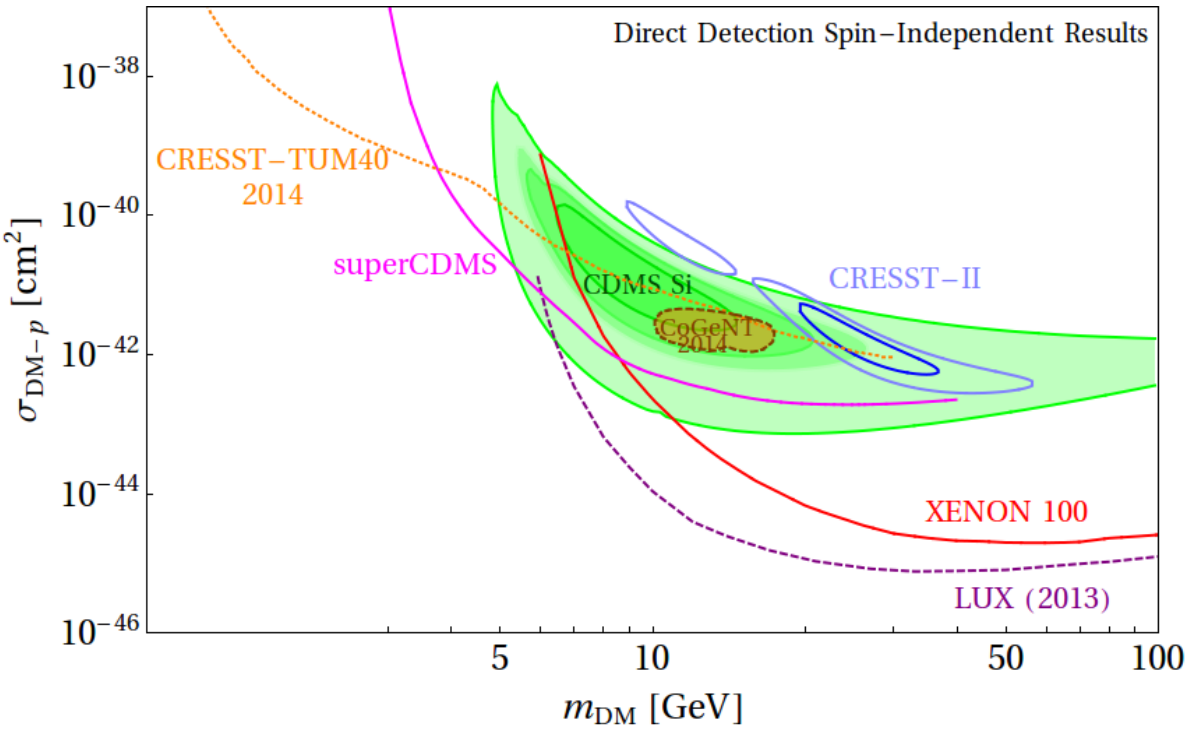

Figure 8: Upper limits and signal regions for spin-independent DM-nucleon cross section for recent measurements. Green shaded region corresponds to the CDMS Si [64, 65] signal at 99, 95, 90 and 68% CL from the lightest to the darkest green, respectively. Brown dashed line corresponds to the CoGeNT 2014 results at 90% CL [66]. Blue curves correspond to the CRESST-II results at 1 (dark blue) and 2 σ (light blue). Red curve is the XENON 100 exclusion limit. Dashed purple line is the LUX 2013 exclusion limit [67]. Dotted orange line is the CRESST-TUM40 2014 exclusion limit [68]. Pink line corresponds to SuperCDMS [69] exclusion bound.

masses ($m_{DM} \gtrsim 6$ GeV) comes from the LUX collaboration [67]. In the mass region 6 GeV $\gtrsim m_{DM} \gtrsim 4$ GeV the superCDMS results are stronger [69]. In the low mass region, $m_{DM} \lesssim 4$ GeV, currently the strongest limit comes from the CRESST-TUM40 experiment [68]. We show all these limits in Fig. 8.

However, some collaborations claimed a success in registering a potential DM scattering event. In Fig. 8 we see the positive 68% C.L to 99% C.L. CDMS-II signal [64, 65], 90% C.L. CoGeNT signal [66], and 1 and 2σ CRESST-II islands [70]. There are also various claims from the DAMA collaboration, that observes not only a signal, but also predicted yearly modulations, see [71]. Unfortunately, the combined 90% C.L. LUX and superCDMS limits

exclude all those positive results.

In July 2014 CRESST collaboration published a follow up analysis, where they exclude most of their previous signal region from [70], see [68]. The current projection for 500 kg days to be realised by the end of 2014 should exclude all of the positive result [72]. Therefore, we will neglect the CRESST-II signal results in further analysis of direct detection in this chapter.

First, one should keep in mind that there are many assumptions behind the evaluation of limits on the spin-independent WIMP-nucleon cross section σ_{DM-p}, shown in Fig. 8. Therefore, as a first step in an attempt to explain discrepancies between experiments, we should revisit these assumptions, in particular, we would like to concentrate on the *hidden* assumption of isospin-conserving DM-nucleon interaction.

In context of models that we analyse later in this thesis, a possibility of DM interacting differently with protons and neutrons is especially interesting. Influence of such isospin-violating interactions on DM direct detection experiments has been first discussed in [73]. Feng *et. al.* pointed out, that if $f_n \neq f_p$, we might observe a destructive interference between protons and neutrons for $f_n/f_p = -Z/(A-Z)$ (see equation (56)). The most favourable value of f_n/f_p, to reconcile XENON, LUX and CDMS limits is the case of $f_n/f_p = -0.7$, see Fig. 9.

Later in the thesis we will consider models with possible isospin violation ($f_n \neq f_p$). To compare the results for the cross section of DM-p (or DM-n) scattering obtained within an isospin-violating model, with the results presented by experimental groups with $f_n = f_p$ assumption, we will define the normalized-to-nucleon cross section $\overline{\sigma}_{DM-p}$, following [73, 74] we have:

$$\begin{aligned} \overline{\sigma}^X_{DM-p} &\equiv \sigma_{DM-p}\,\Theta^X(f_n, f_p), \\ \Theta^X(f_n, f_p) &= \frac{\sum_I \eta_I \mu^2_{A_I} \left[Z_I + \frac{f_n}{f_p}(A_I - Z_I)\right]^2}{\sum_I \eta_I \mu^2_{A_I} A_I^2} \end{aligned} \tag{65}$$

where σ_{DM-p} is the predicted DM-p cross section. Note that for $f_n = f_p$, the rescaling function $\Theta^X(f_n, f_p) = 1$. The value of $\Theta^X(f_n, f_p)$ depends on the detector target X. We will require that $\overline{\sigma}^X_{DM-p}$ satisfies experimental constraints from detector based on a target X.

There are also other ways to ameliorate the discrepancies between direct detection experiments. Mainly, one could introduce inelastic scattering of DM off a nucleus [75, 76]. Such

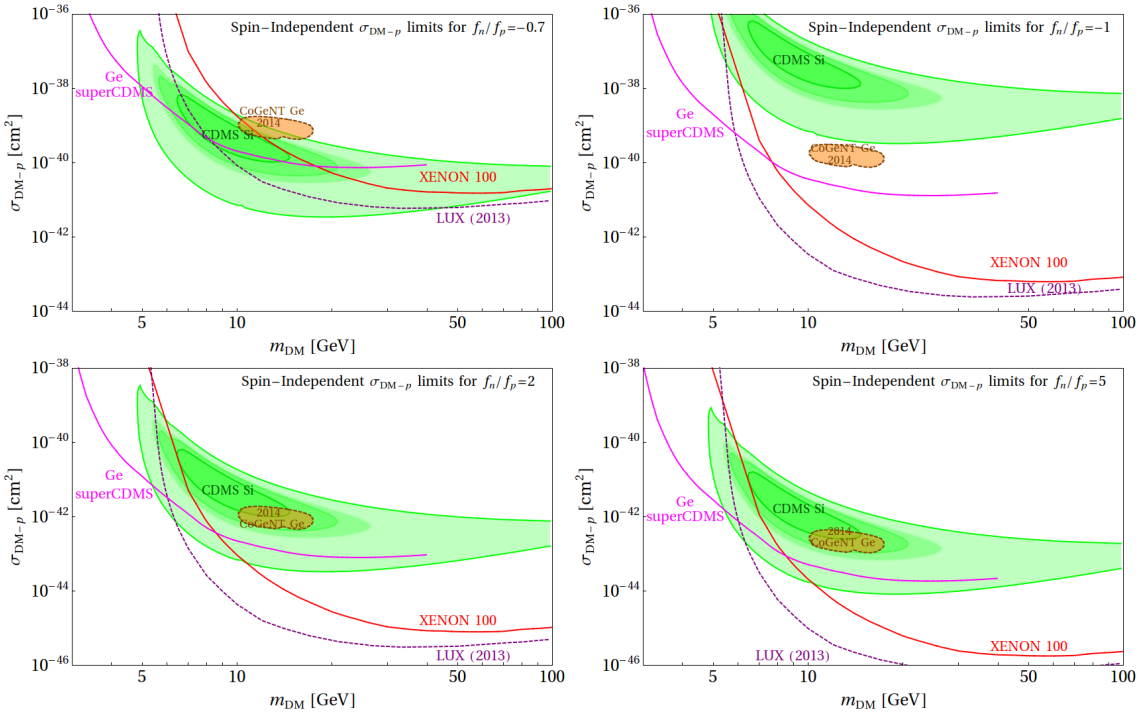

Figure 9: Upper limits and signal regions for spin-independent DM-nucleon cross section for recent measurements, for various f_n/f_p: -0.7 (top left panel), -1 (top right panel), 2 (bottom left panel), 5 (bottom right panel). Green shaded region corresponds to the CDMS Si [64, 65] signal at 99, 95, 90 and 68% CL from the lightest to the darkest green, respectively. Orange dashed line corresponds to the CoGeNT 2014 results at 90% CL [66]. Red curve is the XENON 100 exclusion limit. Dashed purple line is the LUX 2013 exclusion limit. Note, that the vertical axis range is different in the upper and lower panels.

scatterings are possible if there is more than one component of the dark sector. However, such effects would not be further discussed in this thesis.

IV. O(N) SINGLET SCALAR DARK MATTER

As discussed in Section III A, the evidence of DM's presence in our Universe is overwhelming. However, the SM does not provide a DM candidate and physics beyond the SM is necessary. The simplest possible modification of the SM, providing a DM candidate, introduces an additional real scalar field, a gauge singlet. Such singlet extension of the SM is not a new idea, the earliest publication we are aware of is Veltman and Yndurain [77]. However, their motivation was not related to the search of DM; a scalar singlet DM candidate was first introduced in [78] and then followed by other researchers, see for example [26, 79–82].

In this thesis we will discuss an extension of the SM scalar sector with extra N real singlet scalars $\vec{\varphi} = 1, \dots N$, that transform under fundamental representation of a global unbroken O(N) symmetry group. In Section IV A we present the model and in Section IV B we discuss relevant theoretical constraints (vacuum stability, unitarity, perturbativity). In Sections IV C and IV D we discuss the consequences of imposing the relic density and direct detection limits on the parameter space of the $O(N)$ model. We emphasize the issue of the Higgs boson decay into DM. In Section IV E we will adress a very special case of the $O(N)$ model, with feeble couplings.

Significant part of this chapter is based on work in collaboration with B. Grzadkowski and J. Wudka, published in [26]. The issues of little hierarchy problem and triviality constraint in $N = 1$ singlet scalar extension of the SM has been also discussed in the author's Master Thesis [83].

A. The O(N) Model

We would like to consider the SM extended by N real scalars $\vec{\varphi}$, that are singlets under the SM gauge group $SU(3) \times SU(2) \times U(1)$. We also introduce a global O(N) symmetry group with $\vec{\varphi}$ transforming according to the fundamental representation of this group and all SM fields being $O(N)$-singlets.

We assume that O(N) is an exact symmetry of the model, however this condition could be relaxed without significantly altering our final conclusions. If O(N) symmetry is not exact, we would face the presence of many more parameters of the model, and therefore more freedom when constraining the parameters with theoretical and experimental bounds.

Such analysis, however interesting, will not be a part of this thesis.

As the scalar singlets are intended to provide DM candidates, we would like them to be stable and therefore we impose an extra Z_2 symmetry (that must remain unbroken) under which our DM candidate $\vec{\varphi}$ is odd: $\vec{\varphi} \to -\vec{\varphi}$, while all other fields are even[4]. The Lagrangian density for the scalar sector of our model reads:

$$\mathcal{L}_{scalar} = \frac{1}{2}\partial_\mu \vec{\varphi} \partial^\mu \vec{\varphi} + D_\mu H^\dagger D^\mu H - V(H, \vec{\varphi}) \,, \tag{66}$$

where H is the SM $SU(2)$ Higgs isodoublet and the most general renormalizable potential is given by:

$$V(H, \vec{\varphi}) = \mu_H^2 H^\dagger H + \lambda_H (H^\dagger H)^2 + \frac{1}{2}\mu_{\vec{\varphi}}^2 \vec{\varphi}^2 + \frac{1}{4!}\lambda_{\vec{\varphi}} \left(\vec{\varphi}^2\right)^2 + \lambda_x H^\dagger H \vec{\varphi}^2 \,. \tag{67}$$

As in the SM, we have $\mu_H^2 < 0$ and the minimum of the potential breaks spontaneously electroweak symmetry. The Higgs doublet acquires a non-zero vacuum expectation value,

$$\langle H \rangle = (0, v/\sqrt{2}), \qquad v = 246 \text{ GeV}. \tag{68}$$

We require the symmetry to remain unbroken and we will discuss consequences of this condition in detail in Section IV B. As $\langle \vec{\varphi} \rangle = 0$, there will be no mixing between the mass eigenstates φ_i and H. After the spontaneous symmetry breaking we have N+1 physical fields, a Higgs boson with mass

$$m_h^2 = \mu_H^2 + 3\lambda_H v^2 = -2\mu_H^2, \tag{69}$$

and N singlet scalars with degenerate masses, as the consequence of $O(N)$

$$m_\varphi^2 = \mu_\varphi^2 + \lambda_x v^2. \tag{70}$$

This degeneracy might be removed if one considers a generic mass term $(\mu_\varphi^2)_{ij}\varphi_i\varphi_j$, that only breaks O($N$) softly. However, this is beyond the scope of this thesis.

The parameter space of the O(N) model is 5-dimensional: $(m_h, m_\varphi, \lambda_x, \lambda_\varphi, N)$. We will discuss theoretical and experimental constraints on this parameter space in the following sections.

[4] For $N > 1$ this Z_2 symmetry is a consequence of O(N) invariance.

B. Theoretical Constraints on the O(N) Model

Vacuum stability

In order to assure stability of the vacuum at the tree level, we will assume that the scalar potential (67) is bounded from below. This condition implies

$$\lambda_H, \lambda_\varphi > 0\,; \quad \lambda_x > -\sqrt{\frac{\lambda_\varphi \lambda_H}{6}} = -\frac{m_h}{2v}\sqrt{\frac{\lambda_\varphi}{3}}\,. \tag{71}$$

For $\lambda_\varphi = 4\pi$ and $m_h = 125$ GeV the condition on λ_x corresponds to $\lambda_x > -0.58$.

Perturbativity

The absolute values of the quartic couplings in the Feynman rules associated with the mass eigenstates should be below 4π. That implies

$$|\lambda_\varphi| < 4\pi \quad \text{and} \quad 2|\lambda_x| < 4\pi\,. \tag{72}$$

Unitarity

Tree-level unitarity constraints emerge from the SM condition for $V_L V_L$ scattering [84] and from the requirement that all possible scalar-scalar scattering amplitudes are consistent with unitarity of the S matrix [85]. In general, one can observe that those constraints are closely related to the perturbativity constraints. The dominant non-vanishing contribution to amplitudes for two-body scattering at high energy comes from processes mediated by quartic couplings present in the scalar potential. Therefore, constraint for $J = 0$ partial waves, $|a_0| \leq 1/2$, reduces to a constraint on these quartic couplings, and we have

$$m_h^2 < \frac{8\pi}{3}v^2, \quad \lambda_\varphi < 8\pi \quad \text{and} \quad |\lambda_x| < 4\pi\,. \tag{73}$$

In the following sections we present figures with curves corresponding to large coupling constants, even close to the upper unitarity limits. We include those large coupling constants merely to illustrate the dependence of various observables on the corresponding couplings, as they grow. It should be emphasized that we do not draw any physical conclusions based on results obtained for couplings that are close to (and of course above) their unitarity limits.

Global Minimum of a Scalar Potential

Finally, as we need to specify conditions for the global $O(N)$ symmetry to remain unbroken after EWSB. Let's rewrite the potential (67) in terms of the physical field h and $\varphi = |\vec{\varphi}|$:

$$V_1(h,\varphi) = \frac{1}{2}\mu_H^2 h^2 + \frac{\lambda_H}{4}h^4 + \frac{1}{2}\mu_0^2\varphi^2 + \frac{1}{4!}\lambda_\varphi\varphi^4 + \frac{1}{2}\lambda_x\varphi^2 h^2 \tag{74}$$

In general, there can be up to 9 extrema in such potential:

$$\begin{aligned}
&h_1 = 0, \quad \varphi_1 = 0 \\
&h_{2,3} = \pm\sqrt{-\mu_H^2/\lambda_H}, \quad \varphi_{2,3} = 0 \\
&h_{4,5} = 0, \quad \varphi_{4,5} = \pm\sqrt{-6\mu_0^2/\lambda_\varphi} \\
&h_{6,7,8,9} = \pm\frac{\sqrt{6\lambda_x\mu_0^2 - \lambda_\varphi\mu_H^2}}{\sqrt{-6\lambda_x^2 + \lambda_H\lambda_\varphi}}, \quad \varphi_{6,7,8,9} = \pm\frac{\sqrt{6(-\lambda_H\mu_0^2 + \lambda_x\mu_H^2)}}{\sqrt{-6\lambda_x^2 + \lambda_H\lambda_\varphi}}
\end{aligned} \tag{75}$$

Spontaneous symmetry breaking leaves O(N) symmetry unbroken if and only if the global minimum of (74) is attained at $\langle\varphi\rangle = 0$ and $\langle h\rangle = \pm\sqrt{-\mu_H^2/\lambda_H}$. The first from necessary and sufficient conditions is

$$1) \;\; h_{2,3}, \varphi_{2,3} \in R, \;\; \text{therefore} \;\; \mu_H^2 < 0. \tag{76}$$

Then the value of the potential at the global minumum is

$$V_{MIN} = V_1(h_2,\varphi_2) = V_1(h_3,\varphi_3) = -\frac{\mu_H^4}{4\lambda_H}. \tag{77}$$

We should have

$$2) \;\; V_{MIN} < V_1(h_1, s_1) = 0, \tag{78}$$

which is satisfied for $\lambda_H > 0$. For the 4th and 5th extrema we should have:

3) either $h_{4,5}, \varphi_{4,5} \notin R$ (if and only if $\mu_0^2 > 0$ for $\lambda_\varphi > 0$) or $V_{MIN} < V_1(h_{4,5}, s_{4,5})$.

For $\mu_0^2 < 0$ we have

$$-\frac{\mu_H^4}{4\lambda_H} < -\frac{3\mu_0^4}{2\lambda_\varphi} \tag{79}$$

as $\lambda_\varphi > 0$, then from the 4th and 5th extrema we can conclude that

$$\mu_0^2 > -\sqrt{\frac{\lambda_\varphi\mu_H^4}{6\lambda_H}}. \tag{80}$$

For the last 4 extremas we impose analogous condition

4) either $h_{6,7,8,9} \notin R$, $\varphi_{6,7,8,9} \notin R$ or $V_{MIN} < V_1(h_{6,7,8,9}, \varphi_{6,7,8,9})$,

where

$$V_1(h_{6,7,8,9}, \varphi_{6,7,8,9}) = -\frac{6\lambda_H\mu_0^4 - 12\lambda_x\mu_0^2\mu_H^2 + \lambda_\varphi\mu_H^4}{-24\lambda_x^2 + 4\lambda_H\lambda_\varphi} \tag{81}$$

However, for $-6\lambda_x^2 + \lambda_H\lambda_\varphi < 0$ it is always true that $V_{MIN} < V_1(h_{6,7,8,9}, \varphi_{6,7,8,9})$ and the only potentially problematic region is for,

$$-6\lambda_x^2 + \lambda_H\lambda_\varphi > 0 \tag{82}$$

as it implies $V_{MIN} > V_1(h_{6,7,8,9}, \varphi_{6,7,8,9})$, see the blue region in Fig. 10. However, for $\mu_0^2 > 0$, all possible values of λ_x with $m_\varphi > 0$, also provide either $\varphi_{6,7,8,9} \notin \mathcal{R}$ or $V_{MIN} < V_1(h_{6,7,8,9}, \varphi_{6,7,8,9})$. Negative values of $\mu_0^2 < 0$ are also allowed, with a lower limit from (80), and also with additional constraint from the 6th to 9th extrema analysis ($\varphi_{6,7,8,9} \notin \mathcal{R}$ within the problematic blue region in Fig. 10). Therefore the additional constraints that ensure unbroken O(N) are

$$-\sqrt{\frac{\lambda_\varphi\mu_H^4}{6\lambda_H}} < \mu_0^2 \quad \text{and} \quad \lambda_x\mu_H^2 < \lambda_H\mu_0^2. \tag{83}$$

Triviality bound

In $\lambda\phi^4$ quantum field theory, λ increases monotonically with the momentum scale. At a certain energy λ reaches infinity (Landau pole) and the theory becomes non-perturbative. This effect is also observable in quantum electrodynamics, however the pole is located at extremely large energy scale ($\sim 10^{277}$ GeV) and therefore this problem can be safely ignored (as we do not expect QED to be valid up to such extremely large energy scales). In general, only non-interacting (trivial) theory is allowed if one tries to shift the location of the pole to infinity. In this thesis by *'triviality constraint'* we mean the following: *for a given* Λ *there is no pole in the evolution of scalar quartic coupling constants at energies below* Λ.

In the SM with m_h as a free parameter, triviality restricts the initial value of $\lambda_H(\mu = m_W)$, leading to an upper limit on m_h as a function of Λ. Based on the current experimental results [15, 86], the SM might face triviality issues only at a $\sim 3\sigma$ deviation from the current

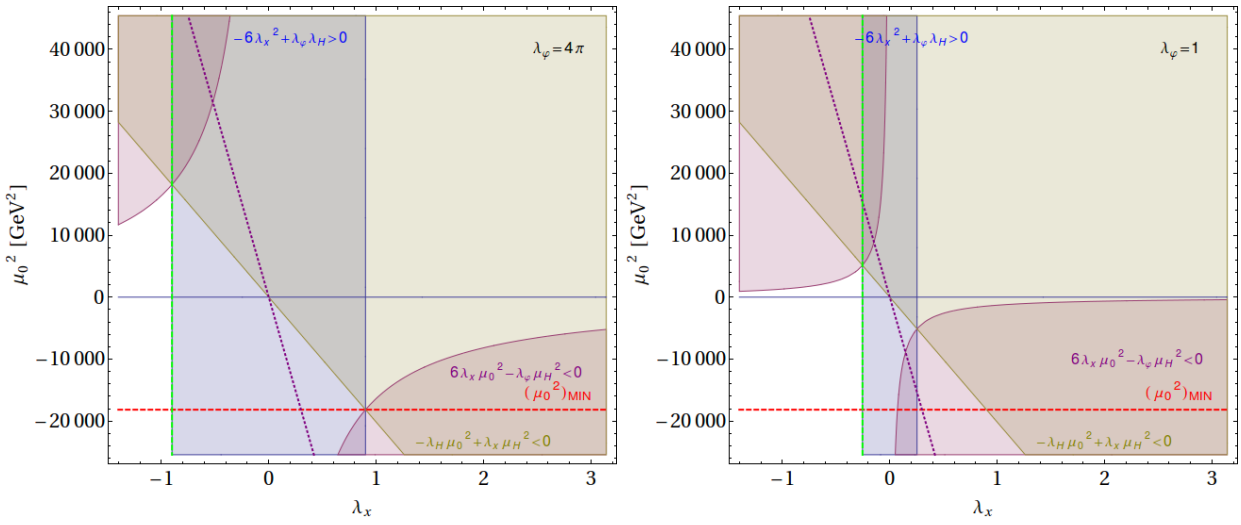

Figure 10: Various constraints imposed on (λ_x, μ_0^2) parameter space. Red line corresponds to the lower limit on μ_0^2, see (80). Green line corresponds to the lower limit on λ_x coming from stability. Dotted purple line corresponds to the lower bound on λ_x coming from positivity of the physical mass, m_φ. The blue region corresponds to (82). Purple region corresponds to $6\lambda_x\mu_0^2 - \lambda_\varphi\mu_H^2 < 0$, therefore if it overlaps with the blue region we have $h_{6,7,8,9} \notin \mathcal{R}$. Yellowish region corresponds to $-\lambda_H\mu_0^2 + \lambda_x\mu_H^2 < 0$, therefore if it overlaps with the blue region, we have $\varphi_{6,7,8,9} \notin \mathcal{R}$. Left panel corresponds to $\lambda_\varphi = 4\pi$, while the right panel corresponds to $\lambda_\varphi = 1$.

measurements of SM parameters (particularly m_h and the top quark mass m_t)[5], and we rather deal with vacuum instability (metastability) problem (the running of quartic coupling λ_H causes λ_H to become negative at a certain energy scale, therefore the effective potential bends down). The presence of extra scalars change this situation. Adding extra terms in the evolution of λ_H generally might speed up the growth of λ_H and therefore not allow for its negative value, however the triviality bound should in this case be revisited.

In order to determine the energy scale of the Landau pole, one should solve the set of RGEs for all of the running parameters of the model. We are interested only in cut-off scales below 50 TeV, therefore it is safe to neglect the running of the gauge and top-quark Yukawa couplings. Thus, we consider only the evolution of λ_H, λ_φ and λ_x, which are determined by

[5] Meaning that at $\sim 3\sigma$ deviation from the current measurements of SM parameters, the Landau pole of the SM Higgs coupling appears at an unacceptably low energy scale.

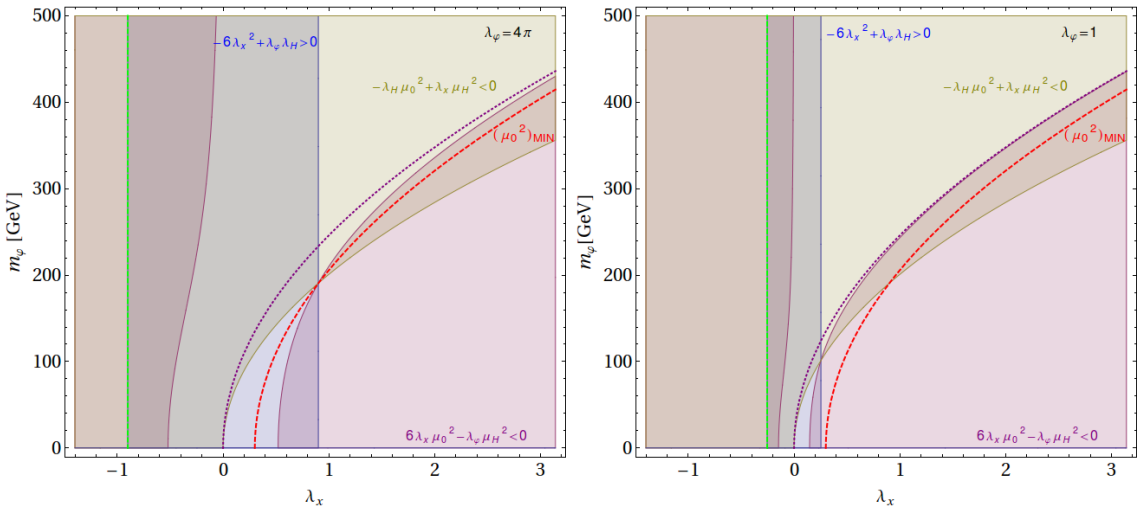

Figure 11: Various constraints imposed on (λ_x, m_φ) parameter space. The colouring and labels are analogous to Fig. 10.

(see [26, 83])

$$16\pi^2\mu\frac{d\lambda_H}{d\mu} = \frac{3}{8}g_1^4+\frac{9}{8}g_2^4+\frac{3}{4}g_1^2g_2^2-6y_t^4+24\lambda_H^2+12y_t^2\lambda_H$$
$$-3g_1^2\lambda_H-9g_2^2\lambda_H+2N\lambda_x^2 \quad (84)$$
$$16\pi^2\mu\frac{d\lambda_x}{d\mu} = \lambda_x\left(12\lambda_H+\lambda_\varphi+8\lambda_x+6y_t^2-\frac{3}{2}g_1^2-\frac{9}{2}g_2^2\right) \quad (85)$$
$$16\pi^2\mu\frac{d\lambda_\varphi}{d\mu} = 48\lambda_x^2+\frac{1}{3}(8+N)\lambda_\varphi^2 \quad (86)$$

where g_1, g_2, g_3 are the gauge couplings of $U(1), SU(2), SU(3)$, respectively, and y_t is the top quark Yukawa coupling. We obtain unique solutions to (84-86) once we specify the initial conditions,

$$\lambda_H(\mu = m_W) = \lambda_{H\,0} \quad (87)$$
$$\lambda_x(\mu = m_W) = \lambda_{x\,0} \quad (88)$$
$$\lambda_\varphi(\mu = m_W) = \lambda_{\varphi\,0}. \quad (89)$$

We would like to show the allowed regions in the $(\Lambda, m_h = v\sqrt{2\lambda_{H\,0}})$ plane. However, the constraint depends on the initial parameters $\lambda_{x\,0}$, $\lambda_{\varphi\,0}$ and the number of scalars N. Note, that if $\lambda_{x\,0} \neq 0$ (as we assume) each quartic coupling constant have the same location of the Landau pole, as the RGEs are coupled.

We illustrate the triviality bound for m_h as a function of Λ in Fig. 12. From this figure one can see how the allowed region shrinks as $\lambda_{x\,0}$ grows (for fixed N). Also, as N increases

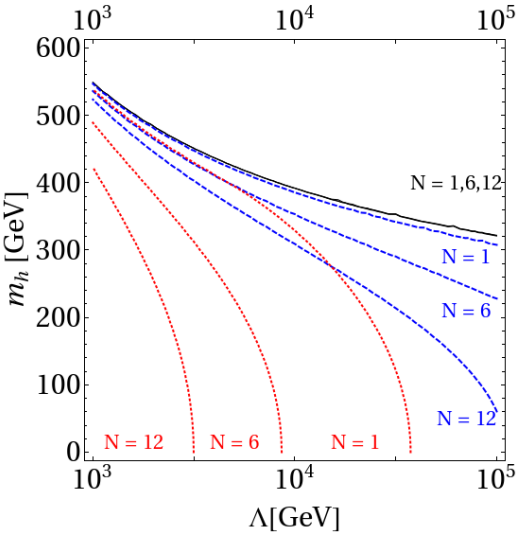

Figure 12: The triviality upper bound on the Higgs mass as a function of the cut-off Λ for $\lambda_\varphi(m_W) = 0.1$, for $\lambda_{x\,0} = 0.1, 1, 2$ (black, blue and red curves, respectively) and $N = 1, 6, 12$ (starting with the uppermost curve). For $\lambda_{x\,0} = 0.1$ non-standard effects are so small that upper boundaries for all N are indistinguishable from each other and the SM limit.

for fixed $\lambda_{x\,0}$, we observe lowering of the upper bound on m_h. This is a consequence of $2N\lambda_x^2$ in (84): increasing N and/or λ_x amplifies the evolution of λ_H. As one can see, for $m_h \sim 125$ GeV, $\lambda_{x\,0}$ values significantly above 1. are dangerous, as the Landau pole might appear for low energy scale. The accuracy of our calculations is up to the one loop order and our results are quantitatively accurate only if the couplings are not too large. However, this limits should not change radically when higher order corrections are included, see *eg.*[87].

For a given (Λ, m_h) and fixed $\lambda_{\varphi\,0}$, there is a range of $\lambda_{x\,0}$ for which the Landau pole occurs above Λ, as illustrated in Fig. 13. Note an asymmetry of the allowed (inner) region, which is a consequence of the $8\lambda_x^2$ term in (85). In Fig. 13 triviality limits on quartic couplings are quite large, however substantially below the unitarity bound, see (73).

1. Little hierarchy problem

If the SM is an effective theory valid only at scales below a UV cut-off Λ, radiative corrections shift the Higgs boson mass m_h to a scale of order $\Lambda/\sqrt{4\pi}$, see [88]. However, the current bounds on the new physics scale require at least $\Lambda > O($ TeV). For $m_h \sim 125$ GeV

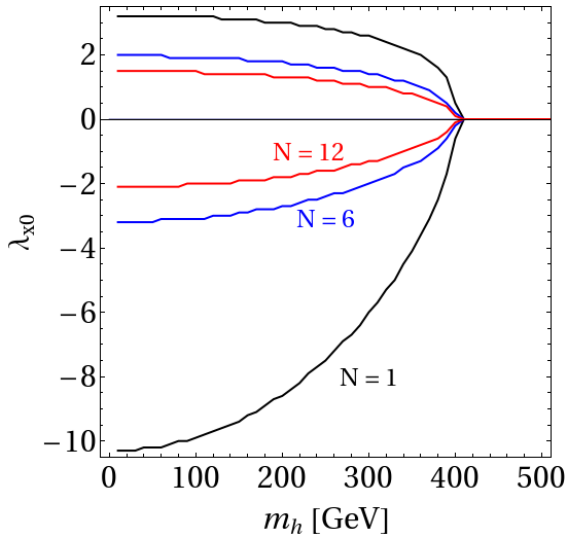

Figure 13: Maximum and minimum $\lambda_{x\,0}$ allowed by the triviality bound for $\Lambda = 10$ TeV, $\lambda_{\varphi\,0} = 0.1$ and $N = 1, 6, 12$.

we have a conflict, that can be alleviated when a cancellation of $O(\Lambda^2)$ contributions to m_h^2 is introduced. Such cancellation naturally occurs when supersymmetry is introduced [89]. This is also possible with singlet scalar extensions of the SM, however fine-tuning is required.

Veltman in [88] first noticed, that the 1-loop quadratic corrections to m_h would completely cancel if $m_h^2 + m_Z^2 + 2m_W^2 - 4m_t^2 = 0$. However, this possibility is now experimentally excluded. In this section we will evaluate the 1-loop quadratic corrections to m_h in the O(N) model.

First we shall estimate the possible effects generated by higher order radiative corrections. Generally, for a theory with many couplings λ_i, leading higher-order contributions to quadratically divergent terms in m_h^2 (by leading we mean containing the highest power of $\log(\Lambda)$) at $(n+1)$ loop level take the following form [90]

$$\delta m_h^2 = \Lambda^2 \sum_{n=0}^{\infty} f_n(\lambda_i) \left[\log\left(\frac{\Lambda}{\mu}\right)\right]^n \tag{90}$$

where μ is the renormalization scale and coefficients f_n are defined by the recursion

$$(n+1) f_{n+1} = \mu \frac{\partial}{\partial \mu} f_n = \beta_i \frac{\partial}{\partial \lambda_i} f_n \,, \tag{91}$$

where $\beta_i = \beta(\lambda_i)$ are the RGE beta functions, $\beta_i = \frac{d\lambda_i}{d\mu}$. Thus two-loop leading logarithmic corrections to the Higgs mass are determined by the one-loop corrections and the first order beta functions. Generic results and applications to the $N = 1$ case has been thoroughly discussed in [83]. One-loop corrections and leading two-loop corrections to m_h^2 for the O(N)

model can be found in [26], we repeat them below for completeness. Note, that the SM result can be recovered from the O(N) model case in the limit $\lambda_x = \lambda_\varphi = 0$.

$$\begin{aligned}\delta m^2_{h\,1-loop} = &\frac{\Lambda^2}{16\pi^2}\left(12\lambda_H + 2N\lambda_x - 12y_t^2 + \frac{3}{2}g_1^2 + \frac{9}{2}g_2^2\right)\\ &- \frac{1}{16\pi^2}\left[6\lambda_H m_h^2\,\log\left(\frac{m_h^2+\Lambda^2}{m_h^2}\right) + 2\lambda_x m_\varphi^2\,\log\left(\frac{m_\varphi^2+\Lambda^2}{m_\varphi^2}\right)\right],\end{aligned} \tag{92}$$

$$\begin{aligned}\delta m^2_{h\,2-loops} = &\frac{\Lambda^2}{(16\pi^2)^2}\,\log\left(\frac{\Lambda}{\mu}\right)\left[25g_1^4 + 9g_1^2g_2^2 - 15g_2^4 + 34g_1^2y_t^2 + 54g_2^2y_t^2\right.\\ &+ 192g_3^2y_t^2 - 180y_t^4\lambda_H - 36g_1^2 - 108g_2^2\lambda_H + 144y_t^2\lambda_H + 288\lambda_H^2\\ &\left.-3Ng_1^2\lambda_x - 9Ng_2^2\lambda_x + 12Ny_t^2\lambda_x + 24N\lambda_H\lambda_x + 40N\lambda_x^2 + 2N\lambda_x\lambda_\varphi\right],\end{aligned} \tag{93}$$

where the logarithmic terms ($\propto m_\varphi^2 \log\Lambda$) in the one-loop correction were kept because of their relevance in the range $m_h \ll m_\varphi \lesssim \Lambda$). Terms $\propto m_h^2 \log\Lambda$ are numerically negligible and we include them for completeness. In the numerical analysis we choose the renormalization scale μ equal to the SM Higgs vacuum expectation value, $\mu = 246$ GeV.

We would like to determine how strong fine tuning is required in our theory. Thus we follow the standard approach of [91] and define the relative radiative contribution to m_h^2, to be constrained by the fine-tuning parameter Δ_h,

$$\left|\frac{\delta m_h^2}{m_h^2}\right| \equiv \left|\frac{\delta m^2_{h\,1-loop} + \delta m^2_{h\,2-loops}}{m_h^2}\right| \leq \Delta_h. \tag{94}$$

We then determine the region in the (Λ, m_h) plane where this constraint is satisfied for a given choice of Δ_h (specifically, we fix N and λ_x, then for each choice of (Λ, m_h) we check if there exist m_φ and λ_φ such that condition (94) is obeyed). The results are shown in Figures 14 and 15.

Note, that the two-loop $\vec{\varphi}$ corrections to m_h (93) grow as $\lambda_x/(16\pi^2)\ln(\Lambda/\mu)$ relative to the one-loop contributions (92). For applicability of the perturbative calculation, this factor should be ≤ 1. This provides a maximal cut-off $\Lambda_{\max}$ above which perturbation theory is not valid:

$$\Lambda \lesssim \Lambda_{\max} = \mu e^{4\pi^2/(5\lambda_x)}. \tag{95}$$

For $\mu = 246$ GeV and $\lambda_x(m_W) = 1$ we have $\Lambda_{\max} \sim 6.6\times 10^5$ GeV, while for $\lambda_x(m_W) = 2$ we have $\Lambda_{\max} \sim 1.3\times 10^4$ GeV. Therefore the regions of large Λ in Figures 14 and 15 should be considered with a special caution, especially if $\lambda_x = \lambda_x(m_W)$ is large. We extend the plot

range of Λ up to 10^6 GeV mainly for the purpose of the SM ($\lambda_x = 0$) and small λ_x cases ($\lambda_x \lesssim 0.95$ for $\mu = 246$ GeV).

Let's now discuss implications of triviality and fine tuning constraints on the regions allowed in (Λ, m_h) plane, for two cases $\lambda_x \geq 0$ and $\lambda_x < 0$.

$$\lambda_x \geq 0.$$

The fine-tuning condition from equation (94) for $\Delta_h = 10, 100$ defines a characteristic region in the (Λ, m_h) plane, with a *funnel*-shaped boundary. As shown with the solid lines in Fig. 14, the bound changes for various choices of λ_x and N. For the Higgs boson with mass ~ 125 GeV, we see that as λ_x and/or N grows, the lower branch of the funnel allows greater regions of Λ for fixed Δ, or smaller Δ_h for fixed Λ; at the same time, the upper branch of the funnel allows smaller regions of Λ for fixed Δ_h, or greater Δ_h for fixed Λ. Discussing the combined effect is quite complicated, for example the range of Λ allowed by the fine tuning condition (94) for $m_h \sim 125$ shrinks as λ_x goes from 1 to 2 when $N = 1$ and as λ_x goes from 0.5 to 1 for $N = 3$. If we fix the coupling λ_x and the number of singlets N, the allowed range of Λ shrinks as Δ_h becomes smaller.

Several other comments are in order here. For the SM limit ($\lambda_x = 0$) there is an allowed region for Λ between $1-10$ TeV and $\sim 10^3$ TeV for $\Delta_h = 100$, which shrinks as Δ_h grows. For instance, if $\Lambda \sim 10^4$ GeV, then the Higgs boson mass of ~ 125 GeV follows very significant fine tuning: $\Delta_h > 100$. If we require $\Delta_h < 100$, either low (~ 1 TeV) or very high $\gtrsim 10^3$ TeV values of Λ must be assumed, or beyond SM effects should be introduced.

Introducing the O(N) extension of the SM, we gain much more freedom. Note that for each point in (Λ, m_h) plane, below the SM ($\lambda_x = 0$) upper bound shown in Figures 14 and 15, there exists λ_x such that the point is allowed. Therefore values of the cut-off much larger than in the SM are allowed for $m_h \sim 125$ GeV.

Let's fix the cut-off to $\Lambda = 10^4$ GeV. As it is seen from the left panels is Fig. 14 for such Λ, for $m_h \sim 125$ GeV and fine tuning $\delta m_h^2/m_h^2$ below 10, one needs $\lambda_x \sim 1.2$ ($\lambda_x \sim 0.6$) for $N = 1$ ($N = 3$). However, if the fine tuning condition is relaxed to $\delta m_h^2/m_h^2 < 100$ (compare with right panels of Fig. 14) then λ_x below 1 is allowed for $N = 1$ and values even smaller than $\lambda_x \simeq 0.5$ for $N = 3$. In general, $\lambda_x = O(1)$ is needed to significantly ameliorate the SM

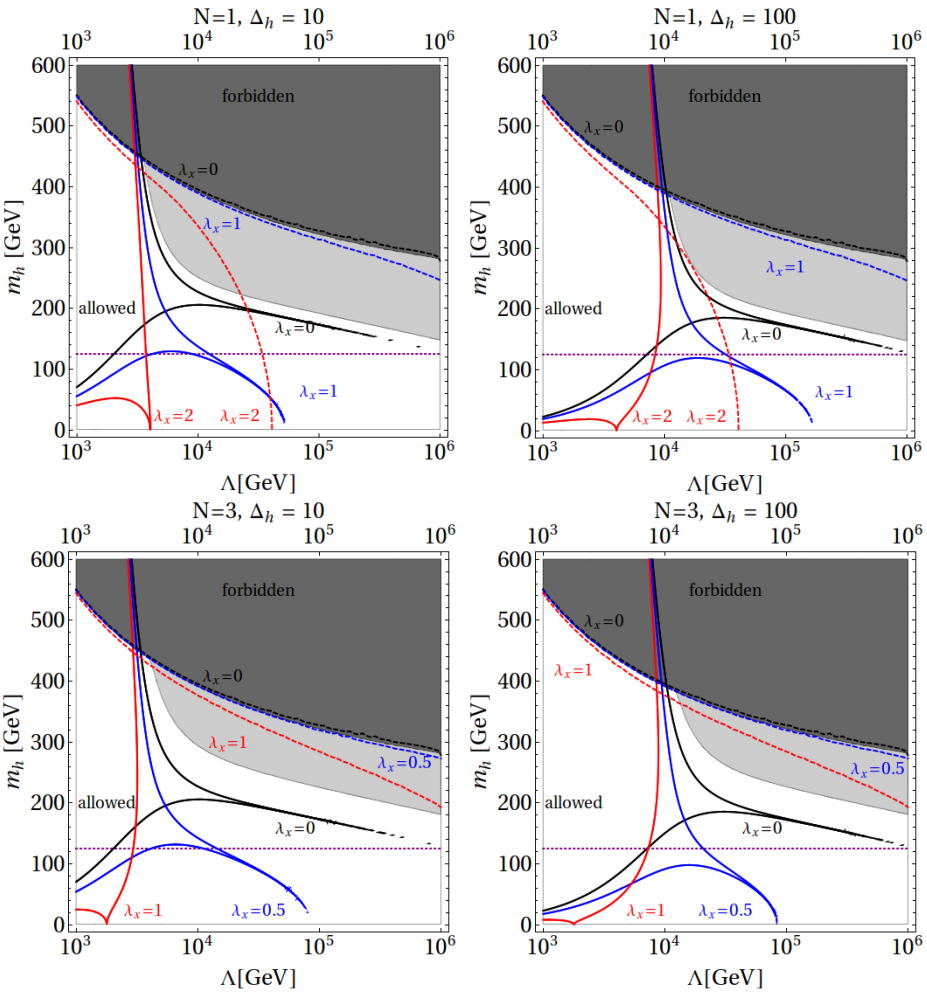

Figure 14: Constraints on $(\Lambda,\, m_h)$ for $\Delta_h = 10, 100$ and $N = 1, 3$. The horizontal purple dashed line shows $m_h = 125$ GeV. The solid lines correspond to the two-loop fine-tuning constraint for the SM ($\lambda_x = 0$, solid black) and singlet extensions for several chosen values of λ_x, as labelled on the plot (solid red and blue curves); regions to the left of the corresponding funnels are allowed by this constraint. Dashed curves correspond to the SM triviality limit ($\lambda_x = 0$, dashed black curve) and O(N) extensions for several chosen values of λ_x (dashed blue and red curves); regions below each curve are allowed by triviality constraint. Points inside the dark (light) gray region are forbidden by the triviality (fine tuning) condition for any value of λ_x. For every allowed point outside the dark gray and gray regions there exist $|\lambda_x| < 8\pi$, 10 GeV $< m_\varphi <$ 10^4 GeV and $0 < \lambda_\varphi < 2$ such that the condition (94) is fulfilled.

fine tuning problem.

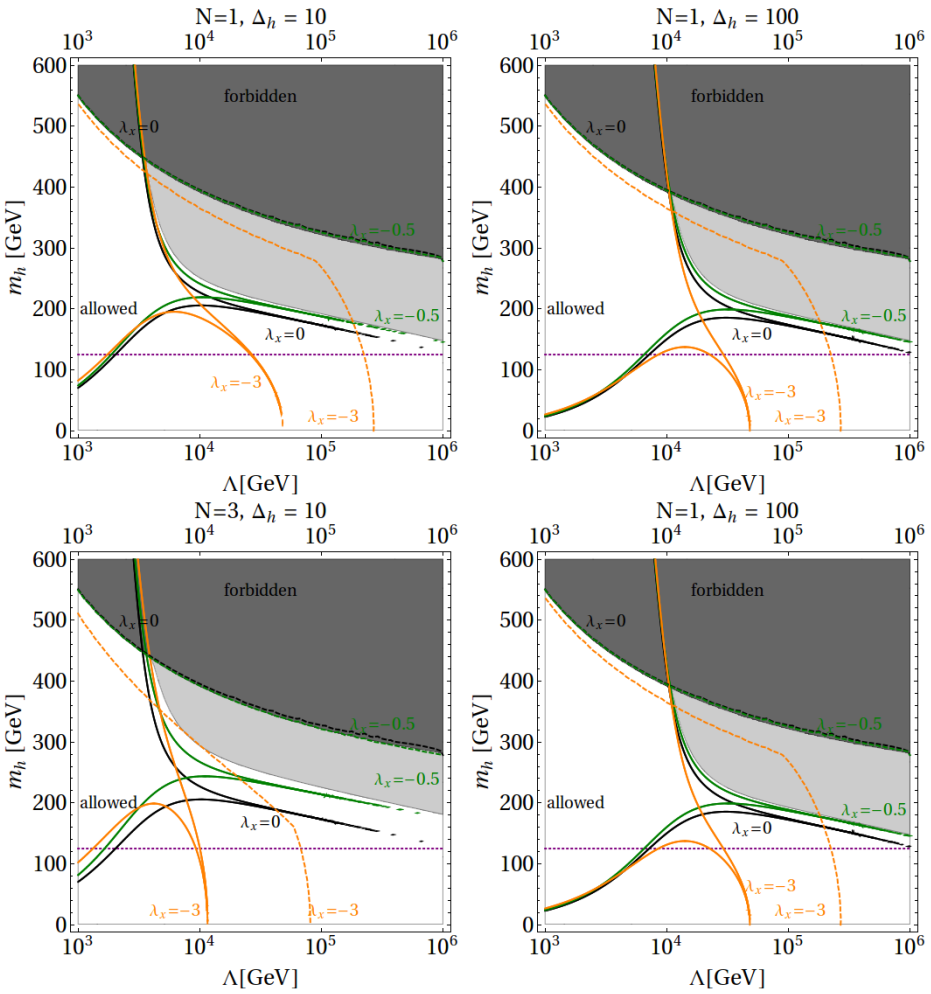

Figure 15: Similar as Fig. 14, but curves for negative values of λ_x are shown.

On the other hand, one should remember that for each choice of m_φ, λ_x is restricted by theoretical conditions.

$$\lambda_x < 0.$$

In this case the theoretical bound from vacuum stability condition (115) becomes important. For $m_h \sim 125$ GeV, this is a strict bound, $|\lambda_x| \lesssim 0.58$ (with maximal value achieved for λ_φ being maximal within perturbativity range). In this range of λ_x the allowed values of Λ are even more restricted when the singlets are included, than for the SM case. This is a consequence of the fact that 1-loop $\vec{\varphi}$-contribution to δm_h^2 from the singlets is of the same sign as the top-quark contribution for $\lambda_x < 0$. Therefore for small λ_x funnels are shifted towards larger values of m_h, in order to compensate the top quark and $\vec{\varphi}$ effects. However, if

one allows for λ_x to increase much beyond 1 in absolute value, the funnels move downwards as a consequence of the growing 2-loop contributions to $\delta m^2_{h\,2-loops}$. But this is not possible within our model. In Fig. 15 we also show triviality limits on m_h for various negative values of λ_x (see also Fig. 13), however those are not applicable in this range of Λ and for allowed λ_x, for $m_h \sim 125$ GeV.

Summarizing this section, one can say, that the O(N) model allows to shift the UV SM cut-off up to $\Lambda \lesssim 10^4$ GeV for $\Delta_h = 10$. The case of $\lambda_x < 0$ is disfavoured (as long as we stay within the perturbative range of parameters), as the cut-off becomes even more severe than in the SM.

C. O(N) Singlet Relic Abundace

All N components of DM in the $O(N)$ model contribute equally to the relic abundance Ω_{DM}, like a single field with N degrees of freedom with the total abundance equal to

$$\Omega^N_{\rm DM} = \sum_i \Omega^i_{\rm DM} = N\Omega^1_{\rm DM} \tag{96}$$

where $\Omega^i_{\rm DM}$ is the dark matter relic density of the i-th scalar field.

As a consequence of the O(N) symmetry the phase space densities of each species $\tilde{f}^{DM}_i$ are equal and the processes $DM_iDM_j \leftrightarrow DM_kDM_l$ to not contribute to the BEQ. It is sufficient to consider just a single BEQ for f_i, for any i, therefore we can write:

$$f_i' = \frac{\langle \sigma_{ii\to SMSM}|v|\rangle}{K}\left(f_i^2 - \left(f_i^{EQ}\right)^2\right), \quad i = 1\ldots N \tag{97}$$

Also, a single-component analytical approximation for DM relic density can be used in this case.

Within the O(N) model we will discuss two different regimes for relic density evaluation: Cold Dark Matter (CDM) and Feebly Interacting Dark Matter (FIDM). We do not consider the hot DM solution, since it would be inconsistent with structure formation at the galaxy scale, see e.g. [92].

In in Fig. 16 we show diagrams contributing to DM annihilation into SM species, $\varphi_i\varphi_i \to SM\,SM$. The corresponding total cross section for φ_i annihilation into SM species, $\langle \sigma_\varphi|v|\rangle$ is available in the literature (e.g. [26, 80, 93]), we also show them for completeness in

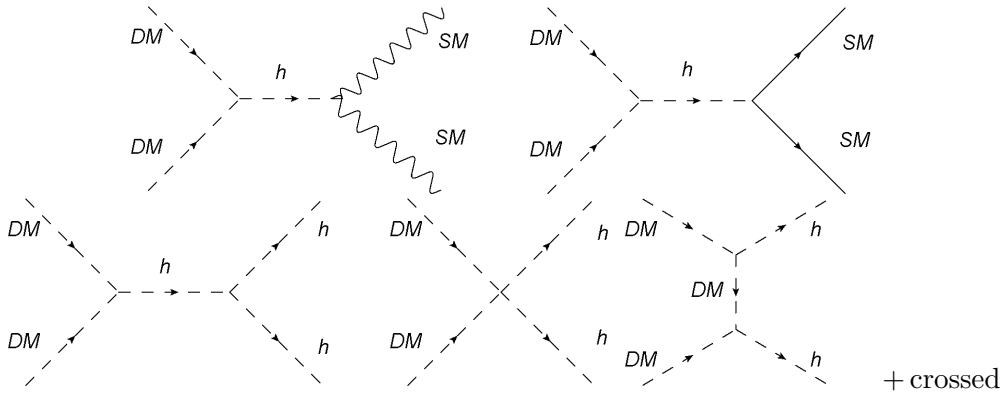

Figure 16: Feynman diagrams illustrating $\vec{\varphi}\vec{\varphi}$ annihilation into SM particles in various channels. $DM = \varphi_i$, and there are N sets of those diagrams for $i = 1 \ldots N$.

Appendix B 4. One should also include the contribution to the Higgs width from possible $\varphi_i\varphi_i$ final states:

$$\Gamma_h = \Gamma_{h\to SM} + \Gamma_{h\to\varphi\varphi} \tag{98}$$

$$\Gamma_{h\to\varphi\varphi} = \frac{Nv^2\lambda_x^2}{8\pi m_h^2}\sqrt{m_h^2 - 4m_\varphi^2}\;\theta_H(m_h^2 - 4m_\varphi^2) \tag{99}$$

where θ_H is the Heaviside function.

D. Cold Dark Matter

For the Boltzmann equation describing single-component DM, the CDM approximation (41) for the $O(N)$ model case yields the relic density

$$\Omega_\varphi^N h^2 = N\frac{\rho_\varphi^1}{\rho_{\rm crit}} = \frac{8\pi G}{3(K(T_\gamma)T_\gamma^2)^2} N f_\varphi T_\gamma^3 m_\varphi \tag{100}$$

where $x_f \equiv m_\varphi/T_f$, and T_f is the freeze-out temperature given in the first approximation by

$$x_f = \log\left[\frac{2\langle\sigma_\varphi|v|\rangle(T_f)}{(2\pi)^{3/2}K(T_f)}\frac{m_\varphi}{x_f^{1/2}}\right]. \tag{101}$$

Note that this expression is N dependent, as N enters through the Higgs width (98). However, it is a weak dependence, even further softened by the logarithm, and can be neglected. If $m_\varphi > m_h$ the t- and u-channel annihilation diagrams are generally present in the calculation, however for small λ_x can be neglected and then abundance depends on N and the combination $(N\lambda_x^2)$.

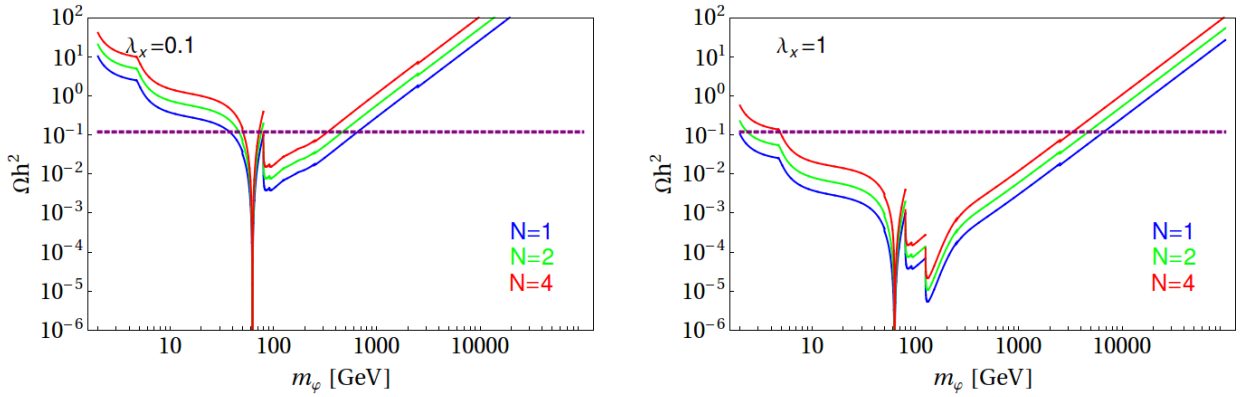

Figure 17: The relic abundance as a function of m_φ for fixed $\lambda_x = 0.1, 1$ for left and right panel, respectively. We show the values of Ωh^2 for 3 different N, $N = 1, 2, 4$. The purple dashed line corresponds to the experimental limit on Ωh^2.

Constraints on the parameter space

In Fig. 17 we show the relic density evaluated within the parameter space of the O(N) model, for some chosen parameters. The results of imposing the relic abundance constraint on the parameter space of the O(N) model are summarized in Fig. 18. We will divide discussion of this constraints into 3 regions of m_φ: large mass region ($m_\varphi > m_h/2$), resonance region ($m_\varphi \sim m_h/2$) and small mass region ($m_\varphi < m_h/2$).

For large m_φ, the t- and u-channel annihilation diagrams with φ exchange can be neglected, $\langle \sigma_\varphi |v| \rangle$ is a function of λ_x^2, therefore the positive and negative solutions in left and right panels in Fig. 18 are the same (some minor differences between positive and negative branch of λ_x appear for $m_\varphi \sim 125$ GeV). However, the maximum value of m_φ allowed within the positive and negative branches of λ_x are different, with ~ 900 GeV for $\lambda_x < 0$ and ~ 100 TeV for $\lambda_x > 0$ (which is smaller for $N > 1$). However, it should be noticed that the solutions presented in Fig. 18 were obtained using a tree level expression for the cross section. Therefore, for large values of λ_x, our results should be treated with extra caution.

We should also look closer into the resonance region. As the DM-Higgs resonance tends to increase the value of the cross section, very small values of λ_x are necessary to satisfy the Planck/WMAP relic abundance constraints. The coupling λ_x can be as small as $\sim 10^{-4}$. Note that $\lambda_x(m_\varphi)$ at around 80 GeV drops suddenly, for all N. This happens because a new channel for annihilation (into WW and soon after into ZZ) opens up. New channels increase

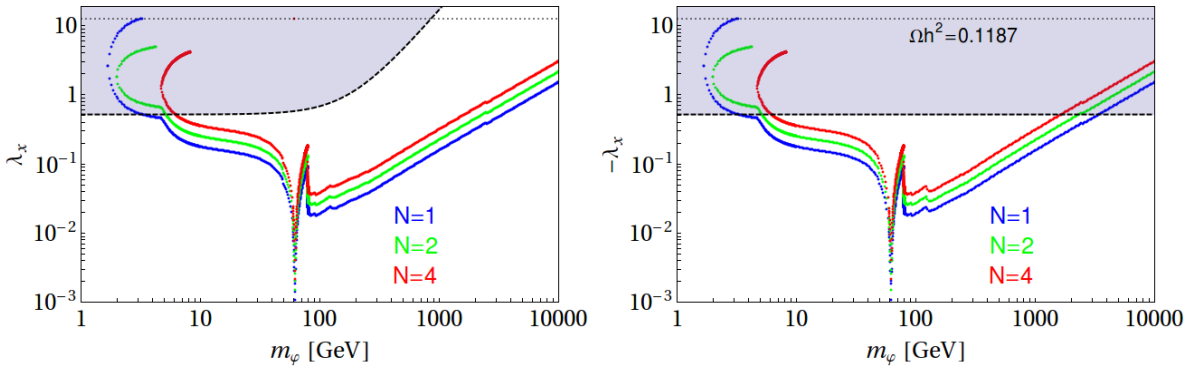

Figure 18: The coupling λ_x as a function of m_φ obtained from the requirement (20); for the Higgs mass $m_h = 125$ GeV, $N = 1, 2$ and 4 (blue, green and red bands, respectively). The positive branch of λ_x is shown in the left panel, while the negative branch of λ_x is shown in the right panel. The blue areas in the left and right panels correspond to the regions disallowed by theoretical bounds: the global minimum condition (83) and stability constraint (115) for $\lambda_\varphi = 4\pi$, respectively. The dotted line is the unitarity and perturbativity limit on λ_x.

the total cross section for φ annihilation, $\langle\sigma_\varphi|v|\rangle$, therefore smaller value of λ_x is required for proper Ωh^2. An effect of the top-quark annihilation channel opening at $m_\varphi \sim 173$ GeV is also visible.

In general there are no CDM solutions for singlet masses below ~ 1 GeV. For $m_\varphi \geq 1$ GeV in the low mass region there might be four values of λ_x for which the (20) is satisfied; two positive and two negative. In this region the main contributions to $\langle\sigma|v|\rangle$ come form the $\bar{b}b$ channel, so the constraint (20) takes the form $\lambda_x^2/(1 + b^2\lambda_x^4) \sim$ const, where the λ_x^4 contribution comes from the Higgs width (99) in the Higgs propagator and we neglected logarithmic dependence on λ_x in evaluating the x_f. However, the non-perturbative region of large λ_x is eliminated by theoretical constraints. The actual lower bound on m_φ is larger than 1 GeV and comes from either the global minimum condition (83) for $\lambda_x > 0$ or stability constraint (115) $\lambda_x < 0$. For positive λ_x we have $m_\varphi \gtrsim 5$ GeV and $\lambda_x \lesssim 0.4$ in this mass region; for negative λ_x we have $m_\varphi \gtrsim 4$ GeV and $\lambda_x < -0.54$; where both constraints were evaluated for $N = 1$ and $\lambda_\varphi = 4\pi$. If $N > 1$ and $\lambda_\varphi < 4\pi$, both constraints are stronger.

E. Feebly Interacting Dark Matter (FIDM)

One can estimate the interaction rate Γ for a relativistic scalar singlet to be $\Gamma \sim \lambda_x^2 T/(8\pi)$, while the expansion rate of the Universe is $H \sim T^2/m_{Pl}$. The equilibrium holds if the interaction rate is larger than the expansion rate, for $T < T_{EQ}$ where

$$T_{EQ} \sim \frac{m_{Pl}\lambda_x^2}{8\pi}\,. \tag{102}$$

If λ_x is very small ($\sim 10^{-9}$) DM particles might not equilibrate until very late times, $T_{EQ} \sim$ 1 GeV. In particular, if $\lambda_x \lesssim 7 \times 10^{-16}$ and $T_{EQ} < 2.7\,^oK$ the singlets would not have equilibrated before the present epoch.

In the following analysis we will consider feeble interaction rate of DM to SM particles. We will also assume that the DM normalised number density f_{DM} was negligible at the Big Bang: $\lim_{T\to\infty} f(T) = 0$. As before, because of the O(N) symmetry, number densities of all N components are the same and we will effectively solve the BEQ for a single species. In practice, because of the initial condition, the BEQ can be simplified as the f_{DM}^2 term on the right-hand side can be neglected until very low temperatures. Following this procedure, one should remember that the electroweak phase transition occurs at $T_{EW} \simeq 300$ GeV. Above this temperature, the only tree level contribution to the annihilation cross section comes from the $\lambda_x H^\dagger H \vec{\varphi}^2$ coupling, therefore

$$\hat{\sigma}_{>300} = \frac{\lambda_x^2}{4\pi}\sqrt{1 - \frac{4m_h^2}{s}}, \tag{103}$$

where the cross section *'with a hat'* ($\hat{\sigma}$) is defined in Appendix B 4. To avoid possibility of double counting we assume that the thermal generation of scalars is happens through the $2 \leftrightarrow 2$ processes with Higgs boson exchange, $DM + DM \leftrightarrow h \leftrightarrow SM + SM$, and we do not separately include Higgs production and decays $\vec{\varphi}\vec{\varphi} \leftrightarrow H$ (one can compare this approach with [45]).

Solutions of (41) describing the evolution of the number density $f(T)$, are shown in Fig. 20, for different singlet masses and couplings λ_x. The general behaviour of f is the following: as the Universe cools down, f slowly increases, until a certain point where it *freezes-in* and remains constant afterwards (the name "freeze-in" is an analogue to the classical CDM solution of the BEQ with a freeze-out). The freeze-in temperature point generally depends on m_φ. The value of f and its growth strongly depends on the coupling λ_x. In order to

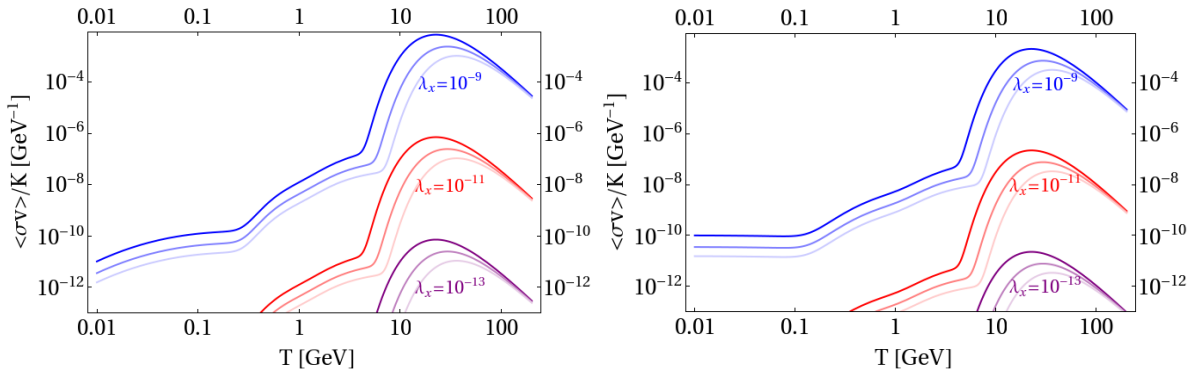

Figure 19: Thermally averaged cross sections $\langle\sigma_\varphi|v|\rangle$, normalized by K, $N = 1$ for two values of m_φ and $m_h = 100$ GeV (thin lines), 130 GeV (medium lines), 160 GeV (thick lines) and $|\lambda_x| = 10^{-13}$ (bottom curves), 10^{-11} (middle curves), 10^{-9} (top curves).

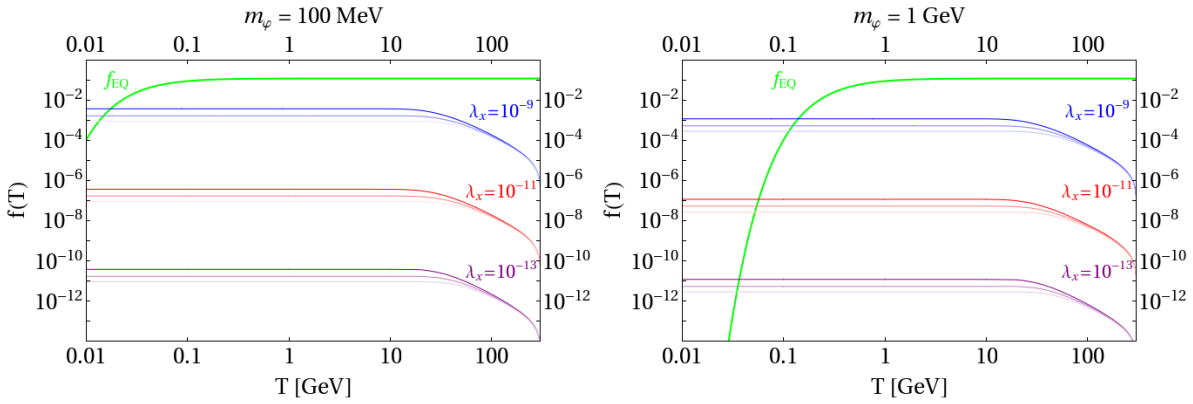

Figure 20: FIDM solutions of the BEQ with boundary condition $f(T = \infty) = 0$, $N = 1$ for two values of m_φ and $m_h = 100$ GeV (thin lines), 130 GeV (medium lines), 160 GeV (thick lines) and $|\lambda_x| = 10^{-13}$ (bottom curves), 10^{-11} (middle curves), 10^{-9} (top curves). The curve labeled f_{EQ} corresponds to the equilibrium distribution.

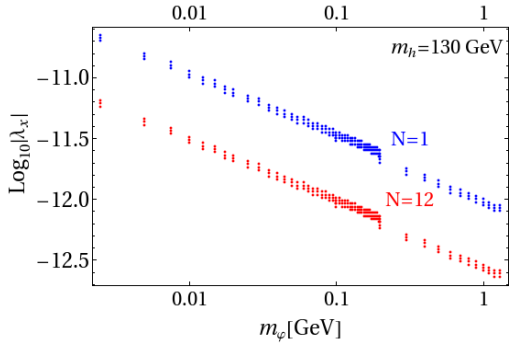

Figure 21: Solutions to the Boltzmann equation for FIDM, for $N = 1, 12$ scalars and $m_h = 130$ GeV.

understand better this behaviour of f we plot in Fig. 19 thermally averaged cross sections as functions of T, corresponding to the solutions shown in Fig. 20. We generally observe that $\langle\sigma_\varphi|v|\rangle/K$ reaches its maximum for $T \sim 20-30$ GeV, and is strongly suppressed for $T \lesssim 10$ GeV, which implies a T-independent f for $T \lesssim 20-30$ GeV, as observed in Fig. 20.

The solutions of the BEQ for parameters that satisfy the relic density constraint (20), are presented in Fig. 21. In FIDM regime we observe $\langle\sigma_\varphi|v|\rangle \propto \lambda_x^2$ up to small corrections, in addition the term $\propto f^2$ on the right-hand side of the BEQ is subdominant, so that to a good approximation $f \propto \lambda_x^2$. It implies the relic density to be proportional to λ_x^2, namely $\Omega_{DM} \propto N m_\varphi \lambda_x^2$ (this behaviour is illustrated in Fig. 21). In particular φ masses above 1 GeV require $\lambda_x < 10^{-13}$.

F. O(N) Singlet Scalar Direct Detection

The FIDM model is definitely far beyond the hope of direct detection - the interaction rate of DM with SM is much too small. In this section we will discuss only the range of parameters that is interesting for the CDM case.

The current status of direct detection experiments has been introduced to the reader in Section III D 3. In this section we will discuss exclusion limits from non-observation of DM, namely the LUX collaboration results [67], superCDMS results [69] and CRESST-TUM40 limit [68]. We also compare O(N) model predictions with CDMS-Si [64], CoGeNT [66] and CRESST-II [70] signal regions.

In the O(N) model the couplings of DM to all nucleons are the same, therefore all limits can be applied directly on our data. The corresponding DM-proton (φ-p) scattering amplitude is shown in Fig. 6. The corresponding cross section evaluated at zero momentum transfer (for details go to Appendix C) reads

$$\sigma_{\varphi-\mathrm{p}} = \frac{\mu^2}{\pi}\frac{\lambda_x^2 m_p^2 \left(\sum_q f_{Tq}^p + \frac{2}{27}\sum_Q f_{TGQ}^p\right)^2}{m_h^4 m_\varphi^2} \tag{104}$$

where the sum runs over light ($q = u, d, s$) and heavy ($Q = c, b, t$) quark flavors, m_p is the proton mass, f_{Tq}^p and f_{TGQ}^p are the nucleon form factors, as defined in Table I, $\mu = m_p m_\varphi/(m_p + m_\varphi)$.

Note that in the case of the O(N) model, we have N DM components contributing equally to DM relic density, each having a scattering cross section $\sigma_{\varphi-\mathrm{p}}$. In general one should average the scattering rate over all contributing DM components, but as those cross sections are identical, $\sigma_{\varphi-\mathrm{p}}$ is the actual DM-nucleon cross section in this case.

In Fig. 22 we show the cross section for φ-proton scattering, evaluated for points satisfying (20) within 3σ range. One can observe, that the cross section is very small in the vicinity of the resonance, $m_\varphi \sim m_h/2$. In this region, as observed in Fig. 18, the coupling λ_x is very small, therefore $\sigma_{\varphi-\mathrm{p}}$ is small and this region happens to be below by the LUX bound. Another allowed area of m_φ is for large masses, $m_\varphi \gtrsim 200$ GeV, where the sensitivity of LUX is reduced. However, for $N > 1$, the bound on m_φ moves towards larger values. The LUX limit allows also for very low masses of DM, below ~ 6 GeV, but this region is excluded by superCDMS and CRESST-TUM40.

Registration of events of DN-nucleus elastic scattering were announced by CRESST-II, CoGeNT and CDMS Si collaborations. However, their results are above exclusion limits from LUX and other experiments, as discussed in Section III D 3. As the situation is unclear, we will also discuss the predictions of the O(N) model for the direct detection cross sections in light of those positive signals.

In Fig. 22, the region preferred by CDMS Si is superimposed with predictions of our model, best for $N = 1,\ 2$, when (20) is imposed. However, even at larger values of N, the 3σ contours and model predictions are expected to overlap. The 90% C.L. results of CoGeNT are below the $N = 1$ model predictions. We also see agreement with CRESST-II experimental result.

There are dramatic consequences for the Higgs boson invisible decay $h \to \vec{\varphi}\vec{\varphi}$ in this parameter range, which is illustrated in Fig. 23, where the branching ratio is plotted against scalar mass m_φ. This plot has been done for $N = 1, 4$ and 8. One can see that the invisible branching ratio of the Higgs boson decay for $m_\varphi < 50$ GeV is above 0.9. To avoid conflict with the LHC results, one should consider masses just above the threshold for Higgs annihilation, $m_\varphi = 70 - 80$ GeV, with couplings $\lambda_x = 0.1 - 0.2$. Such parameters are in agreement with the CDMS Si signal at 3σ C.L..

To conclude, large values of m_φ are allowed by the LUX bound for $m_\varphi \gtrsim 200$ GeV. As it implies closed decay channel of $h \to \varphi\varphi$, this parameter space is indeed allowed within

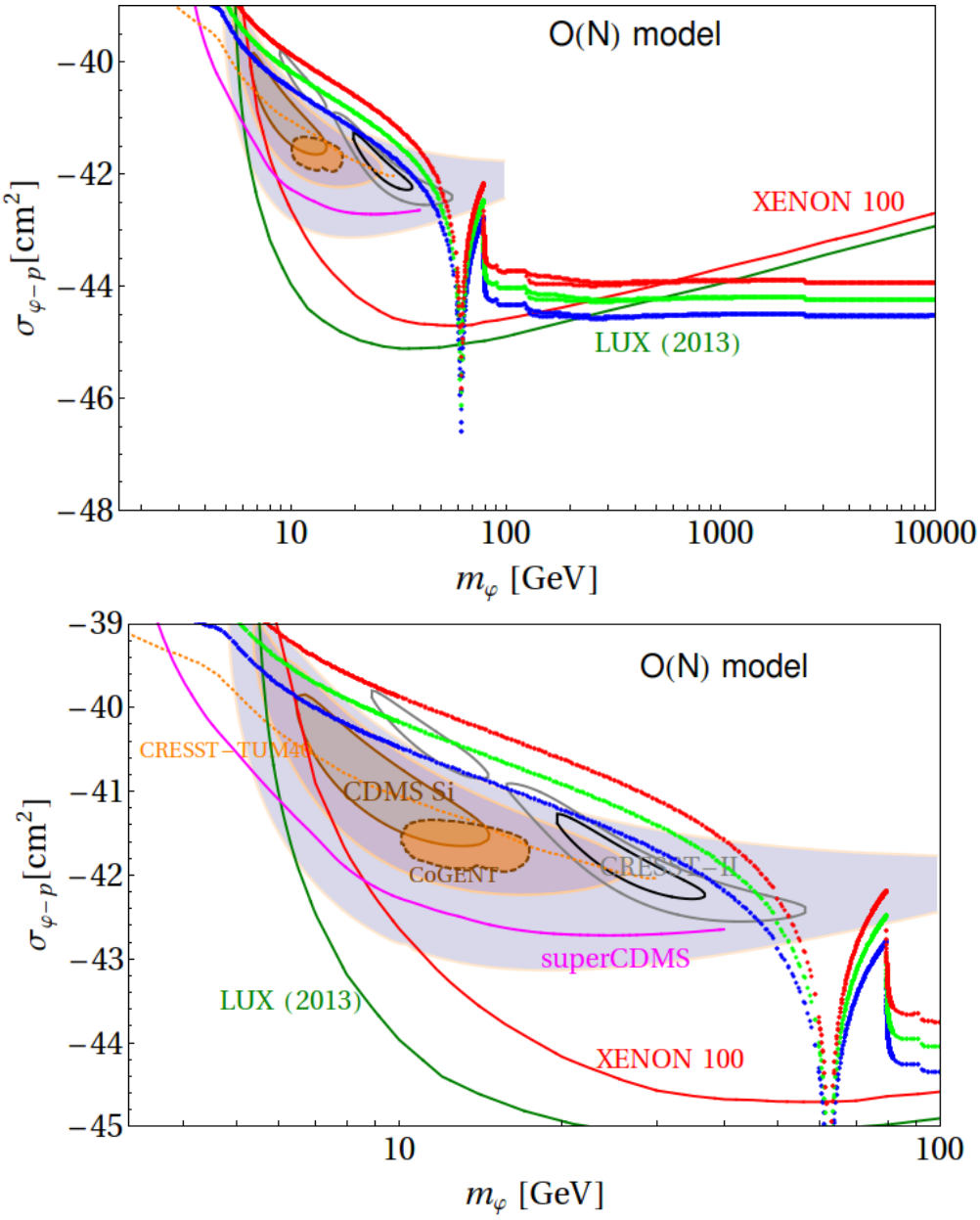

Figure 22: Cross section for φ-p scattering in the O(N) model. All points satisfy all theoretical constraints and Ωh^2 limit within 3σ. Blue, green and red points correspond to $N = 1, 2, 4$, respectively. The pink, green, red and orange lines are the limits from SuperCDMS, LUX, XENON 100 and CRESST-TUM40, respectively. We show the (black and gray) contour for the CRESST-II positive signal (at 68% C.L. and 95% C.L., respectively). For CDMS Si, we display (using various levels of grey) 68%, 95% and 99% C.L. contour. We show 90% C.L. CoGeNT signal.

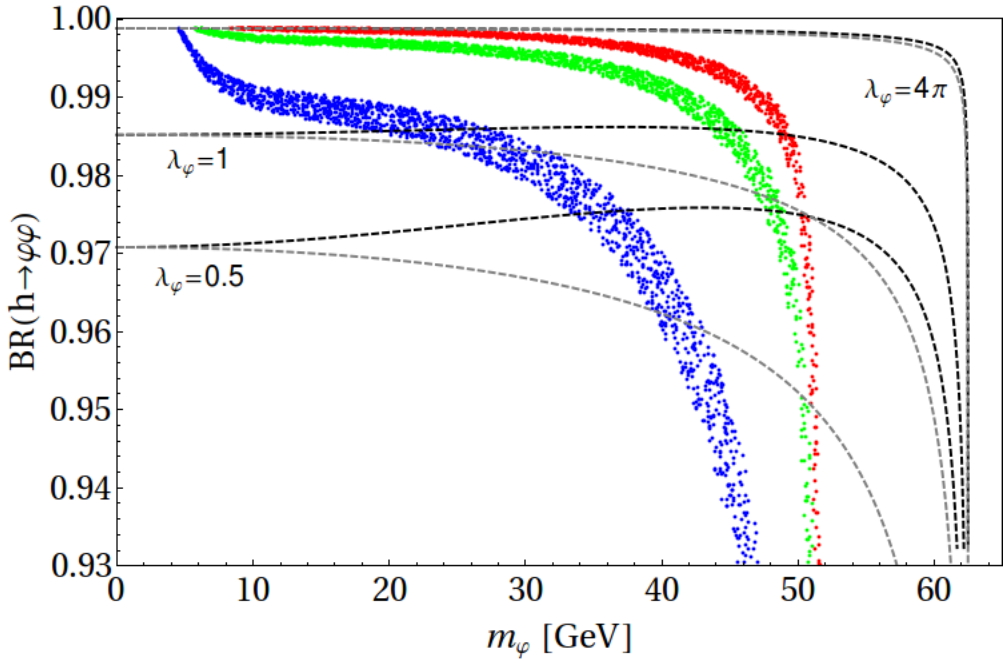

Figure 23: The branching ratio $BR_{h\to\vec{\varphi}\vec{\varphi}}$ as a function of m_φ for $N = 1, 4, 8$ in blue, green and red, respectively. The dashed black lines show theoretical bounds on the positive branch of λ_x for various λ_φ, while the dashed gray lines are stability bounds on the negative branch of λ_x. The quartic self-interaction coupling equals $\lambda_\varphi = 4\pi, 1, 0.5$.

collider limits. Also the resonance region $m_\varphi \sim 62.5$ GeV is allowed, because of very small coupling λ_x in this mass region we are below LUX limits, and also the invisible branching ratio is small. Positive results from CDMS Si and CRESST-II at 2σ C.L. disallow the O(N) model due to too large $BR(h \to SS)$, however at 3σ CDMS Si allows $m_\varphi = 70 - 80$ GeV.

V. TWO-HIGGS DOUBLET MODEL

As mentioned in the Introduction, the $\gamma\gamma$ final state of Higgs boson decay is particularly interesting in light of the ATLAS and CMS data. Higgs decay in this channel seems to be enhanced relative to the SM prediction. The simplest possible extension of the SM that might provide such an effect is the Two-Higgs Doublet Model.

The ATLAS and CMS collaborations have first observed a 5σ Higgs-like particle signal in 2012, [94, 95]. The result was even more exciting due to the unexpected enhancement in the $\gamma\gamma$ channel, as observed by both collaborations. ATLAS announced that the signal rate of the ~ 125 GeV particle decay in two photons was enhanced relatively to the SM signal by 1.9 ± 0.1, and CMS claimed 1.6 ± 0.4. Even though LHC did not observe any beyond SM particle, this enhancement was a hint that there might indeed be new physics involved, maybe even within our reach. At the Moriond 2013 conference, CMS withdraw their claims on the $\gamma\gamma$ enhancement and showed that a suppression of the $\gamma\gamma$ channel is expected [96]. In 2014 this changed again, and CMS claims a very SM-like signal, just a little above the SM rate (Fig. 27), which combined with the current ATLAS result points into the direction of an enhancement in the $\gamma\gamma$ decay mode. We wait impatiently for the new LHC run to clarify this situation.

In other decay modes there was no significant deviation from the SM-expected result. In the $ZZ \to 4l$ channel in the first 2012 results ATLAS was showing a slight enhancement (1.1 ± 0.5), while CMS showing a slight suppression (0.7 ± 0.4). Today for the $ZZ \to 4l$ we still observe a slight enhancement in the ATLAS results (see Fig. 26), but not in CMS results, see Fig. 27.

Enhancements with respect to the SM in the $\gamma\gamma$ channel are generally possible in Two-Higgs Doublet Models (2HDM) of Type I and Type II as explored for example in [6–8, 10–12, 97–100]. In this Chapter we will explore in details what are the possible maximal enhancements after all constraints from B physics and LEP data (B/LEP), precision electroweak data, unitarity and perturbativity are imposed.

In Section V A we introduce 2HDM, and in Section V B we discuss theoretical constraints on its parameter space. In Section V C we introduce various experimental constraints imposed on the model parameters. In Section V D we discuss Higgs boson decay in the SM and in the 2HDM. In Section V E we discuss our results.

This chapter is based on work done in collaboration with B. Grzadkowski, J. Gunion and Y. Jiang, which has been published as [8] and [9].

A. Two Higgs Doublet Model Structure

We will analyse a model with two Higgs doublets Φ_1, Φ_2 with equal $U(1)_Y$ charges. The most general gauge-invariant renormalizable Higgs sector potential reads [101]:

$$\begin{aligned}\mathcal{V}_{2HDM} =& m_{11}^2 \Phi_1^\dagger \Phi_1 + m_{22}^2 \Phi_2^\dagger \Phi_2 - \left[m_{12}^2 \Phi_1^\dagger \Phi_2 + \text{h.c.} \right] \\ &+ \frac{1}{2}\lambda_1 \left(\Phi_1^\dagger \Phi_1 \right)^2 + \frac{1}{2}\lambda_2 \left(\Phi_2^\dagger \Phi_2 \right)^2 + \lambda_3 \left(\Phi_1^\dagger \Phi_1 \right) \left(\Phi_2^\dagger \Phi_2 \right) + \lambda_4 \left(\Phi_1^\dagger \Phi_2 \right) \left(\Phi_2^\dagger \Phi_1 \right) \\ &+ \left\{ \frac{1}{2}\lambda_5 \left(\Phi_1^\dagger \Phi_2 \right)^2 + \left[\lambda_6 \left(\Phi_1^\dagger \Phi_1 \right) + \lambda_7 \left(\Phi_2^\dagger \Phi_2 \right) \right] \left(\Phi_1^\dagger \Phi_2 \right) + \text{h.c.} \right\}. \end{aligned} \tag{105}$$

However, in our study for simplicity we would like to avoid explicit CP violation in the Higgs sector, therefore all λ_i and m_{12}^2 are assumed to be real. We choose a basis in which

$$\Phi_1 = \frac{v}{\sqrt{2}} \begin{pmatrix} 0 \\ \cos\beta \end{pmatrix} \qquad \Phi_2 = \frac{v}{\sqrt{2}} \begin{pmatrix} 0 \\ e^{i\xi} \sin\beta \end{pmatrix},$$

where the v corresponds to the SM vacuum expectation value, $v = (\sqrt{2} G_F)^{-1/2} \approx 246$ GeV. Our convention is to choose $0 \leq \beta \leq \pi/2$. in general even for real parameters the phase ξ could be non-zero, if a spontaneous CP breaking takes place. However, we would like to avoid this and we take $\xi = 0$. Then, we define

$$\Phi_a = \begin{pmatrix} \phi_a^+ \\ (v_a + \rho_a + i\eta_a)/\sqrt{2} \end{pmatrix} \qquad a = 1, 2 \tag{106}$$

with $v_1 = v\cos\beta$ and $v_2 = v\sin\beta$. We have 8 mass eigenstates:
the physical scalars:

$$h = -\rho_1 \sin\alpha + \rho_2 \cos\alpha, \quad H = \rho_1 \cos\alpha + \rho_2 \sin\alpha\,, \tag{107}$$

the physical pseudoscalar state:

$$A = -\eta_1 \sin\beta + \eta_2 \cos\beta\,, \tag{108}$$

the neutral and charged Goldstone bosons:

$$G^0 = \eta_1 \cos\beta + \eta_2 \sin\beta, \quad G^\pm = \phi_1^\pm \cos\beta + \phi_2^\pm \sin\beta, \tag{109}$$

and the charged scalar:

$$H^{\pm} = -\phi_1^{\pm} \sin\beta + \phi_2^{\pm} \cos\beta. \tag{110}$$

Out of this original eight scalar degrees of freedom, three Goldstone bosons are "*eaten*", to give mass to $W^{\pm}$ and Z gauge bosons. We assume that the mixing angle $\alpha \in (-\pi/2, \pi/2)$. Therefore the remaining 5 particles (4 mass eigenstates) are $h, H, A, H^{\pm}$. To express their masses in terms of the couplings λ_i and angles α, β, we will first impose the minimization conditions for the vacuum, following [102] we have:

$$\begin{aligned} m_{11}^2 &= m_{12}^2 \tan\beta - \frac{v^2}{2}\left(\lambda_1 \cos^2\beta + \lambda_{345} \sin^2\beta + 3\lambda_6 \sin\beta\cos\beta + \lambda_7 \sin^2\beta \tan\beta\right) \\ m_{22}^2 &= m_{12}^2 \cot\beta - \frac{v^2}{2}\left(\lambda_2 \sin^2\beta + \lambda_{345} \cos^2\beta + \lambda_6 \cos^2\beta \cot\beta + 3\lambda_7 \sin\beta\cos\beta\right) \end{aligned}$$

where $\lambda_{345} = \lambda_3 + \lambda_4 + \lambda_5$. Then the squared-masses of A and $H^{\pm}$ are:

$$\begin{aligned} m_A^2 &= \frac{m_{12}^2}{\sin\beta\cos\beta} - \frac{v^2}{2}\left(2\lambda_5 + \lambda_6 \cot\beta + \lambda_7 \tan\beta\right) \\ m_{H^{\pm}}^2 &= m_A^2 + \frac{v^2}{2}\left(\lambda_5 - \lambda_4\right) \end{aligned} \tag{111}$$

Remaining h and H fields mix according to $\mathcal{M}$,

$$\mathcal{M} = m_A^2 \begin{pmatrix} \sin^2\beta & -\sin\beta\cos\beta \\ -\sin\beta\cos\beta & \cos^2\beta \end{pmatrix} + \mathcal{B}^2 v^4 \tag{112}$$

where

$$\mathcal{B} = \begin{pmatrix} \lambda_1 \cos^2\beta + \lambda_5 \sin^2\beta + 2\lambda_6 \sin\beta\cos\beta, & \lambda_{34} \sin\beta\cos\beta + \lambda_6 \cos^2\beta + \lambda_7 \sin^2\beta \\ \lambda_{34} \sin\beta\cos\beta + \lambda_6 \cos^2\beta + \lambda_7 \sin^2\beta, & \lambda_2 \sin^2\beta + \lambda_5 \cos^2\beta + 2\lambda_7 \sin\beta\cos\beta \end{pmatrix}$$

where $\lambda_{34} = \lambda_3 + \lambda_4$, and the mass eigenstates are:

$$m_{h,H}^2 = \frac{1}{2}\left(\mathcal{M}_{11}^2 + \mathcal{M}_{22}^2 \mp \sqrt{(\mathcal{M}_{11}^2 - \mathcal{M}_{22}^2)^2 + 4\mathcal{M}_{12}^4}\right) \tag{113}$$

Independent Parameters	
$\lambda_1, \lambda_2, \lambda_3, \lambda_4, \lambda_5, \lambda_6, \lambda_7, m_{12}^2, \tan\beta$	General Basis
$m_h, m_H, m_A, m_{H^{\pm}}, m_{12}^2, \sin\alpha, \tan\beta, \lambda_6, \lambda_7$	Physical Basis

TABLE II: Independent 2HDM parameters in sample basis.

In general, the parameters of the 2HDM can be expressed in various bases [103], see Table II. In our further analysis of the model we use the physical basis (note, that it is possible to use $\tan\beta$ and $\sin\alpha$, as they are single valued in the allowed ranges). In addition, λ_6 and λ_7 are assumed to be zero as a result of a $\mathcal{Z}_2$ symmetry being imposed on on the quartic operators; $\mathcal{Z}_2 : H_1 \to H_1$ and $\mathcal{Z}_2 : H_2 \to -H_2$. We will only allow for a soft breaking of $\mathcal{Z}_2$ with $m_{12}^2 \neq 0$.

1. Yukawa Interactions

The fermion content of the model remains that of the SM. However, both doublets can in general couple to fermions and are responsible for their masses. In this paper we discuss the Type I and Type II 2HDM models, with the fermion coupling patterns as specified in Table III and IV (for more details see [104]). The Yukawa lagrangian written in terms of the fermion couplings to Higgs mass eigenstates is:

$$\mathcal{L}_{Yuk} = \frac{m_f}{v} C_f^h \bar{f} f h + \frac{m_f}{v} C_f^H \bar{f} f H. \tag{114}$$

For numerical results we use 2HDMC [105].

B. Theoretical constraints on 2HDM

Vacuum stability

In order to assure stability of the vacuum at the tree level, we will assume that the scalar potential (105) is bounded from below. This condition is discussed in detail in [74], with the final set of constraints:

$$\lambda_1, \lambda_2 > 0, \quad \lambda_3 + \lambda_4 - |\lambda_5| > -\sqrt{\lambda_1 \lambda_2}, \quad \lambda_3 > -\sqrt{\lambda_1 \lambda_2}, \tag{115}$$

when $\lambda_6, \lambda_7 = 0$ was assumed.

	Type I		
Higgs	up quarks (C_U)	down quarks (C_D)	leptons (C_L)
h	$\cos\alpha/\sin\beta$	$\cos\alpha/\sin\beta$	$\cos\alpha/\sin\beta$
H	$\sin\alpha/\sin\beta$	$\sin\alpha/\sin\beta$	$\sin\alpha/\sin\beta$
A	$\cot\beta$	$-\cot\beta$	$-\cot\beta$

TABLE III: Fermionic couplings $C_f^{h_i}$ normalized to the SM values for 2HDM Type I.

	Type II		
Higgs	up quarks (C_U)	down quarks (C_D)	leptons (C_L)
h	$\cos\alpha/\sin\beta$	$-\sin\alpha/\cos\beta$	$-\sin\alpha/\cos\beta$
H	$\sin\alpha/\sin\beta$	$\cos\alpha/\cos\beta$	$\cos\alpha/\cos\beta$
A	$\cot\beta$	$\tan\beta$	$\tan\beta$

TABLE IV: Fermionic couplings $C_f^{h_i}$ normalized to the SM values for 2HDM Type II.

Perturbativity

We define coupling constant perturbativity by the requirement that all self-couplings (Feynman rules) among the Higgs mass eigenstates are smaller than 4π, namely

$$|\lambda_{h_i h_j h_k h_l}| < 4\pi, \quad h_{i,j,k,l} = h, H, A, H^{\pm}. \tag{116}$$

Unitarity

As mentioned in Section IV B, we should also impose constraints from the tree-level unitarity of the scattering of Higgsses and longitudinal parts of the gauge bosons. This condition has already been studied in the literature, see for example [103, 106–110]. We follow the unitarity check as implemented in 2HDMC code [103].

C. Experimental Constraints on 2HDM

1. Oblique Parameters

The oblique parameters S, T, U [111] are observables that very well probe new physics coupling to the electroweak gauge bosons. For Π_{ij}^{new} being a new physics self-energy contribution, S, T and U are defined as follows [86]:

$$
\begin{aligned}
T &\equiv \frac{1}{\hat{\alpha}(M_Z)} \left(\frac{\Pi_{WW}^{new}(0)}{M_W^2} - \frac{\Pi_{ZZ}^{new}(0)}{M_Z^2} \right) \\
S &\equiv \frac{4\hat{s}_Z^2 \hat{c}_Z^2}{\hat{\alpha}(M_Z)} \left(\frac{\Pi_{ZZ}^{new}(M_Z^2) - \Pi_{ZZ}^{new}()}{M_Z^2} - \frac{\hat{c}_Z^2 - \hat{s}_Z^2}{\hat{c}_Z^2 \hat{s}_Z^2} \frac{\Pi_{Z\gamma}^{new}(M_Z^2)}{M_Z^2} - \frac{\Pi_{\gamma\gamma}^{new}(M_Z^2)}{M_Z^2} \right) \\
S + U &\equiv \frac{4\hat{s}_Z^2}{\hat{\alpha}(M_Z)} \left(\frac{\Pi_{WW}^{new}(M_W^2) - \Pi_{WW}^{new}()}{M_W^2} - \frac{\hat{c}_Z^2}{\hat{s}_Z^2} \frac{\Pi_{Z\gamma}^{new}(M_Z^2)}{M_Z^2} - \frac{\Pi_{\gamma\gamma}^{new}(M_Z^2)}{M_Z^2} \right)
\end{aligned}
\tag{117}
$$

where $\hat{c}_Z$ and $\hat{s}_Z$ are cosine and sine of the Weinberg angle Θ_W, evaluated within minimal subtraction renormalization scheme $\overline{MS}$ ($\hat{s}_Z = 0.2312$), same for $\hat{\alpha}(M_Z)$ ($\hat{\alpha}(M_Z) = 1/127.944$). From equation (117) one can see that the S and $S + U$ parameters are associated with the differences between the Z and W self-energy at $Q^2 = M_{Z,W}^2$ and $Q^2 = 0$, respectively. T is proportional to the difference between the W and Z self-energies at $Q^2 = 0$. Values of these parameters are constrained by the precision measurements at LEP, see [86]. In general, the contribution to the oblique parameters from the second Higgs doublet is small, since scalar doublets do not break custodial symmetry protecting the tree-level relation $\rho = M_W/(M_Z \cos\theta_W) = 1$. However, large mass splitting between new Higgs eigenstates can induce significant contributions at the loop level.

Evaluation of S, T and U is implemented in the 2HDMC code [103], that we have used for our analysis.

2. B physics, LEP constraints and other limits

We adopt several other experimental constraints on the model.

1) We adopt upper limits on $\sigma(e^+e^- \to Z\,h/H)$ and $\sigma(e^+e^- \to A\,h/H)$ from the LEP data, see [112] and [113], respectively.

2) We also impose constraints related to B physics: $BR(B_s \to X_s\gamma)$, R_b, ΔM_{B_s}, ϵ_K, $BR(B^+ \to \tau^+\nu_\tau)$, $BR(B^+ \to D\tau^+\nu_\tau)$, all of them are explained in [101]. Those results imply a lower bound on $m_{H^\pm}$ as a function of $\tan\beta$, as shown in Fig. 15 of [101] in the case of 2HDM Type II and in Fig. 18 of [101] in the case of the 2HDM, Type I.

3) We calculated contributions to the anomalous magnetic moment of the muon, $a_\mu = (g_\mu - 2)/2$. The experimentally measured value for a_μ is $a_\mu = (1165920.80 \pm 0.63) \times 10^{-9}$ [86] and it is different by $\sim 3\sigma$ from the SM prediction. We evaluate correlations between $\delta a_\mu \equiv a_\mu - a_\mu^{SM}$ and the Higgs boson decay signal in the $\gamma\gamma$ channel. However, after imposing all theoretical constraints, B/LEP and STU limits we see that 2HDM one-loop contributions are small and negligible and leading contribution emerges at the two-loop level. It is known as the Barr-Zee diagram [114] and for completeness we included also sub-leading contributions, see [105]. However, we do not use the a_μ measurement as an experimental constraint on the model, as the SM vs experiment discrepancy might be a result of a fluctuation or an underestimation of theoretical errors. We still show the results for δa_μ in tables, in the very last column in units of 10^{-11} and leave the judgment as to whether δa_μ is acceptable to the reader. Within our analysis, extra contributions to a_μ were very small and a_μ discrepancy remains unresolved.

D. Higgs Decay

1. SM Higgs boson and LHC limits on Higgs boson decay

Higgs boson can be produced in the LHC in various modes, see Fig. 24. However, once we have learned the value of m_h, the last unknown parameter of the SM, the properties of the SM Higgs boson are well known - we can compute both production and decay rates (see Fig. 25). Therefore while measuring decay modes of the newly discovered Higgs-like particle, we test the Standard Model and look for any hints on new physics.

We define SM-normalized signal strengths for the scalars from the 2HDM. Therefore, the ratio of the gg-fusion and WW-fusion (VBF) Higgs production cross section times the Higgs

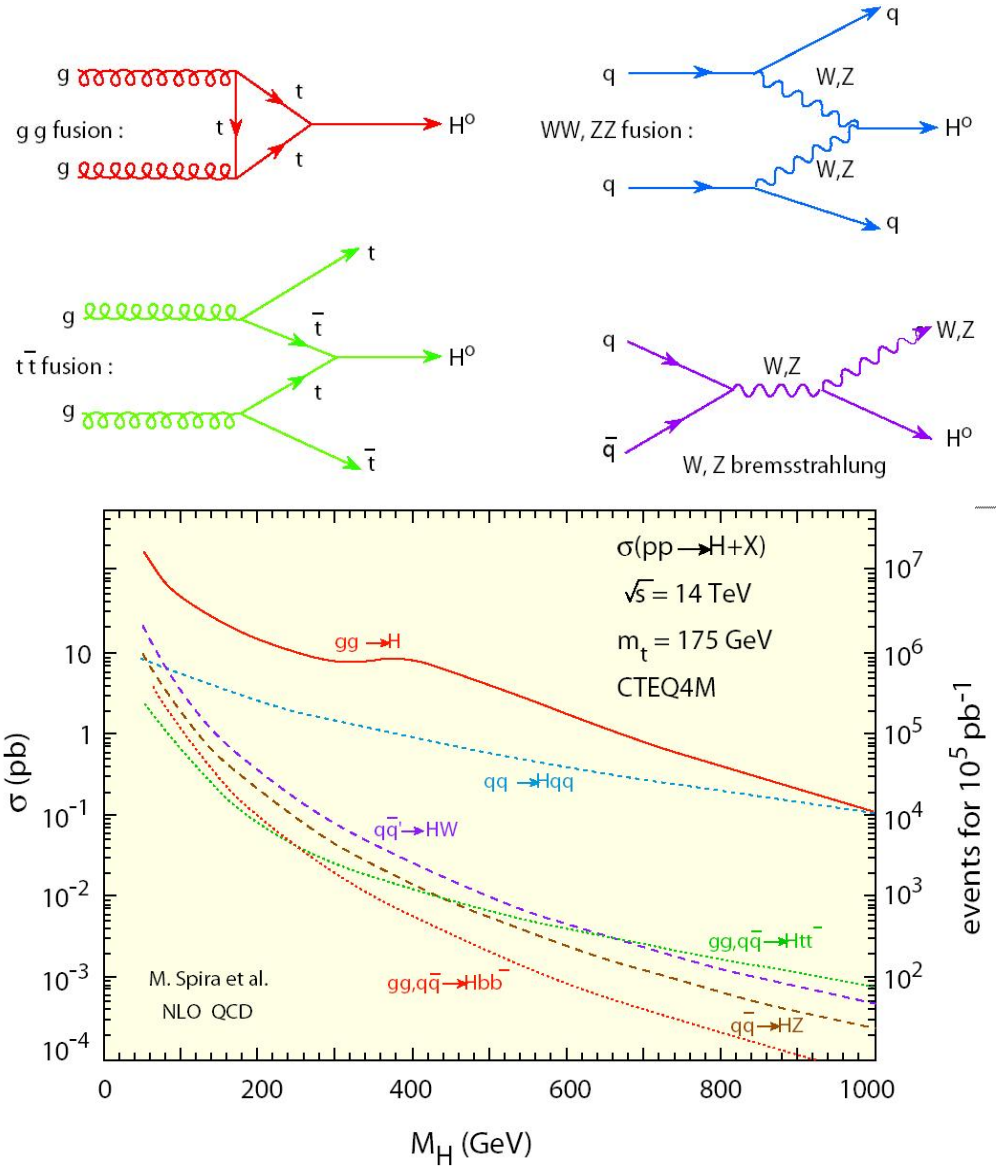

Figure 24: Top panel: Possible channels of the Higgs boson production in the LHC. Bottom panel: cross sections for the Standard Model Higgs production, as a function of Higgs mass, for channels shown above. Source: Imperial College London, High Energy Physics Group Homepage http://www.hep.ph.ic.ac.uk/.

branching ratio to X final state, divided by their corresponding SM values, is given by:

$$R^{h_i}_{gg}(X) \equiv (C^{h_i}_{gg})^2 \, \frac{br(h_i \to X)}{br(h_{sm} \to X)}, \quad R^{h_i}_{\rm VBF}(X) \equiv (C^{h_i}_{WW})^2 \frac{br(h_i \to X)}{br(h_{sm} \to X)}, \tag{118}$$

where $h_i = h, H, A$, h_{sm} is the SM Higgs boson with $m_{h_{sm}} = m_{h_i}$ and $C^{h_i}_{gg}, C^{h_i}_{WW}$ are the ratios of the $gg \to h_i$, $WW \to h_i$ couplings (C^A_{WW} being zero at tree level) to those for the SM, respectively. Such signal strengths can be directly compared to the results from ATLAS

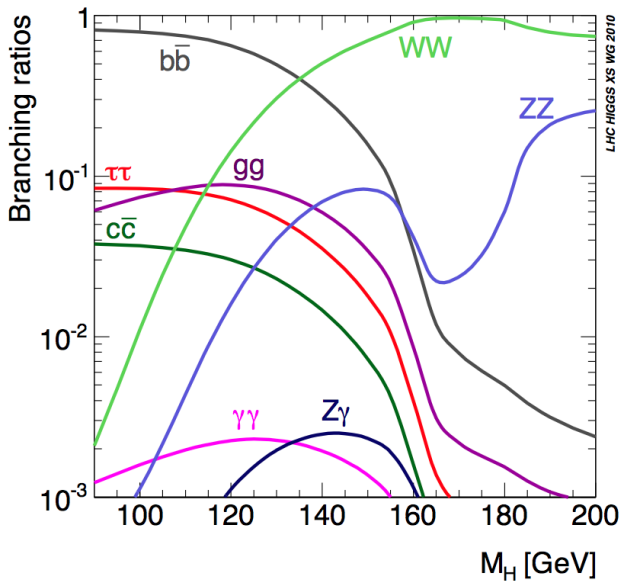

Figure 25: The Standard Model Higgs boson decay branching ratios in various channels, as a function of the SM Higgs mass. Source: [115]

and CMS shown in Fig. 26 and Fig. 27.

Detailed analysis of Higgs decays in 2HDM can be found in [101, 104]. Generally, in Type I model the coupling of the light Higgs h to fermions is the same as in the SM, but multiplied by $\cos\alpha/\sin\beta$ (see Table III) and couplings of h to WW and ZZ are multiplied by $\sin(\alpha-\beta)$. Thus, one can determine the 2HDM h widths relative to the SM in various decay modes by simple multiplication.

For type II 2HDM, the coupling of the light neutral Higgs h to fermions depends on the fermion charge (see Table IV). The coupling of the $Q = 2/3$ quarks is the same as in the type I 2HDM, i.e. it is the Standard-Model coupling times $\cos\alpha/\sin\beta$. On the other hand, the coupling of the $Q = -1/3$ quarks and of the leptons is the Standard-Model coupling times $-\sin\alpha/\cos\beta$. The couplings to gauge bosons are the same as in the type I 2HDM.

E. Enhancement in Higgs $\to \gamma\gamma$ channel

F. Setup of Analysis

We have performed five scans over the parameter space of 2HDM with the range of variation specified in Table V. We have considered various scenarios, amongst them two Higgs

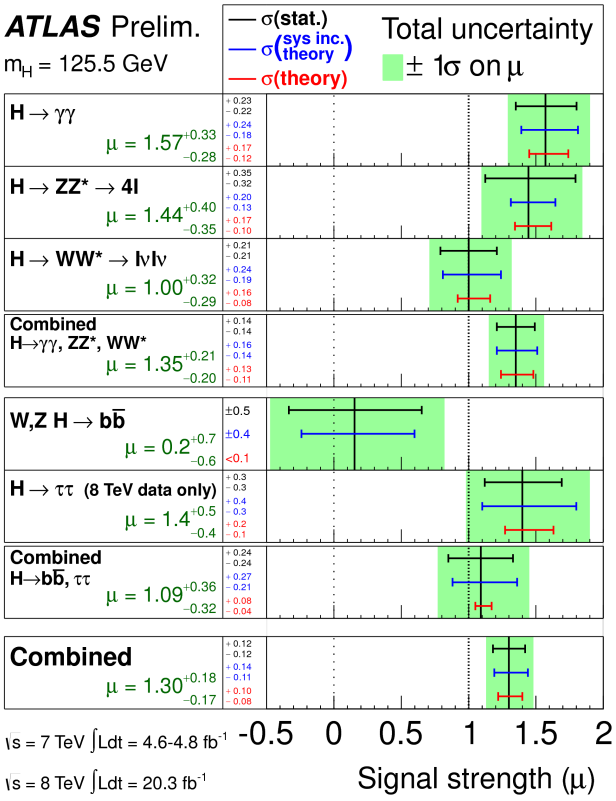

Figure 26: Results from ATLAS; measured signal strengths for a Higgs boson of mass $m_H = 125.5$ GeV, normalised to the SM predictions, for various individual final states and combinations. The best-fit values are shown by the solid vertical lines and total uncertainties $\pm\sigma$ are indicated by green bands. Source: [116]

bosons with degenerate masses as the source of LHC signal. If indeed more than one h_i have mass of ~ 125 GeV (see also [118]), we sum the different R^{h_i} for the production/decay channel of interest, for the combined signal source. In our analysis we always choose masses (see Table V) separated by at least 100 MeV, therefore interference effects for those degenerate bosons are negligible.

We will divide the discussion of our results into 3 parts, following 3 out of 5 scanning scenarios shown in Tables V and VI. We decide not to discuss in details scenarios III and IV, as their results did not contribute any positive results for our analysis, for reasons similar to scenario II.

	scenario I	scenario II	scenario III
m_h [GeV]	125	{5,25,45,65,85,105,124.9}	125
m_H [GeV]	125+$m_{\rm list}$	125	125.1
m_A [GeV]	$m_{\rm list}$	$m_{\rm list}$	$m_{\rm list}$
$m_{H^\pm}$ [GeV]	$\tan\beta$-dependent minimum value consistent with B-physics and other constraints (see caption for details)		
$\tan\beta$	{0.5, 0.9, 1.0, 1.2, 1.4, 1.6, 1.8, 2, 3, 4, 5, 7, 10, 15, 20, 30, 40}		
$\sin\alpha$	{-1, ...,1} in steps of 0.1		
m_{12}^2 [GeV^2]	$\{\pm(1000)^2, \pm(750)^2, \pm(500)^2, \pm(400)^2, \pm(300)^2, \pm(200)^2, \pm(100)^2, \pm(50)^2, \pm(10)^2, \pm(0.1)^2\}$		

TABLE V: Range of parameters adopted in the scans for scenarios I, II and III. In the table, $m_{\rm list}$ corresponds to the sequence of numbers $m_{\rm list}$={0.1,10,50,100,200,300,400,500,750,1000}. The values of $m_{H^\pm}$ are bounded from below by the constraints from B physics, see Fig. 15 and Fig. 18 of [101] for the Type II and Type I models, respectively. We have read off the lower $m_{H^\pm}$ bound values at each of the scanned $\tan\beta$ values from these figures. Aside from a few preliminary scans, we fix $m_{H^\pm}$ at this minimum value while scanning in other parameters. This is appropriate when searching for the maximum $\gamma\gamma$ rate since the charged Higgs loop is largest for the smallest possible $m_{H^\pm}$.

	scenario IV	scenario V
m_h [GeV]	125	{5,25,45,65,85,105,124.9}
m_H [GeV]	125+$m_{\rm list}$	125
m_A [GeV]	125.1	125.1

TABLE VI: Range of parameters adopted in the scans for scenarios IV and V. In the table, $m_{\rm list}$ corresponds to the sequence of numbers $m_{\rm list}$={0.1,10,50,100,200,300,400,500,750,1000}. Other parameters, namely $m_{H^\pm}, \tan\beta, \sin\alpha, m_{12}^2$, were scanned as described in Table V

$\tan\beta$	$R^h_{gg\max}(\gamma\gamma)$	$R^h_{gg}(ZZ)$	$R^h_{gg}(\tau\tau)$	$R^h_{\rm VBF}(\gamma\gamma)$	$R^h_{\rm VBF}(ZZ)$	$R^h_{VH}(b\bar{b})$	m_H	m_A	$m_{H^\pm}$	m_{12}	$\sin\alpha$	$\mathcal{A}^h_{H^\pm}/\mathcal{A}$	δa_μ
0.9	0.95	0.94	0.76	1.17	1.16	0.94	875	750	900	500	-0.8	-0.02	-2.1
1.0	0.97	1.00	1.02	0.95	0.98	1.00	875	750	850	500	-0.7	-0.02	-2.3
1.2	0.98	0.96	0.83	1.13	1.10	0.96	625	750	612	400	-0.7	-0.01	-2.0
1.4	0.99	0.99	0.96	1.02	1.03	0.99	525	750	460	300	-0.6	-0.01	-2.0
1.6	0.96	0.97	0.87	1.07	1.08	0.97	625	400	360	200	-0.6	-0.02	-1.9
1.8	1.01	1.00	0.98	1.03	1.01	1.00	425	400	285	200	-0.5	0.00	-2.0
2.0	0.98	0.98	0.92	1.04	1.04	0.98	425	500	350	200	-0.5	-0.01	-1.8
3.0	1.29	1.00	1.01	1.27	0.99	1.00	225	200	92	100	-0.3	0.12	-1.8
4.0	1.33	0.99	1.07	1.24	0.93	0.99	225	200	90	100	-0.1	0.14	-1.7
5.0	0.98	0.98	1.06	0.90	0.91	0.98	225	400	150	100	-0.0	0.01	-1.6
7.0	1.04	0.99	0.98	1.06	1.01	0.99	135	500	90	50	-0.2	0.02	-1.6
10.0	0.90	0.81	0.74	0.99	0.89	0.81	175	500	150	50	-0.5	0.04	-1.5
15.0	0.46	0.59	0.66	0.41	0.53	0.59	225	400	350	50	0.6	-0.11	-1.4
20.0	1.31	1.00	1.00	1.30	0.99	1.00	225	200	90	50	-0.0	0.13	-1.5

TABLE VII: Table of maximum $R^h_{gg}(\gamma\gamma)$ values for the Type I 2HDM with $m_h = 125$ GeV and associated R values for other initial and/or final states. The input parameters that give the maximal $R^h_{gg}(\gamma\gamma)$ value are also tabulated. $\tan\beta$ values for which the full set of constraints cannot be obeyed are omitted.

$\tan\beta$	$R^h_{gg\max}(\gamma\gamma)$	$R^h_{gg}(ZZ)$	$R^h_{gg}(\tau\tau)$	$R^h_{\rm VBF}(\gamma\gamma)$	$R^h_{\rm VBF}(ZZ)$	$R^h_{VH}(b\bar{b})$	m_H	m_A	$m_{H^\pm}$	m_{12}	$\sin\alpha$	$\mathcal{A}^h_{H^\pm}/\mathcal{A}$	δa_μ
0.5	1.56	2.69	1.84	0.52	0.89	0.61	425	500	600	100	-0.7	-0.06	-0.5
1.0	1.97	3.36	0.39	0.65	1.11	0.13	125	500	500	100	-0.2	-0.06	0.7
1.2	2.16	3.18	0.40	0.95	1.39	0.18	125	400	450	100	-0.2	-0.06	0.8
1.4	2.35	3.37	0.13	1.07	1.54	0.06	225	200	340	100	-0.1	-0.06	1.5
1.6	2.45	3.29	0.15	1.30	1.74	0.08	175	200	320	100	-0.1	-0.05	1.5
1.8	2.51	3.38	0.00	1.31	1.76	0.00	225	200	320	100	-0.0	-0.05	1.6
2.0	2.59	3.36	0.00	1.48	1.92	0.00	225	200	340	100	-0.0	-0.05	1.6
3.0	2.78	3.29	0.00	2.01	2.37	0.00	225	200	320	100	-0.0	-0.05	1.6
4.0	2.84	3.25	0.00	2.24	2.57	0.00	225	200	320	100	-0.0	-0.04	1.6
5.0	2.87	3.23	0.00	2.37	2.66	0.00	225	200	320	100	-0.0	-0.04	1.6
7.0	2.83	3.21	0.00	2.42	2.75	0.00	135	300	320	50	-0.0	-0.05	0.8
10.0	0.34	0.43	1.89	0.22	0.28	1.23	325	200	320	100	0.2	-0.08	3.5
15.0	0.02	0.03	4.06	0.00	0.01	0.87	225	200	320	50	0.6	-0.14	5.3
20.0	2.89	3.19	0.00	2.57	2.83	0.00	225	200	320	50	-0.0	-0.04	2.4

TABLE VIII: Table of maximum $R^h_{gg}(\gamma\gamma)$ values for the Type II 2HDM with $m_h = 125$ GeV and associated R values for other initial and/or final states. The input parameters that give the maximal $R^h_{gg}(\gamma\gamma)$ value are also tabulated. $\tan\beta$ values for which the full set of constraints cannot be obeyed are omitted.

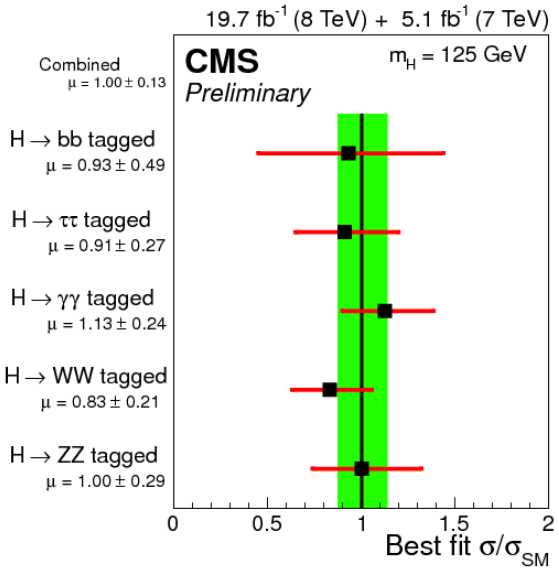

Figure 27: Results from CMS; measured signal strengths for a Higgs boson of mass $m_H = 125.7$ GeV, normalised to the SM predictions, for various individual final states and combinations. The best-fit values are shown by the black squares and total uncertainties $\pm\sigma$ are indicated by red bands. The vertical green band shows the overall uncertainty. Source: [117]

1. $m_h \sim 125\ GeV$

For the case of h with mass $m_h = 125$ GeV, one can evaluate the SM-normalized signal strength, $R^h_{gg}(XX)$, for various decay modes of the Higgs boson. We are particularly interested in understanding possibilities of the enhancement in the $\gamma\gamma$ channel (therefore $R^h_{gg}(\gamma\gamma) > 1$). In Fig. 28 we show the maximal value of $R^h_{gg}(\gamma\gamma)$ as a function of $\tan\beta$, obtained after a scan over all other input parameters, as specified in Table V. We show maximal $R^h_{gg}(\gamma\gamma)$ prior to imposing any constraints and after imposing various combinations of theoretical (SUP stands for *'stability, unitarity and perturbativity'*) and experimental constraints (STU and B/LEP constraints were discussed Sections V C 1 and V C 2, respectively), as specified in the figure legend.

From Fig. 28 we observe that the SUP constraints are especially significant and greatly reduce the maximum value of $R^h_{gg}(\gamma\gamma)$. As a result, in the Type I model maximum $R^h_{gg}(\gamma\gamma)$ values much above 1.3 are not possible, with typical values close to 1. However, in the Type II model maximum $R^h_{gg}(\gamma\gamma)$ values in the range of $2-3$ are possible if $2 \leq \tan\beta \leq 7$ or

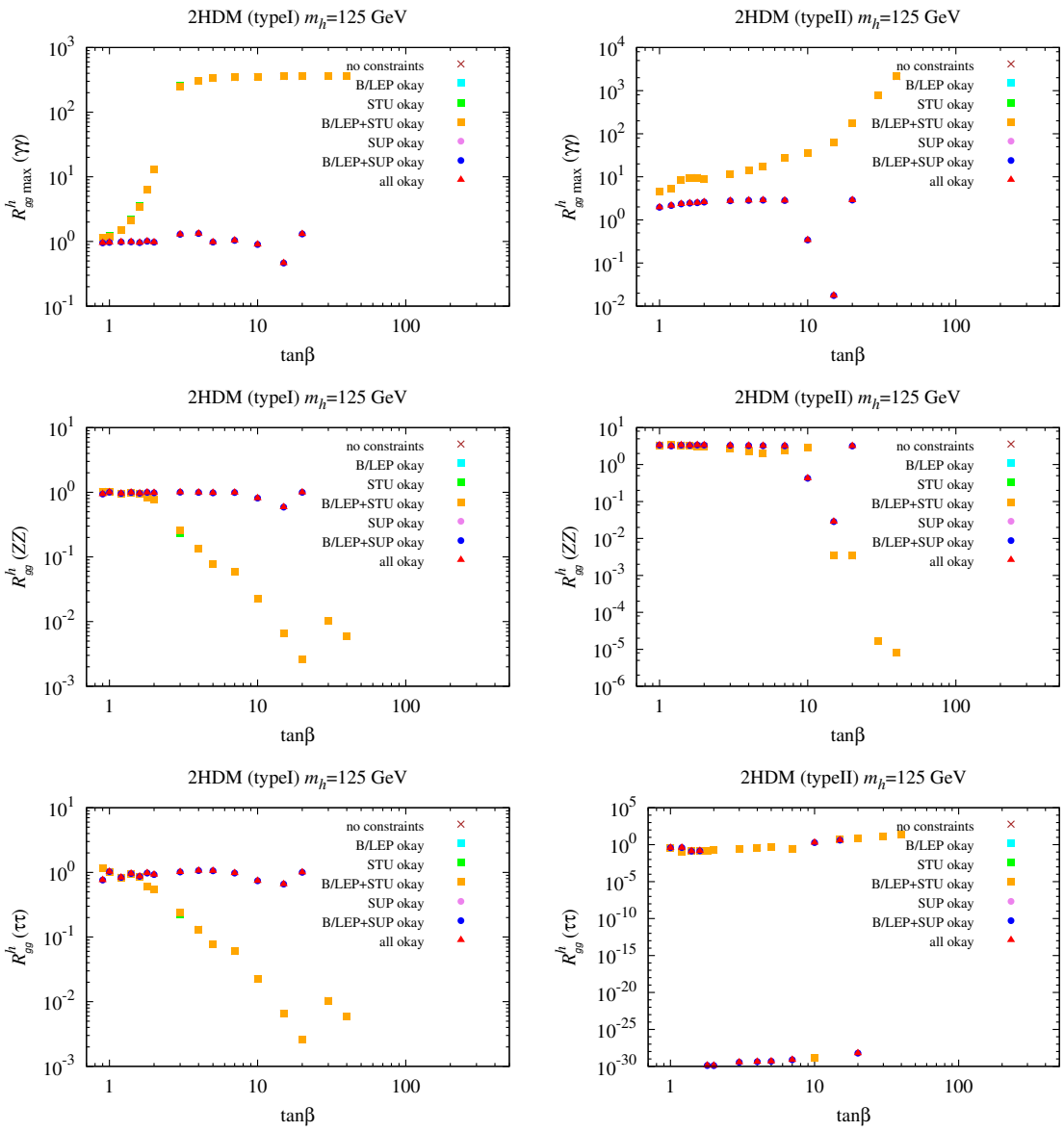

Figure 28: The top two plots show the maximum $R^h_{gg}(\gamma\gamma)$ values in the Type I (left) and Type II (right) models for $m_h = 125$ GeV as a function of $\tan\beta$ after imposing various constraints — see figure legend. Corresponding $R^h_{gg}(ZZ)$ and $R^h_{gg}(\tau\tau)$ are shown in the middle and lower panels. Disappearance of a point after imposing a given constraint set means that the point did not satisfy that set of constraints. In the case of boxes and circles, if a given point satisfies subsequent constraints then the resulting color is chosen according to the color ordering shown in the legend. This same pattern is adopted in the remaining plots.

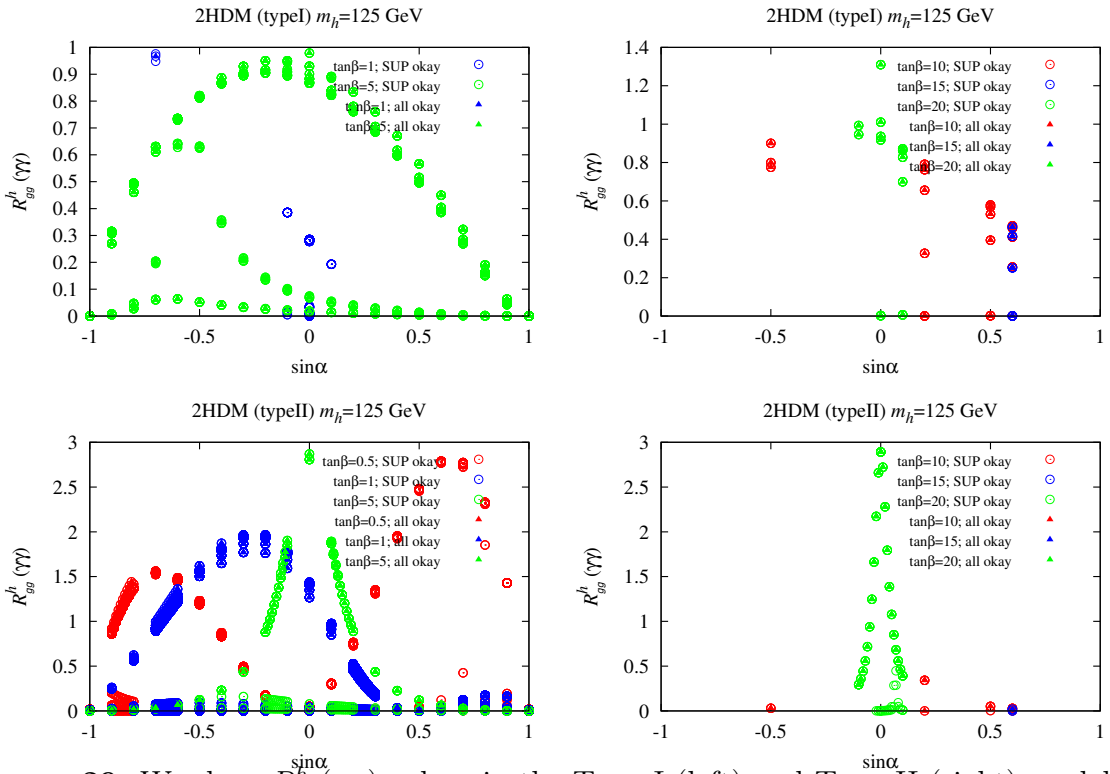

Figure 29: We show $R^h_{gg}(\gamma\gamma)$ values in the Type I (left) and Type II (right) models for $m_h = 125$ GeV as a function of $\sin\alpha$, for various values of $\tan\beta$, after imposing SUP and all constraints – see figure legend.

$\tan\beta = 20$. The dependence on $\sin\alpha$ can be read from Fig. 29. For completeness, in Fig. 28 we also show $R^h_{gg}(ZZ)$ and $R^h_{gg}(\tau\tau)$ for parameter choices giving maximum $R^h_{gg}(\gamma\gamma)$ values.

Contributions from $H^\pm, W$ and fermion loops to the enhanced amplitude for $\gamma\gamma$ in case of $m_h = 125$ GeV are shown in Fig. 30. For the full set of input parameters corresponding to the maximal $R^h_{gg}(\gamma\gamma)$ values see Table VII for Type I and Table VIII for Type II.

It is important to notice that in the Type II model, the value of $R^h_{gg}(ZZ)$ corresponding to the parameters that maximize $R^h_{gg}(\gamma\gamma)$ is typically large, ~ 3. In fact, $R^h_{gg}(ZZ) > R^h_{gg}(\gamma\gamma)$ whenever $R^h_{gg}(\gamma\gamma)$ is even modestly enhanced, see Table VIII. Since, experimentally, the observed signal for ZZ is at most only slightly enhanced, the Type II models seem to be disfavoured within our analysis, if one demands maximal $R^h_{gg}(\gamma\gamma)$.

What is the mechanism behind the enhancement of $R^{h,H}_{gg}(ZZ)$ in the Type II model for large $R^{h,H}_{gg}(\gamma\gamma)$? This effect was discussed in details in [8]. We define r_s, the ratio of $\gamma\gamma$ over

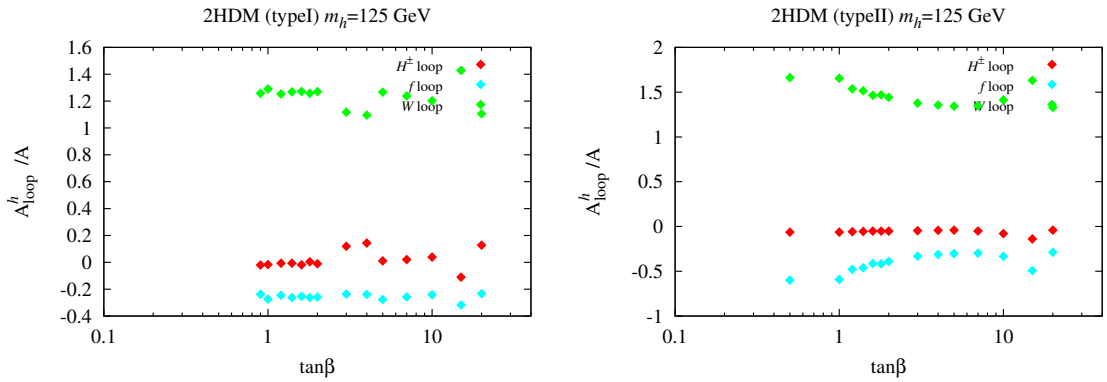

Figure 30: Imaginary parts of the charged Higgs, fermion and $W^\pm$ contributions to the 1-loop amplitudes for $h \to \gamma\gamma$ normalised to the imaginary part of the sum of all contributions, as a function of $\tan\beta$, after imposing all theoretical and experimental constraints. We show only results for the chosen points with maximal $R^h_{gg}(\gamma\gamma)$ on the left panel for Type I and Type II results are on the right. This is a case study of $m_h = 125$ GeV.

ZZ production rates:

$$r_s \equiv \frac{R^s_{gg}(\gamma\gamma)}{R^s_{gg}(ZZ)} = \frac{\Gamma(s \to \gamma\gamma)/\Gamma(h_{sm} \to \gamma\gamma)}{\Gamma(s \to ZZ)/\Gamma(h_{sm} \to ZZ)}, \quad s = h, H. \tag{119}$$

For the decay mode $s \to ZZ^*$ the dominant contribution comes from the tree level amplitude, therefore the denominator reduces to $(C^s_{ZZ})^2$. For the decay mode $s \to \gamma\gamma$ the $s\gamma\gamma$ coupling arises at the one-loop level with the t-loop, W-loop and $H^\pm$-loop being the important contributions. As a result, the numerator can be written as

$$\frac{\Gamma(s \to \gamma\gamma)}{\Gamma(h_{sm} \to \gamma\gamma)} = \left(\frac{C^s_{WW}\mathcal{A}^{SM}_W - C^s_{t\bar{t}}\mathcal{A}^{SM}_t + \mathcal{A}_{H^\pm}}{\mathcal{A}^{SM}_W - \mathcal{A}^{SM}_t}\right)^2 \simeq \left(\frac{C^s_{WW}\mathcal{A}^{SM}_W - C^s_{t\bar{t}}\mathcal{A}^{SM}_t}{\mathcal{A}^{SM}_W - \mathcal{A}^{SM}_t}\right)^2 \tag{120}$$

where $C^s_{t\bar{t}}$ and C^s_{WW} are the $st\bar{t}$ and sWW couplings normalized to the appropriate SM couplings of the h_{sm}, while $\mathcal{A}^{SM}_W$ ($\mathcal{A}^{SM}_t$) is the W-loop (t-loop) amplitudes of the h_{sm}. In the Type II model $\mathcal{A}_{H^\pm}$, the $H^\pm$-loop amplitude, is very small (see Fig. 30) and can be neglected. As $C^s_{ZZ} = C^s_{WW}$ we have,

$$r_s \simeq \left(\frac{\mathcal{A}^{SM}_W - \frac{C^s_{t\bar{t}}}{C^s_{WW}}\mathcal{A}^{SM}_t}{\mathcal{A}^{SM}_W - \mathcal{A}^{SM}_t}\right)^2, \tag{121}$$

and $r_s < 1$ if

$$1 < \frac{C^s_{t\bar{t}}}{C^s_{WW}} < 2\frac{\mathcal{A}^{SM}_W}{\mathcal{A}^{SM}_t} - 1. \tag{122}$$

Also, if $C^s_{t\bar{t}}/C^s_{WW}$ does not satisfy (122), then $r_s > 1$. For $s = h$ we have $C^s_{t\bar{t}}/C^s_{WW} = \cos\alpha/[\sin\beta\sin(\beta-\alpha)]$ implying $r_h < 1$ when

$$1 < \frac{\cos\alpha}{\sin\beta\sin(\beta-\alpha)} < 2\frac{\mathcal{A}_W^{SM}}{\mathcal{A}_t^{SM}} - 1 \simeq 9\,. \tag{123}$$

Maximal $R^h_{gg}(\gamma\gamma)$ is obtained by suppressing the total width Γ_h, which corresponds to choosing α so as to minimize the $hb\bar{b}$ coupling, ($\alpha \sim 0$) and as a result we have $C^h_{t\bar{t}}/C^h_{WW} \sim 1/\sin^2\beta > 1$, therefore $r_h < 1$ and $R^{h,H}_{gg}(ZZ) > R^{h,H}_{gg}(\gamma\gamma)$. This effect can be observed in Fig. 31, where we plot contours of r_h and of $R^h_{gg}(\gamma\gamma)$ in the Type II model. One can read from the plot, that if $\tan\beta$ is large then only small α will maximize $R^s_{gg}(\gamma\gamma)$. In that region r_h is always less than 1.

If both $R^h_{gg}(\gamma\gamma) > 1$ and $r_h > 1$ were required, $\tan\beta \lesssim 1$, which explains the pattern observed in Table VIII and Fig.28. However, such small value of $\tan\beta$ is disfavored by B-physics as it enhances the $H^+\bar{t}b$ coupling too much, see for example [101].

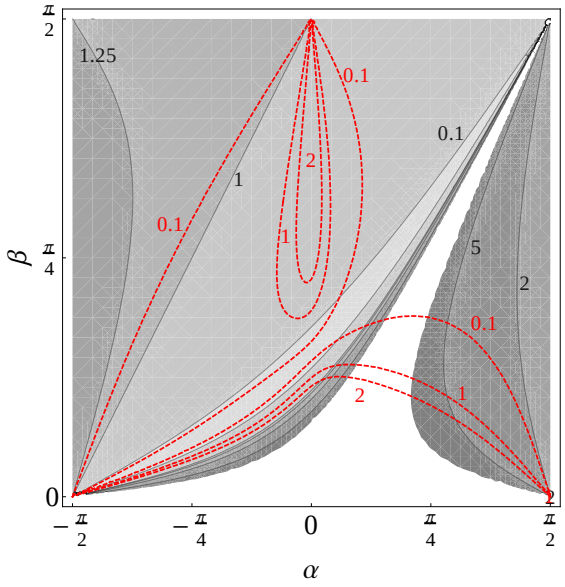

Figure 31: We show contour plots in the (β, α) space for r_h with superimposed red contours for $R^h_{gg}(\gamma\gamma)$, evaluated within a 2HDM, Type II. Red numbers show constant values of $R^h_{gg}(\gamma\gamma)$. The white region corresponds to $r_h > 10.75$.

$\tan\beta$	$R^H_{gg\max}(\gamma\gamma)$	$R^H_{gg}(ZZ)$	$R^H_{gg}(\tau\tau)$	$R^H_{\rm VBF}(\gamma\gamma)$	$R^H_{\rm VBF}(ZZ)$	$R^H_{VH}(b\bar{b})$	m_h	m_A	$m_{H^\pm}$	m_{12}	$\sin\alpha$	$\mathcal{A}^H_{H^\pm}/\mathcal{A}$	δa_μ
1.4	0.91	0.99	0.96	0.94	1.03	0.99	125	500	460	100	0.8	0.00	-2.7
1.6	0.89	0.97	0.87	1.00	1.08	0.97	125	400	360	50	0.8	0.00	-2.5
1.8	0.89	1.01	1.08	0.84	0.95	1.01	125	400	350	50	0.9	-0.06	-2.3
2.0	0.90	1.00	1.02	0.89	0.99	1.00	125	400	350	50	0.9	-0.05	-2.1
3.0	0.89	0.96	0.88	0.97	1.05	0.96	125	400	350	50	0.9	-0.05	-1.8
4.0	0.89	0.97	1.09	0.79	0.86	0.97	105	500	90	50	1.0	-0.03	-1.7
5.0	0.93	0.98	1.06	0.86	0.90	0.98	125	500	90	50	1.0	-0.01	-1.6
7.0	0.88	0.99	1.03	0.85	0.95	0.99	65	400	350	10	1.0	-0.05	-1.6
10.0	0.89	1.00	1.02	0.87	0.98	1.00	45	400	350	0	1.0	-0.05	-1.6
15.0	0.90	1.00	1.01	0.89	0.99	1.00	5	400	350	0	-1.0	-0.05	-1.6
20.0	0.90	1.00	1.00	0.89	0.99	1.00	25	400	350	0	-1.0	-0.05	-1.5
30.0	0.90	1.00	1.00	0.90	1.00	1.00	5	400	350	0	-1.0	-0.05	-1.5
40.0	0.90	1.00	1.00	0.90	1.00	1.00	5	400	350	0	-1.0	-0.05	-1.5

TABLE IX: Table of maximum $R^H_{gg}(\gamma\gamma)$ values for the Type I 2HDM with $m_H = 125$ GeV and associated R values for other initial and/or final states. The input parameters that give the maximal $R^H_{gg}(\gamma\gamma)$ value are also tabulated. $\tan\beta$ values for which the full set of constraints cannot be obeyed are omitted.

$\tan\beta$	$R^H_{gg\max}(\gamma\gamma)$	$R^H_{gg}(ZZ)$	$R^H_{gg}(\tau\tau)$	$R^H_{\rm VBF}(\gamma\gamma)$	$R^H_{\rm VBF}(ZZ)$	$R^H_{VH}(b\bar{b})$	m_h	m_A	$m_{H^\pm}$	m_{12}	$\sin\alpha$	$\mathcal{A}^H_{H^\pm}/\mathcal{A}$	δa_μ
1.0	1.99	3.24	0.52	0.71	1.16	0.19	125	500	500	100	1.0	-0.06	0.7
1.2	1.90	3.34	0.00	0.59	1.04	0.00	125	400	450	100	1.0	-0.06	0.8
1.4	2.20	3.38	0.00	0.86	1.32	0.00	125	300	340	100	1.0	-0.06	1.1
1.6	2.36	3.39	0.00	1.09	1.56	0.00	125	300	320	50	1.0	-0.06	1.1
1.8	2.48	3.38	0.00	1.29	1.76	0.00	125	300	320	50	1.0	-0.06	1.1
2.0	2.56	3.36	0.00	1.46	1.92	0.00	125	300	340	50	1.0	-0.06	1.1
3.0	2.73	3.29	0.00	1.97	2.37	0.00	125	300	320	50	1.0	-0.05	1.0
4.0	2.78	3.25	0.00	2.20	2.57	0.00	125	300	320	50	-1.0	-0.05	1.0
5.0	2.81	3.23	0.00	2.32	2.66	0.00	125	300	320	50	-1.0	-0.05	0.9
7.0	2.80	3.21	0.00	2.40	2.75	0.00	65	300	320	10	-1.0	-0.06	-0.0
10.0	2.81	3.20	0.00	2.46	2.79	0.00	45	300	320	0	-1.0	-0.06	-2.8
15.0	2.82	3.19	0.00	2.49	2.82	0.00	25	300	320	0	-1.0	-0.05	-16.9
20.0	2.82	3.19	0.00	2.50	2.83	0.00	25	300	320	0	-1.0	-0.05	-30.8
30.0	2.82	3.19	0.00	2.51	2.84	0.00	5	300	320	0	-1.0	-0.05	-38.7
40.0	2.82	3.19	0.00	2.51	2.84	0.00	5	300	320	0	-1.0	-0.05	-69.7

TABLE X: Table of maximum $R^H_{gg}(\gamma\gamma)$ values for the Type II 2HDM with $m_H = 125$ GeV and associated R values for other initial and/or final states. The input parameters that give the maximal $R^H_{gg}(\gamma\gamma)$ value are also tabulated. $\tan\beta$ values for which the full set of constraints cannot be obeyed are omitted.

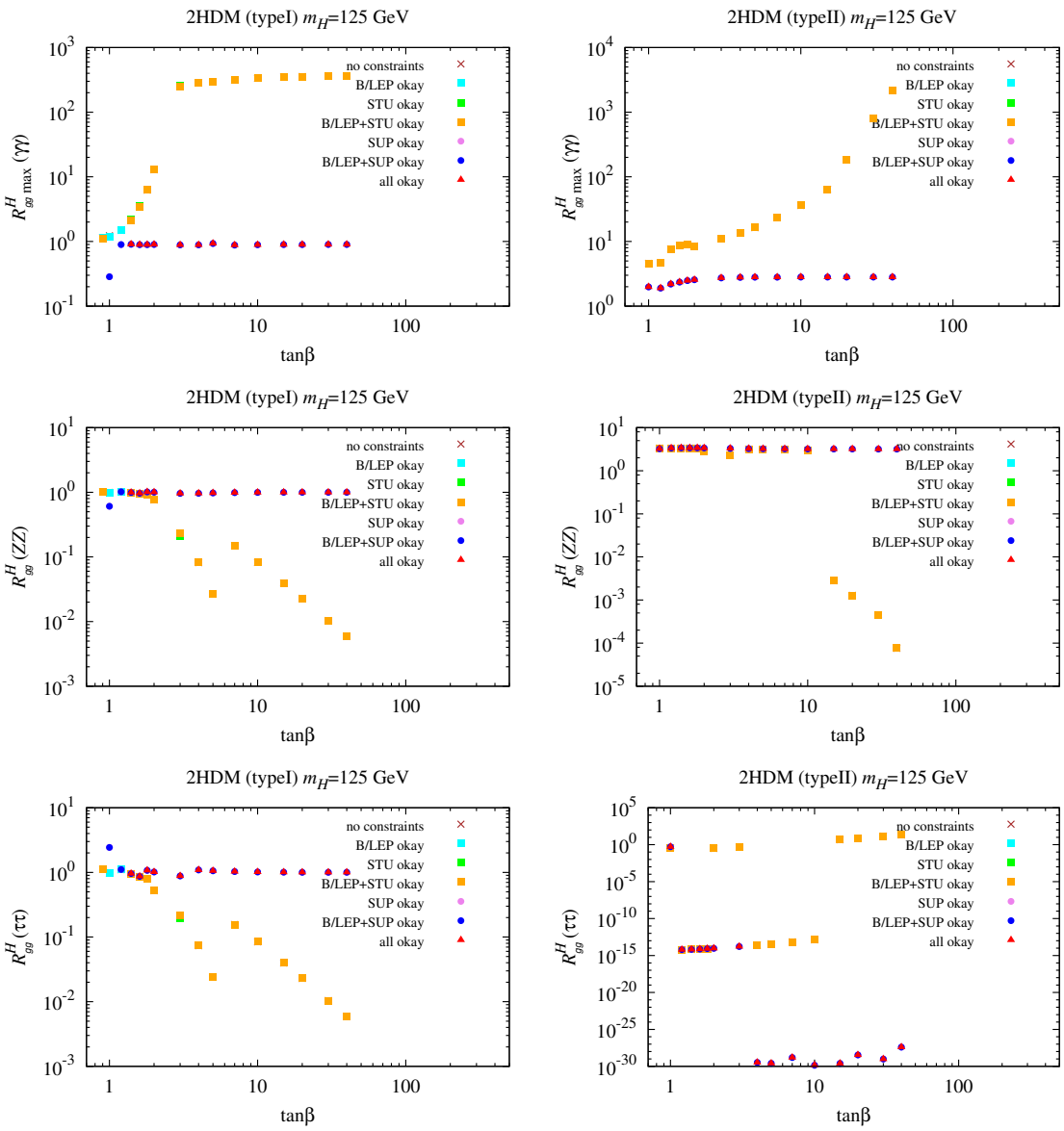

Figure 32: The top two plots show the maximum $R^H_{gg}(\gamma\gamma)$ values in the Type I (left) and Type II (right) models for $m_H = 125$ GeV as a function of $\tan\beta$ after imposing various constraints — see figure legend. Corresponding $R^H_{gg}(ZZ)$ and $R^H_{gg}(\tau\tau)$ are shown in the middle and lower panels. Disappearance of a point after imposing a given constraint set means that the point did not satisfy that set of constraints. In the case of boxes and circles, if a given point satisfies subsequent constraints then the resulting color is chosen according to the color ordering shown in the legend. This same pattern is adopted in the remaining plots.

2. $m_H \sim 125\ GeV$

In Tables IX and X we present full set of input parameters corresponding to the maximal $R^H_{gg}(\gamma\gamma)$ in Type I and Type II models, respectively. In Fig. 32 we plot the maximal $R^H_{gg}(\gamma\gamma)$ as a function of $\tan\beta$, together with the results for other channels.

In the case of the Type I model, an enhanced rate of gluon fusion to the $\gamma\gamma$ seems not to be realizable, after we impose SUP constraints. Large enhancements $R^H_{gg}(\gamma\gamma) \sim 2.8$ are quite typical for the Type II model, however they follow even larger $R^H_{gg}(ZZ)$, therefore they are disfavoured. For Fig. 33 we can see, that large $\tan\beta$, only allows $\alpha \pm \pi/2$ if $R^H_{gg}(\gamma\gamma) > 1$. Unfortunately, it implies $r_H < 1$.

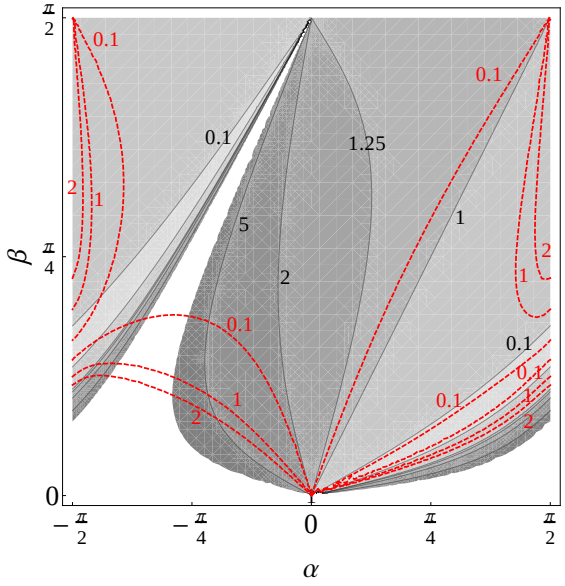

Figure 33: We show contour plots in the (β, α) space for r_H with superimposed red contours for $R^H_{gg}(\gamma\gamma)$, evaluated within a 2HDM, Type II. Red numbers give constant values of $R^H_{gg}(\gamma\gamma)$. The white region corresponds to $r_H > 10.75$.

3. $m_h \& m_A \sim 125\ GeV$

The signal at 125 GeV cannot come from the pseudoscalar A alone, since the A does not couple to ZZ (a final state definitely present at 125 GeV). However, one can imagine that the CP-even h or H and the A both have mass of 125 GeV. In such scenario both particles would contribute to the decay rate in $\gamma\gamma$ channel, while only h or H contributes to the ZZ

$\tan\beta$	$R^{h+A}_{gg\max}(\gamma\gamma)$	$R^{h}_{gg}(\gamma\gamma)$	$R^{A}_{gg}(\gamma\gamma)$	$R^{h+A}_{gg}(ZZ)$	$R^{h+A}_{gg}(\tau\tau)$	$R^{h}_{\rm VBF}(\gamma\gamma)$	$R^{h}_{\rm VBF}(ZZ)$	$R^{h}_{VH}(b\bar{b})$	m_H	$m_{H^\pm}$	m_{12}	$\sin\alpha$	$\mathcal{A}^h_{H^\pm}/\mathcal{A}$	δa_μ
1.2	1.31	0.90	0.41	1.02	3.35	0.83	0.94	1.02	625	612	100	-0.6	-0.05	-3.4
1.4	1.21	0.91	0.30	0.99	2.61	0.94	1.03	0.99	425	460	100	-0.6	-0.05	-2.9
1.6	1.14	0.91	0.23	1.01	2.32	0.87	0.97	1.01	425	360	100	-0.5	-0.05	-2.7
1.8	1.10	0.92	0.18	1.00	1.98	0.94	1.01	1.00	325	285	100	-0.5	-0.04	-2.4
2.0	1.08	0.93	0.15	0.98	1.73	0.99	1.04	0.98	325	230	100	-0.5	-0.04	-2.2
3.0	1.34	1.29	0.06	1.00	1.31	1.27	0.99	1.00	225	92	100	-0.3	0.12	-1.9
4.0	1.35	1.33	0.03	0.99	1.21	1.24	0.93	0.99	225	90	100	-0.1	0.14	-1.8
5.0	0.96	0.95	0.01	1.00	1.07	0.95	1.00	1.00	135	90	50	-0.2	-0.03	-1.7
7.0	1.04	1.04	0.01	0.99	1.00	1.06	1.01	0.99	135	90	50	-0.2	0.02	-1.6
10.0	0.91	0.90	0.01	0.81	0.77	0.99	0.89	0.81	175	150	50	-0.5	0.04	-1.5
15.0	0.42	0.42	0.00	0.59	0.67	0.37	0.53	0.59	225	250	50	0.6	-0.17	-1.4
20.0	1.31	1.31	0.00	1.00	1.00	1.30	0.99	1.00	225	90	50	-0.0	0.13	-1.6

TABLE XI: Table of maximum $R^{h+A}_{gg}(\gamma\gamma)$ values for the Type I 2HDM with $m_h = m_A = 125$ GeV and associated R values for other initial and/or final states. The input parameters that give the maximal $R^{h+A}_{gg}(\gamma\gamma)$ value are also tabulated.

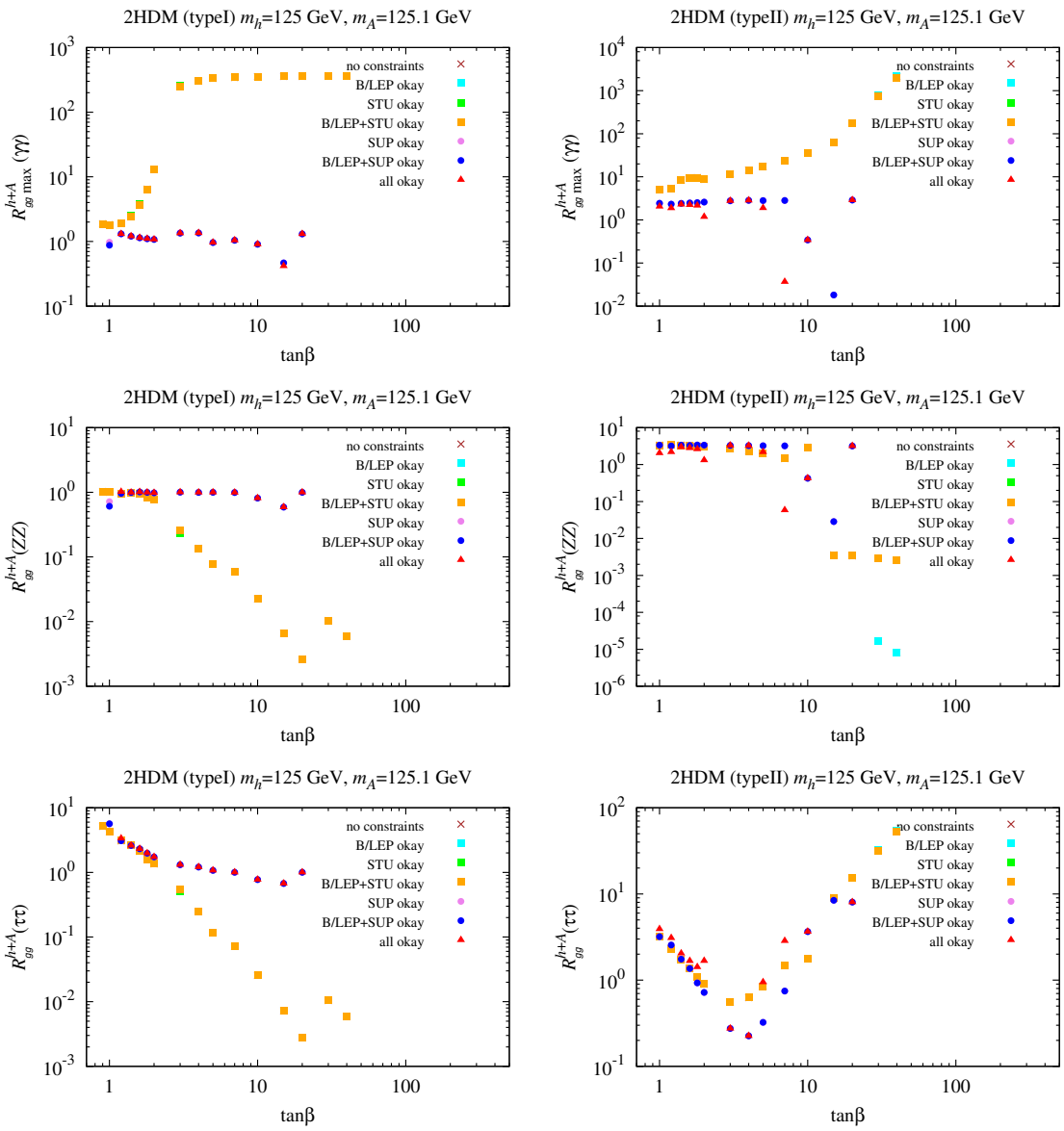

Figure 34: $R_{gg}^{h+A}(\gamma\gamma)$ maximum values when $m_h = m_A = 125$ GeV as a function of $\tan\beta$ after imposing various constraints — see figure legend. Corresponding $R_{gg}^{h}(ZZ)$ and $R_{gg}^{h}(\tau\tau)$ are shown in the middle and lower panels.

rate.

In the scenario of H and A degeneracy, the maximum value achieved for $R_{gg\,\max}^{H+A}(\gamma\gamma)$ is rather modest reaching only 1.04 at small $\tan\beta$. We will not discuss this case further, details can be found in [8].

The other possibility is illustrated in Fig. 34, from which we observe that an enhanced $\gamma\gamma$ rate is indeed possible. We specify the parameters that provide maximal $\gamma\gamma$ enhancement

for this case in Tables XI and XII.

For the Type I model, we can read from Table XI that $R^h_{gg}(\gamma\gamma)$ is enhanced only for the same values of $\tan\beta$ ($\tan\beta = 4$ and $\tan\beta = 20$), as in the case of only $m_h = 125$ GeV. The contrbution $R^A_{gg}(\gamma\gamma)$ turns out to be very small. However, an unwanted implication of the presence of the pseudoscalar, is the possibly increased rate for the $b\bar{b}$ final state. Contributions from the A *can* be substantial and only $\tan\beta = 20$ yields both an enhanced $\gamma\gamma$ rate, $R^{h+A}_{gg\,\max}(\gamma\gamma) = 1.31$, and SM-like rates for the ZZ and $b\bar{b}$ final states. For this case we have $\beta \simeq \pi/2$ and $\alpha = 0$, therefore the light Higgs h couples to fermions and gauge bosons like a SM Higgs boson and the enhancement of $R^{h+A}_{gg\,\max}(\gamma\gamma)$ appears due to the charged Higgs loop.

For the Type II model the pseudoscalar decay rate to $\gamma\gamma$, $R^A_{gg}(\gamma\gamma)$, is negligible as for the Type I case, see Table XII. Again, we observe that the enhancement of $R^{h+A}_{gg}(\gamma\gamma)$ is realised essentially for the same parameters as in the case of $m_h = 125$ GeV, reaching maximum values of order $2-3$. However, as in the pure $m_h = 125$ GeV case, a substantial enhancement of $R^{h+A}_{gg}(\gamma\gamma)$ is for most of the parameter space associated with $R^{h+A}_{gg}(ZZ) > R^{h+A}_{gg}(\gamma\gamma)$ (contrary to the LHC observations). However, in the degenerate scenario it is not *always* the case. Among the $m_h = m_A$ scan we found 56 points in our parameter space for which $R^{h+A}_{gg}(ZZ) < 1.3$ and $R^{h+A}_{gg}(\gamma\gamma) > 1.3$. Unfortunately, for all those points the predicted $b\bar{b}$ signal was too strong to match the LHC results, $R^{h+A}_{gg}(b\bar{b}) > 3.82$ and finally this case is disfavoured in light of the experimental results.

$\tan\beta$	$R^{h+A}_{gg\max}(\gamma\gamma)$	$R^{h}_{gg}(\gamma\gamma)$	$R^{A}_{gg}(\gamma\gamma)$	$R^{h+A}_{gg}(ZZ)$	$R^{h+A}_{gg}(\tau\tau)$	$R^{h}_{\rm VBF}(\gamma\gamma)$	$R^{h}_{\rm VBF}(ZZ)$	$R^{h}_{VH}(b\bar{b})$	m_H	$m_{H^\pm}$	m_{12}	$\sin\alpha$	$\mathcal{A}^{h}_{H^\pm}/\mathcal{A}$	δa_μ
1.0	2.05	1.58	0.47	2.05	3.91	0.93	1.22	0.65	525	500	100	-0.5	-0.06	1.3
1.2	1.88	1.71	0.17	2.19	3.08	1.05	1.34	0.57	425	450	100	-0.4	-0.05	1.5
1.4	2.29	2.22	0.07	2.99	2.04	1.18	1.59	0.23	325	340	100	-0.2	-0.05	1.9
1.6	2.23	2.20	0.03	2.80	1.67	1.34	1.71	0.28	225	320	100	-0.2	-0.05	2.0
1.8	2.15	2.14	0.01	2.63	1.42	1.44	1.77	0.33	225	320	100	-0.2	-0.05	2.0
2.0	1.18	1.17	0.01	1.31	1.68	1.07	1.20	0.87	325	340	100	-0.4	-0.05	1.5
3.0	2.78	2.78	0.00	3.29	0.27	2.01	2.37	0.00	225	320	100	-0.0	-0.05	2.3
4.0	2.84	2.84	0.00	3.25	0.23	2.24	2.57	0.00	225	320	100	-0.0	-0.04	2.3
5.0	1.89	1.89	0.00	2.19	0.95	1.41	1.64	0.47	225	320	100	0.1	-0.05	2.7
7.0	0.04	0.04	0.00	0.06	2.85	0.01	0.02	0.75	325	320	100	0.6	-0.15	5.2
10.0	0.34	0.34	0.00	0.43	3.66	0.22	0.28	1.23	325	320	100	0.2	-0.08	4.7
20.0	2.89	2.89	0.00	3.19	8.03	2.57	2.83	0.00	225	320	50	-0.0	-0.04	5.6

TABLE XII: Table of maximum $R^{h+A}_{gg}(\gamma\gamma)$ values for the Type II 2HDM with $m_h = m_A = 125$ GeV and associated R values for other initial and/or final states. The input parameters that give the maximal $R^{h+A}_{gg}(\gamma\gamma)$ value are also tabulated.

VI. TWO-HIGGS DOUBLET MODEL WITH SCALAR SINGLET DM

Two-Higgs Doublet Model extended with an extra scalar singlet S (2HDMS) is a minimal extension of the Standard Model, that provides a scalar Dark Matter candidate and a possibility of CP violation in the scalar sector. In addition, it opens up a window for isospin-violation in DM-nucleon scattering processes. Advantages of IVDM were discussed in Section III D 3. This model has been studied previously in the literature, see [119–127] and also discussed in context of scale invariance [128] and SO(10) grand unification theory (GUT) [129–131]. In the following analysis we will only discuss a scenario where the light Higgs boson h is the only source of the ~ 125 GeV signal registered at the LHC.

In Section VI A we present 2HDMS, in Section VI B we discuss theoretical bounds and in Section VI C experimental bounds on the model. In Section VI D we briefly review collider constraints imposed on the 2HDM parameter space, while in Sections VI F and VI G we discuss cosmological constraints and direct detection limits. In Sections VI H we discuss results of our analysis.

Analysis presented in this chapter has been preformed in collaboration with B. Grzadkowski, J. Gunion and Y. Jiang and published in [74]. This analysis used results of 2HDM study, performed by B. Dumont, S. Kraml, J. Gunion and Y. Jiang, presented in [132].

A. 2HDMS Structure

In this section we introduce a model with two Higgs doublets H_1, H_2 and a real scalar S, which is a singlet under the SM gauge group. We will assign equal $U(1)_Y$ charges $Y = 1$ to H_1 and H_2. The most general gauge-invariant 2HDM scalar potential has already been shown in equation (105) and its properties were discussed in Section V A. As we later concentrate on cases of Type I and Type II Yukawa interactions, we impose an additional Z_2 symmetry on the model, under which $H_1 \to H_1, H_2 \to -H_2$, $S \to S$. This eliminates the λ_6, λ_7 couplings of equation (105) and forbids couplings like $S^2 H_1^\dagger H_2$. However, we do allow for a soft Z_2 symmetry breaking term, $m_{12}^2 \neq 0$.

We also introduce a Z_2' symmetry under which $S \to -S$ (other fields are taken to be even

under Z_2'), which ensures stability of S. The 2HDMS scalar potential is then:

$$\begin{aligned}\mathcal{V}_{2HDMS} = & m_1^2 H_1^\dagger H_1 + m_2^2 H_2^\dagger H_2 - \left[m_{12}^2 H_1^\dagger H_2 + h.c.\right] + \frac{1}{2} m_0^2 S^2 \\ & + \frac{\lambda_1}{2}(H_1^\dagger H_1)^2 + \frac{\lambda_2}{2}(H_2^\dagger H_2)^2 + \lambda_3 (H_1^\dagger H_1)(H_2^\dagger H_2) + \lambda_4 |H_1^\dagger H_2|^2 \\ & + \left[\frac{\lambda_5}{2}(H_1^\dagger H_2)^2 + h.c.\right] + \frac{1}{4!}\lambda_S S^4 + \kappa_1 S^2 (H_1^\dagger H_1) + \kappa_2 S^2 (H_2^\dagger H_2)\end{aligned} \tag{124}$$

which contains 14 (real) parameters. However, for simplicity we consider a model without explicit CP violation (therefore $\lambda_5 \in \mathcal{R}$) and we only consider parameter choices for which there is no spontaneous CP breaking. As a result, the Higgs VEVs are real.

One of the conditions we require is no VEV for the scalar singlet S. Therefore, despite the presence of the $S^2 H_1^\dagger H_1$ and $S^2 H_2^\dagger H_2$ terms in the Lagrangian, the eigenstates of the 2HDM sector can be discussed independently of S and the usual mass matrices for the 2HDM apply (see Section V A). Presence of non-zero $\langle S \rangle$ after spontaneous symmetry breaking, destabilizes the singlet S, therefore it cannot be considered a DM candidate any more. Such scenario has been discussed in *eg.*[127].

Rewriting the S-dependent part of quartic interactions in terms of the couplings of S to the 2HDM mass eigenstates, $h, H, A, H^\pm$, we have:

$$\mathcal{V}_S = \lambda_H v H S^2 + S^2(\lambda_{HH} HH + \lambda_{hH} hH + \lambda_{hh} hh + \lambda_{AA} AA + \lambda_{H^+H^-} H^+H^-) \tag{125}$$

where the mass of S and the DM-Higgs couplings are

$$m_S^2 = m_0^2 + (\kappa_1 \cos^2\beta + \kappa_2 \sin^2\beta) v^2 \tag{126}$$

$$\lambda_h = -\kappa_1 \sin\alpha \cos\beta + \kappa_2 \cos\alpha \sin\beta \tag{127}$$

$$\lambda_H = \kappa_1 \cos\alpha \cos\beta + \kappa_2 \sin\alpha \sin\beta\,, \tag{128}$$

$$\lambda_{HH} = \frac{1}{2}\left(\kappa_1 \cos^2\alpha + \kappa_2 \sin^2\alpha\right) \tag{129}$$

$$\lambda_{hH} = (-\kappa_1 + \kappa_2)\cos\alpha \sin\alpha \tag{130}$$

$$\lambda_{hh} = \frac{1}{2}\left(\kappa_1 \sin^2\alpha + \kappa_2 \cos^2\alpha\right) \tag{131}$$

$$\lambda_{AA} = \frac{1}{2}\left(\kappa_1 \sin^2\beta + \kappa_2 \cos^2\beta\right) \tag{132}$$

$$\lambda_{H^+H^-} = \kappa_1 \cos^2\beta + \kappa_2 \sin^2\beta. \tag{133}$$

Parameters (m_0, κ_1, κ_2), together with 7 parameters of the Z_2 constrained 2HDM potential constitute a complete set of free parameters of 2HDMS. However, it is more convenient

to use the *physical basis* of the parameters,

$$(\tan\beta, \sin\alpha, m_h, m_H, m_A, m_{H^\pm}, m_{12}^2, m_S, \lambda_h, \lambda_H). \tag{134}$$

We prefer to use the DM mass m_S instead of m_0 and the couplings of S to Higgs mass eigenstates, λ_h and λ_H, instead of κ_1 and κ_2. It is particularly convenient to use λ_h and λ_H as DM annihilation amplitudes in the 2HDMS are directly proportional to λ_h for the h exchange diagrams and λ_H for the H exchange, see Fig. 39.

Because of Z_2 and CP symmetries, there is no trilinear term in the lagrangian with A and S interaction. However, the CP-odd Higgs boson A is involved in our discussion as a product of S annihilation, $SS \longleftrightarrow AA$, see Fig. 39. For the Feynman rules of the 2HDMS see Appendix A 3. The Yukawa structure of our model follows 2HDM Type I and 2HDM Type II, see Section V A 1 and Appendix A 2.

B. Theoretical constraints on the 2HDMS Model

In this section we discuss various theoretical constraints imposed on the model: perturbativity, tree level vacuum stability, unitarity and global minimum constraints.

Perturbativity

We impose perturbativity constraints on all quartic couplings between mass eigenstates $h, H, A, H^\pm$ and S, namely their absolute values must be $\leq 4\pi$. For $h, H, A, H^\pm$ we follow the 2HDM constraints, see Section V B. For the extra S sector we have:

$$g_{h_i h_j SS} \leq 4\pi, \tag{135}$$

where $h_{i,j} = h, H, A, H^\pm$. For definition of $g_{h_i h_j SS}$ go to Appendix A 3. For the quartic S self-interaction we have $|\lambda_S| \leq 4\pi$.

One can show that the absolute values of the quartic Feynman rules for h^2S^2, H^2S^2, A^2S^2, $H^+H^-S^2$ are guaranteed to be smaller than 4π if $|\kappa_1|, |\kappa_2| \leq 4\pi$. However, these maximum values are only allowed for $\alpha = \pm\pi/4$.

Vacuum Stability

For the vacuum to be stable at the tree level, the potential in (124) has to be bounded from below. This requirement gives us a set of constraints – inequalities involving couplings λ_i, κ_i, that has to be satisfied. The detailed derivation is shown in [74], while the constraints can be summed up to:

$$\lambda_1, \lambda_2, \lambda_S > 0, \quad \lambda_3 + \lambda_4 - |\lambda_5| > -\sqrt{\lambda_1 \lambda_2}, \quad \lambda_3 > -\sqrt{\lambda_1 \lambda_2} \tag{136}$$

$$\kappa_1 > -\sqrt{\tfrac{1}{12}\lambda_S \lambda_1}, \quad \kappa_2 > -\sqrt{\tfrac{1}{12}\lambda_S \lambda_2}\,. \tag{137}$$

If κ_1 or $\kappa_2 < 0$, then we have to satisfy also:

$$-2\kappa_1\kappa_2 + \tfrac{1}{6}\lambda_S\lambda_3 > -\sqrt{4\left(\tfrac{1}{12}\lambda_S\lambda_1 - \kappa_1^2\right)\left(\tfrac{1}{12}\lambda_S\lambda_2 - \kappa_2^2\right)} \tag{138}$$

$$-2\kappa_1\kappa_2 + \tfrac{1}{6}\lambda_S(\lambda_3 + \lambda_4 - |\lambda_5|) > -\sqrt{4\left(\tfrac{1}{12}\lambda_S\lambda_1 - \kappa_1^2\right)\left(\tfrac{1}{12}\lambda_S\lambda_2 - \kappa_2^2\right)}\,. \tag{139}$$

After a comparison with Section V B, one can see that the conditions in equation (136) are the standard 2HDM stability conditions.

$\mathcal{S}$-Matrix unitarity

In [74] we describe in more detail the unitarity bounds and give explicit formulae for the scattering matrix of two-body processes in the scalar sector of the 2HDMS model. However, it is important to note that the $2 \to 2$ scattering matrix that is obtained when S-related channels are included always has a maximum eigenvalue that is larger than that of the pure 2HDM $2 \to 2$ scattering matrix. This is called the "bordering theorem" (see [133]). Thus, although our 2HDM points have already been filtered using the 2HDMC code [103, 105] which imposes unitarity in the 2HDM context, the unitarity limits obtained after including the S-related channels are guaranteed to be stronger.

Global Minimum

To stabilize the DM field S, a zero vacuum expectation value of S is necessary. Therefore we must have $S = 0$ at the global minimum of the scalar potential (124). To assure that, for each point in 2HDMS parameter space we find all the minima of (124) numerically and

then eliminate points for which the global minimum is not at $\langle S\rangle = 0, \langle H_1\rangle \neq 0, \langle H_2\rangle \neq 0$. We have to remember that the vacuum expectation values of the Higgses must account for $v = 246$ GeV, namely $v_1^2 + v_2^2 = v^2$.

C. Experimental Constraints

D. 2HDM Collider Constraints

The analysis of the 2HDMS model presented in this chapter is based on the 2HDM results obtained by Beranger Dumont, Sabine Kraml, Jack Gunion and Yun Jiang, presented in [132]. Analysis was based on the combined results from ATLAS [134] and CMS [135]. However, one must keep in mind that in those results an enhanced $\gamma\gamma$ signal was present in the ATLAS analysis, whereas the CMS collaboration claimed a suppression in this channel. As a result, combined data show no $\gamma\gamma$ enhancement and a close–to–SM signal.

However, the situation of the $\gamma\gamma$ signal has been changing repeatedly over the past 2 years, from enhancement to suppression, as we discussed in the beginning of Chapter V. Therefore one might consider this state of affairs as unclear. After the most recent update from ATLAS and CMS an enhancement is again in favour by the combined ATLAS and CMS data. If this enhancement becomes statistically certain after future LHC runs, this could be accommodated in the 2HDM context, as discussed in Section V C. But also can be suppression. The possible deviations from the SM signal rate in 2HDM were studied in the literature with a lot of caution, see *eg.*[74, 132, 136–150]. However, if strong $\gamma\gamma$ enhancement was confirmed, the analysis presented in this thesis and in [8] should be revisited.

The 2HDM study by [132] include:

- theoretical constraints on 2HDM, as discussed in Section V B
- B/LEP physics bounds, see Section V C 2
- agreement with STU measurements, see Section V C 1
- LHC heavy Higgs searches, see [135]
- feed-down processes (production from heavier scalars) see [132, 151]

- fit to the combined LHC and ATLAS data at 68% C.L. [132, 152]

The LHC fit was based on the predicted signal strength ellipses in the $\mu_{\rm ggF}$ versus $\mu_{\rm VBF}$ planes. For each of the $\gamma\gamma$, VV (where $VV \equiv ZZ, WW$), $b\bar{b}b$, and $\tau\tau$ final states, it was required to have $\chi^2 < 2.3$, the contours were established in [152].

In the following analysis we will concentrate on a scenario, where the light Higgs h is the only source of the ~ 125 GeV signal registered at the LHC. The 2HDM analysis for this case can be summarized in a simple manner - as the LHC signal of a ~ 125 GeV particle seem very much SM-like, h looks very much alike a SM Higgs boson. In the literature it is sometimes referred to as the *alignment limit* [153]. To illustrate this, we show the $(\sin\alpha, \tan\beta)$ results of the 2HDM fit at 68% CL from the analysis in [8, 132], see Fig. 35. Note that, especially in the case of the Type II model, we see a very strong corelation between the angles α and β, namely $\beta - \alpha \simeq \pi/2$ (this is the main constraint of the *alignment limit* of the 2HDM). This is not true for all the points surviving the LHC fit at 95% and even a few at 68% C.L.; there is a *wrong-sign Yukawa coupling* branch visible for positive $\sin\alpha$ in Fig. 35, see *eg.*[146].

In Fig. 36 one can see that for the points at 68% CL, the couplings of h to WW, ZZ and $b\bar{b}$, are indeed very close to the SM couplings. For detailed discussion of all the features of the 2HDM under the discussed constraints, see [132].

The general setup for the 2HDMS analysis presented in this thesis and also in [74] is the following: first we use results from the 2HDM analysis, namely points that survived all constrains and a fit to the LHC at 68% C.L. (labelled as "postLHC8-FDOK" in [132]). Then, for those points we expand the model with extra scalar singlet S, as presented in Section VI A, and study various constraints on the parameter space.

E. Higgs Invisible Decay

The CP-even Higgs bosons h and H of the 2HDM may decay to SM particles and pairs of extra scalars AA and H^+H^-; also a decay mode $H \to hh$, might be possible. When additional singlets S are present, h and H might also decay invisibly into SS. Those decays, $h, H \to SS$, are potentially very important, especially decays of the particle with ~ 125 GeV mass. If $h \to SS$ is strong, it could destroy the 68% C.L. level fits to the LHC SM-like signal (that we are going to adopt), done without the scalars present in the model. As $h \to AA$ problem has been managed by [132], we need only to ensure that, for each point in 2HDMS

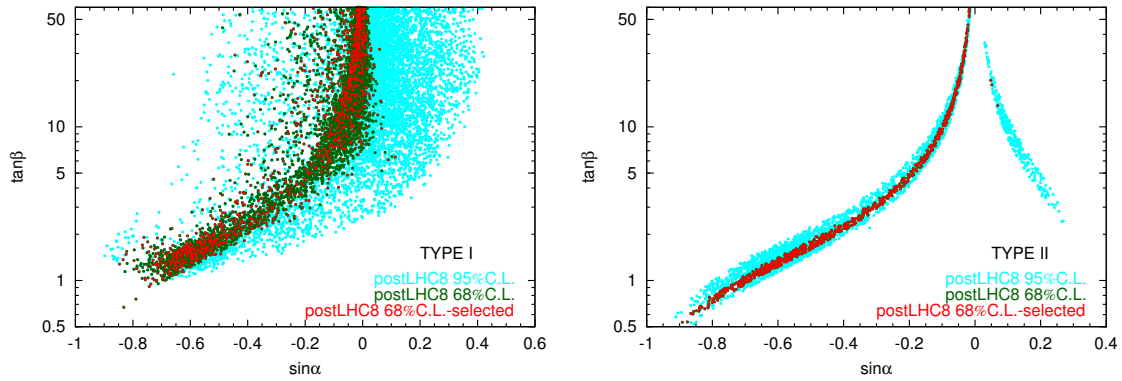

Figure 35: 2HDM points in the $(\tan\beta, \sin\alpha)$ plane that provide a fit the LHC/Tevatron signal strengths at 95% C.L. (cyan) and 68% C.L. (dark green), from the analysis in [152]. In red we have marked the 68% C.L. points used later in the singlet scalar model analysis (for the Type II model we have used all 68% C.L. points).

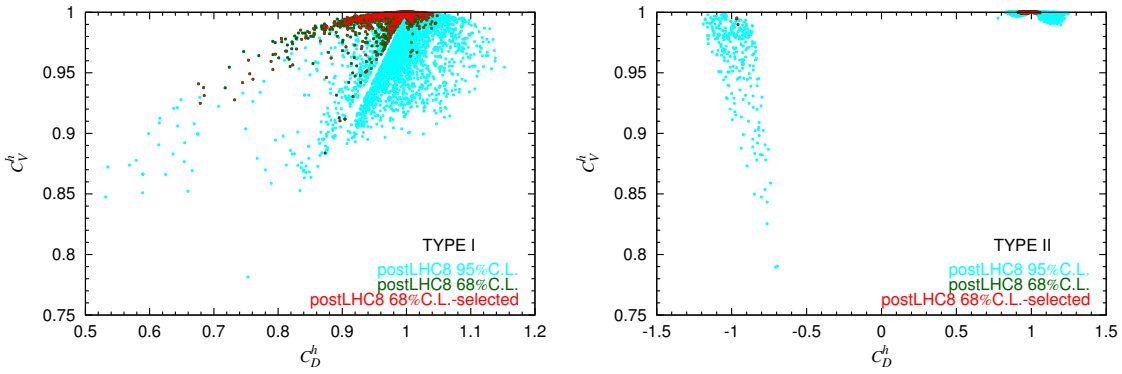

Figure 36: 2HDM coupling of h to the vector bosons VV normalized to the SM value (C_V^h, couplings are the same for $VV = ZZ$ and WW) vs 2HDM coupling of h to the down type quarks normalized to the SM value, C_D^h, using color notation of Fig. 35. For Type I, $C_U^h = C_D^h$.

parameter space, $BR(h \to SS)$ is sufficiently small [152] and does not significantly disturb the fit to the LHC data. Therefore we impose

$$BR(h \to SS) \leq 10\% \tag{140}$$

The $h, H \to SS$ decay widths are given in Appendix B 4.

Values of $BR(h \to SS)$ for various (λ_h, λ_H), before imposing (140), are shown in Fig. 37. In Fig. 38 we show invisible decays of the H, after imposing (140).

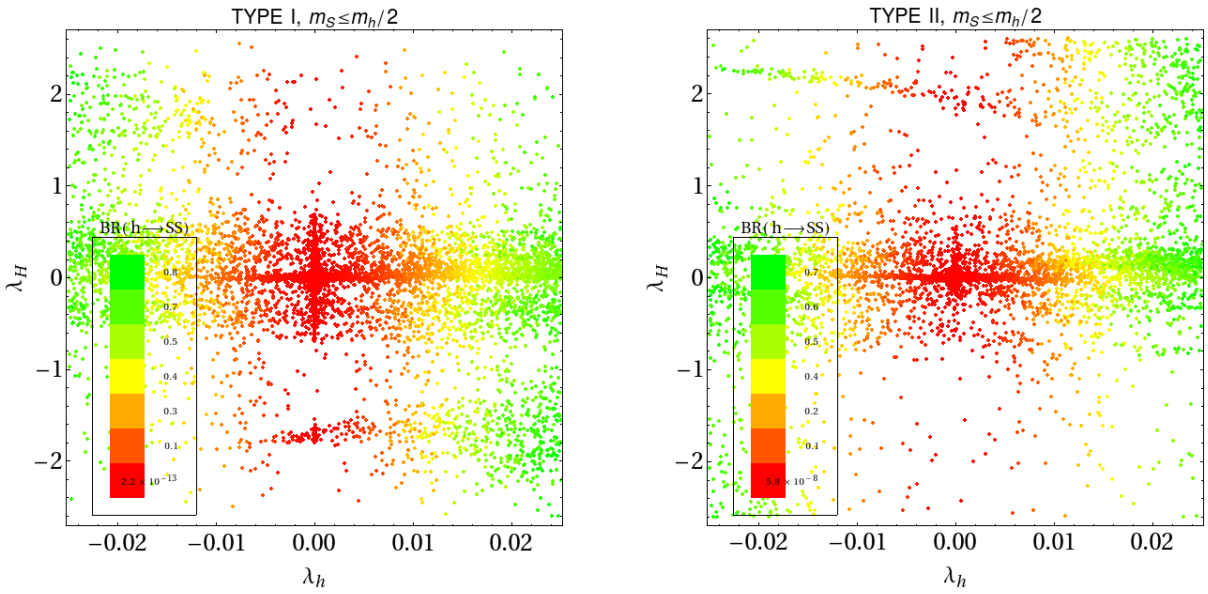

Figure 37: The couplings of h/H to SS after imposing the full set of 2HDM constraints, theoretical constraints on the 2HDMS and Ωh^2. Colouring is according to $BR(h \to SS)$: points with small BR are red, large BR points are green. The 2HDM points employed in this scan are the red points of Fig. 35, will be discussed later. A full scan over the singlet sector parameters is performed subject to the standard P+S+U+EW constraints.

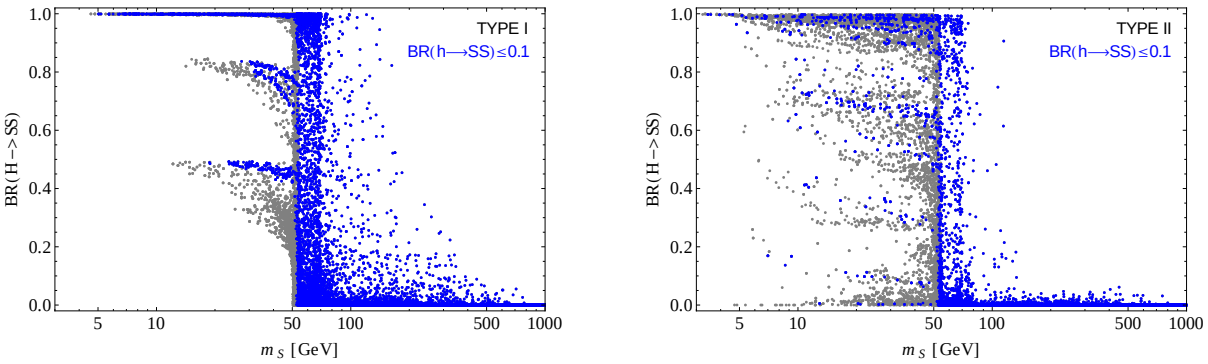

Figure 38: We plot $BR(H \to SS)$ as a function of m_S. The 2HDM points employed in this scan are the red points of Fig. 35. A full scan over the singlet sector parameters is performed subject to the standard P+S+U+EW constraints (gray points) with the additional $BR(h \to SS) \leq 0.1$ requirement (blue points).

F. Relic Density

In this section we discuss implications of the relic abundance constraint (20) on the model. 2HDMS provides a single DM candidate, therefore the standard approximations

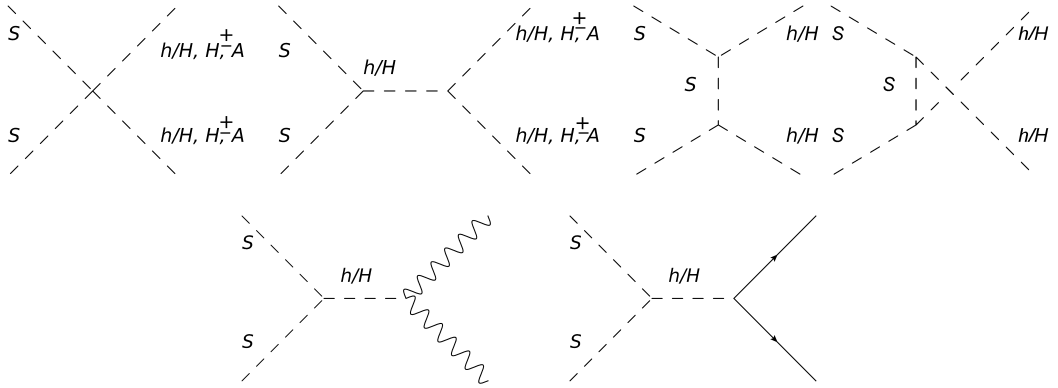

Figure 39: Singlet annihilation diagrams relevant for the relic density calculation.

discussed in Secion III C 2 apply. The total cross section for SS annihilation can be found in Appendix B 4.

The DM SS annihilation diagrams relevant to the relic abundance computation are shown in Fig. 39. We included the following annihilation modes of SS:

- fermion-antifermion pairs $f\bar{f}$, which is usually dominated by $b\bar{b}$ or $t\bar{t}$, depending on m_S;
- gauge boson's pairs, W^+W^- and ZZ; no $\gamma\gamma$ processes at the tree level
- Higgs bosons: hh, hH, HH, AA and H^+H^-.

The processes of annihilation into the SM fermions and gauge bosons are mediated by an s-channel h or H exchange. DM annihilation into AA and H^+H^- final states goes through the contact interaction and also s-channel annihilation, see Fig. 39. Therefore, if $m_S \sim m_h/2$ or $m_S \sim m_H/2$, a resonance appears in the evaluation of Ω, see for example Fig. 40 and Fig. 41. A similar effect was also present and discussed in the case of the O(N) model, see Fig. 18 and discussion in Section IV D.

The other 3 final states containing CP-even Higgs pairs, namely $(H_iH_j) = (hh), (HH), (hH)$, in addition to the s-channel h or H exchange diagrams and the four-point contact term, one has to add contributions from t- and u-channel S exchange. In this case all diagrams in the top row of Fig. 39 are relevant.

Note that in general, depending on m_s, some final states are closed due to kinematics. This is well illustrated in the evaluation of Ωh^2 in the scans over the singlet parameter space, see Figs. 40 and 41. Whenever an extra channel for annihilation opens up with growing m_S, the

relic density Ωh^2 drops down to account for a new contribution to the total DM annihilation cross section (remember that $\Omega \propto 1/\langle\sigma_S|v|\rangle$). For example, a sudden drop in Ωh^2 appears near 80/90 GeV, due to the WW and ZZ final states. A similar threshold is also visible around the $m_S \sim m_t$[6]. In particular, for $m_S < m_h$ only the $f\bar{f}$ (primarily $b\bar{b}$ in most of the m_S range of our interest), WW, ZZ and, AA annihilation modes could be allowed.

The Ωh^2 shown in Figs. 40 and 41 is a result of the scan over singlet parameter space $(m_S, \lambda_h, \lambda_H)$ in the following ranges of parameters: $m_S = 1 - 1000$ GeV, $\lambda_h, \lambda_H = 10^{-2} - 4\pi$. The scan density was not uniform; we have increased the m_S density near the resonances $m_S \simeq m_h/2$ and $m_S \simeq m_H/2$, also scanning through smaller couplings in those regions. For those figures we have chosen some representative 2HDM points (see Table XIII), that were fixed when scanning over the remaining singlet parameters. For the two plots in Fig. 40, the 2HDM parameters were chosen such that low m_S is eliminated when constraints are imposed (stability, unitarity, EWSB, invisible branching ratio). In Fig. 41, a much larger range of m_S values is consistent with EWSB and observed Ωh^2.

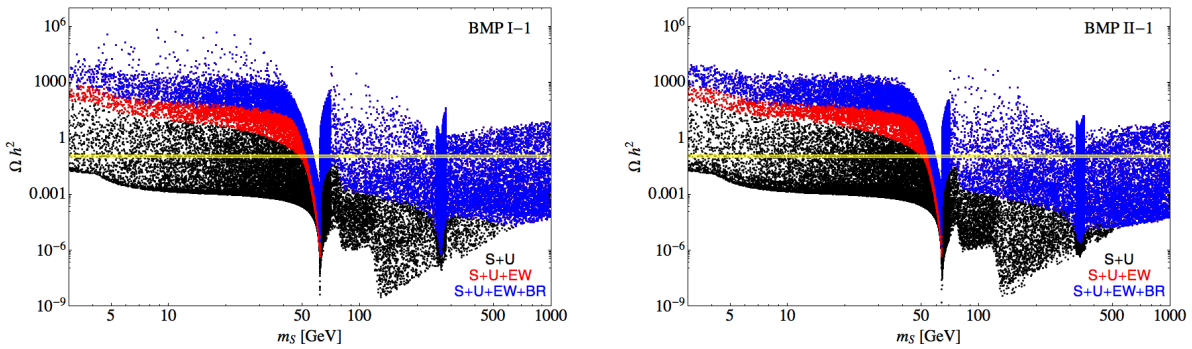

Figure 40: Results for the relic abundance Ωh^2 as a function of m_S from a scan over the singlet parameter space with a fixed 2HDM point. The sample 2HDM parameters employed are given in Table XIII. All points satisfy perturbativity limits, black points satisfy the stability and unitarity conditions, red points satisfy also the EWSB conditions. Blue points satisfy S+U+EW *and* have $BR(h \to SS) \leq 0.1$. The yellow band is the recent $\pm 3\sigma$ Planck window. We emphasize that the LUX and other limits on DM detection are not yet imposed in these plots.

[6] The same effect has been discussed previously in context of the O(N) model, see Section IV D.

BMP #	$\tan\beta$	$\sin\alpha$	m_{12}^2	m_h	m_H	m_A	$m_{H^\pm}$	λ_1	λ_2	λ_3	λ_4	λ_5
I-1	1.586	-0.587	5621	123.71	534.25	645.13	549.25	5.98	1.683	3.203	-1.032	-4.81
II-1	0.969	-0.721	1.251×10^5	127.96	678.98	600.36	563.18	3.463	4.046	-0.997	-0.389	-1.816
I-2	1.346	-0.663	-2236	126.49	168.01	560.92	556.94	1.199	0.59	10.101	-5.12	-5.267
II-2	2.092	-0.4096	-1.264×10^4	125.89	137.86	451.33	398.76	3.984	0.454	5.732	-2.422	-3.896

TABLE XIII: 2HDM parameters for the plots of Figs. **??** and **??**. Masses in GeV; m_{12}^2 in GeV^2.

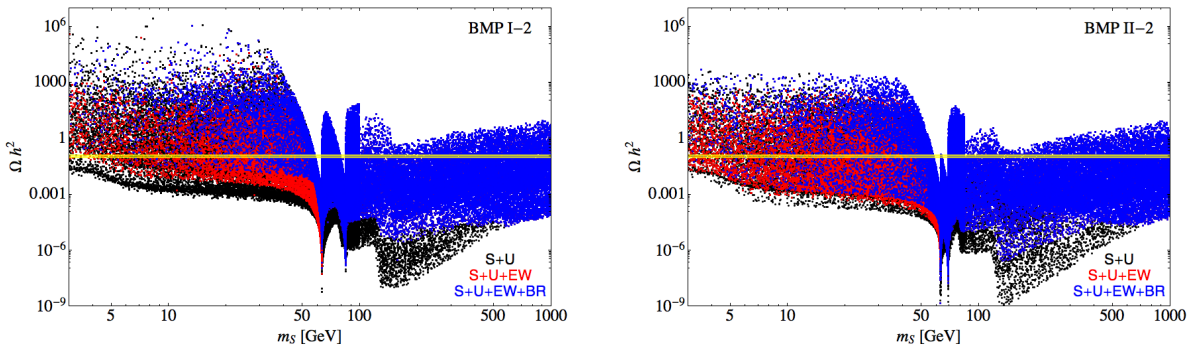

Figure 41: As for Fig. 40, but for different 2HDM points, see the last two points of Table XIII.

G. Direct Detection

The theory of DM direct detection in a generic case was presented in Section III D. In the 2HDMS a particularly interesting effect related to direct detection is a possibility of isospin violation [74]. Therefore S is a potential candidate for isospin-violating DM (IVDM).

The cross section for DM scattering off a nucleus for a generic case is given in equation (59). The definition of the DM-N coupling amplitude f_N for scalar DM is given in equation (57). We repeat for consistency the definition of f_N, the couplings of DM to the proton and neutron (formerly called $f_{\varphi-N}$ for N=p, n),

$$f_N = \frac{m_N}{2m_\varphi}\left(\sum_{q=u,d,s}\lambda_{SSqq}\frac{f_{Tq}^N}{m_q} + \frac{2}{27}\sum_{Q=c,b,t}\lambda_{SSQQ}\frac{f_{TGQ}^N}{m_Q}\right) \tag{141}$$

where m_N is the mass of the nucleon, f_{Tq}^N, f_{TGQ}^N are the form factors of the nucleon (that can be read of Table I) and $\lambda_{SSqq}(\lambda_{SSQQ})$ is the effective couplings of the DM particle S to a ligh (q) and heavy (Q) quark. The diagram for elastic scattering of S off a nucleon with a t-channel exchange of h and H is shown in Fig. 42. In the limit of zero momentum transfer we find:

$$\lambda_{SSqq} = \sum_{h_i=h,H}\frac{g_{h_iSS}g_{h_iq\bar{q}}}{-m_{h_i}^2} = \left(\frac{2\lambda_h}{m_h^2}C_q^h + \frac{2\lambda_H}{m_H^2}C_q^H\right)m_q\,, \tag{142}$$

where g_{h_iSS}, $C_q^{h_i}$, $g_{h_iq\bar{q}}$ are defined in Appendix A 3 and the same applies for heavy quarks Q.

In practice we have implemented the 2HDMS model in micrOMEGAs and used the code to calculate direct detection rates [63], including QCD NLO corrections.

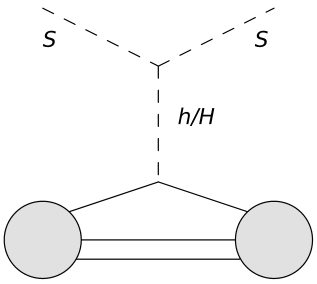

Figure 42: Feynman diagram for the scattering of S off a nucleon in 2HDMS model.

We are particularly interested in the possibility of isospin violation for low mass DM, more precisely 5 GeV $\lesssim m_S \lesssim$ 50 GeV and $f_n/f_p \sim -0.7$ (see discussion in Section III D 3). However, in the case of Type I model, the couplings of h and H with up-type and down-type quarks are universal (see Table III) and $f_n/f_p \simeq 1.012$. This allows for a direct comparison of 2HDMS Type I predictions with all experimental bounds from various direct searches for DM.

However, in Type II model significant deviations from $f_n/f_p = 1$ are possible. We have performed general 2HDMS parameter space scans (using points that survived LHC fits at 68% C.L.) with density increased for points with $-0.6 < f_n/f_p < -0.8$ in the low m_S region. From Fig. 43 one can see that $f_n/f_p \neq 1$ is generally attainable in the 2HDMS, therefore comparison of the cross-section for DM-nucleon scattering with the results presented by the experimental groups requires extra attention. The procedure of working with IVDM model in a generic case has been introduced in details in Section III D.

In order to constrain an IVDM model, we should compute f_n/f_p for each point in the parameter space. In general f_n/f_p depends on both 2HDM and the singlet sector parameters. However, there is an interesting special case in which f_n/f_p dependence on the singlet sector can be neglected.

Positive signals from CDMS Si, CRESST-II and CoGeNT experiments account for low m_S (generally for $m_S < m_h/2$), for which an invisible decay channel $h \to SS$ is open, as discussed in Section VI E. The $BR(h \to SS)$ for this points is large unless λ_h is very small. Therefore it is well motivated to take the limit of $\lambda_h \to 0$ for f_n/f_p in this mass region, in which we neglect the h term in (142). In this limit, the value of f_N depends only on the 2HDM parameters, in particular on the H-quark couplings:

$$f_N = \frac{m_N}{2 m_S m_H^2} \left\{ \left[f_{Tu}^N + \frac{2}{27} \left(f_{TGc}^N + f_{TGt}^N \right) \right] C_u^H + \left(f_{Td}^N + f_{Ts}^N + \frac{2}{27} f_{TGb}^N \right) C_d^H \right\}, \qquad (143)$$

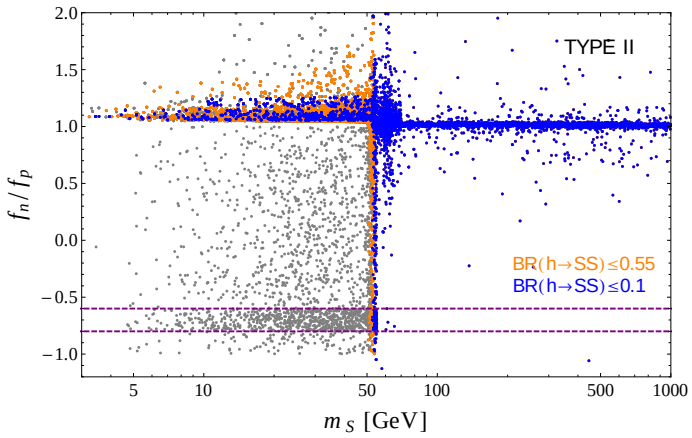

Figure 43: The ratio f_n/f_p as a function of m_S for Type II, as a result of the singlet scan within 2HDM-postLHC8-FDOK points. We show only points that satisfy all theoretical constraints and Ωh^2 within 3σ limit. The blue (orange) points satisfy the $BR(h \to SS)$ limit of 10% (55%). The scan density was not even, with special focus on points with $-0.6 < f_n/f_p < -0.8$.

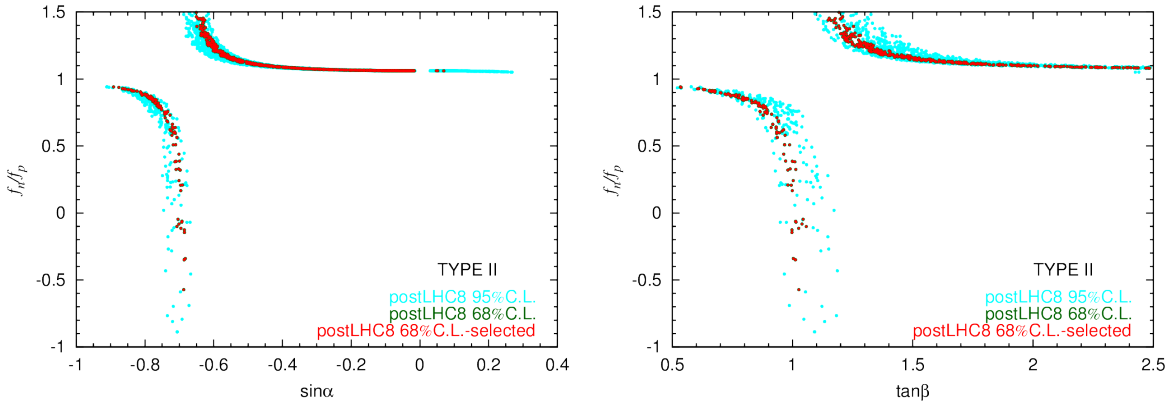

Figure 44: f_n/f_p in the limit of $\lambda_h = 0$ as a function of $\sin\alpha$ for the 68% C.L. Type II 2HDM scan points.

where $N = p, n$. We will also require $\beta - \alpha \simeq \pi/2$, which is a very good approximation for Type II model because of the LHC fit results at 68% C.L. (see Fig. 36). In this case we have $C_u^H \simeq -\cot\beta$, $C_d^H \simeq \tan\beta$ and $\tan\beta$ can be expressed by f_n/f_p and the form factors only (for $\lambda_h = 0$):

$$\tan^2\beta(f_n/f_p) = \frac{\frac{f_n}{f_p}F_u^p - \frac{m_n}{m_p}F_u^n}{\frac{f_n}{f_p}F_d^p - \frac{m_n}{m_p}F_d^n}, \tag{144}$$

where the F_u^N, F_d^N are the summed form factors for up- and down-type quarks, respectively,

$$F_u^N \equiv f_{Tu}^N + \frac{2}{27}\left(f_{TGc}^N + f_{TGt}^N\right) , \quad F_d^N \equiv f_{Td}^N + f_{Ts}^N + \frac{2}{27} f_{TGb}^N . \tag{145}$$

For $f_n/f_p = -0.7$, the expected values of α and β angles are

$$\tan\beta \simeq 1.0 \quad \text{and} \quad \sin\alpha \simeq -0.7. \tag{146}$$

In Fig. 44, we display $\lambda_x \to 0$ limit of f_n/f_p as a function of $\sin\alpha$ evaluated for Type II points from [132], for LHC fits at 95% C.L. or better. While a wide range of f_n/f_p values is visible in this figure, namely $f_n/f_p \in (-0.9, 1.5)$, for the 68% C.L. Type II points included in our study, $f_n/f_p < -0.5$ is associated with a single isolated point close to -0.7, with $\tan\beta, \sin\alpha$ close to the results of (146). This is just an accidental result given the scanning procedure/density employed in [132]. This might not be enough to study thoroughly isospin-violating effects in the 2HDMS model, and might require a follow-up analysis in the future.

It turns out that when $BR(h \to SS) \leq 0.1$ is imposed, the Ωh^2 scan results for the points with $-0.9 < f_n/f_p < -0.5$ (within 95% C.L. agreement with the LHC fit), lie outside the 3σ window that we have allowed. Thus, within the limitations of the analysis so far performed, we have not managed to satisfy *all* the constraints not related to DM-scattering and also have $f_n/f_p \sim -0.7$ within $m_S < 50$ GeV. We generally regard it as possible that much denser scans might reveal such solutions.

H. Results

We will discuss a case of the light Higgs boson h to be a source of the ~ 125 GeV signal. We will adopt the 2HDM phenomenologically allowed points of [132] (labelled as "postLHC8-FDOK"), as a basis for our analysis.

In the case of $m_h \sim 125.5$ GeV [132] found ~ 5200 points consistent with Higgs observations at 68% C.L. in the Type I model, from which we randomly chose 1250 points for further analysis (see red points in Fig. 35). For the case of Type II model, we use all of the ~ 900 points that fall within 68% C.L.. For each 2HDM-postLHC8-FDOK point, we expand the pararameter space with extra singlet parameters: $m_S, \lambda_h, \lambda_H$, and perform a scan. We then check theoretical constraints, as discussed in Section VI B. The singlet constribution to experimental constraints from electroweak precision tests (STU parameters), B physics,

direct searches at LEP and also limits on the heavier Higgs bosons (H and possibly A) are negligible. However, the $h \to SS$ decays of a light scalar S should be included, as discussed in Section VI E, with a 10% limit on the invisible branching ratio of h decay. We use micrOMEGAs [63] to compute the relic abundance of the DM candidate S and require that the predicted Ωh^2 fall within the $\pm 3\sigma$ Planck window, see equation (20). We will later refer to this set of constraints as the 'preLUX' constraints.

Then, for the points satisfying the 'preLUX' constraints, we compute the cross section for the scattering of the singlet S off a nucleon. We rescale the cross section by Θ_X and compare the predicted value $\overline{\sigma}_{\mathrm{DM}-p}$ with the latest experimental limits for the DM-proton (DM-p) cross section, $\sigma^{\mathrm{X}}_{\mathrm{DM}-p}$, where X=LUX, superCDMS, CDMS Si or CoGeNT. If the points obey the condition $\overline{\sigma}_{\mathrm{DM}-p} \leq \sigma^{\mathrm{LUX(superCDMS)}}_{\mathrm{DM}-p}$, they are allowed by LUX (superCDMS) limit.

1. Type I Analysis

In Fig. 45 we present results of imposing the full set of preLUX constraints (in blue), and then the results of additionally imposing the LUX limit (in green), on the λ_h and λ_H values as a function of m_S.

For $m_S \lesssim 50$ GeV we observe that $BR(h \to SS) \leq 0.1$ implies small λ_h. Therefore dominant contributions to the SS annihilation are $SS \to H \to SM$. To satisfy the bound on Ωh^2, λ_H should be substantially large, depending on the value of m_H (see Fig. 46). Note, that each band in Fig. 46 is associated with a particular m_H value in the associated 2HDM point. This structure is discrete, because of the density of our 2HDM scan was not sufficient. However, the it is clearly visible from this figure that larger the value of m_H, larger the value of λ_H is needed for correct Ωh^2.

In contrast, in the vicinity of the resonance, $m_S \sim m_h/2$, a variety of possibilities opens for λ_H, with $|\lambda_H|$ as large as ~ 2.5. However λ_h remains very small, with values even as small as $\sim 10^{-6}$.

For $m_S \geq 55$ GeV points allowed by preLUX constraints are usually also allowed by the LUX bound. There are also few green points at very low m_S that pass the LUX limit, but are excluded by the SuperCDMS and CRESST-TUM40 constraints, see Fig. 47. In this figure we show the cross section σ_{S-p} as a function of m_S for Type I model, together with various direct detection bounds. Predictions for $\sigma_{\mathrm{DM}-p}$ agree pretty well with CDMS Si/CRESST-

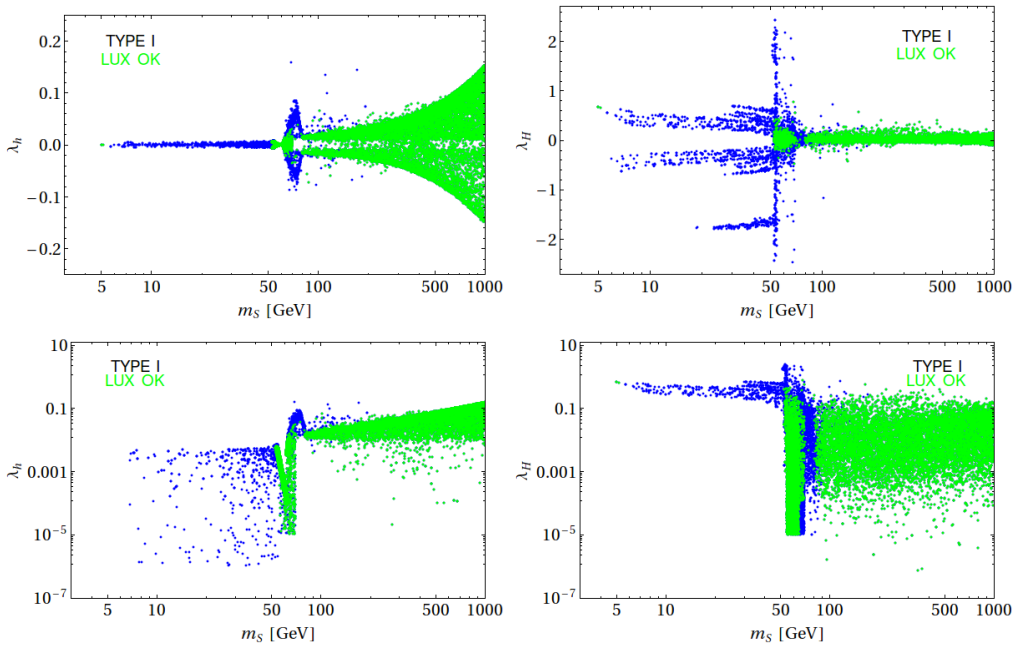

Figure 45: The couplings λ_h and λ_H as a function of m_S for Type I. All points satisfy the full set of preLUX constraints; blue points are excluded by LUX while green points are allowed by LUX results. The sharp cut at 10^{-5} for both couplings in the resonance regions comes from the scanning range. However, in the large m_S range we have scanned over κ_1, κ_2 parameters, therefore a few points with $\lambda_H < 10^{-5}$ appear (and are related to H resonances).

II data at $1-3\sigma$, depending on m_S. However at 90% C.L. they do not account for the CoGeNT results. Note, that the CDMS Si/CRESST-II/CoGeNT regions are not consistent with LUX and SuperCDMS limits, when isospin-violating effects (or other effects discussed in Section III D 3) are absent.

Note, that the allowed points form a very narrow band in the low m_S region. This is a consequence of the invisible branching ratio constraint, requiring effectively $\lambda_h \simeq 0$. If $BR(h \to SS) \leq 0.1$, the heavy Higgs H is responsible for both processes of DM annihilation and scattering off nucleons (just in different channels - the s-channel for annihilation and t-channel for the scattering, see Fig. 4). The cross sections for both processes effectively depend on λ_H/m_H^2 and if $\langle \sigma_S |v| \rangle$ is fixed by $\Omega h^2 \pm 3\sigma$ constraint, then λ_h and λ_H are roughly fixed in the $m_S < 50$ GeV region and σ_{S-p} is also roughly fixed.

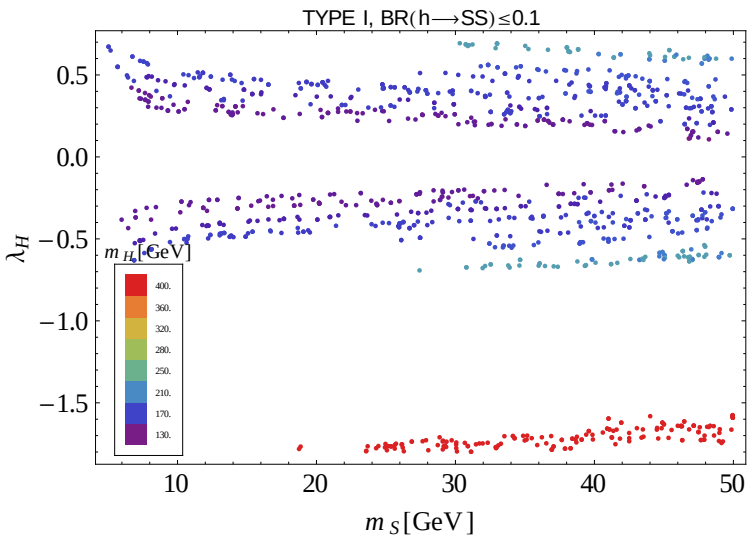

Figure 46: The coupling λ_H as a function of m_S for Type I, coloured due to the value of m_H. All points shown satisfy the full set of preLUX constraints.

I. Type II Analysis

In the Type II model we are particularly interested in isospin-violation and possible consistency between CDMS Si/CoGeNT and LUX/SuperCDMS results. As already discussed, the optimal f_n/f_p ratio in this case is ~ -0.7. We shall not include CRESST-II and CRESST-TUM40 results in the analysis in this section. As the structure of CRESST detector is quite complex, it is difficult to discuss properly isospin-violating effects on the event rate. However, the CRESST-II results are very questionable in context of new CRESST-TUM40 data, therefore such negligence is well motivated.

In Fig. 43 we have illustrated the correlation between f_n/f_p and invisible branching ratio of h, $BR(h \to SS)$. After requiring preLUX constraints with $BR(h \to SS) \leq 10\%$, all points with $f_n/f_p \sim -0.7$ in the low m_S region are excluded (however, those are still possible if $m_S > m_h/2$). In the low m_S region $f_n/f_p \gtrsim 1$. Even relaxing the invisible decay limit to $BR(h \to SS) \leq 55\%$ (which corresponds to the most conservative upper bound on BR_{inv} at the LHC [154]) does not help the situation and still points with $f_n/f_p \sim -0.7$ remain far beyond reach. However, substantial deviations from $f_n/f_p = 1$ are allowed for $m_S \gtrsim 55$ GeV. Thus, it will be important to take into account this variation in DM scattering cross section computation.

To compare the cross section σ_{S-p} with experimental bounds we will evaluate the rescaling

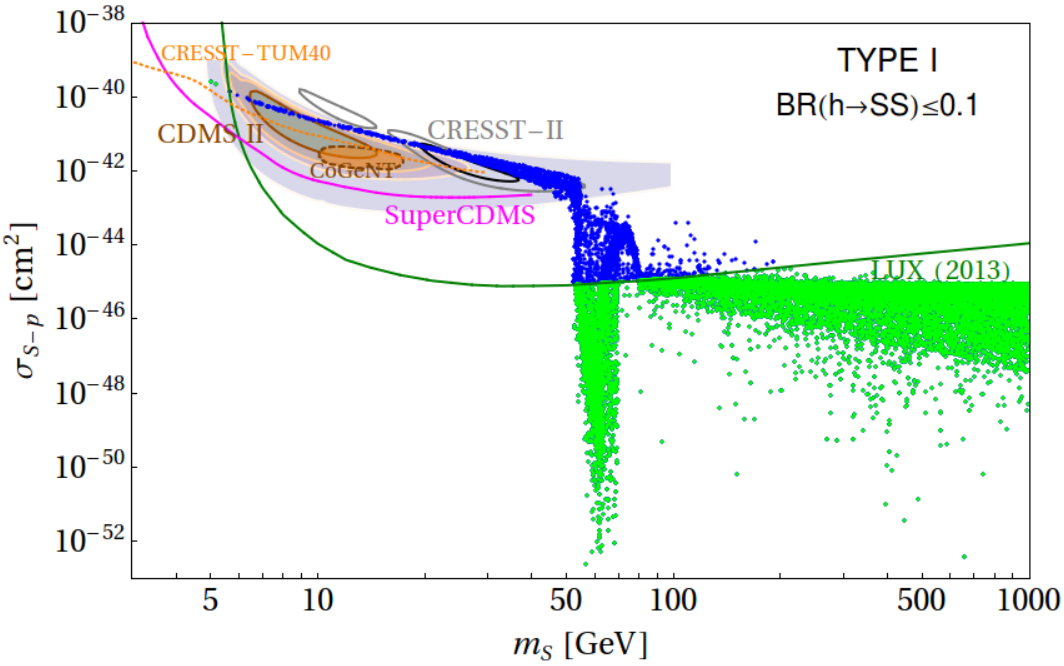

Figure 47: Cross section for S-proton scattering in 2HDMS Type I ($f_n/f_p \sim 1$). All shown points satisfy the full set of preLUX constraints (including $BR(h \to SS) \leq 0.1$), while the green points satisfy also the LUX bound (the green line). The pink line is the SuperCDMS bound and dotted orange line corresponds to the CRESST-TUM40 bound. Also shown are CRESST-II, CoGeNT and CDMS II signal contours. For CRESST-II we show the 68% C.L. (darker black) contour and 95% C.L. (lighter gray) contours. In the case of CoGeNT (orange region) we show 90% C.L. contour. For CDMS II, we display contours at 68%, 90%, 95% and 99% C.L. (from darkest to lightest grey)

factors $\Theta_{\rm X}$, as defined in (65). In particular, we will use $\Theta_{\rm Xe}$ for the Xenon-based detectors (see Fig. 48), $\Theta_{\rm Si}$ for the Silicon-based detectors (see Fig. 49, left panel) and $\Theta_{\rm Ge}$ for the Germanium-based detectors (see Fig. 49, right panel).

The comparison with positive signal regions of CDMS Si and CoGeNT is shown in Fig. 49. We have used appropriate rescaling to account for $f_n/f_p \neq 1$, however we see that for this range of f_n/f_p the rescaling is fairly minimal. We have found, that there are a few points (the large black points in Fig. 49) with $m_S \sim 5.5 - 6.2$ GeV that lie below both the rescaled LUX limits and rescaled SuperCDMS limits and within the 3σ (99% C.L.) CDMS Si contour. Thus, the 2HDMS Type II model allows consistency between the CDMS Si signal region (at 99% C.L.) and the SuperCDMS and LUX limits for this small range of low m_S.

Although there are points consistent with preLUX constraints that lie within the CoGeNT

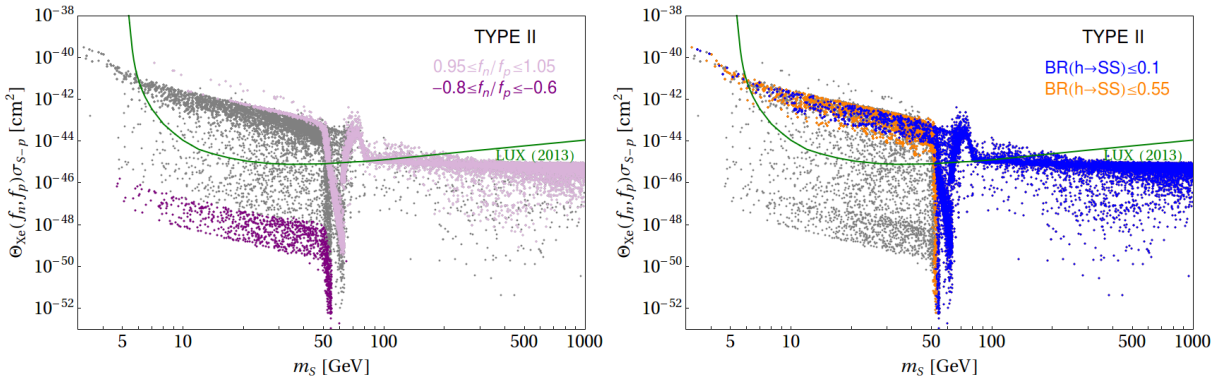

Figure 48: Cross section for S-proton scattering in the Type II model, rescaled by $\Theta_{\rm X}$ (see eq. (65)), X = Xe for a Xenon-based detector. All points plotted satisfy the preLUX constraints *except* $BR(h \to SS) \leq 0.1$ (*i.e.* they satisfy all 2HDM constraints, 2HDM fitting at 68% C.L., theoretical constraints for 2HDMS and the constraint on Ωh^2). Lighter (darker) purple points correspond to the ratio f_n/f_p is within the range (0.95, 1.05) $(-0.8 \leq f_n/f_p \leq -0.6)$. Blue points obey $BR(h \to SS) \leq 0.1$, the orange points obey only the weaker limit of $BR(h \to SS) \leq 0.55$.

90% C.L. signal region for $m_S \sim 10 - 15$ GeV, but those are entirely excluded by the SuperCDMS limit (there is no relative rescaling possible, since both detectors have Germanium targets) and by the rescaled LUX limit. Even though a possibility of agreement with LUX might arise if $f_n/f_p \neq 1$ would be considered, superCDMS and CoGeNT conflict cannot be understood in this manner.

Note also, that there are only very few points in Fig. 49 with low m_S that obey LUX and SuperCDMS constraints in the case of the Type II model. We show the complete set of their parameters in Table XIV. They all have low $\tan\beta$, very modest m_H with $m_A, m_{H^\pm}$ somewhat larger (in the $300 - 600$ GeV range). CRESST-TUM40 exclusion limit also lies above those points (for $f_n/f_p \sim 1$ approximation).

In Fig. 50 we plot λ_h and λ_H vs. m_S for the Type II points that obey preLUX constraints. The resulting point distributions look very similar to those shown in Fig. 45.

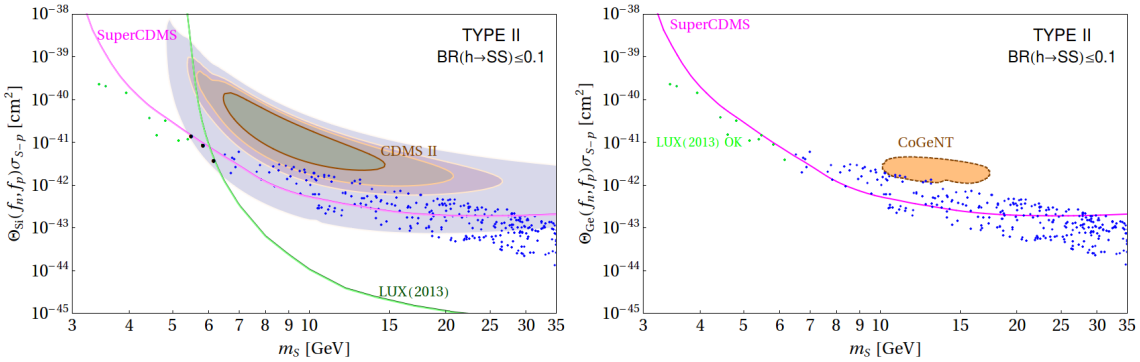

Figure 49: Cross section for S-proton scattering in the Type II model, rescaled by $\Theta_{\rm X}$ (see eq. (65)), where X = Si for a Silicon detector (CDMS Si) on the left and X=Ge for the Germanium detector (CoGeNT) on the right. All points satisfy all the preLUX constraints (*i.e.* they satisfy all 2HDM constraints, 2HDM fitting at 68% C.L., theoretical constraints for 2HDMS, $BR(h \to SS) \leq 0.1$ and the constraint on Ωh^2). The CDMS Si contours shown are at 68%, 90%, 95% and 99% C.L. The CoGeNT contour is the 90% C.L. level contour. Light green points are allowed by LUX results. The larger black points are those allowed by both SuperCDMS and LUX and that also lie within the 99% C.L. CDMS Si contour. Almost degenerate pink and light pink lines are SuperCDMS limits rescaled from the Germanium target to be compared with a Silicon target results $\sigma_{\rm Si}^{\rm SuperCDMS} = \sigma^{\rm SuperCDMS}\Theta_{\rm Si}(f_n,f_p)/\Theta_{\rm Ge}(f_n,f_p)$, for which we used $f_n/f_p = 1.05$ and 1.25 (minimum and maximum values from Fig. 43 for $m_S \leq 35$ GeV). Dark green lines correspond to the analogously rescaled LUX limit, $\sigma_{\rm Si}^{\rm LUX} = \sigma^{\rm LUX}\Theta_{\rm Si}(f_n,f_p)/\Theta_{\rm Xe}(f_n,f_p)$.

$\tan\beta$	$\sin\alpha$	m_H	m_A	$m_{H^\pm}$	m_{12}^2	$(m_S$ [GeV], $\log\Theta_{\rm Xe}(f_n, f_p)\sigma_{S-p}[{\rm cm}^2])$
2.092	-0.41	138	451	399	-12642	(3.44, -39.65); (3.56,-39.69); (3.95, -39.85)
3.121	-0.282	187	546	571	8943	(4.82, -40.50); (5.48, -40.83)
2.192	-0.394	209	488	503	7518	(5.40, -40.93)
1.728	-0.476	177	318	389	9382	(5.16, -40.97)
1.789	-0.461	198	420	430	-6594	(4.44,-40.43); (5.15, -40.96)
1.488	-0.528	157	553	576	-10094	(4.61, -40.83)
2.375	-0.363	259	260	339	15899	(5.83, -41.05)

TABLE XIV: Summary of the properties of the 2HDM Type II points in Fig. 49 which make it possible to realize $m_S < 50$ GeV, after imposing the full set of preLUX constraints together with the LUX and SuperCDMS bounds. All masses are given in GeV units.

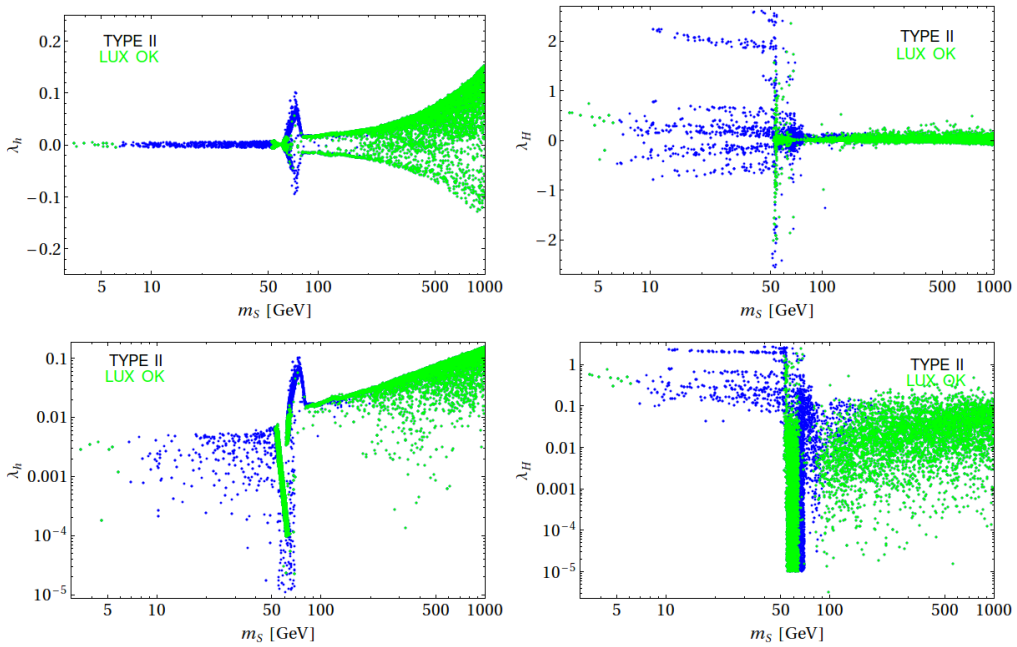

Figure 50: The couplings λ_h and λ_H as a function of m_S for Type II. All points shown satisfy the full set of preLUX constraints; blue points are excluded by LUX while green points are allowed by LUX results. The green points at very low m_S are, however, excluded by SuperCDMS. The sharp cut at 10^{-5} for both couplings in the resonance regions comes from the scanning range. However, in the large m_S range we have scanned over κ_1, κ_2 parameters, therefore a few points with $\lambda_H < 10^{-5}$ might appear (a single point is visible on the plot).

VII. TWO-COMPONENT DARK MATTER

The motivation for studies of multi-component DM has already been discussed in the Introduction to this thesis and also in the first paragraphs of Chapter IV. The literature on the subject is growing [25–30], and even first automated code for the relic density evaluation in two-component DM model very recently appeared, see [155]. In this chapter we would like to investigate a scenario where DM consists of two species – a singlet scalar (φ) and a singlet neutral Majorana fermion (ν) (that we will refer to as a "neutrino"), with possibly significant self-interaction.

A minimal realization of such model contains three new particles, all gauge-singlets: a real scalar φ, and two majorana fermions ν_h and ν. At least two fermions are required to generate non-trivial interactions between the DM components, however only one of them will contribute to the relic density. We will call this model 2CDMM (standing for Two Component Dark Matter Model).

This chapter is organized as follows. In Section VII A we introduce 2CDMM and discuss its general properties. In Section VII B we discuss solutions to the BEQs and relic abundance. In Section VII B 2 we show allowed parameter space after imposing various experimental constraints.

Results presented in this chapter is a collaboration with S. Bhattacharya, B. Grzadkowski and J. Wudka, published in [32] and [33].

A. Minimal Scalar + Fermion DM model

We would like to ensure stability of DM candidates φ and ν, therefore we will assume that the dark sector is invariant under some global symmetry group $\mathcal{G}$. All dark sector fields would transform non-trivially under $\mathcal{G}$, while SM particles are $\mathcal{G}$-singlets. For the minimal realization we choose $\mathcal{G} = \mathbb{Z}_2 \times \mathbb{Z}_2'$. As mentioned previously, we assume that the dark sector is composed of two Majorana fermions, ν_h and ν, and one real scalar φ. We choose the following transformation properties under $\mathcal{G}$:

$$\nu_h \sim [-,+] \quad \nu \sim [+,-] \quad \varphi \sim [-,-]. \tag{147}$$

The Lagrangian density for the scalar sector of our theory is given by:

$$\mathcal{L}_{\text{scal}} = \frac{1}{2}\partial_\mu\varphi\partial^\mu\varphi + D_\mu H^\dagger D^\mu H - V(H,\varphi)\,, \tag{148}$$

where the most general, gauge-symmetric, $\mathcal{G}$-symmetric, renormalizable potential is:

$$V(H,\varphi) = -\mu_H^2 H^\dagger H + \lambda_H (H^\dagger H)^2 + \frac{1}{2}\mu_\varphi^2\varphi^2 + \frac{1}{4!}\lambda_\varphi\left(\varphi^2\right)^2 + \lambda_x H^\dagger H\varphi^2\,, \tag{149}$$

where H is the SM $SU(2)$ Higgs isodoublet. The reader might recall, that the same potential appeared previously in Chapter IV for the special case of the O(N) model with $N = 1$.

As before, we require that the potential breaks spontaneously the electroweak symmetry via non-zero vacuum expectation value of the Higgs doublet

$$\langle H\rangle = (0, v/\sqrt{2}), \quad v = 246 \text{ GeV}. \tag{150}$$

We also require the $\mathcal{G}$ symmetry to remain unbroken. All the theoretical constraints from the O(N) model case, for $N = 1$, apply also here. In particular, we should disallow for spontaneous symmetry breaking (SSB) in the direction of the singlet field, to satisfy $\langle\varphi\rangle = 0$. This has been discussed thoroughly in Section IV B. In this chapter we will impose even a slightly stronger constraint than shown in Section IV B, namely we take $\mu_0^2 > 0$, which forbids existence of minima with $\langle\varphi\rangle \neq 0$ and $\langle H\rangle = 0$.

After SSB, the mass of the Higgs boson (well known from the SM) is

$$m_H{}^2 = -\mu_H^2 + 3\lambda_H v^2 = 2\mu_H^2, \tag{151}$$

while for the singlet scalar we have

$$m_\varphi^2 = \mu_\varphi^2 + \lambda_x v^2. \tag{152}$$

The fermionic part of the DM Lagrangian reads

$$\mathcal{L} = \frac{1}{2}\overline{\nu_h}\, i\partial\!\!\!/\, \nu_h + \frac{1}{2}\overline{\nu}\, i\partial\!\!\!/\, \nu - \frac{1}{2}\nu_h^T C\nu_h M_h - \frac{1}{2}\nu^T C\nu m_\nu + g_\nu\varphi\,\overline{\nu_h}\nu. \tag{153}$$

We would like to draw the reader's special attention to the interactions in 2CDMM, therefore we separate the relevant part of the Lagrangian, $\mathcal{L}_{\text{int}}$. The interaction between the SM and DM, together with the DM self-interaction is generated by just 3 terms:

$$\mathcal{L}_{\text{int}} = -\lambda_x H^\dagger H\varphi^2 - \frac{1}{4}\lambda_\varphi\varphi^4 + g_\nu\varphi\,\overline{\nu_h}\nu, \tag{154}$$

however, the φ quartic self-interaction term is not relevant in the context of DM relic density and direct detection limits evaluation. In general this model can describe even a 3 component DM sector, if masses of particles are appropriate and the decay of the heaviest dark sector particle is forbidden. However, in this thesis we would like to concentrate on a 2-component model and will introduce a constraint

$$M_h > m_\nu + m_\varphi, \tag{155}$$

which allows for the fast decay of the heavier neutrino, $\nu_h \to \varphi\nu$. In this case only ν and φ are DM candidates, that account for the relic density Ωh^2 (see Section III B).

We consider this 2-component model a laboratory for studying the interplay between various components of the dark sector. Note, that there is no tree-level annihilation of the fermionic DM into SM particles. Therefore such processes will be neglected in our analysis of the relic density (they would appear at a 1-loop level), we will only include tree level processes $\varphi\varphi \leftrightarrow \mathrm{SM}, \mathrm{SM}$ (see Fig. 16) and $\varphi\varphi \leftrightarrow \nu\nu$ (see Fig. 51).

Note also, that the dark sector of this model has no conserved Noetherian charges, therefore all the corresponding chemical potentials vanish. In general, one could introduce additional Dirac partners of the dark fermions ν_h and ν, however such analysis is beyond the scope of this thesis.

Our model contains 5 free parameters: 3 masses, m_φ, m_ν, M_h, and 2 couplings, λ_x, g_ν. However, we will fix M_h at the smallest value that ensures the fast decay of ν_h, so we will effectively deal with only 4 remaining parameters.

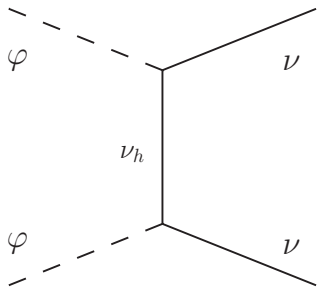

Figure 51: The Feynman diagram for φ annihilation into ν. Other channels of φ annihilation are the same as in the O(N) model, see Fig. 16.

B. BEQ in 2CDMM

An introduction to the BEQ in cosmology and DM relic density evaluation is a part of Section III C 1. The general BEQs describing DM density evolution in case of multi-component DM scenario are presented in Section III C 4. We also show BEQs in the case of 2CDMM; for consistency we repeat those equations:

$$\begin{aligned} f'_\varphi &= \frac{\langle\sigma_{\varphi-SM}|v|\rangle}{K}\left(f_\varphi^2 - \left(f_\varphi^{EQ}\right)^2\right) + \frac{\langle\sigma_{\varphi-\nu}|v|\rangle}{K} f_\varphi^2 - \frac{\langle\sigma_{\nu-\varphi}|v|\rangle}{K} f_\nu^2 \\ f'_\nu &= \frac{\langle\sigma_{\nu-\varphi}|v|\rangle}{K} f_\nu^2 - \frac{\langle\sigma_{\varphi-\nu}|v|\rangle}{K} f_\varphi^2 \end{aligned} \tag{156}$$

where f_X is the number density of species X normalized by temperature cubed, $f_X = n_X/T^3$ and $X = \varphi, \nu$; f_X^{EQ} is the corresponding equilibrium density. The thermally averaged cross sections $\langle\sigma_{\varphi-SM}|v|\rangle$, $\langle\sigma_{\varphi-\nu}|v|\rangle$ and $\langle\sigma_{\nu-\varphi}|v|\rangle$ are given in Appendix B 4. We ignore loop corrections. The coefficient K is generally a function of temperature, $K = K(T)$ and was defined in equation (19).

The interactions between φ and ν involve an exchange of a virtual heavy neutrino ν_h, see Fig. 51; if the corresponding mass M_h is very large, the cross section $\langle\sigma_{\varphi\varphi\to\nu\nu}|v|\rangle$ is strongly suppressed, which leads to an overabundance of ν. For a remedy we will assume M_h is as small as allowed by the requirement of ν_h being unstable. Therefore, we adopt $M_h = m_\varphi + m_\nu + \Delta M_\nu$, with fixed $\Delta M_\nu = 10$ GeV.

The initial conditions are fixed at large temperature $T_{\rm ini} = \max(m_\varphi, m_\nu)$; we assume that the couplings λ_x and g_ν are large enough so that at $T_{\rm ini}$ both DM components are in equilibrium with the SM species and they decouple at nonrelativistic temperatures, hence constitute for CDM candidates. In the following, we will solve the BEQs (156) and determine present DM abundance. The solutions can be classified according to the mass hierarchy in the dark sector:

Case A: $m_\nu > m_\varphi$

Case B: $m_\nu < m_\varphi$

Generally, the dynamics of the DM number density evolution can be very different for these two cases. Those differences emerge mostly because of the behaviour of the thermally averaged cross sections, as illustrated in Fig. 52.

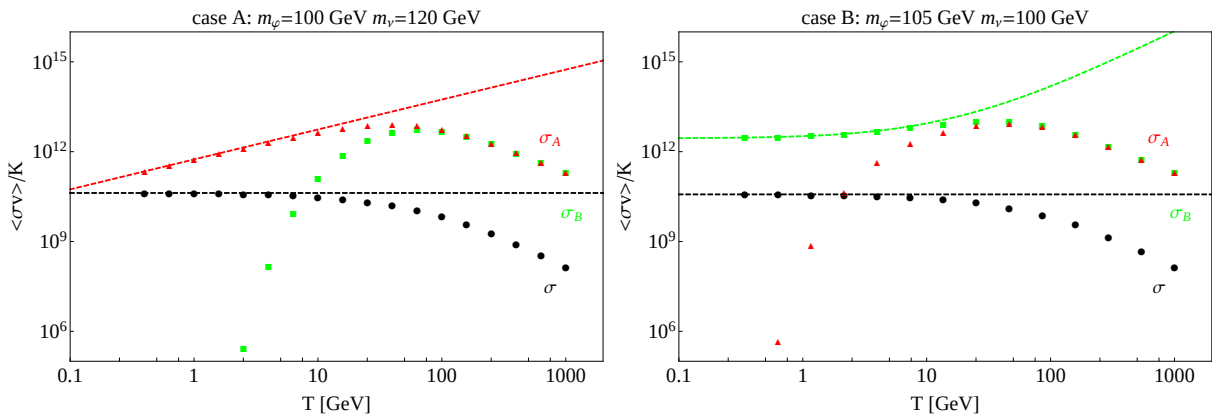

Figure 52: Thermally averaged cross sections $\sigma \equiv \langle \sigma_{\varphi\varphi \to SM\,SM} |v| \rangle / K$ (black points); $\sigma_B \equiv \langle \sigma_{\varphi\varphi \to \nu\nu} |v| \rangle / K$ (green points); $\sigma_A \equiv \langle \sigma_{\nu\nu \to \varphi\varphi} |v| \rangle / K$ (red points), as a function of T for $\lambda_x = .1$ and $g_\nu = 2.5$. In the left panel: $m_\varphi = 100$ GeV, $m_\nu = 120$ GeV (case A); in the right panel: $m_\varphi = 120$ GeV, $m_\nu = 100$ GeV (case B).

If $m_\nu > m_\varphi$ **(Case A.)**, below a certain temperature T_{an}, the scalars φ do not have enough energy to create a pair of heavier neutrinos ν, which in the language of cross sections means that $\langle \sigma_{\varphi\varphi \to \nu\nu} |v| \rangle \to 0$ below T_{an}. At the same time, neutrinos can still annihilate into a pair of scalars φ. This is illustrated in the left panel of Fig. 52 where $\langle \sigma_{\varphi\varphi \to \nu\nu} |v| \rangle / K$ is drops below 10 GeV while $\langle \sigma_{\varphi\varphi \to SM\,SM} |v| \rangle / K$ approaches a constant value at $T \sim 5$ GeV.

However, $\langle \sigma_{\nu\nu \to \varphi\varphi} |v| \rangle / K$ is also vanishing at $T \to 0$. For this cross section, the first term in the temperature expansion (see Appendix B 3) vanishes, as implied by angular momentum and parity conservation. The leading order in the temperature expansion corresponds to the p-wave annihilation [16].

A different behaviour can be observed for $m_\varphi > m_\nu$ **(Case B.)**. In this case it is the cross section for ν annihilation, $\langle \sigma_{\nu\nu \to \varphi\varphi} |v| \rangle / K$, that becomes very small at small temperatures (see right panel of Fig. 52). Other two cross sections contributing to the BEQ, $\langle \sigma_{\varphi\varphi \to SM\,SM} |v| \rangle / K$ and $\langle \sigma_{\varphi\varphi \to \nu\nu} |v| \rangle / K$, approach a constant value for $T \to 0$.

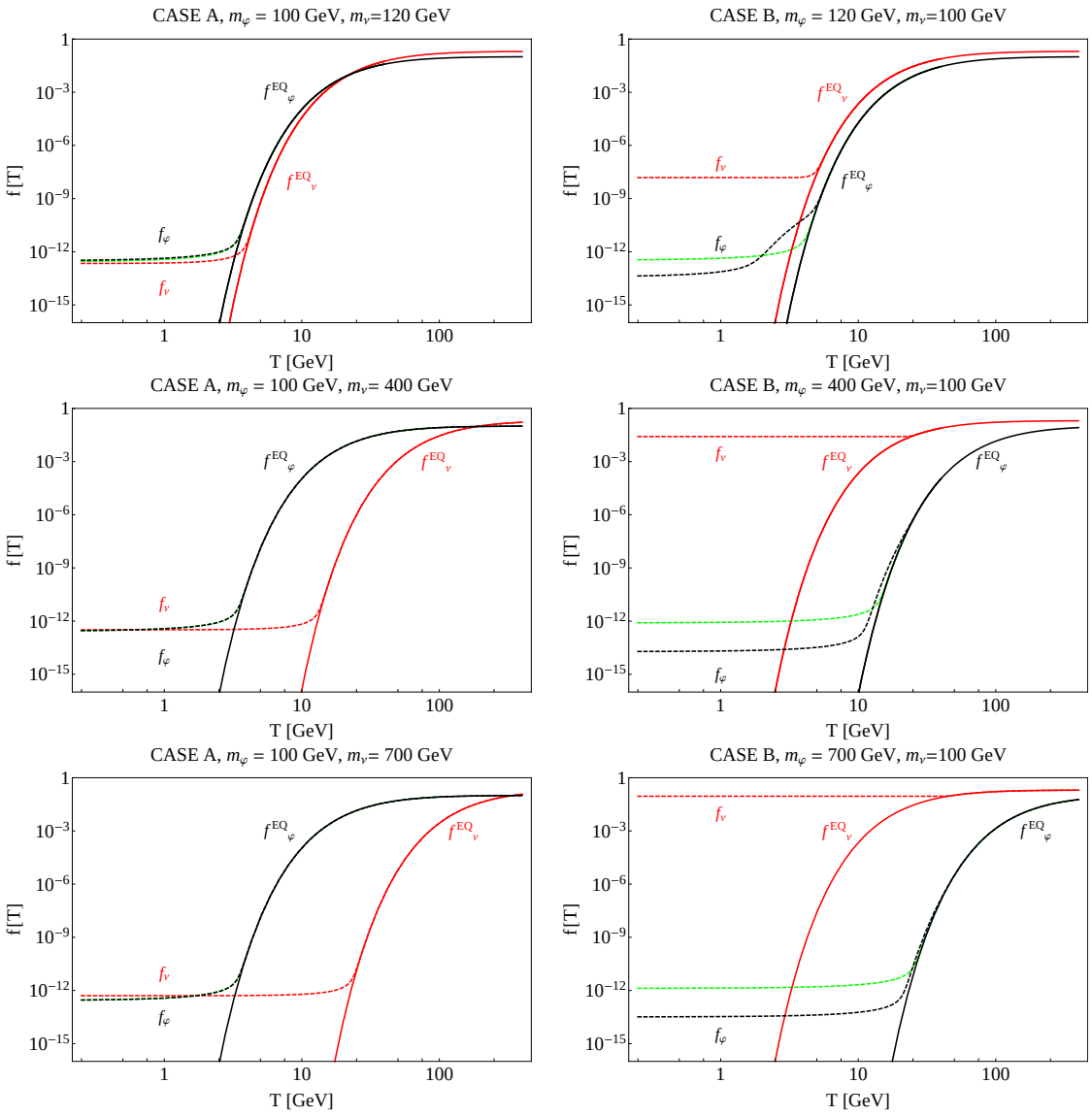

Figure 53: Solutions to the BEQs for the case A (left panels) and case B (right panels) for $\lambda_x = 0.1$ and $g_\nu = 2.5$. Scalar and neutrino DM masses are specified above each panel. Solid black (red) lines correspond to the equilibrium distributions, f_φ^{EQ} (f_ν^{EQ}) for scalars (neutrinos), dashed lines are the corresponding numerical solutions of the BEQs. Green dashed lines show numerical solutions of a single BEQ for scalars without neutrinos present in the theory.

Case A. ($m_\nu > m_\varphi$)

One can rewrite the BEQ for the case A in a simplified form

$$f'_\varphi \;=\; \sigma\left[f_\varphi^2 - f_\varphi^{EQ\,2}\right] + \sigma_A\left[\left(\frac{f_\nu^{EQ}}{f_\varphi^{EQ}}\right)^2 f_\varphi^2 - f_\nu^2\right] \tag{157}$$

$$f'_\nu \;=\; \sigma_A\left[f_\nu^2 - \left(\frac{f_\nu^{EQ}}{f_\varphi^{EQ}}\right)^2 f_\varphi^2\right], \tag{158}$$

where $\sigma \equiv \langle\sigma_{\varphi\varphi\to SM\,SM}v\rangle/K$, $\sigma_A \equiv \langle\sigma_{\nu\nu\to\varphi\varphi}v\rangle/K$. Note, that σ, σ_A have dimensions of $[\mathrm{GeV}]^{-1}$. We solve (158) numerically using LO temperature expansion terms for the cross sections. In case of σ it is a constant term, in case of σ_A, it is the linear term (see [156]). The quality of this approximation is illustrated in the left panel of Fig. 52 and was also verified by comparison of the solutions $f_\varphi(T_{\mathrm{CMB}})$ and $f_\nu(T_{\mathrm{CMB}})$ of BEQs with full temperature dependence of the cross sections to solutions with LO approximations. The relative errors obtained were $\delta_\varphi^A = 2.3\%$ and $\delta_\nu^A = 1.4\%$.

Sample solutions of BEQs for various choices of parameters are given in Fig. 53. For the case A we observe that the dark neutrinos ν (red dashed line) decouple from equilibrium (solid red line) before (i.e. at a higher temperature) the lighter dark scalars φ (black dashed line). Right after the decoupling from equilibrium, neutrinos ν freeze-out. Scalars φ freeze-out a little later. Both particles account for CDM for the chosen parameters and roughly $x_f \sim 20 - 30$. The decoupling temperature of the scalar, T_f^φ, for fixed scalar mass m_φ is insensitive to m_ν, as long as m_ν is significantly larger than m_φ. This can be easily explained – after neutrinos decouple from other species, they do not influence their behaviour significantly any more, but rather evolve independently. This is also visible from the comparison of scalar solutions with the green curve, which corresponds to a single-component DM solution for scalars (without the presence of neutrinos). The influence of neutrinos on the abundance of the scalar DM might seems to be very small, especially if illustrated on a log scale plot with such large y-axis range.

Case A. ($m_\nu > m_\varphi$) - approximate analytical solutions

For a single component CDM case it is easy to find approximate analytical solutions of the BEQs, that allow for an easy evaluation of DM abundance at low temperatures

(see Section III C 2). This approximation is sufficiently accurate in most DM studies. In this subsection we try to derive an analogous approximate solution for our model of two-component DM, for the case A. We follow the procedure presented in Section III C 2 for a single component case.

Let's parametrize the deviation of the normalized number density from equilibrium by $\Delta_\varphi \equiv f_\varphi - f_\varphi^{EQ}$, $\Delta_\nu \equiv f_\nu - f_\nu^{EQ}$. Then we can rewrite the BEQs as:

$$\begin{aligned}\Delta'_\varphi \;=\; & \sigma\Delta_\varphi\left[\Delta_\varphi + 2f_\varphi^{EQ}\right] + \\ & \sigma_A\left[\left(\frac{f_\nu^{EQ}}{f_\varphi^{EQ}}\right)^2\Delta_\varphi(\Delta_\varphi + 2f_\varphi^{EQ}) - \Delta_\nu(\Delta_\nu + 2f_\nu^{EQ})\right] - f_\varphi^{EQ\,\prime} \qquad (159)\end{aligned}$$

$$\Delta'_\nu \;=\; \sigma_A\left[\Delta_\nu(\Delta_\nu + 2f_\nu^{EQ}) - \left(\frac{f_\nu^{EQ}}{f_\varphi^{EQ}}\right)^2\Delta_\varphi(\Delta_\varphi + 2f_\varphi^{EQ})\right] - f_\nu^{EQ\,\prime} \qquad (160)$$

where the primes are temperature derivatives.

In the high, but already non-relativistic temperature region, just before DM decoupling, $f_\varphi(f_\nu)$ tracks $f_\varphi^{EQ}(f_\nu^{EQ})$ very closely and $\Delta_\varphi(\Delta_\nu)$ and $\Delta'_\varphi(\Delta'_\nu)$ are very small. One can neglect $\Delta'_\varphi(\Delta'_\nu)$. From equation (17) we have

$$(f_\nu^{EQ}/f_\varphi^{EQ})^2 \propto e^{-2(m_\nu - m_\varphi)/T}, \qquad (161)$$

therefore $f_\nu^{EQ}/f_\varphi^{EQ}$ terms can be neglected as well.

$$\Delta_\varphi(T) \;\simeq\; \frac{1}{\sigma(\Delta_\varphi + 2f_\varphi^{EQ})}\left(f_\varphi^{EQ\prime} + f_\nu^{EQ\prime}\right) \qquad (162)$$

$$\Delta_\nu(T) \;\simeq\; \frac{f_\nu^{EQ\prime}}{\sigma_A(\Delta_\nu + 2f_\nu^{EQ})} \qquad (163)$$

We define the decoupling temperature for scalars (T_f^φ) and neutrinos (T_f^ν) to be a temperature at which $\Delta_\varphi(T_f^\varphi) = c_\varphi f_\varphi^{EQ}(T_f^\varphi)$ and $\Delta_\nu(T_f^\nu) = c_\nu f_\nu^{EQ}(T_f^\nu)$ with $c_{\varphi,\nu} = O(1)$. We will later assume $c_\varphi(c_\varphi + 2) = c_\nu(c_\nu + 2) = 1$, as this is an optimal choice of c_φ, c_ν accommodating agreement with numerical solutions (and also simplifying analytical expressions). The freeze-out temperatures T_f^φ and T_f^ν can be computed from

$$f_\varphi^{EQ}(T_f^\varphi) \;\simeq\; \frac{1}{c_\varphi(2+c_\varphi)\sigma}\left[\frac{m_\varphi}{T_f^{\varphi 2}} + \frac{f_\nu^{EQ}(T_f^\varphi)}{f_\varphi^{EQ}(T_f^\varphi)}\frac{m_\nu}{T_f^{\varphi 2}}\right] \simeq \frac{m_\varphi}{\sigma T_f^{\varphi 2}}, \qquad (164)$$

$$f_\nu^{EQ}(T_f^\nu) \;\simeq\; \frac{m_\nu}{\sigma_A(T_f^\nu)T_f^{\nu 2}}, \qquad (165)$$

where we have substituted $c_{\nu,\varphi} = \sqrt{2} - 1$. If freeze-out temperatures are known $T_f^{\varphi,\nu}$ from (164 - 165), one can also evaluate $\Delta_\varphi(T_f^\varphi)$ and $\Delta_\nu(T_f^\nu)$ from eqs. (162-163).

After freeze-out number densities remain much larger than their equilibrium counterparts, so that one can approximate $\Delta_{\nu,\varphi} \simeq f_{\nu,\varphi}$ and neglect all terms containing $f_{\varphi,\nu}^{EQ}$ and $f_{\varphi,\nu}^{EQ\prime}$, as well as all terms proportional to $(f_\nu^{EQ}/f_\varphi^{EQ})^2 \propto\ e^{-2(m_\nu - m_\varphi)/T}$. We find that (160) simplifies to $\Delta_\nu' = \sigma_A \Delta_\nu^2$, with the following solutions

$$\begin{aligned} \Delta_\nu(T) = \frac{\Delta_\nu(T_f^\nu)}{1 - \Delta_\nu(T_f^\nu)\int_{T_f^\nu}^T \sigma_A(T')dT'} \quad \Rightarrow \\ \Delta_\nu(T_{\rm CMB}) \simeq \frac{\Delta_\nu(T_f^\nu)}{1 + \sigma_A(T_f^\nu)T_f^\nu\Delta_\nu(T_f^\nu)/2}, \end{aligned} \tag{166}$$

where we assumed $\sigma_A \propto T$, as discussed above and illustrated in Fig. 52. However, from (165) we see that $\sigma_A(T_f^\nu)T_f^\nu\Delta_\nu(T_f^\nu) > 1$ therefore we can write

$$f_\nu(T_{CMB}) \simeq \Delta_\nu(T_{\rm CMB}) \simeq \frac{2}{\sigma_A(T_f^\nu)T_f^\nu} \tag{167}$$

After the freeze-out of ν, the evolution of f_φ can be described by the following differential equation, together with corresponding initial condition,

$$\Delta_\varphi' \simeq \sigma\Delta_\varphi^2 - \sigma_A\Delta_\nu^2, \quad \Delta_\varphi(T_f^\varphi) \simeq c_\varphi m_\varphi/(\sigma {T_f^\varphi}^2), \tag{168}$$

as derived from (164). To solve (168) we first approximate Δ_ν by its value at $T_{\rm CMB}$ and σ_A by its value at T_f^ν. Then, the solution is easy to find, namely

$$\Delta_\varphi(T) = \frac{r_f}{\sigma T_f^\varphi}\frac{u + \tanh[r_f(1 - T/T_f^\varphi)]}{1 + u\tanh[r_f(1 - T/T_f^\varphi)]}; \quad r_f = 2\,\frac{T_f^\varphi}{T_f^\nu}\sqrt{\frac{\sigma}{\sigma_A(T_f^\varphi)}},\ u = \frac{c_\varphi m_\varphi}{r_f T_f^\varphi} \tag{169}$$

Note, that

$$r_f \propto 2\frac{m_\varphi}{m_\nu}\sqrt{\frac{\sigma}{\sigma_A(T_f^\nu)}}, \tag{170}$$

therefore in the case A for $m_\varphi \gg m_\nu$ one can expand (169) around $r_f = 0$ and in the LO we find a single-component DM solution

$$f_\varphi(T) \simeq \Delta_\varphi(T) \simeq \Delta_\varphi(T_{\rm CMB}) \simeq \frac{1}{\sigma T_f^\varphi}\,. \tag{171}$$

This result is also consistent with the illustration in Fig. 53. Note, that the green curve is barely visible for a larger mass splitting between the neutrino and scalar DM, and a small (at a log scale) difference appears for a splitting of 20 GeV,

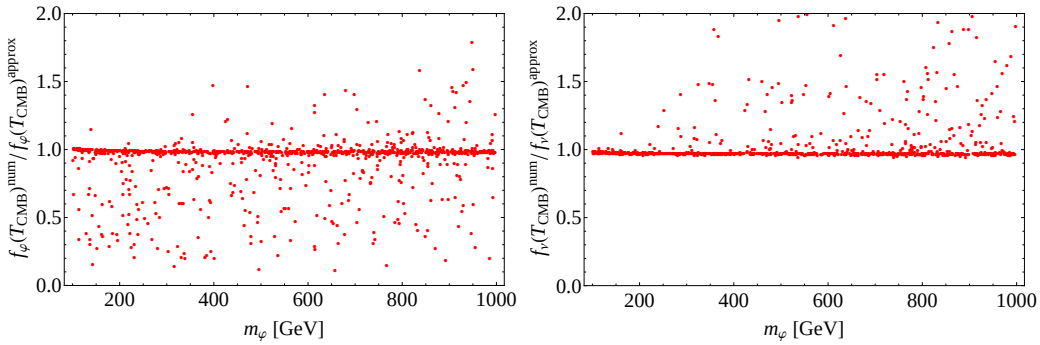

Figure 54: The ratio $f_X(T_{\rm CMB})^{\rm num}/f_X(T_{\rm CMB})^{\rm approx}$ for the case A for scalars (left panel) and neutrinos (right panel) as a function of scalar DM mass. 500 parameter points $(m_\varphi, m_\nu, \lambda_x, g_\nu)$ were chosen randomly within the ranges 10 GeV $< m_\varphi, m_\nu <$ 1 TeV, $0.001 < \lambda_x < 4\pi$ and $0.1 < g_\nu < 4\pi$.

The accuracy of the above results should be checked. We calculate the ratio of $f_X^{\rm num}$ (the numerical solution) over $f_X^{\rm approx}$ (the corresponding analytical approximate solution) at $T = T_{\rm CMB}$. The results are presented in Fig. 54. Approximations are often satisfactory and generally more accurate for large mass splitting between the φ and ν masses (which is understandable, as we are neglecting terms containing $(f_\nu^{EQ}/f_\varphi^{EQ})^2 \propto e^{-2(m_\nu - m_\varphi)/T}$). The quality of this approximation seems to be independent of the couplings (within the scanning ranges) for both f_φ and f_ν.

Case B. $m_\varphi > m_\nu$

For the case B., $m_\varphi > m_\nu$, we also start with equilibrium at relatively high temperatures. When the Universe cools down and DM particles become non-relativistic, neutrinos would no longer have enough energy to produce pairs of heavier scalars through annihilation $\nu\nu \to \varphi\varphi$. This reasoning explains $\langle\sigma_{\nu\nu\to\varphi\varphi}|v|\rangle \to 0$ as $T \to 0$, see the right panel of Fig. 52. However, for $T \to 0$, the rate of ν-pair creation from the singlet scalars is non-zero, (a non-zero limit of $\langle\sigma_{\varphi\varphi\to\nu\nu}|v|\rangle$ as $T \to 0$).

We consider this case as a particularly good illustration of unexpected implications of many DM components and their interactions upon DM density. This will be explained in details in the following.

We recall the BEQ, this time in a simplified form special for the case B,

$$f'_\varphi \;=\; \sigma\left[f_\varphi^2 - f_\varphi^{EQ2}\right] + \sigma_B\left[f_\varphi^2 - \left(\frac{f_\varphi^{EQ}}{f_\nu^{EQ}}\right)^2 f_\nu^2\right], \tag{172}$$

$$f'_\nu \;=\; \sigma_B\left[\left(\frac{f_\varphi^{EQ}}{f_\nu^{EQ}}\right)^2 f_\nu^2 - f_\varphi^2\right], \tag{173}$$

where we approximate the cross section σ^B up to the NNLO terms, namely $\sigma_B \equiv \sigma_0^B + \sigma_1^B T + \sigma_2^B T^2$, see Fig. 52 for illustration. As it is shown in the right panel of Fig. 52, for low temperatures σ is well approximated by a constant. We have estimated the quality of this approximation by comparing the exact numerical integration of the BEQ's with the one obtained with quadratic expansion of σ_B, for a number of points within the ranges of parameters of our interest. This resulted in the errors for $f_\varphi(T_{\rm CMB})$ and $f_\nu(T_{\rm CMB})$ to be $\delta_\varphi^B = 6.3\%$, $\delta_\nu^B = 2.6\%$, respectively.

Numerical solutions of equations (172,173) are shown in the right panel of Fig. 53. For those plots neutrino mass was fixed at $m_\nu = 100$ GeV and we have chosen 3 scalar masses: $m_\varphi = 120, 400$ and 700 GeV (analogously to case A sample choices). An interesting observation is that for this choice of parameters (also $\lambda_x = 0.1$, $g_\nu = 2.5$), ν and φ decouple roughly simultaneously. We have verified this observation numerically with a larger sample [7].

Since the decoupling temperatures of both species are rather the same $T_f^\nu \simeq T_f^\varphi$, and neutrinos are lighter which implies $f_\varphi^{EQ} < f_\nu^{EQ}$ for $m_\nu < m_\varphi$, the asymptotic low-temperature normalized number density $f(T)$ will be larger for neutrinos, $f_\varphi(T_{\rm CMB}) < f_\nu(T_{\rm CMB})$. What we observe studying larger samples of parameter space, is that in case B it is typical for the neutrinos to dominate DM density at low temperatures. It can be also understood intuitively, in a very simple manner. Neutrinos are weakly connected to the SM particles, therefore it is more difficult for them to annihilate at a sufficient rate and therefore they are often overabundant.

Contrary to naive expectation, there is a very strong dependency on m_φ of the T_f^ν freeze out temperature for the neutrino (for fixed m_ν), see right panel of Fig. 53. It varies from $T_f^\nu \simeq 4$ GeV for $m_\varphi = 120$ GeV to $T_f^\nu \simeq 30$ GeV for $m_\varphi = 700$ GeV. However, in this case

[7] Neutrinos would decouple earlier if the Yukawa coupling was small, $g_\nu \sim 0.1$, but this case is not consistent with the DM relic abundance experimental bounds. WMAP/Planck requires Yukawa couplings at least $g_\nu \gtrsim 1.8$.

x_f does not fall into the expected $20-30$ interval. For $m_\varphi = 700$ GeV and $m_\nu = 100$ GeV we have found $x_\varphi^f \simeq 23$ and $x_\nu^f \simeq 3$ (which is however still in the CDM regime). Also it implies a rapid grow of low-temperature f_ν with m_φ (at fixed m_ν): $f_\nu(T_{\rm CMB}) \sim 10^{-8}$ at $m_\varphi = 120$ GeV, to $f_\nu(T_{\rm CMB}) \sim 10^{-1}$ at $m_\varphi = 700$ GeV.

This case illustrates the possible dramatic influence of other DM components and their mutual interactions upon the dynamics of the evolution of energy density. Also, to illustrate influences of the neutrinos on the evolution of scalars after the decoupling from equilibrium, we show in the right panels of Fig.53 the numerical solutions of a single BEQ for scalars without neutrinos present in the theory (green dashed lines). For some sample parameters, the differences are as large as almost 2 orders of magnitude.

Another interesting effect is visible in the first panel on the right in Fig. 53. The scalars φ, after they decouple from the equilibrium, do not freeze-out immediately, which was a standard behaviour in case A, or in single component DM scenario. When f_φ deviates from equilibrium, it is still temperature dependent and freezes out later in time. This is easily understandable - even below the decoupling temperature, φ pairs can still annihilate producing ν pairs. After the ν decouple, we have $f_\nu \gg f_\nu^{EQ}$ and the BEQ for scalars, equation (172) becomes

$$f'_\varphi = (\sigma + \sigma_B)\left(f_\varphi^2 - h_\varphi^2\right) , \quad h_\varphi^2 = f_\varphi^{EQ\,2}\left[\frac{\sigma}{\sigma+\sigma_B} + \left(\frac{f_\nu}{f_\nu^{EQ}}\right)^2 \frac{\sigma_B}{\sigma+\sigma_B}\right] \tag{174}$$

We interpret this effect in terms of the BEQ as follows: after the decoupling of dark neutrinos, scalars φ approach a modified "equilibrium" distribution h_φ, which is also shown in Fig. 55 (blue dashed curve). We show in Fig. 53 and Fig. 55 how with decreasing temperature, the normalized number density f_φ eventually also decouples from the "decoupled distribution" h_φ and then freezes-out. It is not possible to observe such effect in a single-component system, it is a new feature of multi-component and self-interacting DM scenarios.

Also in case B large mass splitting results in very large neutrino low-temperature density, while $f_\varphi(T_{\rm CMB})$ remains small, $f_\varphi(T_{\rm CMB}) \sim 10^{-12} - 10^{-13}$. It follows that when imposing the WMAP/Planck upper limit on Ωh^2, small mass splitting are favourable.

We have also tried to find good approximate analytical solutions of the BEQs in case B. Unfortunately, the accuracy of the best approximations we have obtained was not sufficient, mostly because as a result some special features of this model.

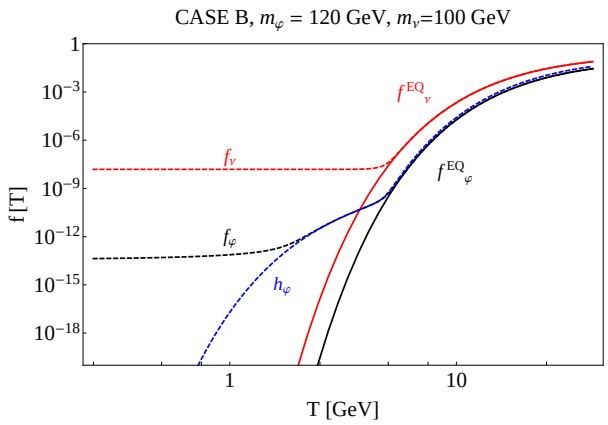

Figure 55: Solution of the BEQs, case B ($m_\varphi = 120$ GeV, $m_\nu = 100$ GeV); for $\lambda_x = 0.1$, $g_\nu = 2.5$. Solid black (red) line illustrates equilibrium distributions, f_φ^{EQ} (f_ν^{EQ}) for scalars (neutrinos), dashed lines are the corresponding numerical solutions of the BEQs. Blue dashed line shows the distribution h_φ from (174).

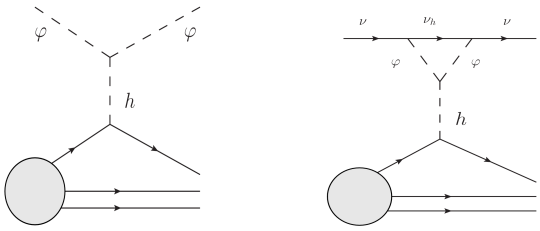

Figure 56: The Feynman diagram for the elastic scattering of DM (φ and ν) off a nucleon.

1. Relic Density in 2CDMM

The total DM energy density in 2CDMM is

$$\Omega_{tot} = \Omega_\nu + \Omega_\varphi = \frac{m_\nu f_\nu + m_\varphi f_\varphi}{\rho_{crit}} T_\gamma^3. \tag{175}$$

Constraints in 2CDMM presented in the following section were evaluated using 3σ WMAP limits [157], namely

$$\Omega_{DM}^{(\mathrm{WMAP})} h^2 = 0.1138 \pm (3 \times 0.0045) \tag{176}$$

The 2013 update from the Planck collaboration (20), taken with 3σ lies inside the 3σ WMAP bound imposed.

2. Direct Detection in 2CDMM

Both fermionic and scalar DM components can scatter elastically off the nucleon N, see Fig. 56. Even though the LO contribution to the scattering of the neutrino ν is a one-loop contribution, it can be significantly strong and will be included in our analysis. The cross section for φ-p scattering has been already shown in discussion of the O(N) model, see Section 104, case $N = 1$. The ν-N scattering cross section is given in Appendix C 1.

In 2CDMM $f_n/f_p \simeq 1$, therefore there are no isospin-violating effects. However, one has to remember that if two DM components are present, a comparison of the elastic scattering cross section for DM-N with experimental limits cannot be done straightway.

The standard limits on DM direct detection assume all DM particles have the same mass and are interacting with the SM at the same rate. In our case, this is not true. The two components might have very different masses, couple differently to a nucleus, and also have different number densities. As the first step in comparing the cross sections in a two-component case with the standard experimental data, we rescale the DM-p cross section of each species by a factor of relative density fraction,

$$\sigma^{\varphi}_{\mathrm{DM-p}} = \frac{n_\varphi}{n_\varphi + n_\nu}\sigma_{\varphi-p}, \qquad \sigma^{\nu}_{\mathrm{DM-p}} = \frac{n_\nu}{n_\varphi + n_\nu}\sigma_{\nu-p}. \tag{177}$$

In general, all the astrophysical assumptions required for translating the experimental results into bounds on $\sigma_{DM-p}(m_{DM})$ should be revisited in a two-component case. However, we will simplify our analysis as much as possible. We will assume that both DM components have the same density profiles and the ratio of abundances of each species is the same at cosmic as well as the galactic scale.

Then, if the masses of both DM species are degenerate, $m_\varphi \simeq m_\nu \simeq m_{DM}$, one should average the scattering rate of DM over the number densities and impose the $\sigma^{(exp)}_{DM-p}(m_{DM})$ bound on such averaged cross section.

If one of the DM components is significantly dominating the total DM number density, we should apply the following strategy. If for the species in minority the bound on a rescaled cross section is below the experimental constraint, contribution from this scattering can be neglected and we only consider the dominant component. If even for the particle with small relative abundance the rescaled cross section is above exclusion limits, this parameters are definitely excluded.

For most of the parameter space points we will incorporate limits from experiments for each species separately and see whether the limits are significant. It turns out that in almost all points of interest, we have either two components with degenerate masses or negligible contribution from one of the species.

C. Constraints on the Two Component DM Model

In order to determine allowed 2CDMM parameters, we performed a random scan over the 4D parameter space of our model $(m_\varphi, m_\nu, \lambda_x, g_\nu)$. We have chosen the following ranges for the analysis:

$$\begin{aligned} &1 \text{ GeV} < m_\varphi < 10 \text{ TeV}, \\ &1 \text{ GeV} < m_\nu < 2 \text{ TeV}, \\ &0.001 < \lambda_x < 4\pi, \\ &0.1 < g_\nu < 4\pi. \end{aligned} \tag{178}$$

The points that satisfy (176) limit are shown in Fig. 57, in the (λ_x, g_ν) plane. We impose all theoretical constraints on 2CDMM. We also impose the bound on DM relic density as in (176). Our results are illustrated on a series of plots shown in this Section, Fig. 57 – Fig. 66.

In Fig. 57 we show results of the scan over the parameter space, after imposing all theoretical constraints and Ωh^2 limit (176), projected into the (λ_x, g_ν) plane. Three panels correspond to 3 various ranges of the scalar mass, and the colouring is due to m_ν. From this figure we see no points that satisfy (176) for small g_ν (we have $g_\nu > 0.92$). To understand this large g_ν requirement, we first illustrate in Fig. 58 rapid growth of the DM neutrino relic abundance, as g_ν drops. This growth is a result of a suppressed annihilation rate of ν into scalar pairs. To avoid overabundance of neutrinos, g_ν must be rather large. In case A this reasoning is additionally supported by approximate analytical solution (167). We have $f_\nu(T_{\text{CMB}}) \propto \sigma_A^{-1} \sim g_\nu^{-4}$, therefore a change in one order of magnitude in g_ν implies 4 orders of magnitude change in the abundance of neutrinos! We should expect that the relic abundance fixes roughly the range of magnitude of the g_ν couplings (in case of other models, like the O(N) model, after fitting to the Ωh^2 bound the model still allows for a range of couplings as wide as $10^{-3}, 4\pi$).

Another observation based on Fig. 57 is that the WMAP constraint requires a growing m_φ

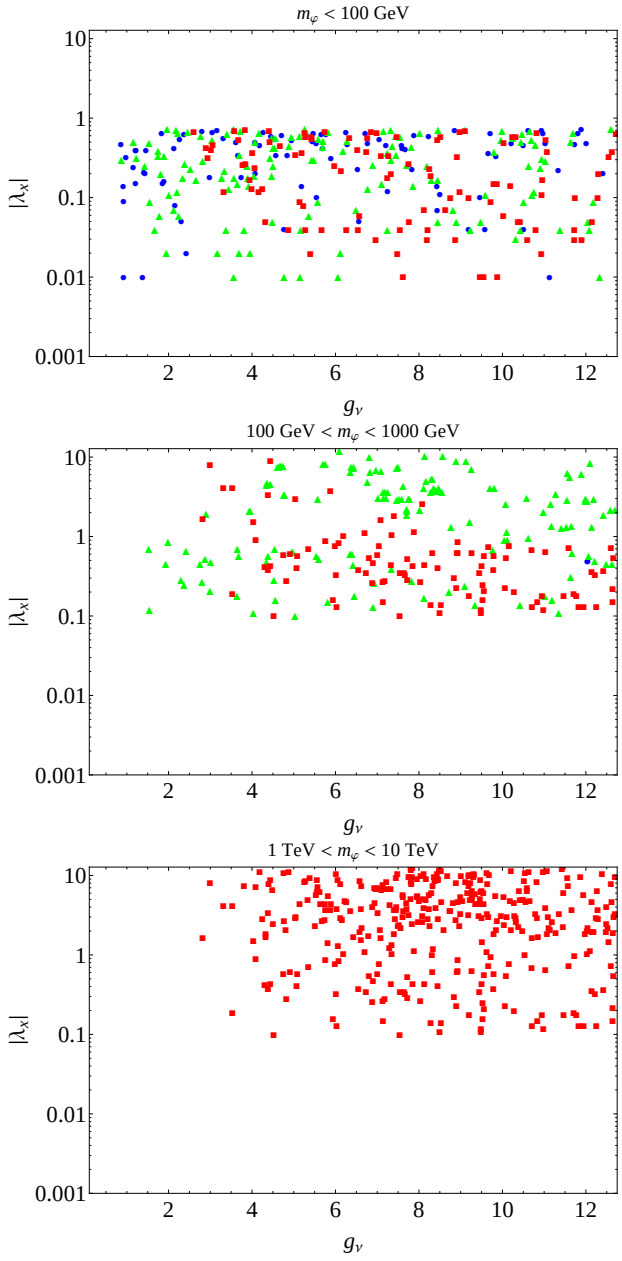

Figure 57: Results of a scan over 2CDMM's parameter space, projected into the (λ_x, g_ν) plane. Ωh^2 3σ limit (176) is imposed. Blue (circles): $m_\nu < 100$ GeV, green (triangles): 100 GeV $< m_\nu <$ 1 TeV red (squares): 1 TeV $< m_\nu <$ 2 TeV. Scalar DM mass ranges are indicated above each panel.

to be correlated with growing $|\lambda_x|$ and g_ν. The $|\lambda_x|$ growth is directly caused by the s-channel contribution to the annihilation amplitude, namely $\sim \frac{\lambda_x}{4m_\varphi^2 - m_h^2}$. Also, from (155) we see that M_h will also grow with m_φ, therefore the t-channel amplitude of the ν annihilation would get smaller. To account for this effect and retrieve a proper cross section for ν annihilation,

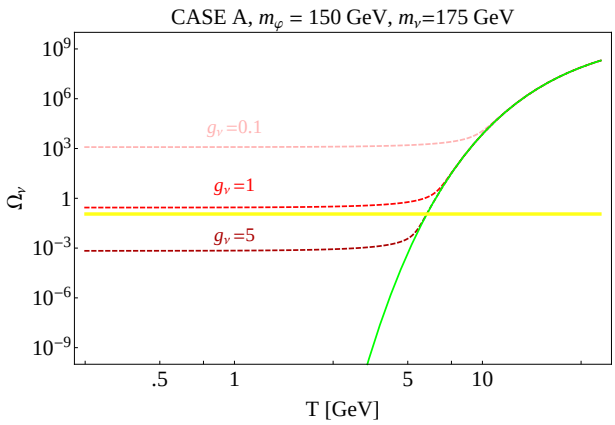

Figure 58: Solutions of the BEQs for $m_\varphi = 150$ GeV, $m_\nu = 175$ GeV (case A), $\lambda_x = 1$. Pink, red, dark red lines correspond to solutions for the neutrino abundance for $g_\nu = 0.1, 1, 5$, respectively. Yellow lines are WMAP 3σ limit on DM abundance. Green line is the equilibrium distribution for neutrinos for m_ν =175 GeV.

the coupling g_ν should get larger.

We would also like to point out, that in the lowest panel of Fig. 57 only red squares survive (only large values of m_ν are allowed for large m_φ). In general, there are very few solutions with the scalar DM mass heavier than the neutrino mass (see case B in Section VII B), and only with a very small mass splitting. The effect of small mass splitting in case B is well illustrated in the last panel of Fig. 59 ($m_\varphi - m_\nu$ projections, see also Fig. 60), see points labelled by dark green squares and are located just below the diagonal line. See also Fig. 61, from which it is clear that in order to reduce f_ν, the dominant low-temperature component of DM, the splitting between m_φ and m_ν must be small. For too large splittings the DM decouples and freezes-out very early ($T_f^\nu \sim O(10)$ GeV), and therefore the neutrinos do not have enough time to disappear into SM particles and are overabundant. When the mass splitting is very small, the neutrino annihilation into scalars (which is followed by scalar annihilation into SM particles) is still sufficiently efficient to account for an acceptable relic abundance. Summarizing, in case B, Ωh^2 bound can be met if and only if both the neutrinos freeze-out relatively late and $m_\nu \simeq m_\varphi$.

Let's try to discuss implications $m_\nu \simeq m_\varphi$ degeneracy more quantitatively. As is illustrated in Fig. 53, if the mass splitting $\Delta m = m_\varphi - m_\nu$ is not too large, then the decoupling from equilibrium occurs in a range of temperatures where the "distance" between distribu-

tions,

$$\Delta f(T) \equiv [\log_{10} f_{\varphi}^{EQ}(T) - \log_{10} f_{\nu}^{EQ}(T)], \tag{179}$$

is approximately T-independent. This distance is mainly a function of Δm. If we alter the coupling constants, it changes the decoupling temperature of both DM particles, but $\Delta f(T)$ remains unaltered. As long as scalars and neutrinos decouple roughly simultaneously, $\Delta f(T_{\rm CMB})$ is then a function of Δm only. Therefore, as long as $m_{\varphi} \simeq m_{\nu}$, the difference between the φ and ν contributions to Ω_{DM} is roughly a function of Δm only,

$$\Delta\Omega = (\log_{10} \Omega_{\varphi} - \log_{10} \Omega_{\nu}). \tag{180}$$

The minimal abundance Ωh^2 found within the results of the numerical scans, for the parameter range specified in (178), is $\Omega \sim 10^{-8}$. Therefore to satisfy the abundance bound, $\Omega h^2 \sim 0.1$, the maximal value of $\Delta\Omega$ should be ~ 7. Then we will do a very rough approximation – with help of Fig. 61 we can estimate that this value of $\Delta\Omega$ corresponds to $\Delta m \lesssim 40$ GeV. And this very rough estimate agrees with our numerical scans, for which we find that (in case B) the maximal allowed splitting between masses of DM components is $\Delta m_{\rm NUM}^{\rm MAX} = 29.8$ GeV.

There are also other properties of 2CDMM, that are well illustrated in Fig. 59. For example we impose theoretical constraints on the positive and negative branch on λ_x, as discussed in Section IV B. As already mentioned, instead of the global minimum constraints from (83) we have chosen a stronger constraints $\mu_0^2 > 0$, corresponding to non-existence of minima with pure singlet VEV. The $\mu_0^2 > 0$ limit can be relaxed, however it would not account for a significant increase in the allowed range of m_{φ}.

The top panel of Fig. 59 or Fig. 60 ((λ_x, m_{φ}) plane) clearly shows the resonance region $m_{\varphi} \simeq m_h/2 \sim 62.5$ GeV. In this m_{φ} range, λ_x should be small to account for the enhancement of the cross section due to the resonant graph with a Higgs boson in the s-channel. If λ_x is not small enough, the resonance yields too large annihilation rate and consequently too small $\vec{\varphi}$ abundance. This resonance effect propagates also to the evaluation of the direct detection cross section, see Fig. 62.

In this analysis we would like to discuss especially XENON 100 and CRESST-II bounds on $\sigma_{\rm DM-N}$, as originally discussed in our paper [32] (which was published before the LUX bounds were known). It should be mentioned that after imposing a 90% C.L. LUX limit

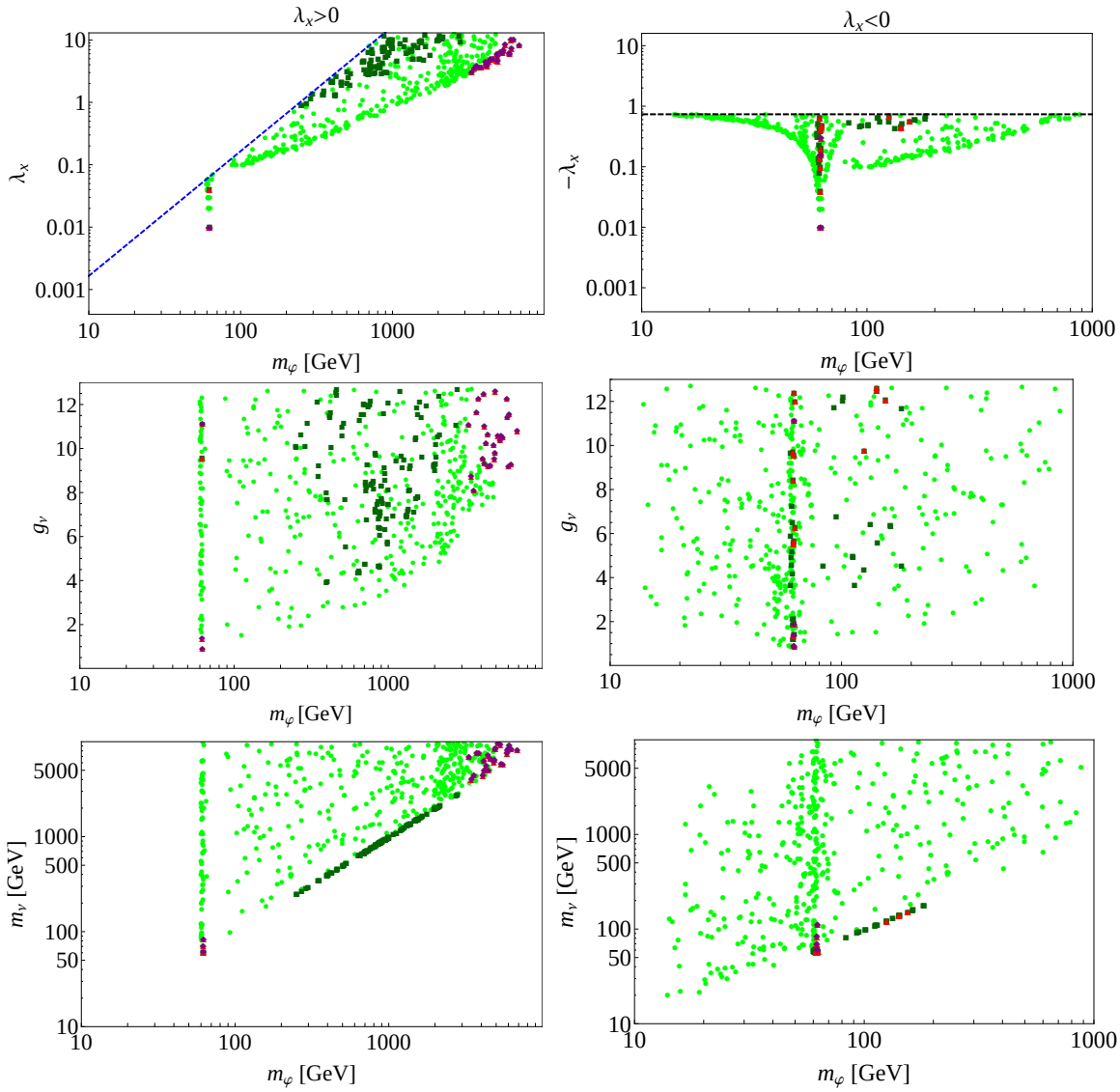

Figure 59: All shown points satisfy theoretical constraints as discussed in Section VII A and WMAP bound (176). Green circles (dark green squares) correspond to case A, $m_\nu > m_\varphi$ (case B, $m_\nu < m_\varphi$). Stability bound and $\mu_0^2 = 0$ line are shown in the top plots, in the right and left panels, respectively. Red triangles and purple diamonds are points for which the XENON100 limit is satisfied, separately for φ and ν, respectively.

on our model, which is approximately one order of magnitude below XENON 100, only the resonance region of the scalar singlet mass remains as a viable solution.

We have included direct detection limits from XENON 100 and and CREST-II in Fig. 59. Points that survive those constraints are marked with red triangles and blue diamonds for XENON and CRESST-II, respectively. We show the bounds on the elastic scattering cross

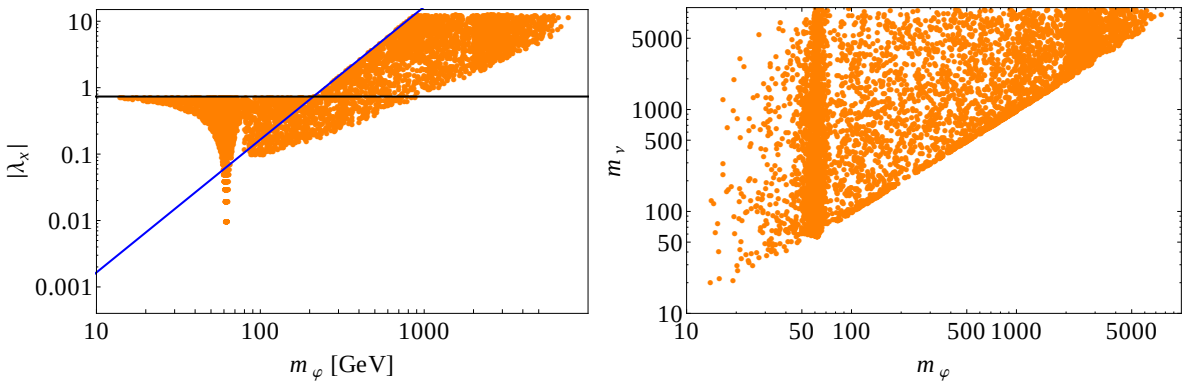

Figure 60: All shown points satisfy theoretical constraints as discussed in Section VII A and WMAP upper bound only (176). On the left panel we show both stability bound (black line) and $\mu_0^2 = 0$ line (blue).

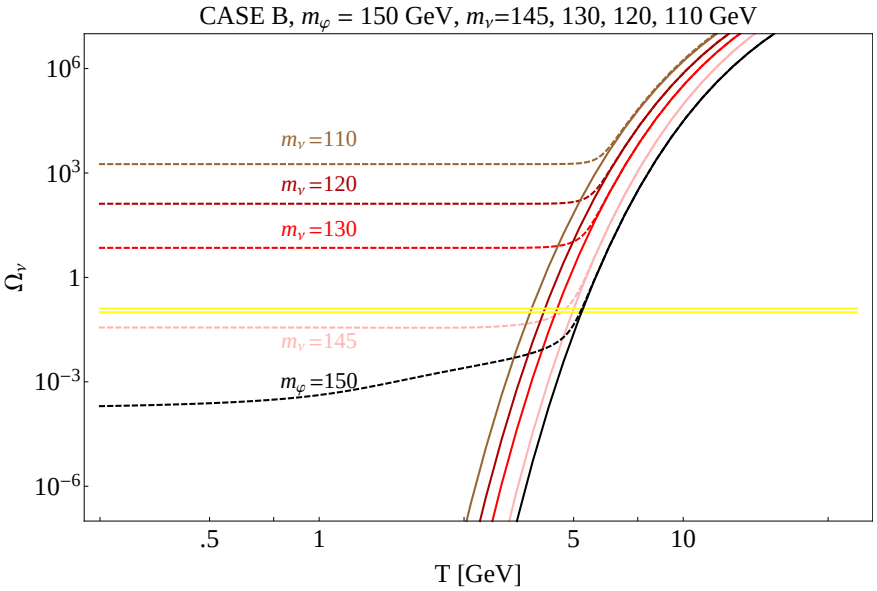

Figure 61: Solutions to the BEQs. Dashed black line is f_φ, solid black line is f_φ^{EQ}. Light red, red, dark red and brown dashed lines correspond to f_ν evaluated for $m_\nu = 145,\ 130,\ 120,\ 110$ GeV, respectively. For the other parameters we choose $m_\varphi = 150$ GeV, $\lambda_x = 1$, $g_\nu = 7.5$. Yellow band corresponds to correct relic abundance.

section directly in Fig. 62. We plot the rescaled cross section $\sigma^\varphi_{\mathrm{DM-N}}$ as a function of m_φ, evaluated for points satisfying 3σ WMAP bounds. We mark cases A and case B points on the left panel, and on the right panel we mark which species is dominant.

It follows from Fig. 62 that there exist three regions of φ mass consistent with XENON100:

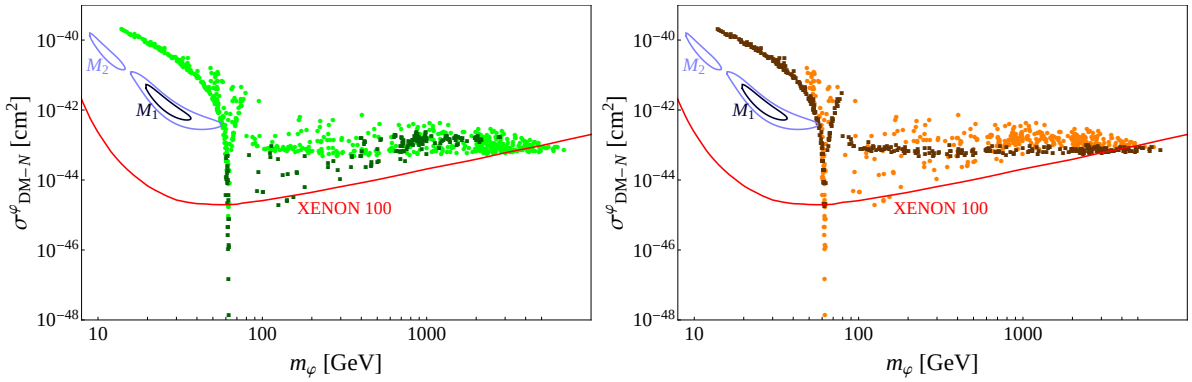

Figure 62: Plot of the cross section σ^{φ}_{DM-N} $(N = p)$ as a function of m_φ for points satisfying the WMAP data within 3σ; the other parameters are randomly chosen in the ranges defined in the text, see (178). Left panel: green circles (dark green squares) correspond to case A (case B) solutions. Right panel: orange circles (dark orange squares) correspond to $\Omega_\varphi < \Omega_\nu$ ($\Omega_\varphi > \Omega_\nu$). The red line shows the XENON 100 90% C.L. bound [158], and the two islands in blue indicate 1 and 2σ CRESST-II results [70].

$m_\varphi \simeq m_h/2$, $m_\varphi \simeq 130 - 140$ GeV and heavy mass region $m_\varphi \gtrsim 3$ TeV. In the *middle mass region* direct detection constraints on $\sigma^{\varphi}_{\mathrm{DM-N}}$ favor case B points ($m_\nu < m_\varphi$). However, for the heavy scalars $m_\varphi \gtrsim 3$ TeV it turns out that $m_\nu > m_\varphi$ (case A) is required. In Fig. 66 we have shown temperature evolution of DM relic abundances Ω for some sample points that satisfy the XENON 100 bound.

The intermediate mass region consistent with XENON100, $m_\varphi \simeq 130 - 140$ GeV requires $\lambda_x < 0$ with large absolute values and $g_\nu \gtrsim 10$ (see Fig. 59). As those points correspond to case B, the neutrino mass is very close to the scalar mass for each point and also there are always more neutrinos in the theory, than scalars (compare with the right panel of Fig. 62). Therefore, for those points, the scattering cross section is suppressed by the percentage of scalar DM in total DM. However, if for those points one requires also that the cross section for the ν-p scattering lies below the xenon bound, those points are excluded. This can be read of Fig. 63. All case B points (dark green squares) in this mass region lie above the XENON 100 bound.

The high scalar mass region consistent with XENON 100 requires large and positive λ_x and also large $g_\nu \gtrsim 8$. Why most of the large mass region, $\gtrsim 200$ GeV is excluded by the

direct detection bound? From (177) we find that

$$\sigma^{\varphi}_{\mathrm{DM-N}} \propto \frac{\lambda_x^2}{m_\varphi^2} \frac{f_\varphi(T_{\mathrm{CMB}})}{f_\varphi(T_{\mathrm{CMB}}) + f_\nu(T_{\mathrm{CMB}})}. \tag{181}$$

Our goal is to minimize the cross section $\sigma^{\varphi}_{\mathrm{DM-N}}$, to fall below the XENON 100 bound. Therefore one should (for a given m_φ) choose as small as possible λ_x and the ratio, $f_\varphi(T_{\mathrm{CMB}})/(f_\varphi(T_{\mathrm{CMB}}) + f_\nu(T_{\mathrm{CMB}}))$. But those factors are not independent. We will first very conservatively estimate the mass m_φ dependence of the coupling λ_x, we choose the lower edge of the allowed (λ_x, m_φ) region from the upper panel of Fig. 59. For 100 GeV $< m_\varphi <$ 1000 GeV we find that

$$\log_{10}(\lambda_{x\,\mathrm{min}}) \simeq \log_{10}\left(\frac{m_\varphi}{1\ \mathrm{GeV}}\right) - 3\,, \tag{182}$$

Then we will take the lower edge of the $f_\varphi(T_{\mathrm{CMB}})/(f_\varphi(T_{\mathrm{CMB}}) + f_\nu(T_{\mathrm{CMB}}))$ region found in Fig. 65. For 100 GeV $< m_\varphi <$ 1000 GeV we have

$$\log_{10}\left[\frac{f_\varphi(T_{\mathrm{CMB}})}{f_\varphi(T_{\mathrm{CMB}}) + f_\nu(T_{\mathrm{CMB}})}\bigg|_{\mathrm{min}}\right] \simeq 0.4 \cdot 10^{-3} \frac{m_\varphi}{1\ \mathrm{GeV}} - 2.4 \tag{183}$$

And after combining equations (181-183) we find that

$$\log_{10}\left[\sigma^{\varphi}_{\mathrm{DM-N}}\big|_{\mathrm{min}}\right] \simeq -43 + 0.4 \cdot 10^{-3} \frac{m_\varphi}{1\ \mathrm{GeV}}. \tag{184}$$

where the constant is such that around $m_\varphi \sim 100$ GeV the scan points are above the XENON100 limit, as shown in Fig. 62. The linearly growing part comes from the m_φ dependence in equation (183), as the mass dependence of $\lambda_{x\,\mathrm{min}}$ and m_φ in (182) and (181) cancel. Note however that the remaining mass dependence is very weak and in fact disappears after saturating (183) around 5 TeV, see Fig. 65.

Since there exist solutions in the resonance region of m_φ we should be aware of the Higgs boson decay branching ratio to $\varphi\varphi$, as those points could have been excluded by measurements of the invisible Higgs-boson width. However, it turns out that for most of those solutions the $BR(h \to \varphi\varphi)$ is typically small, as the coupling λ_x is small and this mass region is agreement with the present invisible decay data [154].

We should also point out, that one can compare the direct detection cross sections predicted within our model, with the positive hints on DM, namely results from CREST-II or CDMS Si, while ignoring the XENON 100 or LUX bounds. This way we have verified that our model could accommodate CREST-II 2σ data, though in that region of $\sigma^{\varphi}_{\mathrm{DM-N}}$, large

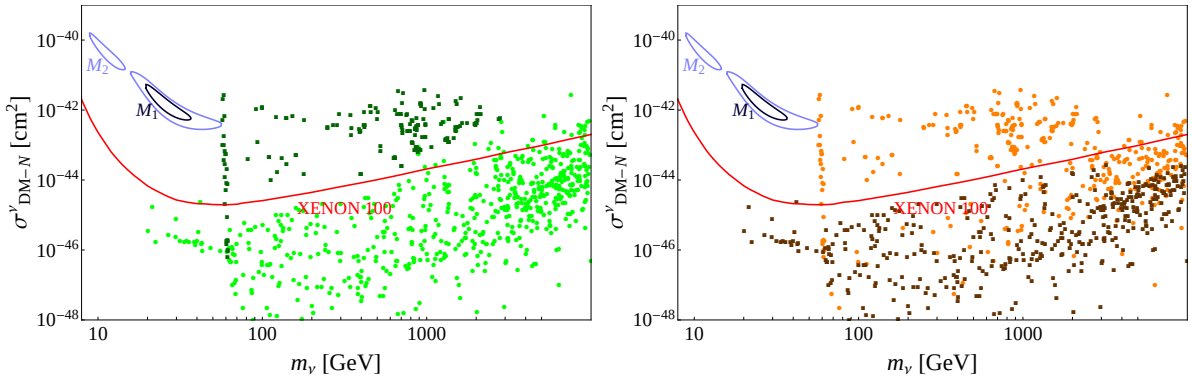

Figure 63: Cross section $\sigma^{\nu}_{\mathrm{DM-N}}$, as a function of m_ν. Ωh^2 within 3σ WMAP limit. Left panel: green circles (dark green squares) correspond to case A (case B) solutions. Right panel: orange circles (dark orange squares) correspond to $\Omega_\varphi < \Omega_\nu$ ($\Omega_\varphi > \Omega_\nu$).The red line shows the XENON100 data, and the two islands in blue indicate 1 and 2σ CRESST-II results.

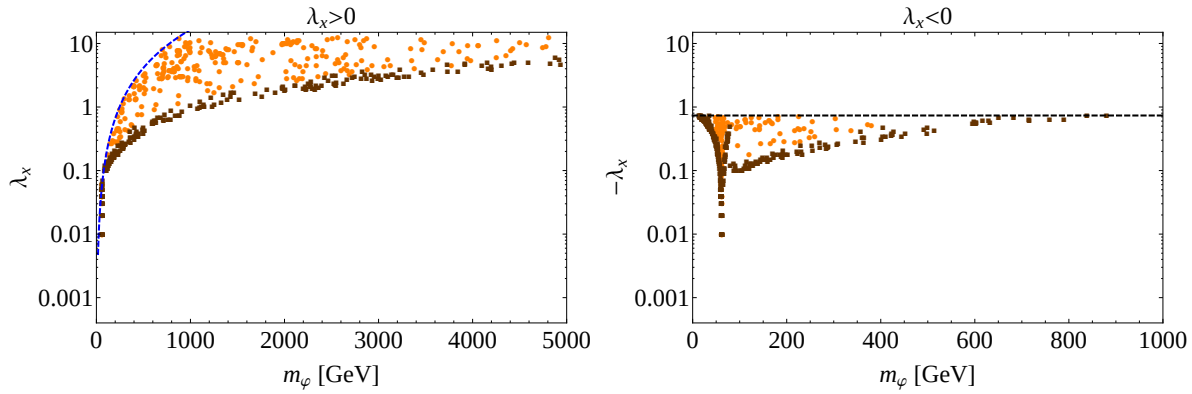

Figure 64: For all points theoretical limits and Ωh^2 within 3σ WMAP limit are satisfied. Orange circles (dark orange squares) correspond to $\Omega_\varphi < \Omega_\nu$ ($\Omega_\varphi > \Omega_\nu$). The blue line corresponds to $\mu_0^2 > 0$ while the black line is the stability bound.

λ_x is necessary; and since $m_\varphi < m_h/2$, the solutions that agree with CREST-II inevitably imply $BR(h \to \varphi\varphi) \sim 1$, which is in conflict with the present LHC data.

However, the CREST-II 2σ region is close to the threshold for $h \to \varphi\varphi$ and a modest (up to $\sim 3\sigma$) extension of the CREST-II region towards the Higgs invisible decay threshold allows us to find acceptable points above the threshold for which $BR(h \to \varphi\varphi) = 0$ (since the decay is kinematically forbidden). We show sample parameter sets for such points in Table XV. Also CDMS Si 3σ region, which is visible on the plots in Fig. 8, overlaps with those

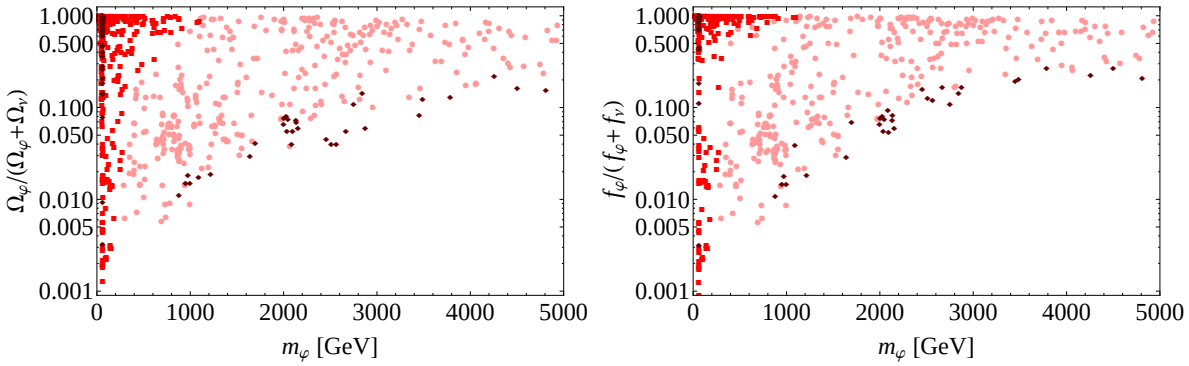

Figure 65: Relative abundance of φ (left panel) and relative number density of φ (right panel) as a function of m_φ for points that satisfy WMAP bound within 3σ. Light red points: $1 < \lambda_x < 10$; red points: $0.1 < \lambda_x < 1$; dark red points: $\lambda_x < 0.1$

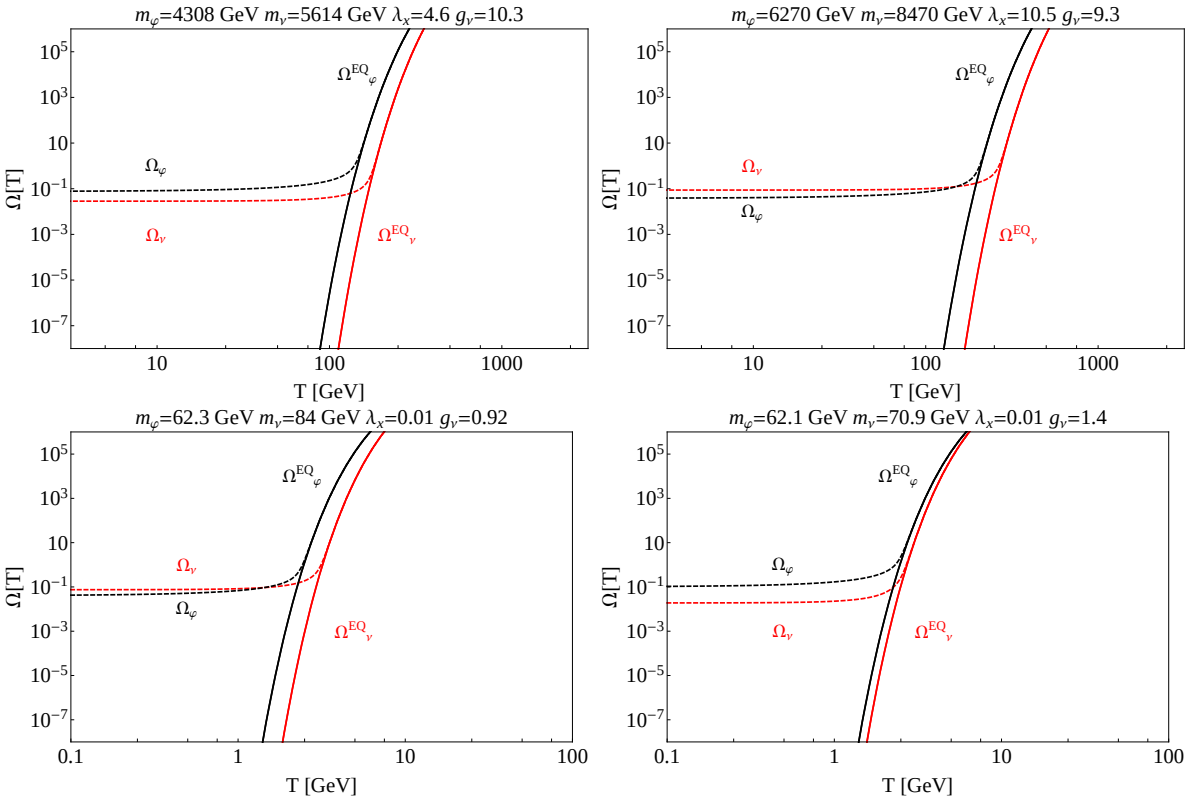

Figure 66: Selected solutions of the Boltzmann equation for parameters that satisfy both WMAP and XENON constraints.

points. One might also notice from Fig. 59 (the middle right panel) that the corresponding Yukawa couplings in the dark sector are $g_\nu \gtrsim 4$, which is not as large, as required by the XENON 100 limit (red triangles) in the resonance region.

m_φ	65.82	66.73	66.94	67.05	67.08
m_ν	776	5373	654	85	4713
λ_x	0.18	0.1	0.11	0.11	0.11
g_ν	2.3	12.	9.6	8.5	11.
$\mathrm{Log}_{10}\sigma^{\vec{\varphi}}_{DM-N}$	-42.3	-42.7	-42.6	-42.6	-42.6

TABLE XV: Points with $BR(h \to \varphi\varphi) = 0$ that satisfy WMAP bound within 3σ range and for which the cross section $\sigma^{\varphi}_{\mathrm{DM-N}}$ is within a 3σ range of the CREST-II region M_1 and with a m_φ that is not more than 10 GeV above the maximal (2σ) mass range for CREST-II.

VIII. SUMMARY

In this thesis we have discussed main features of various scalar extensions of the Standard Model. We studied the O(N) Singlet Scalar model with N DM candidates, Two-Higgs Doublet Model, Two-Higgs Doublet Dodel with Scalar Singlet DM candidate and Two-Component Dark Matter model, where the dark sector is composed of a neutral Majorana fermion (ν) and a neutral real singlet (φ).

We have studied thoroughly theoretical constraints imposed on all those models: perturbativity, unitarity, vacuum stability, triviality and constraints from spontaneous symmetry breaking. We have discussed experimental constraints that could be imposed on those models - various collider and cosmological limits. We have discussed the Boltzmann equations and their solutions for each model providing DM candidates. We have found regions of parameters allowed within each model, after scans performed over the model's parameter space.

In case of the O(N) Singlet Scalar Model, the low mass region $m_\varphi \lesssim 55$ GeV is excluded because of very high branching ratio of the standard Higgs boson into pairs of Dark Matter scalars ($BR(h \to \varphi\varphi) \lesssim 96\%$). However the resonance region $m_\varphi \simeq 62.5$ and heavy mass region $m_\varphi \gtrsim 200$ GeV for $N = 1$ is allowed by all constraints. If $N > 1$ than the lower bound on m_φ is stronger.

We have also shown that the Spergel-Steinhardt solution of the Dark Matter density cusp problem restricts the parameters to a Feebly Interacting Dark Matter region with $\lambda_x \sim 10^{-12} - 10^{-10}$ and scalar masses in the range $m_\varphi \sim$ 0.01-0.05 GeV.

We have also discussed the Type I and Type II 2HDM in search for maximal possible enhancement of the gluon-fusion-induced $\gamma\gamma$ signal observed at the LHC at ~ 125 GeV. We concluded that for $m_h \sim 125$ GeV, the Type II model allows a maximal enhancement of order of 2-3, whereas within the Type I model the maximal enhancement is limited to < 1.3. However, we find that in the Type II model the parameters that give $R^h_{gg}(\gamma\gamma) > 1.3$ are characterized by $R^h_{gg}(ZZ) > R^h_{gg}(\gamma\gamma)$, which is inconsistent with experimental results in the $gg \to h \to ZZ \to 4l$ channel.

We have also discussed a 2HDM suplemented by a real singlet (2HDMS), to study cosmological constraints on the singlet scalar DM candidate. If $m_S > 55$ GeV, in both the Type I and Type II, there are plentiful 2HDMS parameter choices for which the model is

consistent with all theoretical and experimental constraints. For $m_S \leq 55$ GeV, requiring $BR(h \to SS) \leq 0.1$ in order to avoid destroying the LHC fit makes it impossible (almost impossible) in the Type I (Type II) model to find parameter points that give correct Ωh^2 and lie below the LUX and SuperCDMS bounds.

In the case of the 2HDMS Type II model, a significant isospin violation in DM-nucleon scattering is possible, even reaching the value of $f_n/f_p \sim -0.7$ that would allow consistency of the LUX limit with the CDMS Si signal region. However, at the low m_S values corresponding to the CDMS Si signal region, we find that points with $f_n/f_p \sim -0.7$ either have $BR(h \to SS)$ too large or does not provide correct Ωh^2. In the end, one does find a few points ($m_S \sim 5.5-6.2$ GeV) that lie below both the SuperCDMS and LUX limits and, interestingly, also fall within (but are outside) the 99% C.L. (95% C.L.) CDMS Si signal region.

In case of 2CDMM, the Boltzmann equations for number densities of ν and φ species were solved. It has been shown that the agreement with the relic abundance and direct detection data requires that $m_\varphi \sim 62.5$ GeV and m_φ could not be much larger than m_ν.

In conclusion, simple extensions of the scalar sector of the SM are well motivated and provide solutions to various problems of the SM. They might explain theoretical problems of the SM, the newly discovered Higgs boson properties, provide Dark Matter candidates and account for the matter-antimatter asymmetry. We hope that new experimental results will help us investigate the nature of the theory of elementary particles and models presented in this thesis could be further analysed.

Appendix A: Feynman Rules

Below we present Feynman rules for various models discussed in this thesis.

1. O(N) Model

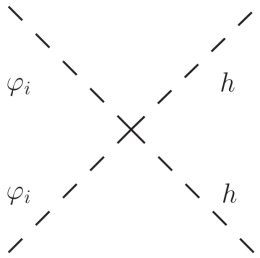

Figure 67: $i\lambda_x$

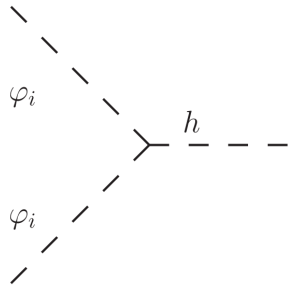

Figure 68: $i2\lambda_x v$

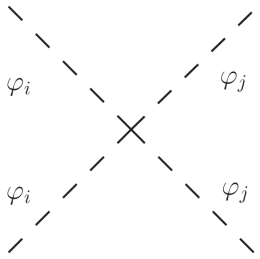

Figure 69: $\frac{i}{6}\lambda_\varphi(1+5\delta_{ij})$

Other Feynman rules follow as in the Standard Model.

2. 2HDM

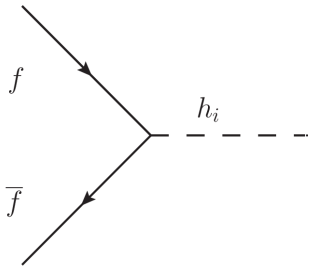

Figure 70: $-ig_{hf\bar{f}} = -i\frac{gm_f}{2m_W}C_f^{h_i}$

The quark coupling factors $C_f^{h_i}$ for Type I and II models as listed in Table III and IV. Feynman rules for the extended scalar sector of 2HDM can be found for example in [104].

3. 2HDMS

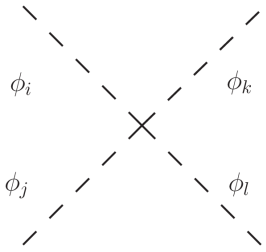

Figure 71: $ig_{\phi_i\phi_j\phi_k\phi_l}$

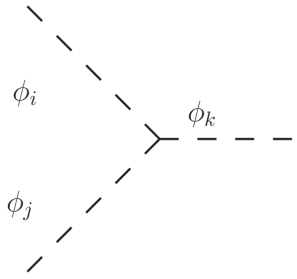

Figure 72: $ig_{\phi_i\phi_j\phi_k}$

We used a common notation for all scalars, $\phi_i = h, H, A, H^{\pm}, S$. Feynman rules for the extended scalar sector of 2HDM can be found for example in [104]. The trilinear and quadrilinear couplings of 2HDM scalars with the singlet S convert to Feynman rules according

to:

$g_{hSS,HSS} = -2\lambda_{h,H}v, \qquad g_{hhSS,HHSS} = -4\lambda_{hh,HH},$

$g_{hHSS} = -2\lambda_{hH}, \qquad g_{AASS} = g_{H^+H^-SS} = -4\lambda_{AA}.$

Appendix B: Annihilation Cross Sections

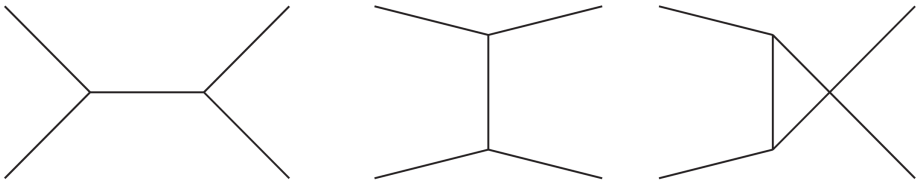

Figure 73: Diagrams for s, t and u channels momentum exchange.

We will evaluate thermally averaged cross section for a $2 \to 2$ process $12 \to 1'2'$, $\langle \sigma_{12\to 1'2'} v \rangle$. The incoming particles $1, 2$ have masses m_1 and m_2 and momenta p_1, p_2, while outgoing states $1', 2'$ have masses m_1', m_2' and momenta k_1, k_2. The amplitudes for O(N) Model, 2HDMS and 2CDMM are given in Section B 4.

1. Mandelstam variables

We define 3 Mandelstam variables s, t, u, associated with energy transfer in 3 various $2 \to 2$ processes, see Fig. 73:

$$\begin{aligned} s &= (k_1 + k_2)^2 = (p_1 + p_2)^2, \\ t &= (p_1 - k_1)^2 = (p_2 - k_2)^2, \\ u &= (p_1 - k_2)^2 = (p_2 - k_1)^2. \end{aligned} \tag{B1}$$

Those are Lorentz invariant quantities, therefore we can choose freely the reference frame for our calculation. In the CM reference frame we have:

$$\vec{p}_1 + \vec{p}_2 = 0, \qquad s = (E_1 + E_2)^2, \tag{B2}$$

$$\begin{aligned} |\vec{p}_1|^2 = |\vec{p}_2|^2 &= \frac{1}{4s}(s^2 + (m_2^2 - m_1^2)^2 - 2s(m_2^2 + m_1^2)), \\ |\vec{k}_1|^2 = |\vec{k}_2|^2 &= \frac{1}{4s}(s^2 + (m_2'^2 - m_1'^2)^2 - 2s(m_2'^2 + m_1'^2)). \end{aligned} \tag{B3}$$

We can express t and u in terms of masses and momenta:

$$\begin{aligned} t &= m_1^2 + m_1'^2 - 2\sqrt{|\vec{p}_1|^2 + m_1^2}\sqrt{|\vec{k}_1|^2 + m_1'^2} + 2|\vec{p}_1||\vec{k}_1|\cos\theta, \\ u &= m_1^2 + m_2'^2 - 2\sqrt{|\vec{p}_1|^2 + m_1^2}\sqrt{|\vec{k}_2|^2 + m_2'^2} + 2|\vec{p}_1||\vec{k}_2|\cos(\theta + \pi). \end{aligned} \tag{B4}$$

Special Case I)

We evaluate t and u in the case of DM DM $\to 1'2'$. We have $m_1 = m_2 = m_{DM}$, $s = 4m_{DM}^2$ and $|\vec{p_1}| = |\vec{p_2}| = 0$.

$$
\begin{aligned}
&|\vec{k}_1|^2 = |\vec{k}_2|^2 = \frac{1}{16m_{DM}^2}(16m_{DM}^4 + (m_2'^2 - m_1'^2)^2 - 8m_{DM}^2(m_2'^2 + m_1'^2)), \\
&t = m_{DM}^2 + m_1'^2 - 2m_{DM}\sqrt{|\vec{k}_1|^2 + m_1'^2} = m_{DM}^2 + m_1'^2 - \frac{1}{2}|4m_{DM}^2 + m_1'^2 - m_2'^2|, \\
&u = m_{DM}^2 + m_2'^2 - 2m_{DM}\sqrt{|\vec{k}_2|^2 + m_2'^2} = m_{DM}^2 + m_2'^2 - \frac{1}{2}|4m_{DM}^2 - m_1'^2 + m_2'^2|.
\end{aligned}
\tag{B5}
$$

For $m_1 = m_h$ and $m_2 = m_H$ (see 2HDMS model, Section VI A), we have:

$$
t = u = -m_S^2 + \frac{1}{2}(m_h^2 + m_H^2). \tag{B6}
$$

Special Case II)

In the case of DM DM $\to 1'1'$ (two identical particles at the end) we have $s = 4m_{DM}^2$, $m_1 = m_2 = m_{DM}$, $m_1' = m_2'$, and $|\vec{p_1}| = |\vec{p_2}| = 0$. Then

$$
\begin{aligned}
&|\vec{k}_1|^2 = |\vec{k}_2|^2 = (m_{DM}^2 - m_1'^2), \\
&t = m_{DM}^2 + m_1'^2 - 2m_{DM}^2 = -m_{DM}^2 + m_1'^2, \\
&u = m_{DM}^2 + m_2'^2 - 2m_{DM}^2 = -m_{DM}^2 + m_1'^2.
\end{aligned}
\tag{B7}
$$

2. Thermally Averaged Cross Section

We will calculate the thermally averaged cross section for a $2 \to 2$ process $12 \to 1'2'$, $\langle \sigma_{12\to 1'2'} v \rangle$. The incoming particles have masses m_1, m_2 and momenta p_1, p_2. The outgoing particles have masses m_1' and m_2' and momenta k_1, k_2, respectively. By definition we have (see also equation (29)):

$$
\begin{aligned}
\langle \sigma_{1+2\to 1'2'} |v| \rangle &= \frac{1}{n_1^{EQ} n_2^{EQ}} \int d\Pi_1 d\Pi_2 d\Pi_1' d\Pi_2' (2\pi)^4 \delta^4(P) |\mathcal{M}|^2 \tilde{f}_1^{EQ} \tilde{f}_2^{EQ} \\
&= \frac{1}{n_1^{EQ} n_2^{EQ}} \int d\Pi_1 d\Pi_2 F \sigma_{1+2\to 1+2'} \tilde{f}_1^{EQ} \tilde{f}_2^{EQ},
\end{aligned}
\tag{B8}
$$

where $F = 4E_1E_2|v|$, $|v|$ is the Mϕller velocity (see also [42] and Section III C), the momentum $P = p_1+p_2-k_2-k_2$ and $|\mathcal{M}|^2$ is the amplitude for $12 \to 1'2'$ process, averaged over initial and final spins. The amplitude should be evaluated using the common Feynman rules, including all appropriate symmetry factors.

We will perform the following substitution of variables:

$$d^3p_1d^3p_2 = 4\pi p_1E_1dE_1 4\pi p_2E_2dE_2\frac{1}{2}d(cos\theta), \tag{B9}$$

$$E_+ = E_1 + E_2, E_- = E_1 - E_2, \tag{B10}$$

$$s = m_1^2 + m_2^2 + 2E_1E_2 - 2p_1p_2cos\theta, \tag{B11}$$

$$d^3p_1d^3p_2 = 2\pi^2E_1E_2dE_+dE_-ds, \tag{B12}$$

The Jacobian of this transformation is $\frac{1}{4p_1p_2}$. The integration region: $E_1 \geq m_1$, $E_2 \geq m_2$ and $|\cos\theta| < 1$ provides the following ranges for the new variables:

$$\begin{aligned} &s \geq (m_1+m_2)^2, \qquad E_+ \geq \sqrt{s}, \\ &|E_-| \leq \sqrt{1-\frac{(m_1+m_2)^2}{s}}\sqrt{E_+^2 - s}. \end{aligned} \tag{B13}$$

We will approximate $\tilde{f}^{EQ}(E_1,T) \sim \exp(-E_1/T)$ and for simplicity neglect the internal degrees of freedom count g_i therefore:

$$\langle\sigma_{1+2\to1'2'}|v|\rangle = \frac{1}{n_1^{EQ}n_2^{EQ}}\frac{1}{32\pi^4}\int \sigma|v|\, e^{-E_+/T}\, E_1E_2dE_+dE_-ds, \tag{B14}$$

where I have simplified the notation $\sigma = \sigma_{1+2\to1+2'}$. The factor F is a function of s and masses, namely

$$F = 4\sqrt{(p_1p_2)^2 - m_1^2m_2^2} = 4\sqrt{\frac{1}{4}\left(s - m_1^2 - m_2^2\right)^2 - m_1^2m_2^2}. \tag{B15}$$

After the intergration over E_- we get:

$$\begin{aligned} \langle\sigma_{1+2\to1'2'}|v|\rangle = \frac{1}{n_1^{EQ}n_2^{EQ}}\frac{1}{16\pi^4}\int E_1E_2\,\sigma|v|\times \\ \sqrt{1-\frac{(m_1+m_2)^2}{s}}ds\, e^{-E_+/T}\sqrt{E_+^2-s}\, dE_+. \end{aligned} \tag{B16}$$

At this step we should remind ourselves of the modified Besses functions of order 1 and 2:

$$K_1(z) \;=\; z\int_1^\infty e^{-zx}(x^2-1)^{1/2}dx, \tag{B17}$$

$$K_2(z) \;=\; \frac{1}{3}z^2\int_1^\infty e^{-zx}(x^2-1)^{3/2}dx. \tag{B18}$$

We change the integrating variable $E_+ \to E_+/\sqrt{s}$ and use the Bessel functions to express the result of the integration:

$$\begin{aligned}\langle\sigma_{1+2\to1'2'}|v|\rangle &= \frac{1}{n_1^{EQ}n_2^{EQ}}\frac{T}{16\pi^4}\int E_1E_2\,\sigma v_{M\phi L}\sqrt{\left(s-(m_1+m_2)^2\right)}\,K_1(\frac{\sqrt{s}}{T})\,ds \\ &= \frac{1}{n_1^{EQ}n_2^{EQ}}\frac{T}{16\pi^4}\int \sigma\sqrt{\left(\frac{1}{4}\left(s-m_1^2-m_2^2\right)^2-m_1^2m_2^2\right)}\sqrt{\left(s-(m_1+m_2)^2\right)}\,K_1(\frac{\sqrt{s}}{T})\,ds.\end{aligned} \tag{B19}$$

In the special case of DM annihilation, $DM + DM' \to X_1 + X_2$ process, with DM mass $m_{DM} = m'_{DM}$, we have:

$$\langle\sigma_{1+2\to1'2'}|v|\rangle = \frac{T}{32\pi^4\left(n_{DM}^{EQ}\right)^2}\int_{4m_{DM}^2}^{\infty}\sigma\sqrt{s}\left(s-4m_{DM}^2\right)\,K_1(\frac{\sqrt{s}}{T})\,ds \tag{B20}$$

3. Non-Relativistic Limit

We are interested in the low temperature expansion of $\langle\sigma_{DM+DM\to1'2'}|v|\rangle$ in $x = m_{DM}/T$ [156]. We first recall the general formula for this cross section, where we approximate $\tilde{f}^{EQ}(E,T) \simeq e^{-E/T}$ and simplify the notation for the cross section (σ):

$$\langle\sigma|v|\rangle = \frac{1}{\left(n_{DM}^{EQ}\right)^2}\int d\Pi_{DM}d\Pi'_{DM}d\Pi'_1d\Pi'_2(2\pi)^4\delta^4(P)|\mathcal{M}|^2e^{-E_1/T}e^{-E_2/T} \tag{B21}$$

We define an auxiliary variable w:

$$w(s) = \sigma|v|4E_1E_2 = \int d\Pi'_1d\Pi'_2|\mathcal{M}|^2(2\pi)^4\delta^4(P). \tag{B22}$$

Then

$$\langle\sigma|v|\rangle = \frac{1}{32\pi^4\left(n_{DM}^{EQ}\right)^2}\int\,w(s)e^{-(E_1+E_2)/T}p_1dE_1p_2dE_2 \tag{B23}$$

We change the variables $E_{1,2} \to y_{1,2}$ in the following way:

$$E_{1,2} = m_{DM}(1+y_{1,2}/x), \tag{B24}$$

$$p_{1,2} = m_{DM}\sqrt{2y_{1,2}/x + y_{1,2}^2/x^2}. \tag{B25}$$

Therefore:

$$\langle\sigma|v|\rangle = \frac{m_{DM}^4e^{-2x}}{32\pi^4\left(n_{DM}^{EQ}\right)^2x^3}\int\,w(s)\,e^{-(y_1+y_2)}\sqrt{2y_1+\frac{y_1^2}{x}}\sqrt{2y_2+\frac{y_2^2}{x}}\,dy_1dy_2d(\cos\theta) \tag{B26}$$

Now we expand in x:

$$n_{DM}^{EQ} = \frac{e^{-x} m_{DM}^3}{(2\pi)^{3/2}} \left(\left(\frac{1}{x}\right)^{3/2} + \frac{15}{8}\left(\frac{1}{x}\right)^{5/2} + \frac{105}{128}\left(\frac{1}{x}\right)^{7/2} + \dots \right). \tag{B27}$$

We should also express s in terms of new variables:

$$\tilde{s} = \frac{s}{4m_{DM}^2} = 1 + \frac{1}{2}\left(\frac{y_1}{x} + \frac{y_2}{x}\right) - \frac{1}{2x}\sqrt{2y_1 + \frac{y_1^2}{x}}\sqrt{2y_2 + \frac{y_2^2}{x}}\cos\theta. \tag{B28}$$

We perform a Taylor expansion of $w(\tilde{s})$:

$$\begin{aligned} w(\tilde{s}) &= w(1) + \frac{1}{x}w'(1)\left(\frac{y_1+y_2}{2} + \sqrt{y_1 y_2}\cos\theta\right) + \\ &+ \frac{1}{2x^2}\left(w''(1)\left(\frac{y_1+y_2}{2} + \sqrt{y_1 y_2}\cos\theta\right)^2 + w'(1)\left(\frac{1}{2}y_1^{3/2}\sqrt{y_2} + \frac{1}{2}y_2^{3/2}\sqrt{y_1}\right)\cos\theta \right), \end{aligned} \tag{B29}$$

and finaly we arrive with

$$\langle \sigma |v| \rangle = \frac{w(1)}{4m_{DM}^2} + \frac{3(w'(1) - 2w(1))}{8m_{DM}^2 x} - \frac{3(5w''(1) - 11w'(1) + 16w(1))}{32 m_{DM}^2 x^2} + \dots \tag{B30}$$

The formula above contains a correction to the result obtained in [156]. For the $1/x^2$ term we have $-11w'(1)$, while in [156] the corresponding term is $-8w'$ (note that there is also a difference in the definition of the w function, by a factor of 4).

4. DM Annihilation Cross Sections

In this section we present results for the total DM annihilation cross sections for the models discussed in this Thesis.

The O(N) Model

We define an auxiliary cross section $\hat{\sigma}$ as

$$\hat{\sigma}(s) = 2\sqrt{s(s - 4m_\varphi^2)}\sigma(s) \tag{B31}$$

For the total cross section for φ_i annihilation we need to sum over all possible final states,

$$\hat{\sigma}_\varphi(s) = \hat{\sigma}_{WW}(s) + \hat{\sigma}_{ZZ}(s) + \sum_f \hat{\sigma}_{\bar{f}f}(s) + \hat{\sigma}_{hh}(s), \tag{B32}$$

where we sum over all fermions f. Only tree level processes are included in our analysis, therefore there is no $\varphi_i\varphi_i \to \gamma\gamma$. The relevant cross sections are:

$$\hat{\sigma}_{WW}(s) = \frac{\lambda_x^2}{2\pi}\sqrt{1-\frac{4M_W^2}{s}}\frac{s^2}{(s-m_h^2)^2+m_h^2\Gamma_h^2}\left(\frac{12M_W^4}{s^2}-\frac{4M_W^2}{s}+1\right), \tag{B33}$$

$$\hat{\sigma}_{ZZ}(s) = \frac{\lambda_x^2}{4\pi}\sqrt{1-\frac{4M_Z^2}{s}}\frac{s^2}{(s-m_h^2)^2+m_h^2\Gamma_h^2}\left(\frac{12M_Z^4}{s^2}-\frac{4M_Z^2}{s}+1\right), \tag{B34}$$

$$\hat{\sigma}_{\bar{f}f}(s) = \frac{\lambda_x^2}{\pi}\left(\sqrt{1-\frac{4m_f^2}{s}}\right)^3\frac{m_f^2\, s}{(s-m_h^2)^2+m_h^2\Gamma_h^2}, \tag{B35}$$

$$\begin{aligned}\hat{\sigma}_{hh}(s) = \frac{\lambda_x^2}{4\pi}\sqrt{1-\frac{4m_h^2}{s}}\Bigg(&\frac{(s+2m_h^2)^2}{(s-m_h^2)^2}+\frac{32v^4\lambda_x^2}{(s-2m_h^2)^2}\left(\frac{1}{1-\xi^2}+\tilde{F}(\xi)\right)\\ &-\frac{16v^2\lambda_x(s+2m_h^2)}{(s-2m_h^2)(s-m_h^2)}\tilde{F}(\xi)\Bigg),\end{aligned} \tag{B36}$$

where $\tilde{F}(\xi) = \mathrm{ArcTanh}(\xi)/\xi$, $\xi = \sqrt{(s-4m_h^2)(s-4m_\varphi^2)}/(s-2m_h^2)$. The total thermally averaged cross section for φ_i annihilation can be written in this simple form:

$$\langle\sigma_\varphi|v|\rangle = \frac{x}{16m_\varphi^5K_2^2(x)}\int_{4m_\varphi^2}^{\infty}dsK_1(\sqrt{s}/T)\sqrt{s-4m_\varphi^2}\hat{\sigma}_\varphi(s). \tag{B37}$$

2HDMS

In case of the 2HDMS, the total cross section of S pair annihilation at the tree level is a sum over various final states: $f\bar{f}$, W^+,W^-, ZZ, hh, hH, HH, AA, H^+H^-, see [74, 120, 125]. The general formula for the thermally averaged cross section of S pair annihilation is

$$\langle\sigma_{SS\to X\bar{X}}|v|\rangle = \sum_{\mathcal{H}=h,H}\left|\frac{g_{\mathcal{H}SS}C_X^{\mathcal{H}}}{4m_S^2-m_{\mathcal{H}}^2+i\Gamma_{\mathcal{H}}m_{\mathcal{H}}}\right|^2\frac{\Gamma_{\mathrm{SM}}(\mathcal{H}^*\to X\bar{X})}{2m_S} \tag{B38}$$

where $C_X^{\mathcal{H}}$ are the couplings of $\mathcal{H}$ to $X\bar{X}$ relative to the coupling of the SM Higgs boson (see Appendix A 2) to $X\bar{X}$, $\Gamma_{\mathrm{SM}}(\mathcal{H}^*\to X\bar{X})$ stands for the SM partial width in the $X\bar{X}$ final state calculated at invariant mass $\sqrt{s}=2m_S$ and $\Gamma_{\mathcal{H}}$ is the total width of $\mathcal{H}=h,H$. For the other channels we have:

$$\langle\sigma_{SS\to AA}|v|\rangle = \frac{1}{64\pi m_S^2}\left(1-\frac{m_A^2}{m_S^2}\right)^{1/2}\left|g_{AASS}+\sum_{\mathcal{H}=h,H}\frac{g_{\mathcal{H}SS}g_{\mathcal{H}AA}}{4m_S^2-m_{\mathcal{H}}^2+i\Gamma_{\mathcal{H}}m_{\mathcal{H}}}\right|^2 \tag{B39}$$

where the various $g_{\phi_i\phi_j\phi_k}$, $g_{\phi_i\phi_j\phi_k\phi_l}$ couplings are the Feynman rules given in Appendix A 3, see also [102].

$$\langle\sigma_{SS\to H^+H^-}|v|\rangle = \frac{1}{32\pi m_S^2}\left(1-\frac{m_{H^\pm}^2}{m_S^2}\right)^{1/2}\left|g_{H^+H^-SS}+\sum_{\mathcal{H}=h,H}\frac{g_{\mathcal{H}SS}g_{\mathcal{H}H^+H^-}}{4m_S^2-m_{\mathcal{H}}^2+i\Gamma_{\mathcal{H}}m_{\mathcal{H}}}\right|^2 \quad \text{(B40)}$$

For final states containing CP-even Higgs pairs, $(H_iH_j)=(hh),(HH),(hH)$, there are contributions from t- and u-channel S exchange (the last two diagrams with different topologies in the top row of Fig. 39) in addition to the s-channel h or H exchange diagrams and the four-point contact self-coupling. For $(H_iH_i)=(hh)$ or (HH) one obtains

$$\langle\sigma_{SS\to H_iH_i}|v|\rangle = \frac{1}{64\pi m_S^2}\left(1-\frac{m_{H_i}^2}{m_S^2}\right)^{1/2}\left|g_{H_iH_iSS}+\sum_{\mathcal{H}=h,H}\frac{g_{\mathcal{H}SS}g_{\mathcal{H}H_iH_i}}{4m_S^2-m_{\mathcal{H}}^2+i\Gamma_{\mathcal{H}}m_{\mathcal{H}}}+2\frac{g_{H_iSS}^2}{m_{H_i}^2-2m_S^2}\right|^2, \quad \text{(B41)}$$

whereas for the (hH) final state the result is

$$\begin{aligned}\langle\sigma_{SS\to hH}|v|\rangle \;=\; & \frac{1}{32\pi m_S^2}\left(1-\frac{m_h^2+m_H^2}{2m_S^2}+\frac{(m_h^2-m_H^2)^2}{16m_S^4}\right)^{1/2} \\ & \times\left|g_{hHSS}+\sum_{\mathcal{H}=h,H}\frac{g_{\mathcal{H}SS}g_{\mathcal{H}hH}}{4m_S^2-m_{\mathcal{H}}^2+i\Gamma_{\mathcal{H}}m_{\mathcal{H}}}+2\frac{g_{hSS}g_{HSS}}{\frac{1}{2}(m_h^2+m_H^2)-2m_S^2}\right|^2 \quad \text{(B42)}\end{aligned}$$

The decay width of h, H within the 2HDM is known (see [104]), however, in 2HDMS model, as discussed in Section VI E, there is an additional channel of decay present of $H_i\to SS$, $H_i=h,H$, with the decay rate:

$$\Gamma(H_i\to SS)=\frac{1}{2\pi}\frac{g_{H_iSS}^2}{m_{H_i}}\sqrt{1-\frac{4m_S^2}{m_{H_i}^2}}. \quad \text{(B43)}$$

2CDMM

For the cross section for $\varphi_i\varphi_i\to SM\,SM$ see Appendix B 4, the O(N) Model. The remaining DM↔DM cross sections are

$$\begin{aligned}\hat{\sigma}_{\vec{\varphi}\vec{\varphi}\to\nu\nu}(s) \;&=\; \int d\Pi_\nu d\Pi'_\nu |M_{\vec{\varphi}\vec{\varphi}\nu\nu}|^2(2\pi)^4\delta^4(P-p_\nu-p'_\nu) \\ \hat{\sigma}_{\nu\nu\to\vec{\varphi}\vec{\varphi}}(s) \;&=\; \int d\Pi_{\vec{\varphi}} d\Pi'_{\vec{\varphi}} |M_{\vec{\varphi}\vec{\varphi}\nu\nu}|^2(2\pi)^4\delta^4(P-p_{\vec{\varphi}}-p'_{\vec{\varphi}}) \quad \text{(B44)}\end{aligned}$$

where $d\Pi_X = g_X d^3p_X/[(2\pi)^3 2E_X]$, P is the incoming momenta and the matrix element is given by

$$|M_{\vec{\varphi}\vec{\varphi}\nu\nu}|^2(s) \;=\; -\frac{g^4\,(4m_n u^2-s)\,A(s,\theta)}{2B(s,\theta)^2C(s,\theta)^2}, \quad \text{(B45)}$$

where the coefficients A, B and C are given by

$$
\begin{aligned}
A &= 64\left(2(m_n u - M_h)^2(m_n u + M_h)^4 + 4(m_n u - M_h)M_h(m_n u + M_h)^2 m_\varphi^2 + (m_n u^2 + 2M_v)^2 m_\varphi^4\right) \\
&\quad 16\left(4(m_n u - M_h)(m_n u + M_h)^2(m_n u + 2M_h) + 2(m_n u^2 + 2m_n u M_h + 4M_h^2)m_\varphi^2 - m_\varphi^4\right) s \\
&\quad +4\left(3m_n u^2 + 8m_n u M_h + 8M_h^2 - 2m_\varphi^2\right) s^2 + s^3 + \left(4m_n u^2 - s\right)\left(-4m_\varphi^2 + s\right)^2 \mathrm{Cos}[4\theta] \\
&\quad -16 m_n u^2\left(4m_\varphi^2 - s\right)\left(4(m_n u - M_h)(m_n u + M_h)^2 + 4M_h m_\varphi^2 - (m_n u + 2M_h)s\right)\mathrm{Cos}[2\theta], \\
B &= \left(2m_n u^2 - 2M_h^2 + 2m_\varphi^2 - s + \sqrt{-4m_n u^2 + s}\sqrt{-4m_\varphi^2 + s}\mathrm{Cos}[\theta]\right), \\
C &= \left(-2m_n u^2 + 2M_h^2 - 2m_\varphi^2 + s + \sqrt{-4m_n u^2 + s}\sqrt{-4m_\varphi^2 + s}\mathrm{Cos}[\theta]\right).
\end{aligned}
$$

Appendix C: Direct Detection Cross Section

In this Appendix we present details of the calculation of the zero-momentum transfer elastic spin-independent scattering $DM + N \to DM + N$, as defined in equation (48). This part is based on the lecture notes by John F. Gunion [53] and other work on direct detection methods [51, 52]. In Section C 1 we give explicit formula for a 1-loop scattering of the fermionic DM off a nucleon in 2CDMM.

The incoming particles DM, N have masses m_{DM} and m_N and momenta p_1, p_2, respectively. Outgoing states DM', N' have momenta k_1, k_2, respectively. The momentum transfer q is defined as $q = k_1 - p_1 = p_2 - k_2$. Relative velocity $\vec{v}_{rel}$ is equal to $\vec{v}_{rel} = \vec{v}_{DM} - \vec{v}_N$. At rest the momentum of the nucleon is $p_2 = (m_N, \vec{0})$. Therefore we have

$$m_N^2 = (q - k_2)^2 = E_q^2 - |\vec{q}|^2 + 2E_q m_N + m_N^2, \tag{C1}$$

from which we conclude, that for low energies:

$$E_q \ll |\vec{q}|, \qquad |\vec{q}|^2 = 2E_q m_N \tag{C2}$$

In the CMS frame, for particles colliding along the z axis, we can write a non-relativistic approximation of DM energy and momentum:

$$\begin{aligned} p_1 &= \left(m_{DM} + \frac{m_{DM} v_{CM}^2}{2},\, 0,\, 0,\, m_{DM} v_{CM} \right) \\ p_1' &= \left(m_{DM} + \frac{m_{DM} v_{CM}^2}{2},\, m_{DM} v_{CM} \sin\theta,\, 0,\, m_{DM} v_{CM} \cos\theta \right) \end{aligned} \tag{C3}$$

In the nucleon rest frame we have the following relation between DM velocities:

$$v_{CM} = \frac{m_N}{m_{DM} + m_N} v_{LAB}. \tag{C4}$$

Note that this follows that the momentum transfer is equal to:

$$|\vec{q}|^2 \simeq -q^2 = \frac{2 m_{DM} m_N}{(m_{DM} + m_N)^2} v_{LAB}^2 (1 - \cos\theta). \tag{C5}$$

We know that the cross section is (see for example [43, 159]):

$$\frac{d\sigma}{dt} = \frac{1}{64\pi s} \frac{1}{|\vec{p}_1^{\,CM}|^2} \overline{|\mathcal{M}|^2}. \tag{C6}$$

where $\overline{|\mathcal{M}|^2}$ is the amplitude squared summed over outgoing and averaged over incoming degrees of freedom. From (C4) follows that $|\vec{p}_1^{CM}|^2 = |\vec{p}_1^{LAB}|^2 m_N/\sqrt{s}$ and $|\vec{p}_1^{LAB}| = m_{DM} v_{LAB}$, we have

$$|\vec{p}_1^{CM}| = \frac{m_{DM} m_N v_{LAB}}{\sqrt{s}} \tag{C7}$$

For $t \sim |\vec{q}|^2$ and $v = v_{LAB}$, using the definition of cross section at zero momentum transfer (48), we can write

$$\sigma_0 = \frac{1}{64\pi m_{DM}^2 m_N^2 v^2} \int_0^{4\mu_N^2 v^2} \overline{|\mathcal{M}|^2}\Big|_{|\vec{q}|^2=0} = \frac{\mu_N^2}{16\pi m_{DM}^2 m_N^2} \overline{|\mathcal{M}|^2}\Big|_{|\vec{q}|^2=0} \tag{C8}$$

Note, that $|\mathcal{M}|$ is assumed to be computed in relativistic state normalization.

1. Elastic DM Neutrino Scattering in 2CDMM

The diagram for neutrino scattering off a nucleon at 1-loop level is shown in Fig. 56. The amplitude squared for a scattering $\nu q \to \nu q$ reads:

$$|M_{\nu\nu qq}|^2 = \left(\frac{g_\nu^2 \lambda_x m_q}{32\pi^2 M_h}\right) \left(\frac{\xi(m_\nu/M_h, m_\varphi/M_h, \sqrt{t}/M_h)}{t - m_h^2}\right) \left(4m_\nu^2 - t\right) \left(4m_q^2 - t\right) \tag{C9}$$

where

$$\xi(a,b,c) = \int_0^1 dz \frac{z(1+az)}{1 - z - z(1-z)a^2 + zb^2 - z^2 u(1-u)tc^2} \tag{C10}$$

The cross section at zero momentum transfer reads

$$\sigma_{\nu-N} = \int_0^{4\mu_N^2 v^2} \frac{d\sigma(t=0)}{dt} dt = \frac{\mu_N^2}{\pi} \left(\frac{g_\nu^2 \lambda_x \xi(m_\nu/M_h, m_\varphi/M_h) m_N F_T}{32\pi^2 M_h m_h^2}\right), \tag{C11}$$

where v is the relative velocity of DM to the nucleon, $F_T = \left(\sum_q f_{Tq}^N + \frac{2}{27}\sum_Q f_{TGQ}^N\right)$, where q runs over light quarks and Q runs over heavy quarks (see Section III D or [52]), μ_N is the reduces mass defined as in 48.

Appendix D: Bibliography

[1] **Planck Collaboration** Collaboration, P. Ade et al., *Planck 2013 results. XVI. Cosmological parameters*, arXiv:1303.5076.

[2] W. de Blok, *The Core-Cusp Problem*, Adv.Astron. **2010** (2010) 789293, [arXiv:0910.3538].

[3] L. Canetti, M. Drewes, and M. Shaposhnikov, *Matter and Antimatter in the Universe*, New J.Phys. **14** (2012) 095012, [arXiv:1204.4186].

[4] **ATLAS Collaboration** Collaboration, G. Aad et al., *Observation of a new particle in the search for the Standard Model Higgs boson with the ATLAS detector at the LHC*, Phys.Lett. **B716** (2012) 1–29, [arXiv:1207.7214].

[5] **CMS Collaboration** Collaboration, S. Chatrchyan et al., *Observation of a new boson at a mass of 125 GeV with the CMS experiment at the LHC*, Phys.Lett. **B716** (2012) 30–61, [arXiv:1207.7235].

[6] P. Ferreira, R. Santos, M. Sher, and J. P. Silva, *Could the LHC two-photon signal correspond to the heavier scalar in two-Higgs-doublet models?*, Phys.Rev. **D85** (2012) 035020, [arXiv:1201.0019].

[7] P. Ferreira, R. Santos, M. Sher, and J. P. Silva, *Implications of the LHC two-photon signal for two-Higgs-doublet models*, Phys.Rev. **D85** (2012) 077703, [arXiv:1112.3277].

[8] A. Drozd, B. Grzadkowski, J. F. Gunion, and Y. Jiang, *Two-Higgs-Doublet Models and Enhanced Rates for a 125 GeV Higgs*, JHEP **1305** (2013) 072, [arXiv:1211.3580].

[9] A. Drozd, B. Grzadkowski, J. F. Gunion, and Y. Jiang, *2HDM and Enhanced Rates in gamma gamma Channel*, Acta Phys.Polon. **B44** (2013), no. 7 1417–1428.

[10] D. S. Alves, P. J. Fox, and N. J. Weiner, *Higgs Signals in a Type I 2HDM or with a Sister Higgs*, arXiv:1207.5499.

[11] H. Cheon and S. K. Kang, *Constraining parameter space in type-II two-Higgs doublet model in light of a 126 GeV Higgs boson*, JHEP **1309** (2013) 085, [arXiv:1207.1083].

[12] S. Chang, S. K. Kang, J.-P. Lee, K. Y. Lee, S. C. Park, et al., *Comprehensive study of two Higgs doublet model in light of the new boson with mass around 125 GeV*, JHEP **1305** (2013) 075, [arXiv:1210.3439].

[13] J. F. Gunion, Y. Jiang, and S. Kraml, *The Constrained NMSSM and Higgs near 125 GeV*, Phys.Lett. **B710** (2012) 454–459, [arXiv:1201.0982].

[14] B. Grzadkowski and J. Wudka, *Pragmatic approach to the little hierarchy problem: the case for Dark Matter and neutrino physics*, Phys.Rev.Lett. **103** (2009) 091802, [arXiv:0902.0628].

[15] G. Degrassi, S. Di Vita, J. Elias-Miro, J. R. Espinosa, G. F. Giudice, et al., *Higgs mass and vacuum stability in the Standard Model at NNLO*, JHEP **1208** (2012) 098, [arXiv:1205.6497].

[16] E. W. Kolb and M. S. Turner, *The Early Universe*, Front.Phys. **69** (1990) 1–547.

[17] J. Wilford, *Jan H. Oort, Dutch Astronomer In Forefront of Field, Dies at 92*, 12 November, 1992.

[18] F. Zwicky, *Die Rotverschiebung von extragalaktischen Nebeln*, Helv.Phys.Acta **6** (1933) 110–127.

[19] K. Begeman, A. Broeils, and R. Sanders, *Extended rotation curves of spiral galaxies: Dark haloes and modified dynamics*, Mon.Not.Roy.Astron.Soc. **249** (1991) 523.

[20] D. Clowe, M. Markevitch, M. Bradac, A. H. Gonzalez, S. M. Chung, et al., *On Dark Peaks and Missing Mass: A Weak Lensing Mass Reconstruction of the Merging Cluster System Abell 520*, Astrophys.J. **758** (2012) 128, [arXiv:1209.2143].

[21] G. Bertone, J. Silk, B. Moore, J. Diemand, J. Bullock, et al., *Particle Dark Matter: Observations, Models and Searches*, .

[22] L. Bergstrom, *Nonbaryonic dark matter: Observational evidence and detection methods*, Rept.Prog.Phys. **63** (2000) 793, [hep-ph/0002126].

[23] M. Markevitch, A. Gonzalez, D. Clowe, A. Vikhlinin, L. David, et al., *Direct constraints on the dark matter self-interaction cross-section from the merging galaxy cluster 1E0657-56*, Astrophys.J. **606** (2004) 819–824, [astro-ph/0309303].

[24] D. Clowe, M. Bradac, A. H. Gonzalez, M. Markevitch, S. W. Randall, et al., *A direct empirical proof of the existence of dark matter*, Astrophys.J. **648** (2006) L109–L113, [astro-ph/0608407].

[25] S. Profumo, K. Sigurdson, and L. Ubaldi, *Can we discover multi-component WIMP dark matter?*, JCAP **0912** (2009) 016, [arXiv:0907.4374].

[26] A. Drozd, B. Grzadkowski, and J. Wudka, *Multi-Scalar-Singlet Extension of the Standard Model - the Case for Dark Matter and an Invisible Higgs Boson*, JHEP **1204** (2012) 006, [arXiv:1112.2582].

[27] D. Feldman, Z. Liu, P. Nath, and G. Peim, *Multicomponent Dark Matter in Supersymmetric Hidden Sector Extensions*, Phys.Rev. **D81** (2010) 095017, [arXiv:1004.0649].

[28] J.-H. Huh, J. E. Kim, and B. Kyae, *Two dark matter components in dark matter extension of the minimal supersymmetric standard model and the high energy positron spectrum in PAMELA/HEAT data*, Phys.Rev. **D79** (2009) 063529, [arXiv:0809.2601].

[29] M. Aoki, J. Kubo, and H. Takano, *Two-loop radiative seesaw mechanism with multicomponent dark matter explaining the possible gamma excess in the Higgs boson decay and at the Fermi LAT*, Phys.Rev. **D87** (2013), no. 11 116001, [arXiv:1302.3936].

[30] P.-H. Gu, *Multi-component dark matter with magnetic moments for Fermi-LAT gamma-ray line*, Phys.Dark Univ. **2** (2013) 35–40, [arXiv:1301.4368].

[31] S. Esch, M. Klasen, and C. E. Yaguna, *A minimal model for two-component dark matter*, arXiv:1406.0617.

[32] S. Bhattacharya, A. Drozd, B. Grzadkowski, and J. Wudka, *Two-Component Dark Matter*, JHEP **1310** (2013) 158, [arXiv:1309.2986].

[33] S. Bhattacharya, A. Drozd, B. Grzadkowski, and J. Wudka, *Constraints on Two-Component Dark Matter*, Acta Phys.Polon. **B44** (2013), no. 11 2373–2379, [arXiv:1310.7901].

[34] F. Governato, C. Brook, L. Mayer, A. Brooks, G. Rhee, et al., *At the heart of the matter: the origin of bulgeless dwarf galaxies and Dark Matter cores*, Nature **463** (2010) 203–206, [arXiv:0911.2237].

[35] M. Rocha, A. H. Peter, J. S. Bullock, M. Kaplinghat, S. Garrison-Kimmel, et al., *Cosmological Simulations with Self-Interacting Dark Matter I: Constant Density Cores and Substructure*, Mon.Not.Roy.Astron.Soc. **430** (2013) 81–104, [arXiv:1208.3025].

[36] A. H. Peter, M. Rocha, J. S. Bullock, and M. Kaplinghat, *Cosmological Simulations with Self-Interacting Dark Matter II: Halo Shapes vs. Observations*, arXiv:1208.3026.

[37] M. V. Medvedev, *Cosmological Simulations of Multi-Component Cold Dark Matter*, arXiv:1305.1307.

[38] V. Semenov, S. Pilipenko, A. Doroshkevich, V. Lukash, and E. Mikheeva, *Dark matter halo formation in the multicomponent dark matter models*, arXiv:1306.3210.

[39] R. Peccei, *The Strong CP problem and axions*, Lect.Notes Phys. **741** (2008) 3–17, [hep-ph/0607268].

[40] K. R. Dienes and B. Thomas, *Dynamical Dark Matter: I. Theoretical Overview*, Phys.Rev.

D85 (2012) 083523, [arXiv:1106.4546].

[41] L. M. Carpenter, A. Nelson, C. Shimmin, T. M. Tait, and D. Whiteson, *Collider searches for dark matter in events with a Z boson and missing energy*, Phys.Rev. **D87** (2013), no. 7 074005, [arXiv:1212.3352].

[42] P. Gondolo and G. Gelmini, *Cosmic abundances of stable particles: Improved analysis*, Nucl.Phys. **B360** (1991) 145–179.

[43] M. E. Peskin and D. V. Schroeder, *An Introduction to quantum field theory*, .

[44] V. Mukhanov, *Physical foundations of cosmology*, .

[45] J. McDonald, *Thermally generated gauge singlet scalars as selfinteracting dark matter*, Phys.Rev.Lett. **88** (2002) 091304, [hep-ph/0106249].

[46] L. J. Hall, K. Jedamzik, J. March-Russell, and S. M. West, *Freeze-In Production of FIMP Dark Matter*, JHEP **1003** (2010) 080, [arXiv:0911.1120].

[47] C. E. Yaguna, *The Singlet Scalar as FIMP Dark Matter*, JHEP **1108** (2011) 060, [arXiv:1105.1654].

[48] E. Molinaro, C. E. Yaguna, and O. Zapata, *FIMP realization of the scotogenic model*, JCAP **1407** (2014) 015, [arXiv:1405.1259].

[49] M. Blennow, E. Fernandez-Martinez, and B. Zaldivar, *Freeze-in through portals*, arXiv:1309.7348.

[50] M. W. Goodman and E. Witten, *Detectability of Certain Dark Matter Candidates*, Phys.Rev. **D31** (1985) 3059.

[51] G. Jungman, M. Kamionkowski, and K. Griest, *Supersymmetric dark matter*, Phys.Rept. **267** (1996) 195–373, [hep-ph/9506380].

[52] G. Belanger, F. Boudjema, A. Pukhov, and A. Semenov, *Dark matter direct detection rate in a generic model with micrOMEGAs 2.2*, Comput.Phys.Commun. **180** (2009) 747–767, [arXiv:0803.2360].

[53] J. Gunion, *Lecture Notes*, higgs.physics.ucdavis.edu/gunion/.

[54] M. Reid, *The distance to the center of the galaxy*, Ann.Rev.Astron.Astrophys. **31** (1993) 345–372.

[55] M. Weber and W. de Boer, *Determination of the Local Dark Matter Density in our Galaxy*, Astron.Astrophys. **509** (2010) A25, [arXiv:0910.4272].

[56] M. C. Smith, G. Ruchti, A. Helmi, R. Wyse, J. Fulbright, et al., *The RAVE Survey:*

Constraining the Local Galactic Escape Speed, Mon.Not.Roy.Astron.Soc. **379** (2007) 755–772, [astro-ph/0611671].

[57] F. J. Kerr and D. Lynden-Bell, *Review of galactic constants*, Mon.Not.Roy.Astron.Soc. **221** (1986) 1023.

[58] J. Herrero-Garcia, T. Schwetz, and J. Zupan, *On the annual modulation signal in dark matter direct detection*, JCAP **1203** (2012) 005, [arXiv:1112.1627].

[59] K. Freese, M. Lisanti, and C. Savage, *Annual Modulation of Dark Matter: A Review*, Rev.Mod.Phys. **85** (2013) 1561–1581, [arXiv:1209.3339].

[60] **DAMA Collaboration, LIBRA Collaboration** Collaboration, R. Bernabei et al., *New results from DAMA/LIBRA*, Eur.Phys.J. **C67** (2010) 39–49, [arXiv:1002.1028].

[61] M. A. Shifman, A. Vainshtein, and V. I. Zakharov, *Remarks on Higgs Boson Interactions with Nucleons*, Phys.Lett. **B78** (1978) 443.

[62] R. Barbieri and G. Curci, *On the Higgs Coupling to Nucleons and Pions*, Phys.Lett. **B219** (1989) 503.

[63] G. Belanger, F. Boudjema, A. Pukhov, and A. Semenov, *micrOMEGAs 3: A program for calculating dark matter observables*, Comput.Phys.Commun. **185** (2014) 960–985, [arXiv:1305.0237].

[64] **CDMS Collaboration** Collaboration, R. Agnese et al., *Silicon detector results from the first five-tower run of CDMS II*, Phys.Rev. **D88** (2013) 031104, [arXiv:1304.3706].

[65] **CDMS Collaboration** Collaboration, R. Agnese et al., *Silicon Detector Dark Matter Results from the Final Exposure of CDMS II*, Phys.Rev.Lett. **111** (2013) 251301, [arXiv:1304.4279].

[66] C. Aalseth, P. Barbeau, J. Colaresi, J. D. Leon, J. Fast, et al., *Maximum Likelihood Signal Extraction Method Applied to 3.4 years of CoGeNT Data*, arXiv:1401.6234.

[67] **LUX Collaboration** Collaboration, D. Akerib et al., *First results from the LUX dark matter experiment at the Sanford Underground Research Facility*, Phys.Rev.Lett. **112** (2014) 091303, [arXiv:1310.8214].

[68] **CRESST-II Collaboration** Collaboration, G. Angloher et al., *Results on low mass WIMPs using an upgraded CRESST-II detector*, arXiv:1407.3146.

[69] **SuperCDMS Collaboration** Collaboration, R. Agnese et al., *Search for Low-Mass WIMPs with SuperCDMS*, Phys.Rev.Lett. **112** (2014) 241302, [arXiv:1402.7137].

[70] G. Angloher, M. Bauer, I. Bavykina, A. Bento, C. Bucci, et al., *Results from 730 kg days of the CRESST-II Dark Matter Search*, Eur.Phys.J. **C72** (2012) 1971, [arXiv:1109.0702].

[71] R. Bernabei, P. Belli, F. Cappella, V. Caracciolo, S. Castellano, et al., *Final model independent result of DAMA/LIBRA-phase1*, Eur.Phys.J. **C73** (2013) 2648, [arXiv:1308.5109].

[72] R. STRAUSS, "New results from the cresst experiment." talk @ Astroparticle Physics 2014, Amsterdam.

[73] J. L. Feng, J. Kumar, D. Marfatia, and D. Sanford, *Isospin-Violating Dark Matter*, Phys.Lett. **B703** (2011) 124–127, [arXiv:1102.4331].

[74] A. Drozd, B. Grzadkowski, J. F. Gunion, and Y. Jiang, *Extending two-Higgs-doublet models by a singlet scalar field - the Case for Dark Matter*, arXiv:1408.2106.

[75] D. Tucker-Smith and N. Weiner, *Inelastic dark matter*, Phys.Rev. **D64** (2001) 043502, [hep-ph/0101138].

[76] P. W. Graham, R. Harnik, S. Rajendran, and P. Saraswat, *Exothermic Dark Matter*, Phys.Rev. **D82** (2010) 063512, [arXiv:1004.0937].

[77] M. Veltman and F. Yndurain, *RADIATIVE CORRECTIONS TO W W SCATTERING*, Nucl.Phys. **B325** (1989) 1.

[78] V. Silveira and A. Zee, *SCALAR PHANTOMS*, Phys.Lett. **B161** (1985) 136.

[79] J. McDonald, *Gauge singlet scalars as cold dark matter*, Phys.Rev. **D50** (1994) 3637–3649, [hep-ph/0702143].

[80] C. Burgess, M. Pospelov, and T. ter Veldhuis, *The Minimal model of nonbaryonic dark matter: A Singlet scalar*, Nucl.Phys. **B619** (2001) 709–728, [hep-ph/0011335].

[81] A. Djouadi, O. Lebedev, Y. Mambrini, and J. Quevillon, *Implications of LHC searches for Higgs–portal dark matter*, Phys.Lett. **B709** (2012) 65–69, [arXiv:1112.3299].

[82] J. M. Cline, K. Kainulainen, P. Scott, and C. Weniger, *Update on scalar singlet dark matter*, Phys.Rev. **D88** (2013) 055025, [arXiv:1306.4710].

[83] A. Drozd, *RGE and the Fine-Tuning Problem*, arXiv:1202.0195.

[84] B. W. Lee, C. Quigg, and H. Thacker, *Weak Interactions at Very High-Energies: The Role of the Higgs Boson Mass*, Phys.Rev. **D16** (1977) 1519.

[85] G. Cynolter, E. Lendvai, and G. Pocsik, *Note on unitarity constraints in a model for a singlet scalar dark matter candidate*, Acta Phys.Polon. **B36** (2005) 827–832,

[hep-ph/0410102].

[86] **Particle Data Group** Collaboration, J. Beringer et al., *Review of Particle Physics (RPP)*, Phys.Rev. **D86** (2012) 010001.

[87] B. Grzadkowski and M. Lindner, *Stability of Triviality Mass Bounds in the Standard Model*, Phys.Lett. **B178** (1986) 81.

[88] M. Veltman, *The Infrared - Ultraviolet Connection*, Acta Phys.Polon. **B12** (1981) 437.

[89] R. Barbieri and G. Giudice, *Upper Bounds on Supersymmetric Particle Masses*, Nucl.Phys. **B306** (1988) 63.

[90] M. Einhorn and D. Jones, *The Effective potential and quadratic divergences*, Phys.Rev. **D46** (1992) 5206–5208.

[91] C. F. Kolda and H. Murayama, *The Higgs mass and new physics scales in the minimal standard model*, JHEP **0007** (2000) 035, [hep-ph/0003170].

[92] J. R. Primack, *Dark matter and structure formation*, astro-ph/9707285.

[93] W.-L. Guo and Y.-L. Wu, *The Real singlet scalar dark matter model*, JHEP **1010** (2010) 083, [arXiv:1006.2518].

[94] ATLAS, *Latest results from atlas higgs search*, July, 2012.

[95] CMS, *Observation of a new particle with a mass of 125 gev*, July, 2012.

[96] **CMS Collaboration** Collaboration, *Combination of standard model Higgs boson searches and measurements of the properties of the new boson with a mass near 125 GeV*, .

[97] B. Swiezewska and M. Krawczyk, *Diphoton rate in the inert doublet model with a 125 GeV Higgs boson*, Phys.Rev. **D88** (2013), no. 3 035019, [arXiv:1212.4100].

[98] W. Altmannshofer, S. Gori, and G. D. Kribs, *A Minimal Flavor Violating 2HDM at the LHC*, Phys.Rev. **D86** (2012) 115009, [arXiv:1210.2465].

[99] C.-Y. Chen and S. Dawson, *Exploring Two Higgs Doublet Models Through Higgs Production*, Phys.Rev. **D87** (2013), no. 5 055016, [arXiv:1301.0309].

[100] A. Celis, V. Ilisie, and A. Pich, *LHC constraints on two-Higgs doublet models*, JHEP **1307** (2013) 053, [arXiv:1302.4022].

[101] G. Branco, P. Ferreira, L. Lavoura, M. Rebelo, M. Sher, et al., *Theory and phenomenology of two-Higgs-doublet models*, Phys.Rept. **516** (2012) 1–102, [arXiv:1106.0034].

[102] J. F. Gunion and H. E. Haber, *The CP conserving two Higgs doublet model: The Approach to the decoupling limit*, Phys.Rev. **D67** (2003) 075019, [hep-ph/0207010].

[103] D. Eriksson, J. Rathsman, and O. Stal, *2HDMC: Two-Higgs-Doublet Model Calculator Physics and Manual*, Comput.Phys.Commun. **181** (2010) 189–205, [arXiv:0902.0851].

[104] J. F. Gunion, H. E. Haber, G. L. Kane, and S. Dawson, *The Higgs Hunter's Guide*, Front.Phys. **80** (2000) 1–448.

[105] D. Eriksson, J. Rathsman, and O. Stal, *2HDMC: Two-Higgs-doublet model calculator*, Comput.Phys.Commun. **181** (2010) 833–834.

[106] B. Swiezewska, *Warunki Unitarnosci Dla Inert Doublet Model*, unpublished **in polish** (2011).

[107] A. G. Akeroyd, A. Arhrib, and E.-M. Naimi, *Note on tree level unitarity in the general two Higgs doublet model*, Phys.Lett. **B490** (2000) 119–124, [hep-ph/0006035].

[108] A. Arhrib, *Unitarity constraints on scalar parameters of the standard and two Higgs doublets model*, hep-ph/0012353.

[109] J. Horejsi and M. Kladiva, *Tree-unitarity bounds for THDM Higgs masses revisited*, Eur.Phys.J. **C46** (2006) 81–91, [hep-ph/0510154].

[110] I. Ginzburg and I. Ivanov, *Tree-level unitarity constraints in the most general 2HDM*, Phys.Rev. **D72** (2005) 115010, [hep-ph/0508020].

[111] G. Funk, D. O'Neil, and R. M. Winters, *What the Oblique Parameters S, T, and U and Their Extensions Reveal About the 2HDM: A Numerical Analysis*, Int.J.Mod.Phys. **A27** (2012) 1250021, [arXiv:1110.3812].

[112] **OPAL Collaboration** Collaboration, G. Abbiendi et al., *Decay mode independent searches for new scalar bosons with the OPAL detector at LEP*, Eur.Phys.J. **C27** (2003) 311–329, [hep-ex/0206022].

[113] **OPAL Collaboration** Collaboration, G. Abbiendi et al., *Flavor independent h0A0 search and two Higgs doublet model interpretation of neutral Higgs boson searches at LEP*, Eur.Phys.J. **C40** (2005) 317–332, [hep-ex/0408097].

[114] S. M. Barr and A. Zee, *Electric Dipole Moment of the Electron and of the Neutron*, Phys.Rev.Lett. **65** (1990) 21–24.

[115] **LHC Higgs Cross Section Working Group** Collaboration, S. Dittmaier et al., *Handbook of LHC Higgs Cross Sections: 1. Inclusive Observables*, arXiv:1101.0593.

[116] T. A. collaboration, *Updated coupling measurements of the Higgs boson with the ATLAS detector using up to 25 fb^{-1} of proton-proton collision data*, .

[117] **CMS Collaboration** Collaboration, C. Collaboration, *Precise determination of the mass of the Higgs boson and studies of the compatibility of its couplings with the standard model*, .

[118] J. F. Gunion, Y. Jiang, and S. Kraml, *Could two NMSSM Higgs bosons be present near 125 GeV?*, Phys.Rev. **D86** (2012) 071702, [arXiv:1207.1545].

[119] X.-G. He, T. Li, X.-Q. Li, J. Tandean, and H.-C. Tsai, *Constraints on Scalar Dark Matter from Direct Experimental Searches*, Phys.Rev. **D79** (2009) 023521, [arXiv:0811.0658].

[120] B. Grzadkowski and P. Osland, *Tempered Two-Higgs-Doublet Model*, Phys.Rev. **D82** (2010) 125026, [arXiv:0910.4068].

[121] M. Boucenna and S. Profumo, *Direct and Indirect Singlet Scalar Dark Matter Detection in the Lepton-Specific two-Higgs-doublet Model*, Phys.Rev. **D84** (2011) 055011, [arXiv:1106.3368].

[122] X.-G. He, B. Ren, and J. Tandean, *Hints of Standard Model Higgs Boson at the LHC and Light Dark Matter Searches*, Phys.Rev. **D85** (2012) 093019, [arXiv:1112.6364].

[123] Y. Bai, V. Barger, L. L. Everett, and G. Shaughnessy, *Two-Higgs-doublet-portal dark-matter model: LHC data and Fermi-LAT 135 GeV line*, Phys.Rev. **D88** (2013), no. 1 015008, [arXiv:1212.5604].

[124] X.-G. He and J. Tandean, *Low-Mass Dark-Matter Hint from CDMS II, Higgs Boson at the LHC, and Darkon Models*, Phys.Rev. **D88** (2013) 013020, [arXiv:1304.6058].

[125] Y. Cai and T. Li, *Singlet dark matter in a type II two Higgs doublet model*, Phys.Rev. **D88** (2013), no. 11 115004, [arXiv:1308.5346].

[126] L. Wang, *A simplified 2HDM with a scalar dark matter and the galactic center gamma-ray excess*, arXiv:1406.3598.

[127] C.-Y. Chen, M. Freid, and M. Sher, *The Next-to-Minimal Two Higgs Doublet Model*, Phys.Rev. **D89** (2014) 075009, [arXiv:1312.3949].

[128] J. Guo and Z. Kang, *Higgs Naturalness and Dark Matter Stability by Scale Invariance*, arXiv:1401.5609.

[129] M. Kadastik, K. Kannike, and M. Raidal, *Matter parity as the origin of scalar Dark Matter*, Phys.Rev. **D81** (2010) 015002, [arXiv:0903.2475].

[130] M. Kadastik, K. Kannike, and M. Raidal, *Dark Matter as the signal of Grand Unification*, Phys.Rev. **D80** (2009) 085020, [arXiv:0907.1894].

[131] M. Kadastik, K. Kannike, A. Racioppi, and M. Raidal, *EWSB from the soft portal into*

Dark Matter and prediction for direct detection, Phys.Rev.Lett. **104** (2010) 201301, [arXiv:0912.2729].

[132] B. Dumont, J. F. Gunion, Y. Jiang, and S. Kraml, *Constraints on and future prospects for Two-Higgs-Doublet Models in light of the LHC Higgs signal*, arXiv:1405.3584.

[133] R. A. Horn and C. R. Johnson, *Matrix Analysis, page 185*, 1985. Cambridge University Press.

[134] **ATLAS Collaboration** Collaboration, *Measurements of the properties of the Higgs-like boson in the two photon decay channel with the ATLAS detector using 25* fb^{-1} *of proton-proton collision data*, .

[135] **CMS Collaboration** Collaboration, C. Collaboration, *Search for a heavy Higgs boson in the H to ZZ to 2l2nu channel in pp collisions at sqrt(s)= 7 and 8 TeV*, .

[136] C.-W. Chiang and K. Yagyu, *Implications of Higgs boson search data on the two-Higgs doublet models with a softly broken Z_2 symmetry*, JHEP **1307** (2013) 160, [arXiv:1303.0168].

[137] B. Grinstein and P. Uttayarat, *Carving Out Parameter Space in Type-II Two Higgs Doublets Model*, JHEP **1306** (2013) 094, [arXiv:1304.0028].

[138] B. Coleppa, F. Kling, and S. Su, *Constraining Type II 2HDM in Light of LHC Higgs Searches*, JHEP **1401** (2014) 161, [arXiv:1305.0002].

[139] O. Eberhardt, U. Nierste, and M. Wiebusch, *Status of the two-Higgs-doublet model of type II*, JHEP **1307** (2013) 118, [arXiv:1305.1649].

[140] N. Craig, J. Galloway, and S. Thomas, *Searching for Signs of the Second Higgs Doublet*, arXiv:1305.2424.

[141] V. Barger, L. L. Everett, H. E. Logan, and G. Shaughnessy, *Scrutinizing the 125 GeV Higgs boson in two Higgs doublet models at the LHC, ILC, and Muon Collider*, Phys.Rev. **D88** (2013), no. 11 115003, [arXiv:1308.0052].

[142] S. Chang, S. K. Kang, J.-P. Lee, K. Y. Lee, S. C. Park, et al., *Two Higgs doublet models for the LHC Higgs boson data at* $\sqrt{s} = 7$ *and 8 TeV*, arXiv:1310.3374.

[143] K. Cheung, J. S. Lee, and P.-Y. Tseng, *Higgcision in the Two-Higgs Doublet Models*, JHEP **1401** (2014) 085, [arXiv:1310.3937].

[144] A. Celis, V. Ilisie, and A. Pich, *Towards a general analysis of LHC data within two-Higgs-doublet models*, JHEP **1312** (2013) 095, [arXiv:1310.7941].

[145] J. Baglio, O. Eberhardt, U. Nierste, and M. Wiebusch, *Benchmarks for Higgs Pair Production and Heavy Higgs Searches in the Two-Higgs-Doublet Model of Type II*, Phys.Rev. **D90** (2014) 015008, [arXiv:1403.1264].

[146] P. Ferreira, J. F. Gunion, H. E. Haber, and R. Santos, *Probing wrong-sign Yukawa couplings at the LHC and a future linear collider*, Phys.Rev. **D89** (2014) 115003, [arXiv:1403.4736].

[147] S. Kanemura, H. Yokoya, and Y.-J. Zheng, *Complementarity in direct searches for additional Higgs bosons at the LHC and the International Linear Collider*, Nucl.Phys. **B886** (2014) 524–553, [arXiv:1404.5835].

[148] V. Ilisie and A. Pich, *Low-mass fermiophobic charged Higgs phenomenology in two-Higgs-doublet models*, arXiv:1405.6639.

[149] S. Kanemura, K. Tsumura, K. Yagyu, and H. Yokoya, *Fingerprinting non-minimal Higgs sectors*, arXiv:1406.3294.

[150] D. Das, L. Mitzka, and W. Porod, *Discovery of Charged Higgs through gamma gamma final states*, arXiv:1408.1704.

[151] A. Arhrib, P. Ferreira, and R. Santos, *Are There Hidden Scalars in LHC Higgs Results?*, JHEP **1403** (2014) 053, [arXiv:1311.1520].

[152] G. Belanger, B. Dumont, U. Ellwanger, J. Gunion, and S. Kraml, *Global fit to Higgs signal strengths and couplings and implications for extended Higgs sectors*, Phys.Rev. **D88** (2013) 075008, [arXiv:1306.2941].

[153] M. Carena, I. Low, N. R. Shah, and C. E. Wagner, *Impersonating the Standard Model Higgs Boson: Alignment without Decoupling*, JHEP **1404** (2014) 015, [arXiv:1310.2248].

[154] **CMS Collaboration** Collaboration, S. Chatrchyan et al., *Search for invisible decays of Higgs bosons in the vector boson fusion and associated ZH production modes*, Eur.Phys.J. **C74** (2014) 2980, [arXiv:1404.1344].

[155] G. Belanger, F. Boudjema, A. Pukhov, and A. Semenov, *micrOMEGAs4.1: two dark matter candidates*, arXiv:1407.6129.

[156] M. Srednicki, R. Watkins, and K. A. Olive, *Calculations of Relic Densities in the Early Universe*, Nucl.Phys. **B310** (1988) 693.

[157] **WMAP** Collaboration, G. Hinshaw et al., *Nine-Year Wilkinson Microwave Anisotropy Probe (WMAP) Observations: Cosmological Parameter Results*, Astrophys.J.Suppl. **208** (2013) 19, [arXiv:1212.5226].

[158] **XENON100 Collaboration** Collaboration, E. Aprile et al., *Dark Matter Results from 225 Live Days of XENON100 Data*, Phys.Rev.Lett. **109** (2012) 181301, [arXiv:1207.5988].

[159] M. Srednicki, *Quantum field theory*, .